The Dual Photochemistry of Anthracene-9,10-endoperoxide:

Exploring the Competing Ultrafast Photoinduced Reactions of a Model Aromatic Endoperoxide

Dissertation

zur Erlangung des Doktorgrades

am Fachbereich Physik
der Freien Universität Berlin

eingereicht von
Alexandra Lauer

Berlin, Dezember 2010

Diese Dissertation wurde in der Arbeitsgruppe von Prof. K. Heyne in der Zeit vom 01. Februar 2006 bis zum 07. Dezember 2010 erstellt.
Hiermit versichere ich, dass ich diese Arbeit selbständig ohne unerlaubte Hilfe angefertigt und alle verwendeten Quellen und Hilfsmittel angegeben habe.

Berlin, 07. Dezember 2010

Alexandra Lauer

Erstgutachter: Prof. K. Heyne

Zweitgutachter: Prof. L. Wöste

Datum der Disputation: 26. Januar 2011

Für meine Eltern, und für Alexander.

Danke für Alles.

"Was ist die Wirklichkeit? Wie definiert man das: Realität?
Wenn du darunter verstehst, was du fühlst, riechen, schmecken oder sehen kannst ist Wirklichkeit nichts weiter als elektrische Signale interpretiert von deinem Verstand."

Morpheus in "Matrix"

"Mein Universum sind meine Augen und meine Ohren. Alles andere ist nur Gerücht."
"Woher soll ich wissen, ob die Vergangenheit keine Fiktion ist, die nur erfunden ist, um den Zwiespalt zwischen meinen augenblicklichen Sinneswahrnehmungen und meiner Geistesverfassung zu erklären?"

Herrscher des Universums, in "Macht's gut, und danke für den Fisch"
(Teil 4 von "Per Anhalter durch die Galaxis")

Contents

Kurzfassung

Aromatische Endoperoxide können $^1O_2$, den Hauptwirkstoff in der Photodynamischen Krebstherapie, in einer intramolekularen Cycloreversions-Reaktion erzeugen. Je nachdem, in welchem Spektralbereich die Lichtanregung erfolgt, können jedoch auch andere Photoprodukte auftreten. Die Frage, welche elektronischen Zustände für die verschiedenen Reaktionswege verantwortlich sind, wurde in der Literatur kontrovers diskutiert; die vorgeschlagene Konkurrenz zwischen zwei primären Reaktionskanälen, die über verschiedene elektronisch angeregte Singulett-Zustände verlaufen, wird als Duale Photochemie bezeichnet.
In der vorliegenden Arbeit wird eine neue Zuordnung der elektronisch angeregten Singulett-Zustände von Anthrazen-9,10-Endoperoxid (APO) vorgeschlagen, die aus polarisationsaufgelösten Femtosekunden UV-Pump / IR-Probe Experimenten, unterstützt durch quantenchemische ab-initio Berechnungen, hervorgeht. Insbesondere wird der umstrittene S_1-Zustand bei 290 nm lokalisiert; die beiden Absorptions-Schultern bei 280 und 270 nm werden dem S_2- bzw. dem S_4-Zustand zugeordnet. Des weiteren wird zum erstenmal Emission von einem aromatischen Endoperoxid beobachtet, die vermutlich vom Anthrazen-1,4-Endoperoxid-Isomer stammt.
Auf Basis dieser neuen Zuordnung der elektronischen Zustände werden nun wellenlängen-abhängige Messungen der Photoprodukt-Quantenausbeuten durchgeführt, die Einsicht in die zustands-spezifischen Reaktionspfade geben sollen; dabei werden ^1H NMR- und Absorptions-Spektren zu Quantifizierung verwendet. Anthrazen (AC) und $^1O_2$ treten nur bei Anregungs-Energien oberhalb von S_1 auf. Der Großteil des AC entsteht im elektronischen Grundzustand, neben 1 – 2 % Triplett-AC. Die maximale Quanten-Ausbeute für die AC-Erzeugung beträgt 29 %, bei Anregung mit 270 nm, was darauf hindeutet, dass die AC-Bildung effizient mit der inneren Konvesion zum S_1-Zustand konkurrieren kann. Ausgehend vom S_1-Zustand, der entweder durch direkte Anregung oder durch innere Konversion von höher gelegenen Zuständen populiert wurde, sind nur Reaktionsprodukte zu beobachten, die aus einer Spaltung der Peroxid-Bindung resultieren. Als Zwischenprodukt wird ein Biradikal vorgeschlagen; ein Diepoxid (DE) ist jedoch das erste beobachtbare Reaktionsprodukt. Das DE ist instabil und reagiert weiter zu Anthrachinon, was auch bei RT als einziges Thermolyseprodukt auftritt. Darüber hinaus kann das DE zu einem bicyclischen Acetal weiterreagieren, falls das DE selbst wiederum durch Licht angeregt wird. Alle aus der Peroxid-Spaltung hervorgehenden Produkte zusammen dominieren gegenüber der AC-Erzeugung bei allen Anregungswellenlängen, mit Ausbeuten von über 70 %. Alle chemischen Reaktionen zusammen machen bei Wellenlängen < 310 nm annähernd 100 % aus, was bedeutet dass nicht-chemische Relaxation von angeregtem APO so gut wie nicht auftritt. Bei erhöhter Temperatur und/oder höher konzentrierter Lösung werden noch weitere Nebenprodukte gebildet, die aus bimolekularen Reaktionen stammen könnten. Einblicke in die zugrunde liegenden Prozesse können Experimente mit hoher Zeitauflösung gewähren. Femtosekunden-aufgelöste transiente Absorptionsmessungen enthüllen die ultraschnellen Zeitskalen der konkurrierenden Photoreaktionen: Sowohl AC als auch das DE sind bereits innerhalb von weniger als 3 ps vorhanden. Auf einer Zeitskala von 18 – 21 ps geben beide die ursprünglich vorhandene Schwingungsenergie ab. Während AC im elektronischen Grundzustand erzeugt wird, verbleibt das DE für mehr als 100 ps in einem elektronisch angeregten Zustand. Die hier beobachtete ultraschnelle AC-Bildung kann die Effizienz der Reaktion aus höher angeregten Zuständen erklären und somit eine Begründung für das Phänomen der Dualen Photochemie liefern.

Abstract

Aromatic endoperoxides can create $^1O_2$, the main active agent in photodynamic therapy of cancer, in an intramolecular cycloreversion reaction. However, depending on excitation wavelength, various other photoproducts are also generated. The question which electronic states are responsible for the different reaction pathways has been a controversial issue in literature; the suggested competition between two primary photoreaction channels that proceed via different excited singlet states is denoted as dual photochemistry.

A new assignment for the electronic excited singlet states of anthracene-9,10-endoperoxide (APO) is now proposed as a conclusion from polarization-resolved femtosecond UV pump – IR probe experiments, which are supported by high-level *ab initio* calculations. In particular, the disputed S_1 state is located around 290 nm; the absorption shoulders at 280 and 270 nm are now assigned to the S_2 and S_4 states, respectively. Furthermore, emission from an aromatic endoperoxide is observed for the first time, which presumably originates from the anthracene-1,4-endoperoxide isomer.

With the new electronic state assignment at hand, wavelength dependent photoproduct quantum yields measurements are now performed to elucidate the state-specific reaction pathways, using ^1H NMR and absorption measurements. Anthracene (AC) and $^1O_2$ formation is only observed upon photo-excitation with energies above S_1. The majority of AC is generated in the electronic ground state, along with 1 – 2 % triplet state AC. The maximum AC photoproduct quantum yield is 29 % at 270 nm, indicating that AC formation efficiently competes with IC to S_1. From the S_1 state, populated either upon direct excitation or after IC from higher excited states, only photoproducts are formed that involve initial cleavage of the endoperoxide bond. A biradical intermediate is suggested, and a diepoxide (DE) is observed as the primary reaction product. The DE is not stable and reacts further to anthraquinone , which is also found as the only thermolysis product at RT. Moreover, DE generates a bicyclic acetal if DE itself is photoexcited. The photoproduct generation from all O-O cleavage products together dominates over AC formation at all excitation wavelengths, with a yields of > 70 %. The total chemical conversion is close to 100 % upon excitation at < 310 nm, indicating that relaxation paths other than chemical conversion are virtually absent. At higher temperatures and/or higher concentrations, additional minor products are formed, which may originate from bimolecular reactions.

To gain insight into the underlying processes, the photoreactions are examined in a time resolved experiment with high temporal resolution. Femtosecond UV pump – supercontinuum probe transient absorption spectroscopy reveals the ultrafast time scales of the competing primary photoreactions: Both primary photoproducts, AC and DE, are already formed within less than 3 ps. The initially high vibrational excess energy is dissipated on time scales of 18 – 21 ps for both AC and DE. While AC is generated in the electronic ground state, DE resides in an electronic excited state for more than 100 ps. The ultrafast AC formation observed here can help explaining the efficient competition with IC from higher excited states, and thus elucidate the phenomenon of dual photochemistry in aromatic endoperoxides.

1 Introduction

1.1 Motivation

Photodynamic Therapy of Cancer

Cancer is the second most important cause of death and morbidity in Europe (Eurostat[1], 2003); new methods for effective cancer treatment are therefore excessively searched for. A promising approach for this challenge is the Photodynamic Therapy (PDT) method; the general procedure[2] is illustrated in figure 1.1. After systemic administration of a photosensitizer drug, it takes several

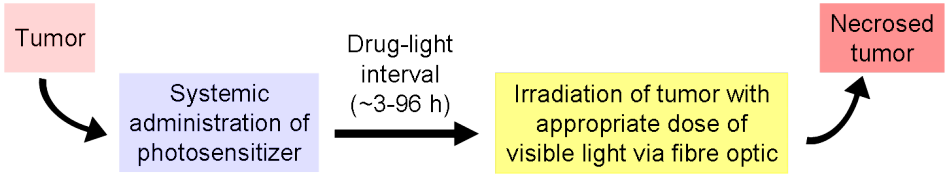

Figure 1.1: The Photodynamic Therapy procedure. - Schematic representation adapted from Bonnett[2]

.

hours until the necessary drug concentration is reached inside the tumor. Then, the tumor tissue is selectively irradiated with visible (or near-infrared) light, which activates the photosensitizer drug inside the tumor. Activated photosensitizer molecules initiate cytotoxic oxidation reactions. Two mechanism types[3] are involved, as illustrated in figure 1.2, that are characterized either by proton/electron transfer to the substrate (type I), or by energy transfer to molecular oxygen (type

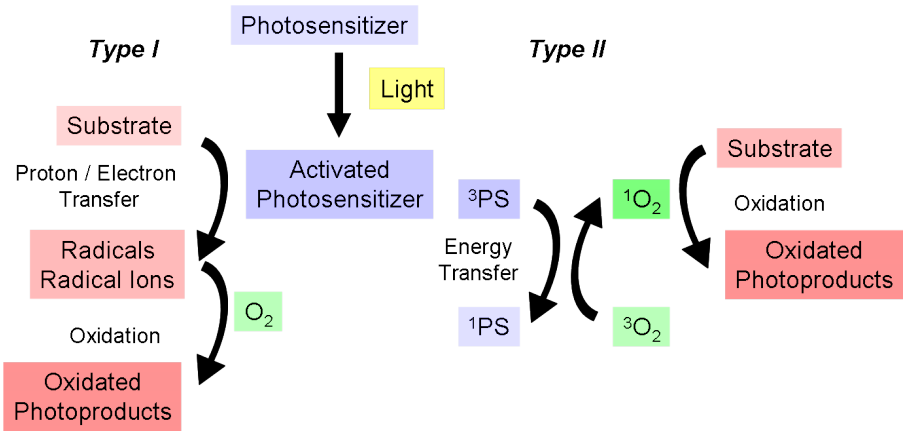

Figure 1.2: Mechanism types I and II of Photodynamic Therapy. - Illustration adapted from Dolmans *et al.*[3]

.

II). Highly reactive oxygen species play a major role in both types, and the reactive singlet oxygen generated in type II is the main active agent in PDT.

Properties of Singlet Oxygen

A unique feature of molecular oxygen is its triplet configuration in the ground state. As presented in figure 1.3, the two highest occupied molecular orbitals are energetically degenerate and therefore occupied by two electrons with parallel spins, giving rise to the triplet state $^3\Sigma_g^-$. The two lowest singlet states are the $^1\Delta_g$ and $^1\Sigma_g^+$, which lie 7882 cm^{-1} (1269 nm) and 13 120 cm^{-1} (762 nm) above the triplet ground state[4], see figure 1.4.

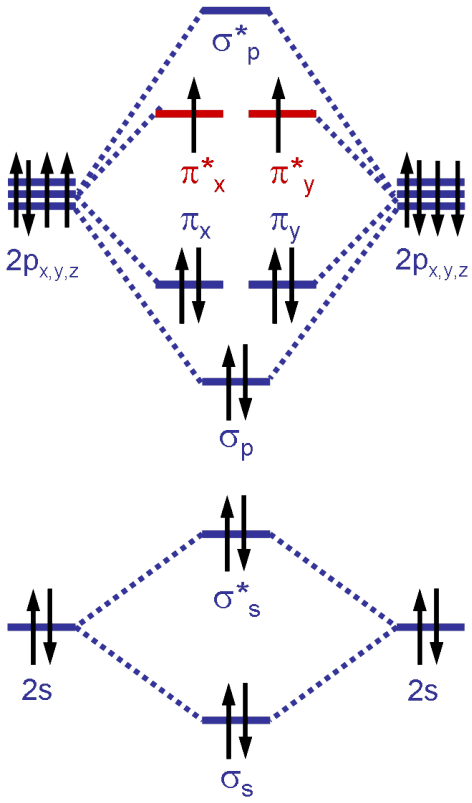

Figure 1.3: Molecular orbital scheme of ground state dioxygen ($^3O_2$)[5].

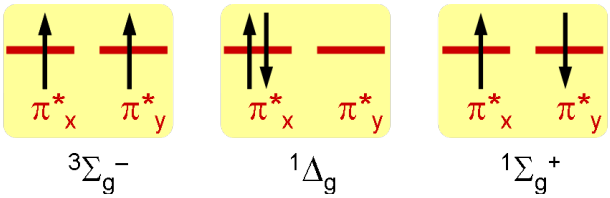

Figure 1.4: The three possible configurations of two electrons in the highest occupied molecular orbitals (π^*) in molecular oxygen.

Applications of Singlet Oxygen

Singlet oxygen $^1O_2$ is highly reactive, in particular a strong oxidizing agent. When dye molecules are exposed to (sun)light in the presence of oxygen, singlet oxygen can be formed that causes oxidative damage to organisms, which can be an unwanted effect like in case of sunburns, or applied to the benefit in case of PDT. Another side-effect is for instance the photo-degradation of polymeric materials[6]. The highly efficient oxidizing power of $^1O_2$ is also used in industrial oxidation processes, e.g. in steel manufacturing, and in chemical synthesis[7]. Further applications include purification of waste water[8], and photoinduced deactivation of viruses and bacteriae[9]. An overview of "Photosensitized singlet oxygen and its applications" is given by DeRosa and Crutchley[10].

Generation of Singlet Oxygen

Singlet oxygen can be generated either in a sentisized photoreaction from ground state oxygen, or in a chemical reaction from an oxygen-containing educt, like peroxides.

(A) Photosensitized $^1O_2$ ***Generation***. A photosensitizer absorbs light and subsequently transfers energy to an acceptor molecule. In the presence of molecular oxygen, the latter is converted into singlet oxygen, while the triplet sensitizer is relaxed back to the singlet ground state. This mechanism, illustrated in figure 1.5, also explains why oxygen acts as a triplet quencher.

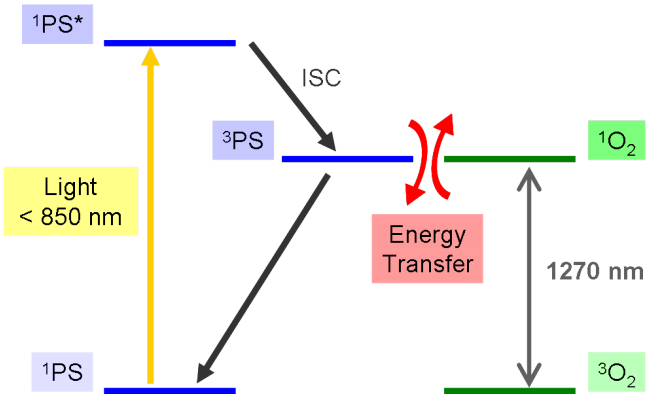

Figure 1.5: Energy transfer (ET) mechanism from an excited photosensitizer (PS) to ground state oxygen. - This singlet oxygen ($^1O_2$) generation method is applied in the type II reaction of Photodynamic Therapy[2].

A typical photosensitizer used in PDT is a haematoporphyrin derivative[9], known as Photofrin, with an absorption maximum at 630 nm; its structure is depicted in figure 1.6.

(B) Intramolecular $^1O_2$ ***Release***. Peroxides contain a $-O-O-$ unit that can serve as a source of singlet oxygen, which can be released in an intramolecular elimination reaction. An example is given in figure 1.7: Cyclopentadiene-endoperoxide eliminates singlet oxygen (more precisely, $^1\Delta_g$) in a cycloreversion reaction. The reverse process, the synthesis of the organic endoperoxide, is a Diels-Alder type 1,4-cycloaddition reaction.

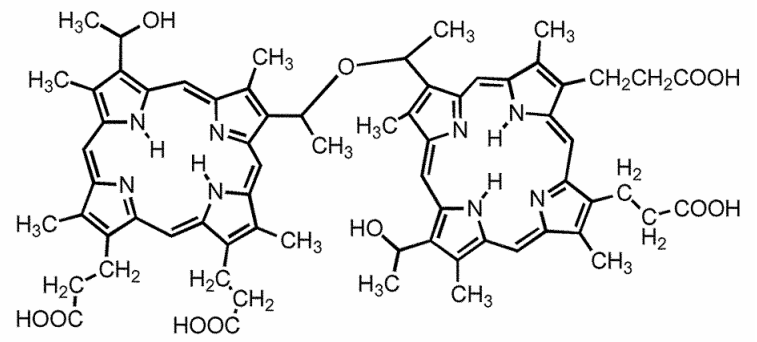

Figure 1.6: Haematoporphyrin derivative (HPD). - Also known as Photofrin, a typical example of a photosensitizer in PDT; from Hamblin and Hasan[9].

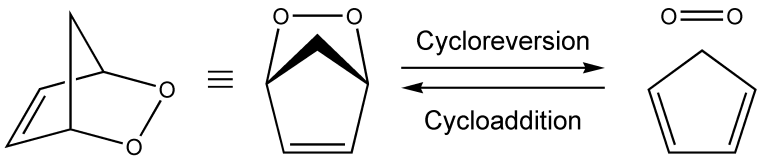

Figure 1.7: Cycloreversion reaction of cyclopentadiene-endoperoxide that generates singlet oxygen[11]. - The reverse reaction, i.e. the synthesis of the endoperoxide, is a Diels-Alder type cycloaddition reaction.

Improved Singlet Oxygen Generation for PDT: Endoperoxides

A promising approach to improve the $^1O_2$ generation is to combine the two methods (A) and (B) described above: A molecule that not only serves as photosensitizer, but in addition contains peroxide units, so that it can release $^1O_2$ in an intramolecular elimination reaction. A candidate for such a compound was synthesized by Freyer and Flatau [12]: Palladium octaphenyl-tetraanthraporphyrazine was modified to contain four endoperoxide bridges, as indicated in fig. 1.8. This molecule has the possibility to eliminate each of its endoperoxide groups to form a maximum of four $^1O_2$, while the parent molecule is recovered.

The great advantage of intramolecular $^1O_2$ generation is that this reaction is independent from the occurence of molecular oxygen in the tumor cells. This is particularly important in the case of PDT, because the vasculature is damaged by PDT, causing oxygen deficiency in the cells.

Disputed Photochemistry of Anthracene-Endoperoxide

The endoperoxide units of the photosensitizer molecule in figure 1.8 are situated at four anthracene moieties, and it therefore appears most reasonable to first have a closer look at this sub-unit. Interestingly, the photoreactions of anthracene-endoperoxide have been heavily disputed in literature: A dual mode of photochemistry has been suggested, i.e. different photoreaction pathways depending on the excited electronic state. The cases of wavelength dependent photochemistry are rare; usually, the photoreaction is independent of excitation wavelength, just as the fluorescence spectrum is, as suggested by Kasha's rule.

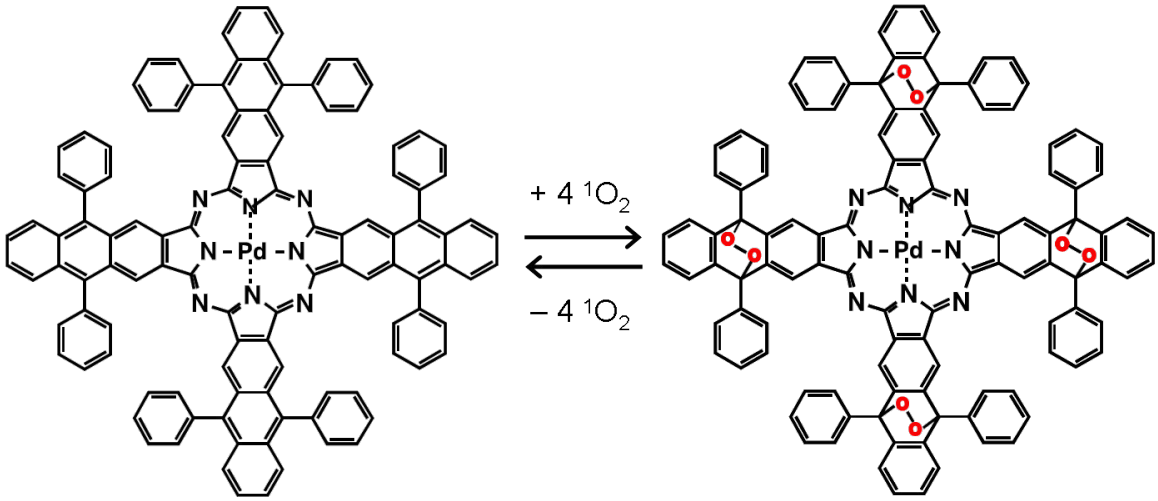

Figure 1.8: Palladium octaphenyltetraanthraporphyrazine (left, absorbtion maximum 846 nm) and its derivative with four endoperoxide bridges in the anthracene units (right, new absorbtion maximum 662 nm)[12].

Dual Photochemistry and Kasha's Rule

Kasha's rule[13] states that all emission (and, in generalization, likewise all chemical reactions) are observed exclusively from S_1, because the internal conversion (IC) from higher electronic excited states into the first excited state ($S_n \rightarrow S_1$) usually occurs with unrivaled rapidity. This is because the energy gaps are smaller and the overlaps better, thus the transitions faster, between higher excited states (e.g. $S_2 \rightarrow S_1$) than for the $S_1 \rightarrow S_0$ transition. Consequently, emission processes from higher excited states are not able to compete with the fast IC process to S_1; therefore emission is usually observed only from S_1. This behavior is illustrated schematically on the left in figure 1.9.

Exceptions from Kasha's Rule

Two possible explanations are conceivable for photoreactions from higher excited states, which would justify an exception from Kasha's rule. First, IC becomes slower, and therefore easier to compete with, when the energy gaps between excited states are larger, as illustrated in the middle of figure 1.9. This is for instance the case in azulene[14], which is one of the rare examples for compounds that indeed show emission from higher excited states.
Alternatively, photoreactions from higher excited states could still occur with significant yields if the initial step is fast enough to compete with the rapid IC process, as indicated on the right in figure 1.9. Whether this is the case can be verified by a time-resolved investigation that reveals the time scale of the reaction from higher excited states. As the processes of interest are assumed to occur on time scales of few picoseconds (1 ps $= 10^{-12}$ s), the experimental temporal resolution should be sufficiently high. This is achieved by applying femtosecond (1 fs $= 10^{-15}$ s) laser pulses in a pump-probe transient absorption experiment.

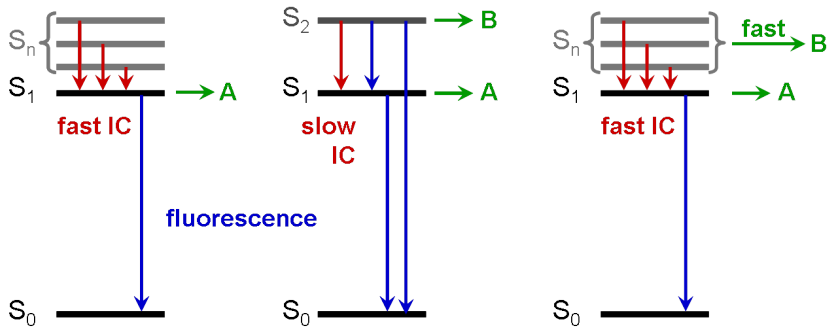

Figure 1.9: Left: Illustration of Kasha's rule: fast internal conversion (IC) $S_n \rightarrow S_1$, fluorescence and reactions (one channel A) occuring exclusively from S_1.
Middle: Case with larger engergy gap $S_2 - S_1$, leading to slower IC and additional fluorescence contributions attributed to $S_2 \rightarrow S_1$ and $S_2 \rightarrow S_0$ transitions, as well as a second reaction channel B from S_2.
Right: Kasha's case as on the left, but with additional fast reaction channel B from higher excited states.

Investigation of the Model System Anthracene-Endoperoxide

For further progress in the application of aromatic endoperoxides in $^1O_2$ generation, it is crucial to gain in-depth insight into the complex reaction mechansims. A thorough examination is complicated because of the (potential) dual photochemistry and the variety of products that can be generated upon illumination of aromatic endoperoxides.

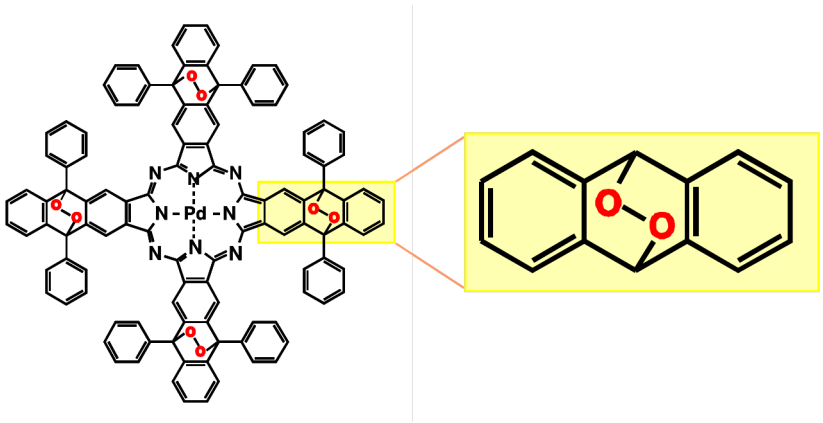

Figure 1.10: Anthracene-endoperoxide (right side) as a model system for the endoperoxide-containing porphyrazine derivative[12] (left side, compare fig. 1.8)

First of all, the highly controversial dual photochemistry issue needs to be settled for the model system anthracene-9,10-endoperoxide (figure 1.10). In order to resolve the question, it is necessary to find out whether or not it is excitation to the S_1 state that is responsible for the O-O cleavage reaction pathway, or if this channel is due to triplet population, or even purely thermal. The logical first step is therefore to find an unambiguous assignment for the lowest excited singlet states of anthracene-9,10-endoperoxide (chapter 4). Next, the potential products need to be identified (chapter 3), and the photochemistry needs to be examined thoroughly, especially in terms of wavelenghth dependency of product formation (chapter 5). With all of this information

available, one can draw a conclusion regarding whether or not dual photochemistry occurs in anthracene-9,10-endoperoxide.
If this turns out to be the case, it raises the question whether the reason for the phenomenon lies in the ultrafast rapidity of the cycloreversion reaction from higher excited states. Therefore, the time scale of cycloreversion, and possibly also of O-O cleavage, needs to be revealed by means of a real-time examination with sub-picosecond temporal resolution (chapter 6).
The combined results establish a sound basis for future work on $^1O_2$ generation from aromatic endoperoxides.

1.2 Aromatic Endoperoxides in Literature

Competition between 1,4- and 9,10-Endoperoxide Generation

In the synthesis of aromatic endoperoxides with an anthracene backbone, two isomers may be formed,[15] with the peroxide bond in the 1,4- or in the 9,10-positions, as indicated in figure 1.11. Investigations by Rigaudy in 1968[15] revealed a strong side group dependence, as exemplified in table 1.1. While anthracene and 9,10-diphenyl-anthracene result in 100 % of the 9,10-isomer, ether

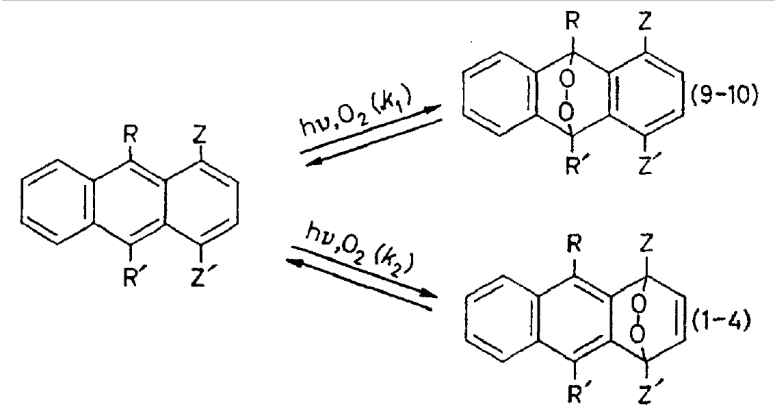

Figure 1.11: Competiton between generation of 1,4- and 9,10-isomers of aromatic endoperoxides, studied by Rigaudy in 1968[15].

Table 1.1: Side group dependence of isomer ratio, illustrated by selected examples from reference [15]. - Z, Z' and R, R' refer to the side groups as depicted in figure 1.11.

Z, Z'	R, R'	9,10 (%)	1,4 (%)
H	H	100	0
H	C_6H_5	100	0
OCH_3	H	0	100
OCH_3	C_6H_5	0	100
CH_3	C_6H_5	30	70

side groups in the 1,4-positions (Z,Z') lead to the reversed case of 100 % 1,4-isomers. Methyl groups in 1,4-positions represent an intermediate case with 70 % 1,4- and 30 % 9,10-isomer. Since the subject of this work is anthracene-9,10-endoperoxide, the main focus is on 9,10-endoperoxides.

Reactions of Aromatic Endoperoxides

Aromatic endoperoxides can decompose both thermally and photolytically. Two primary reaction channels are found to compete in both cases[16], as scatched in figue 1.12: On the one hand, cycloreversion can generate the parent hydrocarbon and molecular oxygen; on the other hand, the endoperoxide bond between the two oxygen atoms can break homolytically, forming a biradical intermediate that further rearranges or decomposes to stable products. Upon photoexcitation, both reaction channels can contribute, depending on excitation wavelength, whereas under thermal conditions, one pathway is favored for a specific endoperoxide.

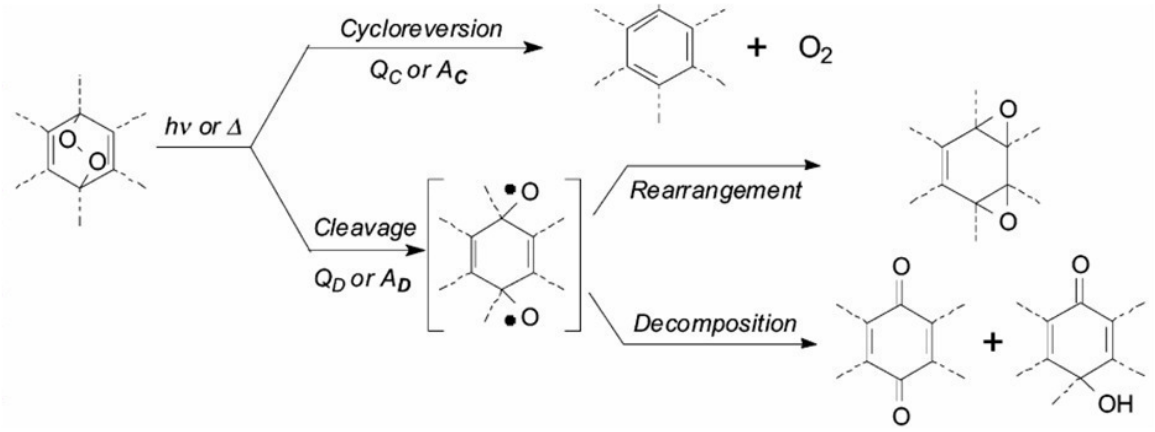

Figure 1.12: Reaction pathways of aromatic endoperoxides as described by Aubry in 2003[16].

1.2.1 Thermal Reactions

The instability of solid anthracene-9,10-endoperoxide (APO) was demonstrated already in 1954:[17] only 68 % APO were left after half a year at room temperature (RT), even under high-vacuum conditions in the dark. The thermal reaction at RT therefore needs to be taken into account as a pathway that potentially competes with photoinduced reactions. The side groups attached to the aromatic moiety play a major role in the determination of the reaction pathway that is favored under thermal conditions[16]. For instance, thermal cycloreversion is not observed for APO, while 9,10-diphenyl-APO undergoes this reaction to 100 %, and the intermediate case of the monosubstituated phenyl-APO shows 22 % cycloreversion[16].

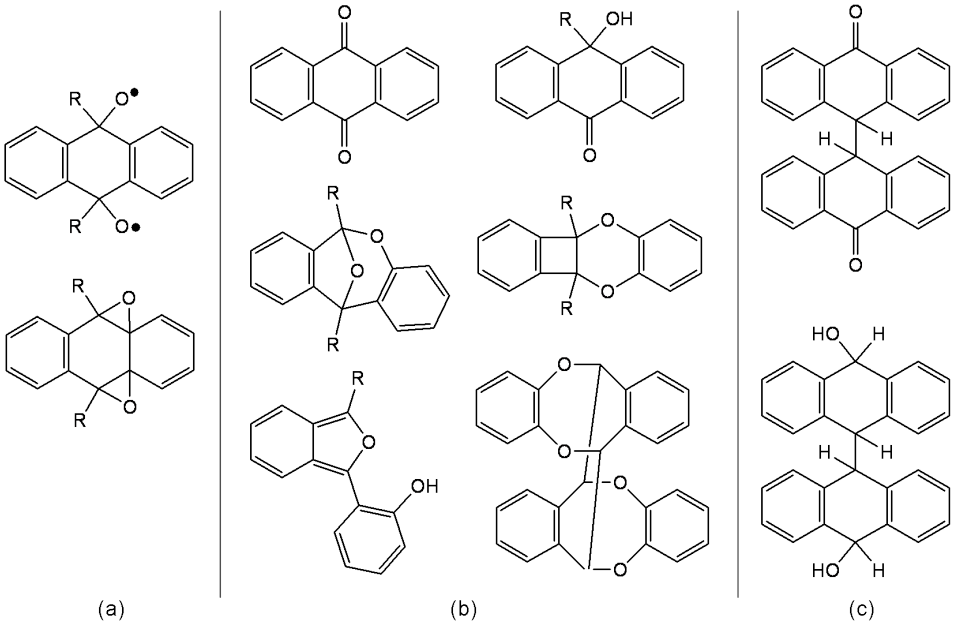

Figure 1.13: Thermal products of aromatic endoperoxides after O-O cleavage, as published by Rigaudy *et al.*[20, 21]: (a) biradical intermediate and diepoxide, (b) products; (c) additional dimers found by Dabestani[22].

Thermal Cycloreversion

The molecular oxygen released by phenyl substituated aromatic endoperoxides was studied by Turro *et al.* in 1981[18]. The results implied two competing mechanisms, yielding different ratios of $^1O_2$ *vs.* $^3O_2$. A stepwise mechanism is supposed to start with the homolytic cleavage of one C-O bond and generation of a biradical, followed by cleavage of the second C-O bond and detachment of mainly triplet molecular oxygen. In an alternative mechanism, a concerted cleavage of both C-O bonds appears to directly generate nearly quantitative amounts of singlet molecular oxygen[18]. Which mechanism is favored, and thus the singlet oxygen yields, depends on the aromatic endoperoxide structure. In case of 1,4-endoperoxides, the thermal $^1O_2$ yield is found to be considerably higher than for 9,10-endoperoxides.

Thermal Cleavage of the Endoperoxide Bond

The existence of a biradical intermediate (first structure in fig. 1.13) in case of O-O cleavage was deduced for APO[19] based on its accelerating effect on styrene polymerization at 50 – 70 °C. A study[20] of the thermal rearrangement reactions of APO at 80 – 110 °C yielded the intermediates and products summarized in figure 1.13.a-b. Both reports suggest the same biradical as precursor of the main primary product diepoxide, which rearranges to stable compounds, including dimers for higher concentrations (one example is shown in fig. 1.13.b). Differently structured dimers (fig. 1.13.c) were found in an investigation[22] of the photodecomposition of anthracene on dry surfaces.

1.2.2 Photoinduced Reactions

Upon photoexcitation, the ratio between the two primary reaction channels is determined by the photon energy of the exciting light, i.e. the excitation wavelength. For APO, dimethyl-, and diphenyl-APO, the homolytic O-O cleavage occurs from the lowest electronic excited states, while cycloreversion proceeds only upon excitation of $S_{n\geq 2}$[23, 24]. Due to competing internal conversion to S_1, rearrangement reactions still dominate at shorter wavelengths associated with $S_0 \rightarrow S_{n\geq 2}$ transitions; for APO at 270 nm, for instance, 22 % cycloreversion and 75 % O-O cleavage are observed[24].

Photoinduced Cycloreversion

The molecular oxygen released by photoinduced cycloreversion of diphenyl-APO was identified as singlet oxygen in 1967 by Wasserman and Scheffer[25], based on the ability to induce typical singlet oxygen reactions. Five years later, $^1\Delta_g$ oxygen was more specifically suggested as the species generated in the cycloreversion reaction[26].

Photoinduced Cleavage of the Endoperoxide Bond

In a study on the photochemistry of diphenyl-APO[27], the rearrangement reactions summarized in figure 1.14 were observed next to cycloreversion. The transient occurence of a biradical intermediate and an unstable diepoxide was deduced indirectly, by chemical trapping as *N*-methyl-maleimide adduct. It was concluded that the unstable diepoxide rearranges thermally and undergoes photoinduced isomerization upon irradiation at short wavelengths[27].

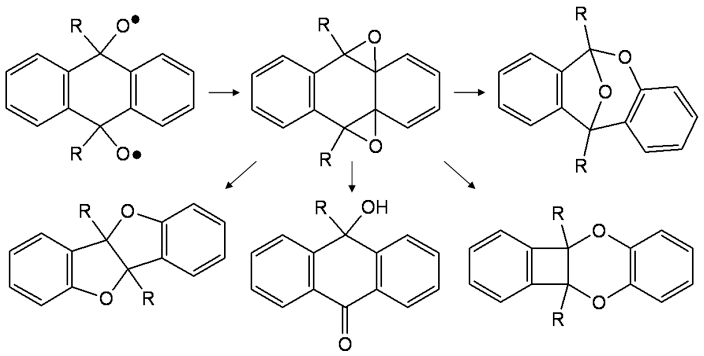

Figure 1.14: Photoproducts of aromatic endoperoxides after O-O cleavage, according to Rigaudy[27].

One year later, isolation of the diepoxide of APO was achieved by Rigaudy *et al.*[28], upon illumination at wavelengths longer than 435 nm. This finding was frequently cited thereafter as support in the assignment of the electronic excited states debate.

1.2.3 Competition between Cycloreversion and O-O Cleavage

In 1986, Schmidt and Brauer[29] presented the scheme reproduced in figure 1.15 that summarizes the competing reaction pathways for aromatic endoperoxides. Photoexcitation of higher electronic excited states (A) results in cycloreversion (left side) with quantum yield Q_c, in competition with internal convesion to S_1, a repulsive potential energy surface that leads to the O-O biradical (right side). From there, both the back-reaction to the endoperoxide and the rearrangement to the diepoxide are possible. The repulsive potential can also be accessed by direct photoexcitation (B) at longer wavelengths. Alternatively, both reaction channels might as well be availabe thermally, where the energy barriers vary depending on the endoperoxide structure. Because of the suggested repulsive character of the potential energy surface of S_1, all population is trasferred from there to the birdical, and no emission from S_1 is expected, in agreement with experimental results[29]. For some endoperoxides, the back reaction from the biradical to the educt might be favored and lead to minimal yields of rearrangement products.

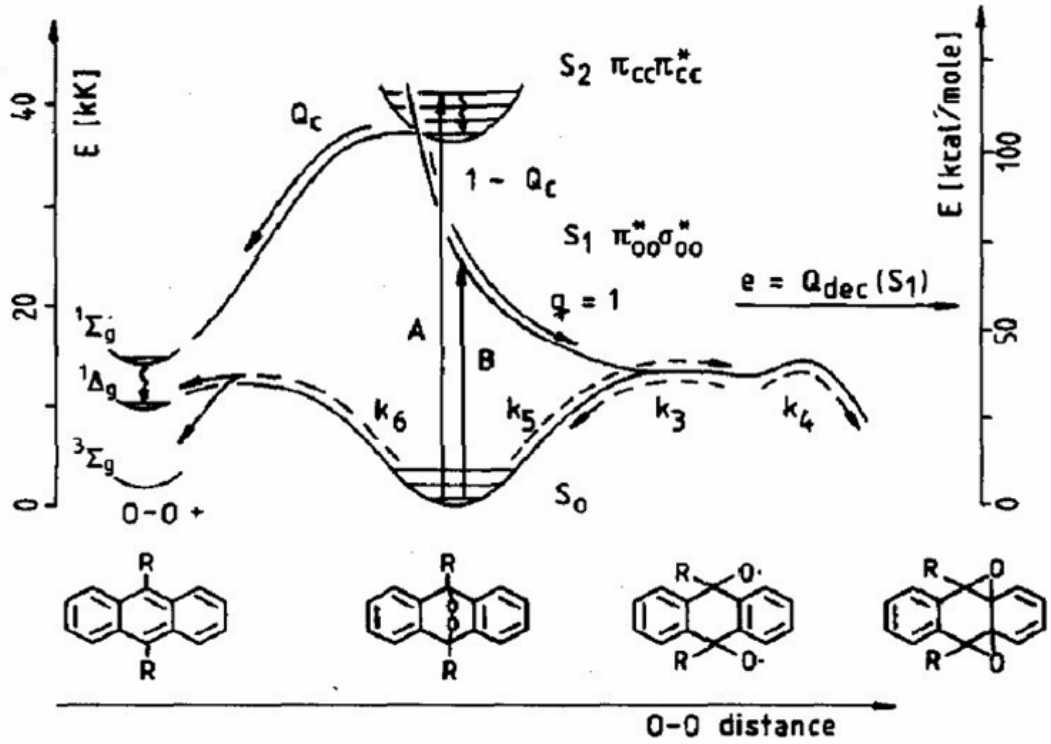

Figure 1.15: Scheme of the reaction channels of aromatic endoperoxides, summarized by Schmidt and Brauer[29].

1.2.4 Dispute about the Assignment of Electronic Excited States

Theoretical Predictions by Kearns (1969)[11]

A theoretical study[11] on addition reactions of singlet oxygen from 1969 includes investigations of the thermal and photochemical properties of endoperoxides. Based on molecular orbital and state correltion diagrams for cyclopentadiene-endoperoxide (reproduced in figure 1.16), important predictions were made that are decades later still considered strong arguments in APO debates. $^1\Delta$ oxygen was predicted to be reactive and undergo allowed 1,4 cycloaddition reactions with dienes, while $^3\Sigma$ and $^1\Sigma$ oxygen were expected to be unreactive in cycloaddition reactions. It was further proposed that the endoperoxide should be thermally unstable regarding either cleavage of the O-O bond or cycloreversion, depending on energy barriers and resonance stabilization gain of the considered endoperoxide. The photodecomposition of endoperoxides was predicted to be wavelength dependent: Excitation of lower lying excited states of σ^*_{OO} character was expected to cause cleavage of the O-O bond, while population of higher lying excited states of σ^*_{CO} type was predicted to lead to molecular oxygen detachment and formation of the parent hydrocarbon[11]. Since experiments agreed with this theoretical study, it has later been generalized to apply to all aromatic endoperoxides, with the exception that the energetic order of the two reaction pathways may be reversed depending on endoperoxide structure.

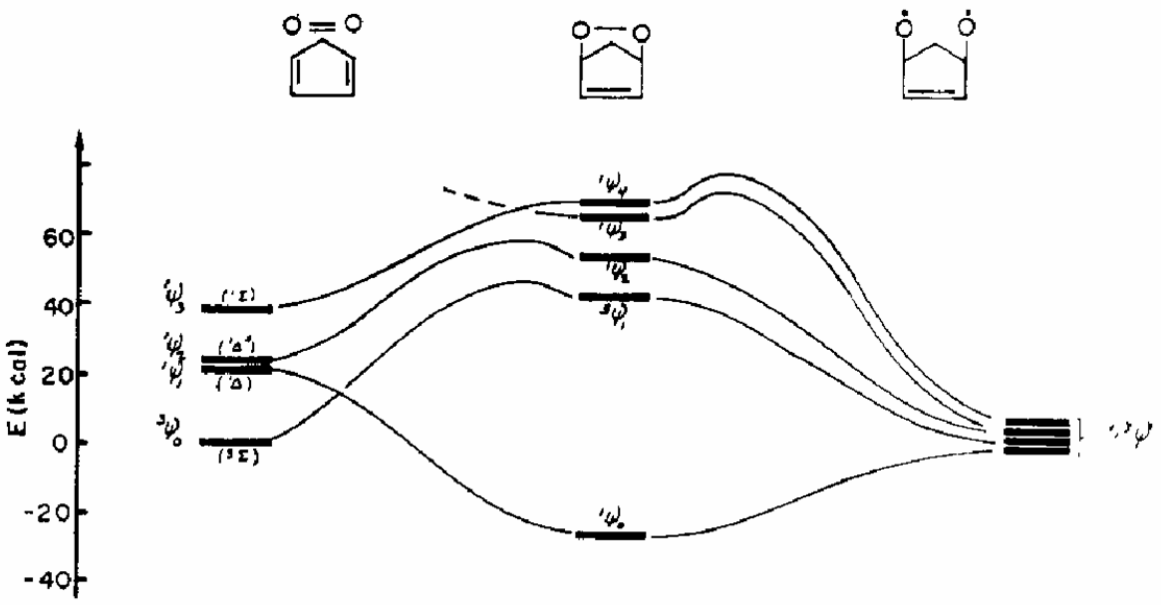

Figure 1.16: State correlation diagrams by Kearns[11]: Addition of molecular oxygen to cyclopentadiene (left), and decompsition of the endoperoxide by cleavage of O-O bond (right).

Assignment by Schmidt *et al.* (1984)[24]

Schmidt *et al.*[24] suggested in 1984 that the $S_0 \rightarrow S_1$ transition of APO is located in the long weak tail above 300 nm that is visible in the absorption spectrum of APO, shown in figure 1.17. In order to locate the S_1 position more precisely, the O-O cleavage reaction that is supposed[11] to occur from S_1 was considered: The synthesis of the primary O-O cleavage product (a diepoxide) by Rigaudy *et al*[28] was only achieved using light $\geq$ 435 nm (or $\leq$ 23 000 cm^{-1}). Based on this experimental result, it was concluded[24] that the $S_0 \rightarrow S_1$ transition should be located $\leq$ 23 000 cm^{-1}. In figure 1.17, it can be seen that this suggested S_1 position is very far from the lowest discernible APO absorption. Anyway, this S_1 assignment had not been contradicted until 1999.
The $S_0 \rightarrow S_2$ transition was assigned to the first clear shoulder in the absorption spectrum (35 000 cm^{-1}), and S_3 was deduced to be located $\geq$ 40 000 cm^{-1}.

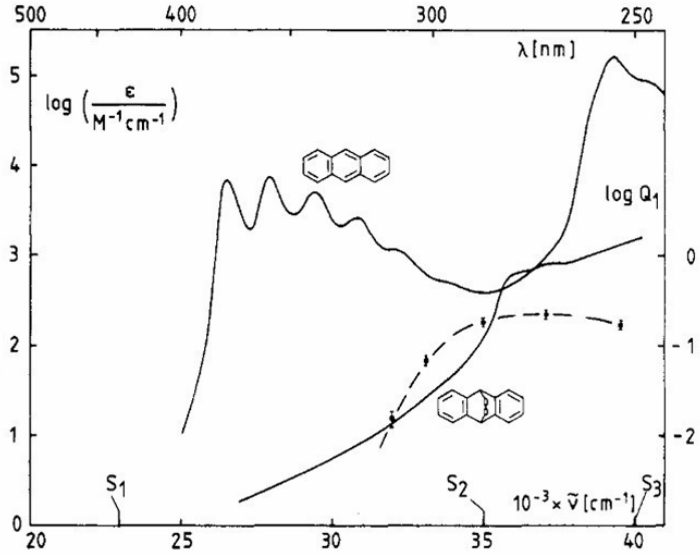

Figure 1.17: Absorption spectra of APO (and of anthracene), with S_1, S_2, and S_3 positions of APO indicated, as published by Schmidt *et al.* in 1984[24].

Assignment by Klein *et al.* (1999)[30]

Klein *et al.*[30] were the first to contradict the assignment by Schmidt *et al.*[24] in 1999, based on semiempirical calculations as well as on experimental data obtained on APO in argon matrix. Their calculations did not reveal transitions to electronic excited singlet states below 36 000 cm^{-1}. Consequently, the former S_2 state was now identified as the true S_1 state. The O-O cleavage reaction upon excitation at lower energies was explained to occur from triplet states. This new assignment holds the advantage that it circumvents the dual photochemistry from two different singlet states, as it claims that one reaction is due to singlet, the other due to triplet excitation. However, this publication did not settle the dispute about the APO S_1 assignment.

Defense by Schmidt and Brauer (2000)[31]

Schmidt and Brauer[31] defended their assignment, or attacked the opinion of Klein *et al.*[30], the following way. Upon excitation at 270 nm, S_1 according to Klein[30], only 22 % cycloreversion, but 75 % O-O cleavage are observed[24] for APO in solution. The first step of the cycloreversion reaction, the rupture of one C-O bond, was found[32] to occur on ultrafast time scales $<$ 350 fs. If the O-O cleavage reaction occured from triplet states, intersystem crossing (ISC) needed to be fast enough to compete with the first step of the cycloreversion reaction, i.e. the ISC had to proceed $\ll$ 1 ps, a time scale unknown[31] for compounds without heavy atom effects. By contrast, if the rearrangement reaction occured from the S_1 state, internal conversion (IC) had to proceed on that time scale, and ultrafast IC is not unusual[33].

Reply by Klein and Gudipati (2000)[34]

In their reply, Klein and Gudipati[34] argued that in their own experiments in argon matrix, at 275 nm excitation, the cycloreversion was the only reaction, with 100 % yield. Therefore, their triplet assignment did not contradict their own experiments. They emphasized the necessity for detailed *ab initio* calculations that explore the multidimensional potential hypersurface.
Indeed, such *ab initio* calculations were recently provided by Corral *et al.*[35], and are presented together with experimental evidence in chapter 4.

1.2.5 Time Constants of Cycloreversion

Results from LIF an Transient Absorption Experiments

Most of the time resolved investigations were performed by application of the laser induced fluorescence (LIF) method: The photo-generated product is excited by a delayed narrow-band laser pulse and detected by its fluorescence. The photoproduct formation time deduced might be contaminated by spectral shifts due to relaxation processes, a drawback that is considered negligible by the authors of the presented studies[36, 37].
The endoperoxide investigated by LIF that is most closely related to APO is 9-phenyl-APO; similar compounds include 9,10-diphenyl-APO, 1,4-dimethyl-9,10-diphenyl-APO, and the 1,4-isomer of the latter. For these endoperoxides, LIF experiments found photoproduct formation times in the range of 50 – 95 ps. Several endoperoxide derivatives were studied in which the phenyl groups are more rigidly connected to the core, as shown in figure 1.18. Time constants were found to depend strongly on the exact endoperoxide structure, as even similar-looking compounds showed large variations. For the molecules in figure 1.18, cycloreversion times between 1.7 ps for HOCD-PO[38] and 68 ps for BDX-PO[39] were found.
Another time resolved method is transient absorption spectroscopy; details of the method are presented in the experimental section 2.6. Since the rise of the product absorption is observed over a broader spectral range, spectal shifts can be included in the analysis. Thus, this method might be able to give more accurate information about the photoproduct formation time than the narrow-band LIF method.
Transient absorption spectroscopy was applied to HOCD-PO[32]; the deduced time constant of 1.6 ps is very similar to the one obtained by LIF[38], and is the fastest cycloreversion time reported so far for aromatic endoperoxides.

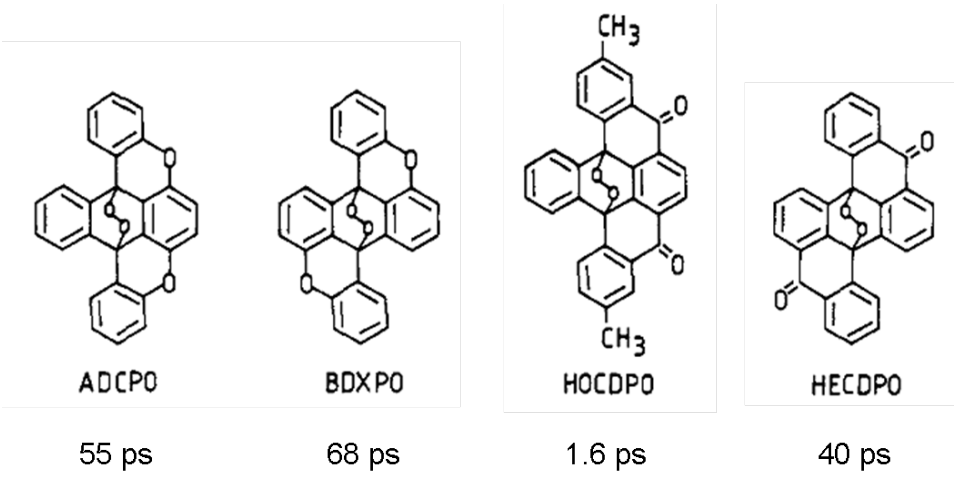

Figure 1.18: Structures of some aromatic endoperoxides investigated by Jesse and Comes[38, 40].

Proposed Photoreaction Mechanism

The large span of cycloreversion product formation times between 1.6 ps and 95 ps was explained[38, 32] by a stepwise mechanism: In a first step, a $C^{\bullet}, O^{\bullet}$-biradical intermediate is formed upon homolytic C-O cleavage. The $^1O_2$ elimination occurs in a rate-determining second step, so that the time constants measured by LIF reflect the lifetimes of the related biradicals.
For the competing photoreaction pathway, homolytic cleavage of the peroxide bridge that generates a diepoxide and further rearrangement products, a similar stepwise mechanism was proposed. In this case, the formation time of the diepoxide could be related to the lifetime of the $O^{\bullet}, O^{\bullet}$-biradical intermediate.

1.3 Outline

Questions that Remain to be Solved

Whether or not APO shows dual photochemistry has been discussed controversely[24, 30, 31, 34], as outlined in section 1.2.4. The dispute clearly indicates the necessity for a more detailed investigation of the photochemistry of APO. The issue can be devided into three aspects:

1. Unambiguous identification of the first excited singlet states of APO;
2. Quantitative exploration of the wavelength dependency of photoproduct formation;
3. Real-time determination of cycloreversion and diepoxide formation times.

Further Organization

Chapter 2: Experimental Methods

The experimental methods used in the presented studies are explained. This includes theoretical background, practical applications, and data analysis.

Chapter 3: Spectral Properties of APO and Products

Characterization of APO and its reaction products by application of ^1H NMR, IR, and UV/vis absorption and emission experiments.

Chapter 4: Identifying the Excited Singlet States of APO

Polarization resolved femtosecond pump-probe experiments in combination with calculations allow to locate the lowest electronic excited singlet states of APO, especially the disputed S_1 state.

Chapter 5: Quantitative Investigation of Reaction Pathways

Thermal and photochemical reaction pathways and their dependency on experimental conditions are explored; particular attention is paid to the wavelength dependent photoproduct quantum yields.

Chapter 6: Primary Photoreaction Steps studied in Real-Time

Photoinduced product formation is studied in real time by femtosecond transient absorption spectroscopy with supercontinuum probing. Reaction times for both the cycloreversion and the O-O cleavage reaction are deduced.

Chapter 7: Final Summary and Conclusions

Finally, the main results and conclusions are assembled, and the picture is completed by implications to the original motivation and an outlook for future challenges.

2 Experimental Methods

2.1 Concepts

Light-Matter-Interaction

The electromagnetic field interacts with a molecule and induces oscillations of the electrons with the light frequency; the material response is governed by the complex refractive index $n = n_R - in_I$. The oscillating electrons produce a secondary electromagnetic field with a reduced speed (real part of refractive index ⇒ refraction) that is exponentially attenuated in vicinity of resonance frequencies (imaginary part of refractive index ⇒ absorption).
The damping at a resonance frequency is due to the absorption of a photon by the molecule, which can result in a rotational, vibrational, and/or electronic transition. The reverse process of emission can occur both induced or spontaneous.
A measure for the intensity of a transition is given by the oscillator strength f:

$$f = \frac{8\pi^2 m_e}{3he^2} \cdot \nu \left|\mu\right|^2$$

(m_e - electron mass, e - electron charge), which depends on the transition frequency ν and the square of the transition dipole moment (TDM) μ. Experimentally, the intensity of an absorption is observed as the optical density (OD) in the absorption spectrum. The OD depends on the extinction coefficient ϵ_λ, as well as on the sample concentration (c) and pathlength (d)given by the Lambert-Beer law:

$$-\lg \frac{I}{I_0} = \epsilon_\lambda c d = OD. \tag{2.1}$$

The integrated extinction coefficent is directly proportional to the oscillator strength f of a transition:

$$f = \frac{4m_e c\epsilon_0 \ln 10}{N_A e^2} \cdot \int \epsilon(\nu)\, d\nu.$$

The probability w of a stimulated transition (absorption or emission) depends on the energy density ρ of the incident radiation: $w = B\rho$. The proportionality factor B is the Einstein coefficient for stimulated absorption or emission (eq. 2.2). Spontaneous emission is independent of the incident light and depends only on the Einstein coefficient A.

$$B = \frac{1}{6\epsilon_0 \hbar^2} \cdot \left|\mu\right|^2; \quad A = \left(\frac{8\pi h}{c^3}\right) \nu^3 \cdot B. \tag{2.2}$$

According to equation 2.2, the rate of spontaneous emission is proportional to the third power of the frequency, i.e. large energy gaps cause high emission probabilities, while small energy gaps allow for competition by non-radiative relaxation pathways. Since energy differences between excited states are typically smaller than the $S_0 - S_1$ gap, emission usually only occurs from the S_1 state, what is known as Kasha's rule[13].

Energy Relaxation

Upon photoexcitation of a molecule, several relaxation processes compete[14], as illustrated in figure 2.1. Photoexcitation is follwed by intramolecular vibrational redistribution (IVR) (1) and vibrational relaxation (2a) to the vibrational ground state. IVR (1, $\nu_n \rightarrow \nu_{n-x}$, 0.1 – 1 ps) denotes the distribution of the vibrational energy that was initially concentrated in few vibrational modes over all available vibrational degrees of freedom of the molecule; this implies that the vibrational energy in the in the Franck-Condon mode decreases e.g. from ν_n to ν_{n-x}. As an intramolecular process, IVR typically occurs on subpicosecond time scales. Vibrational cooling (2, $\nu_n \rightarrow \nu_0$, $\approx$ 10 ps), on the other hand, describes the collision induced transfer of vibrational energy to the surrounding medium, i.e. solvent molecules; this intermolecular process typically occurs on a $\approx$ 10 ps time scale.

From S_1, three possible relaxation pathways compete: Fluorescence (3, $S_1, \nu_0 \rightarrow S_0$, 1 ps – 100 ns) leads directly to the vibrationally relaxed singlet ground state S_0, while internal conversion (4, $S_1, \nu_0 \rightarrow S_0, \nu_n$, 1 ps – 1 μs) or intersystem crossing (5a, $S_1, \nu_0 \rightarrow T, \nu_n$, 1 ps – 1 μs) produce vibrationally excited S_0 or T_1 states, respectively; either case (4) or (5a) is followed by vibrational cooling (2b, 2c). From the vibrationally relaxed triplet state T_1, either phosphorescence (6, $T_1, \nu_0 \rightarrow S_0$, 1 μs – 1 ms), or another ISC (5b) followed by cooling (2d), finally also reform S_0, ν_0. In addition, the excitation might induces a chemical reaction, so that the ground state of the educt is not recovered, and the absorption and emission properties of the photoproduct molecules may be observed.

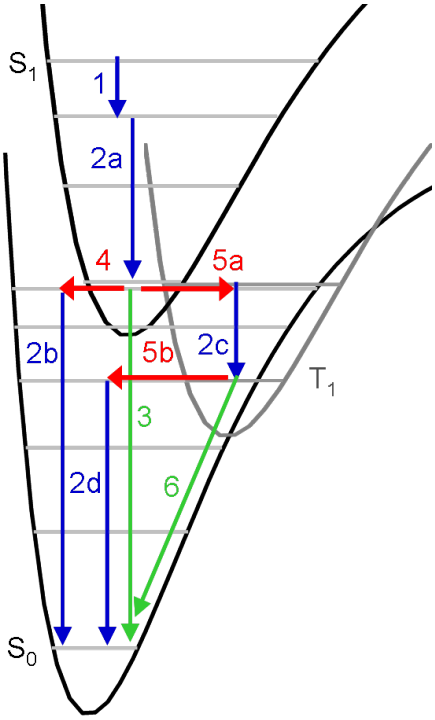

Figure 2.1: Illustration of the relaxation processes discussed in the text. Blue: IVR (1) and vibrational cooling (2); green: fluorescence (3) and phosphorescence (6); red: IC (4) and ISC (5).

2.2 Nuclear Magnetic Resonance (NMR) Spectroscopy

Atomic nuclei can have half-integral spin quantum numbers[41] $I = 0, \frac{1}{2}, 1, \frac{3}{2}, \ldots$, and the component of the nuclear spin along the spatial z axis in laboratory frame, m_I, is restricted to values of $m_I = I, I-1, \ldots -I$, resulting in a total of $2I+1$ possible spacial orientations. For hydrogen nuclei (protons), $I = \frac{1}{2}$ and thus $m_I = \frac{1}{2}, -\frac{1}{2}$. Nuclei with spin quantum numbers $I > 0$ have a magnetic moment μ, with components $\mu_z = \gamma\hbar m_I = g_I \mu_N m_I$. The magnetic moment can be expressed by either the gyromagnetic ratio γ, or the g-factor g_I and the nuclear magneton μ_N ($\mu_N = (e\hbar)(2m_p)$, e: electron charge, m_p: proton mass).
In an external magnetic field B, the spin orientations are no longer energetically degenerate: A splitting into different energy levels occurs, with energies $E_{m_I} = -\mu_z B = \gamma\hbar B m_I$. Irradiation by an electromagnetic field of the Lamor frequency ν_L that fulfills the relation $E_{m_I} = -m_I h\nu_L$ can induce transitions between the energy levels. The required resonance condition gives name to the nuclear magnetic resonance method. In case of the proton, the two spin orienations are denoted α ($m_I = \frac{1}{2}$) and β ($m_I = -\frac{1}{2}$). The energy gap between the two levels amounts to $\Delta E = E_\beta - E_\alpha = \gamma\hbar B = h\nu_L$.

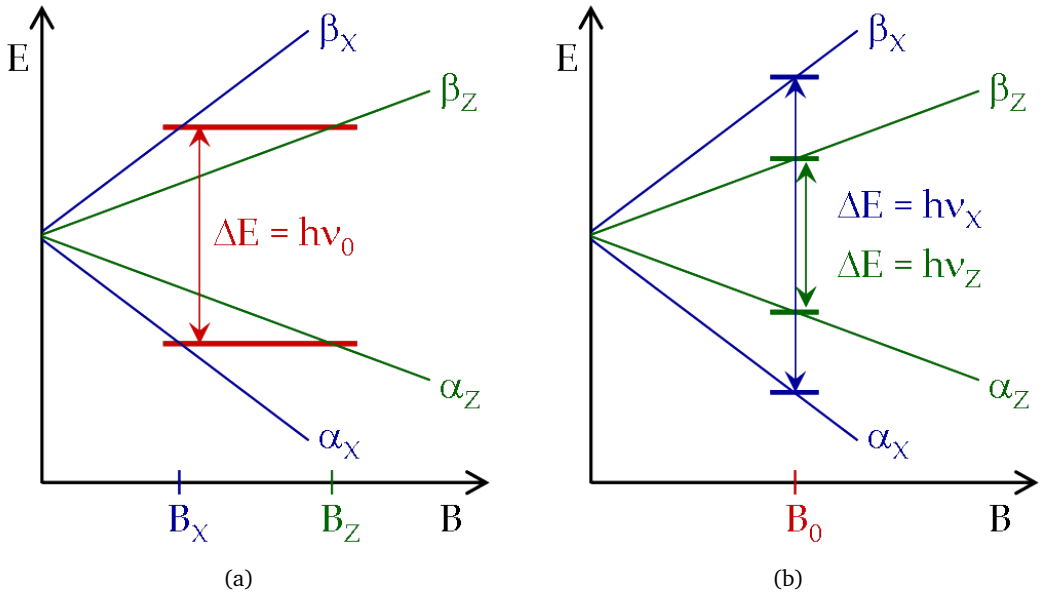

Figure 2.2: Energetic splitting of spin states α and β as a function of the external magnetic field B. X and Z denote different chemical surroundings of the respective protons. The resonance condition is fulfilled...
(a) ...for a specific frequency ν_0 at external magnetic fields B_X or B_Z, respectively.
(b) ...for a specific magnetic field B_0 at frequencies ν_X or ν_Z, respectively.

Local magnetic fields lead to distinct shielding effects, which are characteristic for the local chemical surroundings. The total field is the weaker the stronger the shielding is, and hence a lower external magnetic field is necessary to arrive at the same energy gap. In figure 2.2, the energetic splitting of spin states α and β are sketched as a function of the external magnetic field B. X and Z denote different chemical surroundings of the respective protons. The resonance condition $\Delta E = h\nu_0$ is fulfilled at B_X or B_Z, respectively, depending on the chemical surrounding X or Z (fig. 2.2.a).
Alternatively, an external magnetic field B_0 requires different resonance frequencies ν_X or ν_Z, respectively (fig. 2.2.b).

In practice, the deviations between the frequencies are very small compared to the frequency ν_0, and the dimensionless chemical shift δ is defined as

$$\delta = \frac{\nu_X - \nu_0}{\nu_0} \cdot 10^6;$$

the factor 10^6 is indicated by "ppm" (parts per million).
The influence of the neighboring protons lead to couplings, which appear as splitting in the ^1H NMR spectra. These patterns can help to assign the signals to the protons within the molecular structure. The characteristic chemical shift ranges for all types of chemical surroundings are available in literature[41]; for instance, aromatic protons are found around 7 – 9 ppm, while typical values for alkyl protons are around 1 – 3 ppm.
The ^1H NMR spectra presented in this work were recorded on a Bruker AMX-500 spectrometer at 500 MHz.

2.3 Infrared (IR) Absorption Spectroscopy

To describe the stretching vibration of a molecular bond, an anharmonic oscillator model is used, like the Morse potential sketched in figure 2.3 (blue). In contrast to a harmonic oscillator (grey), the Morse model includes the repulsion at short distances and the dissociation at long nuclear distances. As a consequence, the energetic distances decrease between higher vibrational levels (red). The anharmonic oscillator is a good model for two-atomic molecules, but has limited application for polynuclear molecules, because it reflects a stretching vibration localized at two atoms. The vibrations of larger molecules, however, may include nuclear motions of several or all atoms of the molecule.

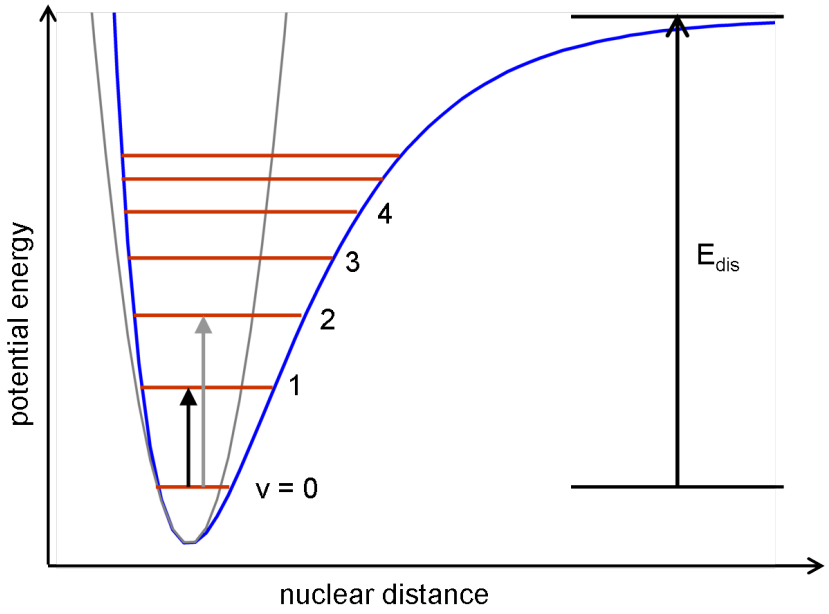

Figure 2.3: The Morse potential (blue) with a harmonic oscillator potential (grey) for comparison. The vibrational levels are indicated in red, the transition $0 \rightarrow 1$ with $\Delta v = +1$ (black) and the overtone $0 \rightarrow 2$ with $\Delta v = +2$ (light grey). The dissociation Energy E_{dis} is illustrated on the right side.

Functional groups, like hydroxy (-O-H) or carbonyl (-C=O), have characteristic modes that are rather independent of the residual molecule; therefore, IR spectroscopy is used in qualitative analysis. On the other hand, vibrational modes that include the whole molecular backbone can be characteristic for a certain compound; the corresponding spectral regions are often referred to as the fingerprint regions (usually < 1300 cm^{-1}).
Conventionally, frequencies of IR vibrations are given in wavenumbers (unit cm^{-1}): $\tilde{\nu} = \frac{1}{\lambda} = \frac{\nu}{c}$.
Stretching vibrations are indicated e.g. by $\nu(O-H)$, and bending vibrations by $\delta(O-H)$.

The typical IR spectrometer setup is schematically shown in figure 2.4. Besides the IR light source, the focussing into the sample cell, and the signal detection, the setup includes a Michelson interferometer that transforms the spectrum in the frequency domain into a spectrum in the time domain. This is because the frequencies interfer depending on the position of the moving mirror and thus the time interval between both beams. To obtain back the frequency spectrum, it is necessary to fourier transform the measured spectrum[42]:

$$I(\tilde{\nu}) = 2\int_0^\infty I(\delta)\cos 2\pi\tilde{\nu}\delta \; d\delta,$$

with δ - path difference between the two beams. This fourier transform (hence the name FTIR) is implemented in the spectrometer program, so that the user directly obtains the frequency spectrum (usually in wavenumbers $\tilde{\nu}$).

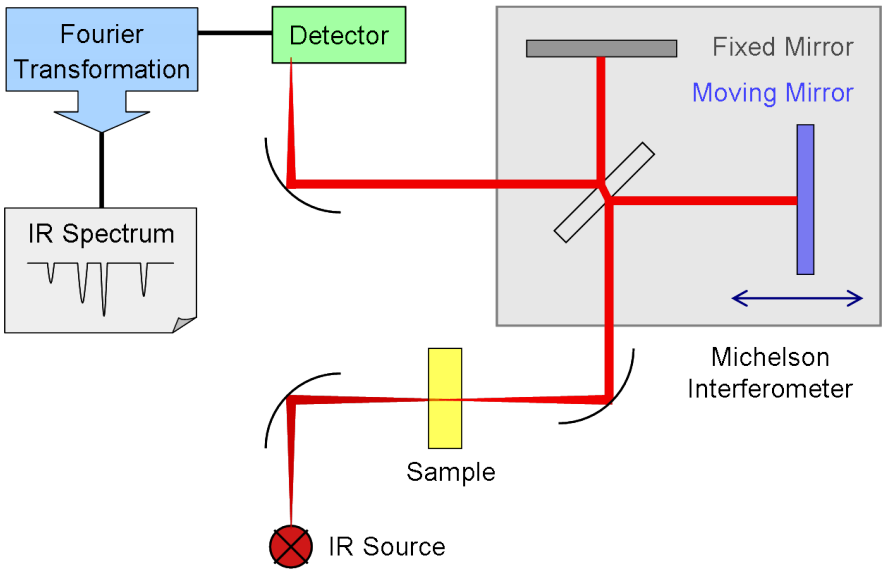

Figure 2.4: Schematic illustration of a fourier-transform IR spectrometer.

Vibronic Transitions

Molecular vibrations are not only observed directly in IR measurements, but also appear in UV/vis spectra, because electronic transitions may populate several vibrational levels (vibronic transition). As a result, electronic absorption bands consist of several vibrational bands, of which the 0-0 band has the lowest energy, followed by 0-1, 0-2,·; this vibrational structure is called vibrational progression.

2.4 Ultraviolet and visible (UV/vis) Absorption Spectroscopy

Molecules that absorb light in the UV or visible wavelength region must have an electronic transition with the appropriate energy distance available. The electronic transition with the lowest energy of such a molecule is typically a $\pi \rightarrow \pi^*$ transition between the highest occupied (bonding) molecular π orbital (HOMO) and the lowest unoccupied (anti-bonding) molecular π^* orbital (LUMO) of an aromatic system. In anthracene-9,10-endoperoxide, the lowest electronic excitation corresponds to a $\pi^*_{OO} \rightarrow \sigma^*_{OO}$ transition, according to the results of chapter 4.

A UV/vis absorption spectrometer consists of an appropriate light source (or two exchangable sources to cover the whole desired wavelength region), a sample cell, and a detector. To scan the wavelengths, it is necessary to use a monochromator, e.g. a tunable grating monochromator with an adjustable slit. Another useful implementation is a second beam path that transverses a reference cell, which might be empty or filled with the pure solvent for direct comparison. Such a double beam setup is schematically drawn in figure 2.5.

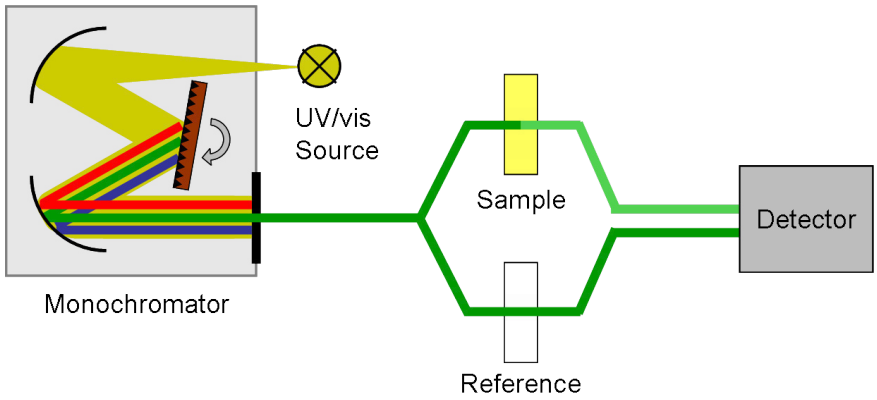

Figure 2.5: Schematic illustration of a UV/vis absorption spectrometer.

The absorption spectra presented in this work were taken on a Shimadzu UV-1601PC and a Cary 100 UV-visible absorption spectrometer in (deuterated) chloroform or in acetonitrile. Typical wavelength ranges were from 200 – 800 nm, measured in 0.5 or 1.0 nm steps. A series of absorption spectra was taken to exclude that the UV excitation during the absorpiton measurements affects the photolabile anthracene-9,10-endoperoxide solution.

Solvent absorption in the UV region is routinely subtracted prior to analysis. Absorption spectra of pure compounds are taken whenever the pure substances are available, i.e. for anthracene-9,10-endoperoxide (APO), anthracene, and anthraquinone. Spectra of the other reaction products of APO could only be deduced from reaction mixtures after subtraction of the known spectral contributions. For a quantitative analysis, the Lambert-Beer law was applied (eq. 2.1).

2.5 Emission and Emission Excitation Spectroscopy

Two types of emission processes are distiguished: fluorescence is a transition between states of the same multiplicity (usually singlet-singlet), while phosphorescence involves a change in multiplicity, typically from a triplet state to the singlet ground state. Although a change in spin multiplicity is forbidden for electronic transitions, this selection rule is not strictly valid in the presence spin-orbit coupling. Phosphorescence processes therefore have low oscillator strengths and occur relatively slow, on time scales of typically 1 μs – 1 ms.
Due to similar vibrational level structures in both ground and excited electronic states, the emission spectrum usually resembles a mirror image of the absorption spectrum, with the $0 \longleftrightarrow 0$ transitions at the same spectral position. Deviations in equilibrium nuclear configurations for the two electronic states may lead to shifted Franck-Condon transitions; e.g. for absorption, the $0 \rightarrow 2$ transition may be most intense, while for emission it might be the $1 \leftarrow 0$ transition. A shift of the $0 \leftarrow 0$ emission position relative to the $0 \rightarrow 0$ absorption position is called Stokes shift, and is due to solvent interaction. The solvent surrounding stabilizes the excited state nuclear configuration, while the ground state configuration is destabilized in that new surrounding, so that the energetic distance between ground and excited state minima is decreased while the molecule resides in the excited state, and thus the emission is red-shifted.

Emission Spectrometer

After electronic excitation of the molecule in the sample solution, the (spontaneous) emission goes centro-symmetrically in all spatial directions. To avoid disturbances by the excitation beam, the emission is detected in a 90 ° direction, as illustrated in figure 2.6. Monochromators are implemented both before and after the sample cell, enabling to scan either the excitation wavelengths or the emission wavelengths.

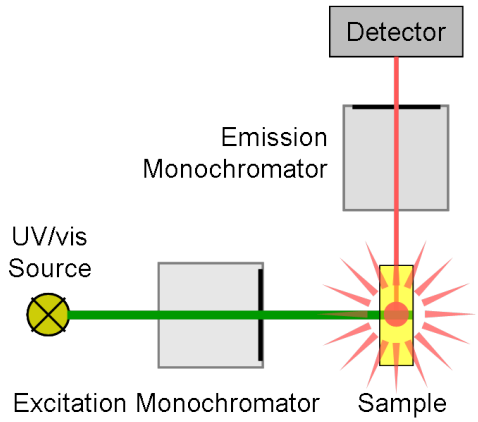

Figure 2.6: Schematic illustration of an emission spectrometer.

Emission Spectrum

An emission spectrum is measured at a fixed excitation wavelength (e.g. at the maximum of the absorption band of the sample), while the emission wavelength is scanned. As long as the substance under investigation obeys Kasha's rule[13], a change in excitation wavelength should not affect the emission spectrum. This is because non-radiative relaxation processes from higher excited states are very fast, and the only state that lives long enough to allow for competition by emission is the S_1 state; the emission yield and spectrum are therefore expected to be independent of excitation wavelength.

Emission spectra need to be corrected for apparatus sensitivity. The sample absorption in the emission wavelength region should not exceed ≈ 0.1 OD to avoid reabsorption effects. Otherwise, a correction is needed: The original emission intensity can be calculated assuming that it is generated in the middle of the cuvette and transverses half the sample thickness, whereby it is absorbed according to the Lambert-Beer law (eq. 2.1):

$$I_0(\lambda) = I(\lambda) \cdot 10^{0.5\,OD(\lambda)},$$

where λ refers to all wavelengths in the emission region.

Since emission is measured as intensity per wavelength interval, which does not scale linearly with energy, it is necessary to apply a λ^2 correction upon conversion into the wavenumber scale[43]:

$$I(\tilde{\nu}) = \lambda^2\, I(\lambda).$$

Emission Excitation Spectrum

The emission excitation spectrum is measured at a fixed emission wavelength, while the excitation wavelength is scanned. Within the framework of Kasha's rule[13], the emission excitation spectrum is expected to resemble the absorption spectrum, because the emission intensity only depends on the absorption intensity. Strong deviations from the absorption spectrum of the supposed emissive species indicate that either Kasha's rule is not valid in this case, or that a different emission source needs to be considered.

Emission excitation spectra need to be corrected for the lamp profile prior to analysis.

The presented emission and emission excitation spectra were recorded on a Spex FluoroMax-3 system.

2.6 Time- and Polarization Resolved Pump – Probe Transient Absorption Spectroscopy

2.6.1 Nonlinear Optics

Ultrashort Light Pulses

The time scales of chemical reactions correlate with structural changes of the molecules, i.e. with the nuclear motions. Since a molecular vibration typically takes tens to hundreds[44] of femtoseconds[1] (fs), the temporal resolution needed to follow reactions lies in the same range, and ultrashort laser pulses are needed. Monitoring photoreactions in real-time is achieved by pump-probe experiments: The reaction is triggered by an incident pump pulse, and the induced changes are monitored by a delayed probe pulse.

Contrary to continuous laser light, the spectral bandwidth $\Delta\nu$ of a short pulse has a lower limit, which is related to the temporal duration Δt of the pulse by the time-bandwidth product[14]. For Gauss pulses, the relation is:

$$\Delta t \, \Delta\nu \gtrsim 0.441.$$

Further, the different wavelengths do not neccessarily have identical temporal behavior, but can be shifted in time; this phenomenon is denoted as chirp. Arbitrarily tailored laser pulses can be applied to optimize photoinduced reactions[45].

Ultrashort light pulses exhibit another unique property: Because the energy is highly compressed both temporally and, if focussed, spatially, immensely high intensities can be reached, on the order of 10^{13} W cm^{-2}. These high intensities can induce nonlinear optical effects, which are widely used, for instance in optical parametric processes applied in wavelength conversion.

Application of Nonlinear Processes

In a linear approximation, the induced polarization P is related with electromagnetic field E by the electric susceptibility χ

$$P = \chi \varepsilon_0 E.$$

The electric susceptibility χ is related to the dielectric constant (or permittivity) ε: $\chi = \varepsilon - 1$ ($\varepsilon = \varepsilon_r \varepsilon_0$, relative permittivity times vacuum permittivity).

The above equation only holds as long as the intensity of the incident field is not too high, so that nonlinear processes can be excluded. If this is not the case, an expansion of P into a power series is necessary that includes higher orders of P:

$$P = \varepsilon_0 \left(\chi^{(1)} E + \chi^{(2)} E^2 + \chi^{(3)} E^3 + \ldots \right),$$

with $\chi^{(n)}$ - n^{th} order susceptibility. Second-order nonlinear optical processes are applied in second harmonic generation (SHG), sum frequency generation (SFG), and difference frequency generation (DFG). For the two incident electromagnetic fields $E_1 e^{i\omega_1 t}$ and $E_2 e^{i\omega_2 t}$ with the two frequencies ω_1 and ω_2, the second order polarization $P^{(2)}$ contribution includes

$$E_1^2 e^{i(2\omega_1)t} + E_2^2 e^{i(2\omega_2)t} + 2E_1^2 + 2E_2^2 + 2E_1 E_2 e^{i(\omega_1 - \omega_2)t} + 2E_1 E_2 e^{i(\omega_1 + \omega_2)t} \tag{2.3}$$

[1] femtosecond: 1 fs = 10^{-15} s

Hence, new frequencies are generated:

$$\underbrace{2\omega_1}_{\text{SHG}} \quad \underbrace{2\omega_2}_{\text{SHG}} \quad \underbrace{\omega_1+\omega_2}_{\text{SFG}} \quad \underbrace{\omega_1-\omega_2.}_{\text{DFG}}$$

These processes are important to generate the desired wavelengths in femtosecond spectroscopy; a schematic illustration is given in figure 2.7.

For the pump-probe experiments described in section 2.6.2, SHG, SFG, and DFG are used. Another important process is optical parametric amplification (OPA), which is similar to DFG. The lower energy wave is weak compared to the pump wave and only "seeds" the parametric process to yield the desired signal–idler wavelength pair.

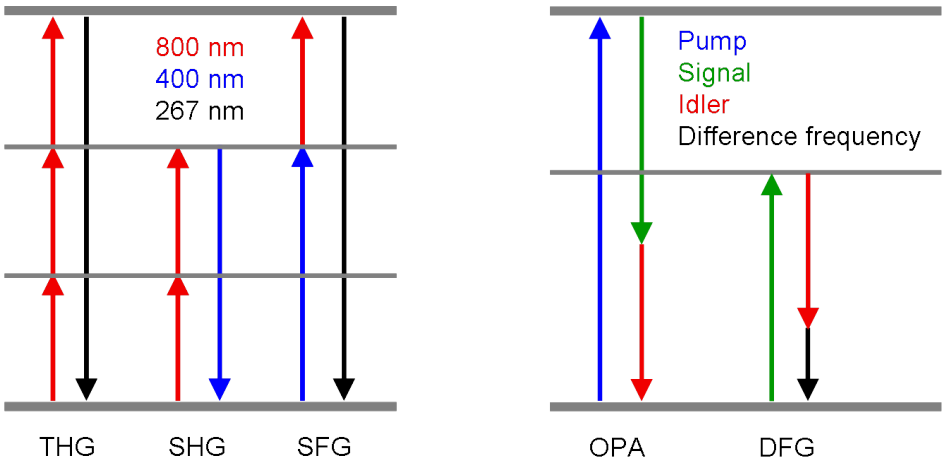

Figure 2.7: (a) Generation of UV pump: either directly by third harmonic generation (THG), or stepwise by SHG followed by SFG. (b) Generation of IR probe: OPA gives rise to signal and idler, which are subsequently applied in a DFG process.

Since processes of even order are forebidden if the medium has inversion symmetry, crystals used for application in frequency conversion have distinct axes. A typical material is BBO (β-barium-borate), which has birefringent properties, i.e. the crystal has an ordinary and an extraordinary optical axis with different polarization-dependent refractive indices. As a consequence, the polarizations of the incident beams and the crystal angle can be chosen to allow for (approximate) phase-matching. This is necessary because not only the energy must be conserved – e.g. for SFG, $\omega_3 = \omega_1 + \omega_2$, but also the momenta of the travelling waves. For the wave vectors k, the following equation applies in case of SFG:

$$k_3 = k_1 + k_2 + \Delta k,$$

where the phase mismatch Δk needs to be minimized.

2.6.2 Femtosecond Laser Pulse Generation and Pump-Probe Setup

General Pump-Probe Scheme

Figure 2.8 provides an overview on the genral aspects of a pump-probe experiment: After pump and probe pulse generation, the probe beam is directed over a delayline that is used to move a pair of mirrors and thereby vary the probe pathlength. This way, the time delay between the pump and probe pulses can be scanned up to several hundreds of picoseconds (ps)[2]. A chopper in the path of the pump beam blocks every second pulse, i.e. at a rate of 1 kHz, one pump pulse hits the sample every two milliseconds. The unpumped signals are used to determine the absorption change that is induced by the pump pulse. Part of the probe beam is split off as a reference beam.The other part is focussed in the same position as the pump and adjusted to yield a maximal spatial overlap. Both probe and reference beam are spectrally dispersed and directed into suitable detector arrays. The data are collected by the computer program, which is also used to control chopper and delayline, and to synchronize them with the trigger from the laser system.

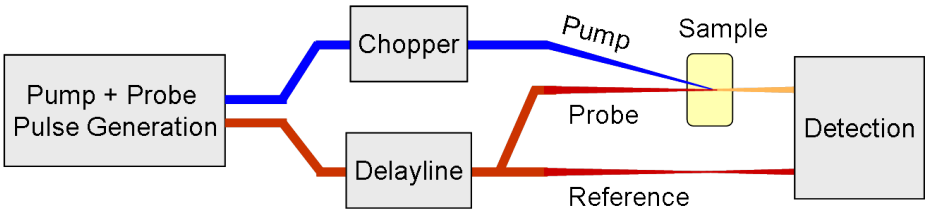

Figure 2.8: Schematic illustration of the principal pump-probe setup.

Setup for Polarization resolved UV Pump – IR Probe Experiments

The UV pump – IR probe setup was built from scratch; a schematic illustration is presented in figure 2.9. The pump and probe pulses are generated from the fundamental $\approx$ 800 nm of a Ti:Sapphire femotsecond laser system (50 fs, 1 kHz, USP-1, Coherent). The UV pump pulse of about 272 nm (36 700 cm^{-1}, FWHM = 440 cm^{-1}, 1 -- 2 μJ) corresponds to the third harmonic (THG) of the fundamental $\approx$ 820 nm (see also figure 2.7.a.). Pragmatically, the generation is achieved stepwise. In a first step, $\approx$ 408 nm are generated as the second harmonic (SHG) of 820 nm, and in the second step, the sum frequency (SFG) of 820 nm and 408 nm results in the anticipated UV wavelength.

For the IR probe pulse (see also fig. 2.7.b), a small part of the $\approx$ 800 nm fundamental is directed into a sapphire plate to yield a white light continuum (WLG, white light generation), which is then used as a seed for the optical parametic amplification (OPA). The white light is temporally and spatially overlapped with the 800 nm pump in a BBO crystal. Depending on the crystal angle and the relative orientation of the linear polarizations of seed and pump, the generated wavelength can be adjusted. The obtained signal and idler pulses are amplified in a second step: They are redirected into the BBO and overlapped with a second pump beam. Difference frequency generation (DFG) in a silver gallium sulfide ($AgGaS_2$) crystal is then applied to generate probe pulses in the IR around 1170 cm^{-1} as the differnce frequency between signal and idler output of the two-step OPA. The cross-correlation of the pump and probe pulses is $\approx$ 200 fs (FWHM).

[2]One nanosecond (1 ns= 10^{-9} s= 1000 ps) is the time is takes light to transverse a beam path of 30 cm length.

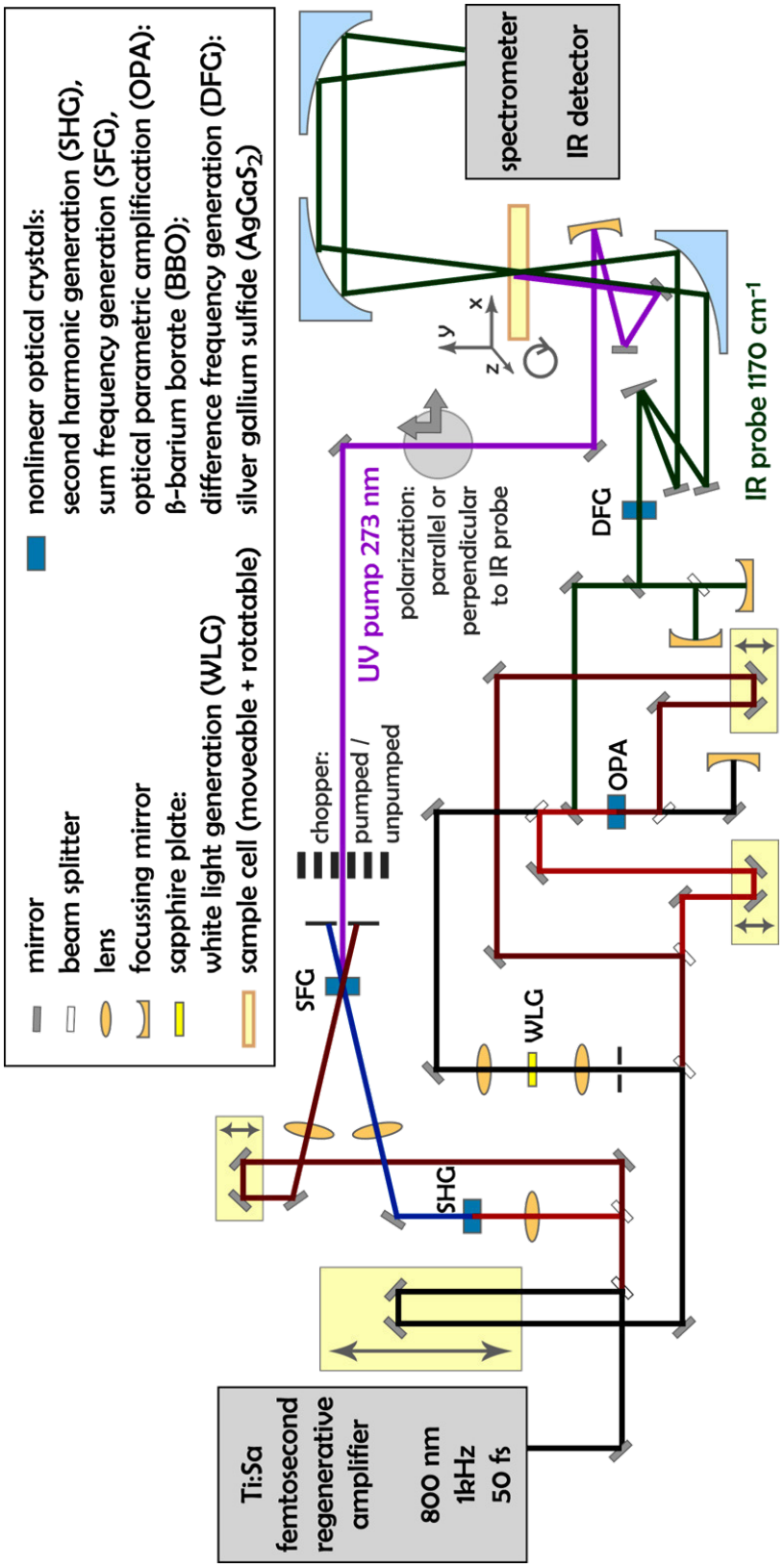

Figure 2.9: The pump-probe setup for polarization resolved experiments with ≈ 272 nm pump and 1170 cm^{-1} probe pulses.

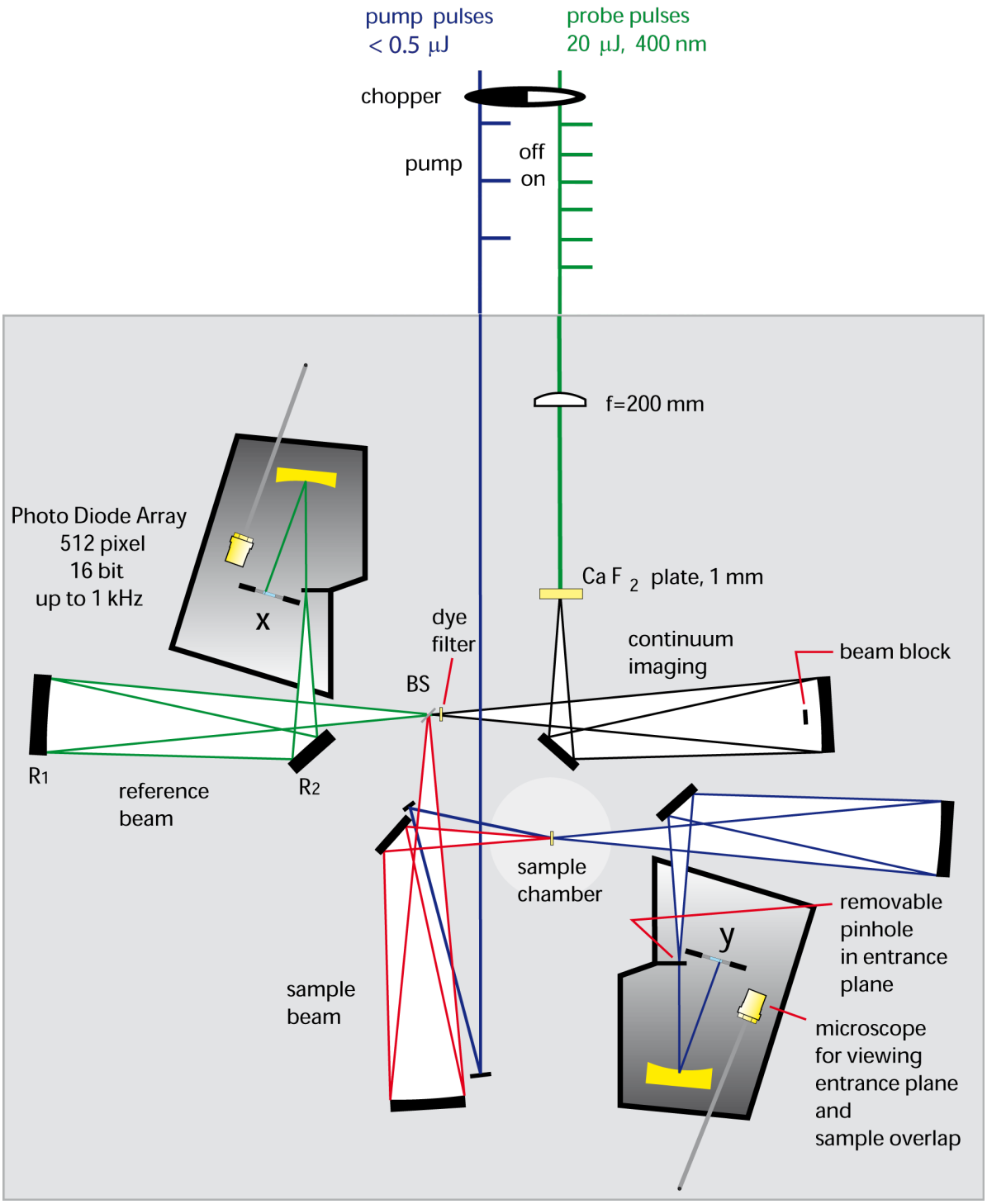

Figure 2.10: Pump-probe setup for time resolved experiments with UV pump and supercontinuum probe pulses. Picture by courtesy of Prof. N.P. Ernsting.

To arrive at a polarization resolved experiment, the linear polarization of the pump beam is changed by a $\lambda/2$ plate between being parallel and perpendicular with respect to the linear probe beam polarization, alternating from one measurement to the other. The reference beam also traverses the sample cell, but in a different spot than the pump and probe beams. The sample cell is made of BaF_2 windows with a sample thickness of 100 μm. The cell is continously rotated during the measurements to exchange and thereby refresh the sample volume before the next shot, to avoid excitation of photoproduct molecules generated by the previous pump pulse. The sample solution contained anthracene-9,10-endoperoxide with a concentration of 70 mM in deuterated chloroform ($CDCl_3$). The probe and reference beams are directed into a grating monochromator and detected by a double MCT (Mercury-Cadmium-Telluride, HgCdTe) photodiode array.

Setup for the Time resolved UV pump – IR probe Experiment

Basically, the setup for this experiment is similar; the pump-probe configuration is schematically shown in figure 2.10. A 0.5 kHz Ti:Sa laser system (Femtolasers, 30 fs)[46] is used to generate UV pump pulses by optical parametric amplification in a commercial TOPAS (Traveling-wave Optical Parametric Amplifier of Superfluorescence, Light Conversion). The pump pulses are tuned to the wavelengths 266, 282 or 376 nm, depending on the experiment. Supercontinuum probe pulses[47], covering a range from 290 to 650 nm, are generated by focussing the $\approx$ 400 nm second harmonic of the Ti:Sa fundamental into a 1 mm CaF_2 plate. The pump and probe pulse polarizations are adjusted to the magic angle (54.7 °) to avoid polarization effects. The pulses have energies below 0.5 μJ and durations of about 50 fs, giving an overall temporal resolution below 100 fs. The reference beam is not directed through the sample cell. The light from the probe and reference beams is dispersed in grating spectrographs, and transient signals are detected by a photodiode array (512 pixels, Hamamatsu). The samples have typical optical densities at the excitation wavelengths of 0.4 -– 0.8 OD over the 0.5 mm pathlength. The solutions are continuously pumped through the sample cell to exchange the sample volume for the next pump pulse. The closed system contains a total sample volume of 5 ml to slow down the overall increase of photoproduct concentration.

2.6.3 Analysis of Pump-Probe Data

Transient Absorption Spectra

The data that are obtained from a pump-probe measurement are arranged in a matrix, with spectra as columns and time traces as rows, as exemplified in figure 2.11. For analysis, the data are plotted as transient spectra at selected delay times (or temporal regions), or as temporal evolution of the signal (transients) at selected wavelengths (or wavelength regions).

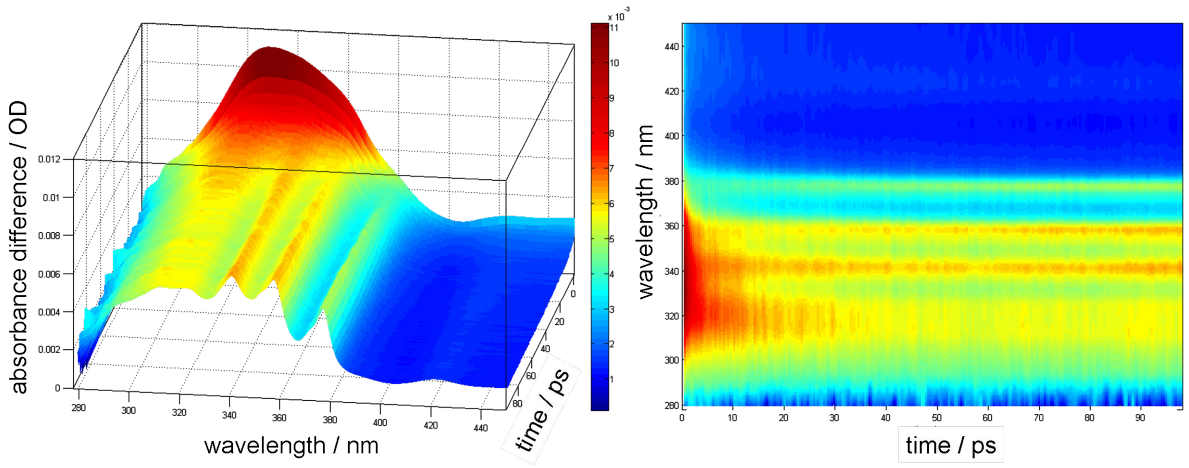

Figure 2.11: Transient absorption as a function of both wavelength and delay time: Anthracene-9,10-endoperoxide, pumped at 272 nm and probed with supercontinuum (discussed in chapter 6.)

In case of the polarization resolved experiments, the signals remain constant from $4 - 100$ ps and are therefore combined in one spectrum for parallel and one for perpendicular pump and probe polarizations. Their relative signal intensities are then used to calculate the relative orientations of pumped and probed transition dipole moments.
In the time resolved experiment, the spectrally broad supercontinuum probe pulses covered a range from 290 – 650 nm, and corrections for the probe chirp and solvent signal contributions were performed routinely prior to analysis. Furthermore, possible product molecule signal contributions were explicitly considered in the analysis.

Transient Absorption Contributions

To follow photoinduced reactions in real-time, the transient absorption changes with and without application of the pump pulse are compared, and thus the changes induced by the photoreaction are observed. When the delay time between the pump and probe pulses is systematically changed, a series of transient absorption spectra describes the temporal evolution of the reaction.
Three main contributions caused by excited molecules are distinguished:

Bleach — Upon excitation, population is depleted from the ground state, resulting in a reduced absorption (negative contribution) at the positions of stationary absorption bands.

Stimulated Emission — Excited molecules can be stimulated by the probe pulse to release their energy by emission, which gives rise to a negative transient absorption contribution.

Excited State Absorption Alternatively, the probe pulse can induce absorption of excited molecules, leading to positive absorption contributions.

Photoinduced reactions that generate product molecules can lead to additional contributions:

Ground State Absorption Newly created photoproduct molecules absorb at their stationary absorption positions (positive contribution). Because only absorption changes are monitored, previously created product molecules in the ground state do not contribute.

Excited Products By contrast, previously generated photoproduct molecules can contribute with BL, SE, and ESA if they are excited by the pump pulse.

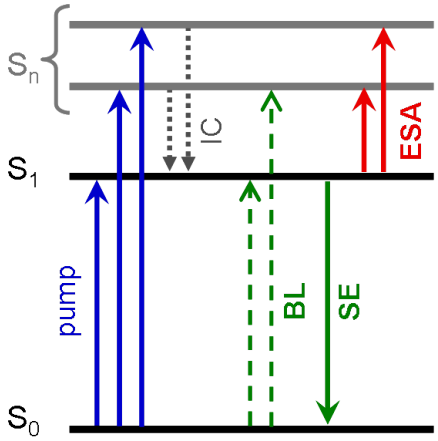

Figure 2.12: Schematic illustration of ground state bleach (BL), stimulated emission (SE), and excited state absorption (ESA) processes, after electronic excitation by a pump pulse followed by fast internal conversion (IC) to the first excited state S_1.

Effects of Vibrational Cooling

Both in the ground state and in electronic excited states, several vibrational levels might be occupied due to photoexcitation, internal conversion, or "hot" product generation. In transient absorption spectra, the vibrational cooling processes are visible by changes in spectral position and bandwidth. The vibrational cooling of a product that is generated in the hot ground state (as anthracene in section 6.3.3), transient absorption bands become sharper and blue-shifted with time, just as in stationary absorption spectra for higher → lower temperatures. Fig. 2.13.a compares the anthracene spectra at two different temperatures, and fig. 2.13.b illustrates (1) that the 0-0 transition is broader in hot spectra due to contributions from 1-1, 2-2… transitions with slightly deviating energies, and (2) that absorption bands are blue-shifting during cooling, because the lower energy transitions 1-1, 2-2… loose influence. Furthermore (3), new 1-0, 2-0, 2-1… transitions at considerably lower energies might emerge if higher vibrational levels are significantly populated.

Similarly, the excited state absorption (ESA) signal in transient absorption spectra show a blue-shift, as illustrated in figure 2.14. Vibrationally hot excited states are for instance populated upon direct photoexcitation, or after internal conversion from higher electronic excited states as assumed in figure 2.14.

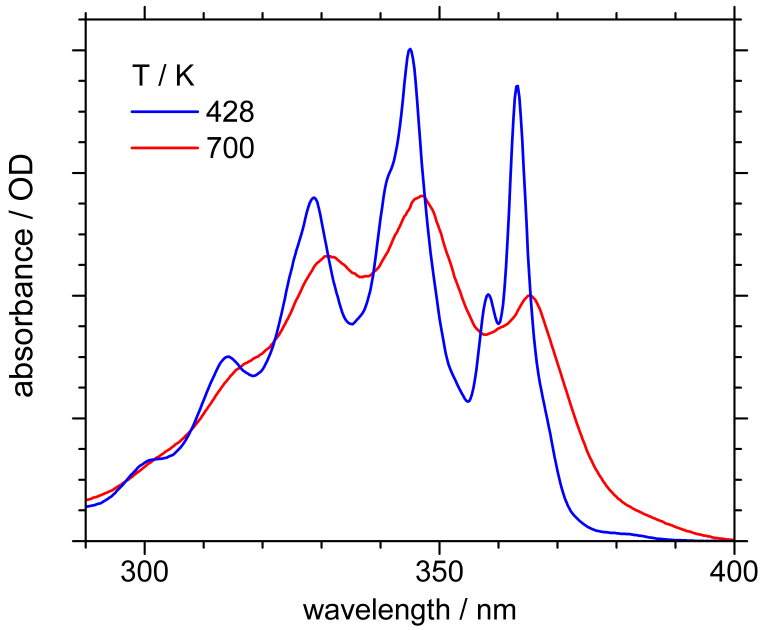

(a)

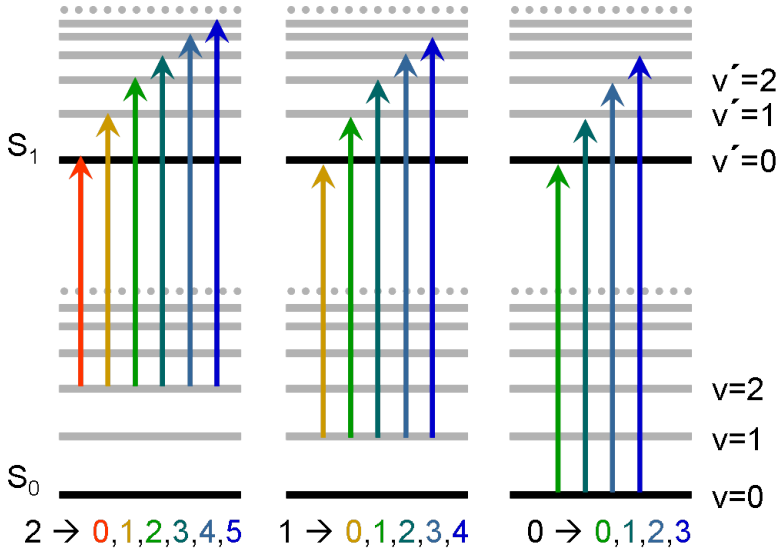

(b)

Figure 2.13: (a) Stationary absorpion spectra of AC in gas phase, at 428 K (155 °C, blue) and 700 K (427 °C, red). (b) From left to right: Schematic illustration of the vibrational cooling effects.

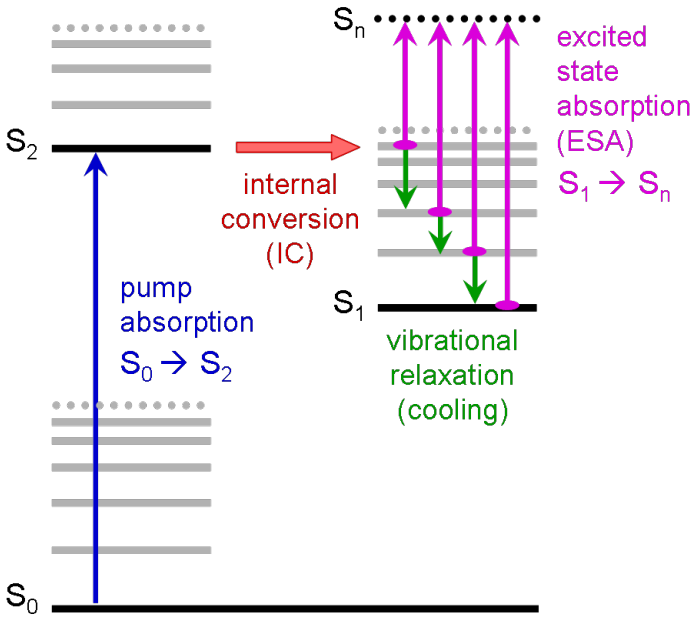

Figure 2.14: Schematic illustration of the blue-shift of excited state absorption (ESA) during vibrational cooling in the S_1 state.

Band Integrals

To analyze the temporal evolution, spectral regions of common behavior are conveniently united. The integral intensity of the signal, or the band integral[48] is given by

$$BI(t;\lambda_b,\lambda_r) = \int_{\lambda_b}^{\lambda_r} \Delta OD(t,\lambda)\cdot(d\lambda/\lambda) = \int_{\nu_b}^{\nu_r} \Delta OD(t,\nu)\cdot(d\nu/\nu),$$

with λ_b (blue) and λ_r (red) - considered wavelength region. If the band integral is taken over the whole absorption band of one transition, it is proportional to the population of the electronic state and insensitive to occupation changes in vibrational levels (internal temperature); it therefore allows to separate the analysis of population changes from vibrational cooling effects.

Global Analysis

Assuming that the spectral evolution can be understood as a combination of first-order steps, it can be fitted globally by a multi-exponential decay function $S(t,\lambda)$ with time constants τ_j:

$$S(t,\lambda) = \sum_{j=1}^{n} A_j(\lambda)\cdot\exp\left(-\frac{t}{\tau_j}\right).$$

Here, $A_j(\lambda)$ is the spectral amplitude associated with the time constant τ_j, also denoted as decay associated spectrum (DAS). DAS represent spectral changes and can in general not be attributed to individual species.

Polarization Resolved Experiment

The linear polarization of the pump pulse influences which molecules of an isotropic ensemble are excited: Those molecules with the corresponding transition dipole moment in the direction of the pump pulse polarization are more likely excited. More precisely, excitation with linear polarized light results in excited molecules with a cos-square distribution of TDM orientations. Due to this photoselection, the probe pulse response depends on the relative angles between pumped and probed TDM orientations. The transient absorption signals of probe pulse with parallel or perpendicular polarizations with respesct to the pump pulse polarization therefore show different intensities. Quantitatively, this is expressed in the dichroitic ratio D[49], with $A_{\parallel}$ and $A_{\perp}$ as the signals detected with parallel or perpendicular pump and probe pulse polarizatios, respectively. From the measured dichroitic ratio, the angle θ between the pumped and probed TDM orientations can be derived according to the following equations:

$$D = A_{\parallel}/A_{\perp}, \quad \theta = \arccos\sqrt{\frac{2D-1}{D+2}}.$$

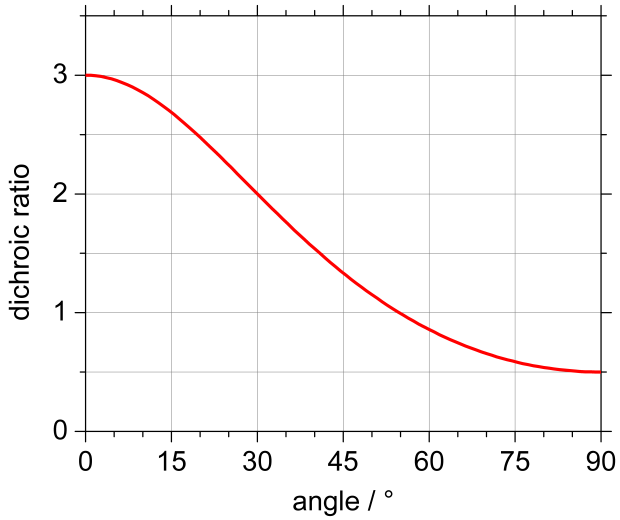

Figure 2.15: Structure of palladium tetra(tert-butyl)porphyrazine, the photosensitizer used in the synthesis of anthracene-endoperoxide[50].

2.7 Substances

2.7.1 Commercially Available Substances

Solvents

The solvents used include acetonitrile and deuterated acetonitrile, chloroform and deuterated chloroform, and butyronitrile. The solvents were used as purchased from Sigma-Aldrich.

Anthracene and Anthraquinone

The commercially available chemicals anthracene and anthraquinone were purchased from Sigma-Aldrich and used without further purification.

2.7.2 Synthesis of Anthracene-9,10-endoperoxide

APO was synthesized by Dr. W. Freyer at the Max-Born-Institute (Berlin), using palladium tetra(tert-butyl)porphyrazine as an external photosensitizer, which resulted in a considerably higher quantum yield than the reported procedure with polymer bound rose Bengal [7]. APO's purity was checked by thin layer chromatography (silica gel 60, Merck), using benzene/cyclohexane (3:2) containing 3% tetrahydrofuran as eluent.

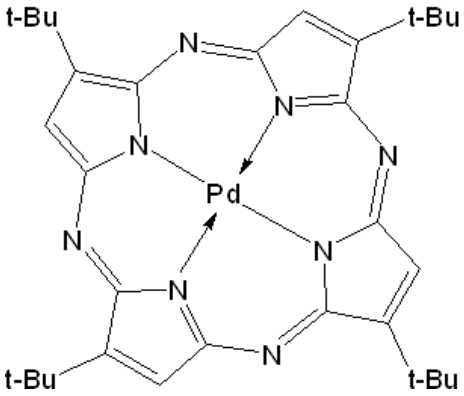

Figure 2.16: Structure of palladium tetra(tert-butyl)porphyrazine, the photosensitizer used in the synthesis of anthracene-endoperoxide[50].

The synthesis of APO is a Diels-Alder type reaction (see fig. 2.17, compare fig. 1.7) from the precursors anthracene and molecular oxygen via photosensitisation by palladium tetra(tert-butyl)porphyrazine[50] (fig. 2.16).

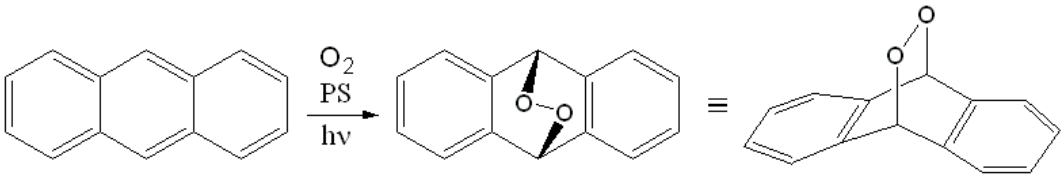

Figure 2.17: Diels-Alder type cycloaddition from anthracene to the corresponding anthracene-9,10-endoperoxide using oxygen and a photosensitizer (fig. 2.16).

The ratio of the 9,10- and 1,4-endoperoxide isomers depends on the functional groups attached to the anthracene moiety; APO was reported[15] to be generated to 100 % as the 9,10-isomer. However, it is conculded in the present work that the alternative 1,4-isomer is formed as a minor side product. In figure 2.18, the two isomeric structures of APO are compared.
Because of the close similarity of both isomers and the supposedly low percentage (< 0.5 %), 1,4-APO was detected neither in thin layer chromatography nor in ^1H NMR spectra.

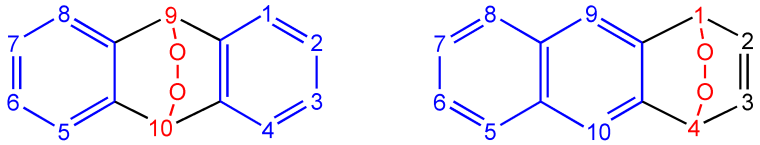

Figure 2.18: The two isomeric structures of anthracene-endoperoxide (APO)

2.8 Computational Details to the Calculations used in Chapter 4[35]

All electronic calculations were performed on the MP2/6-311 G(d,p) optimized structure of APO summarized in figure 4.1.a. The vertical excited spectrum was computed at the MS-CASPT2/CASSCF level of theory[51, 52] and the ANO-S basis set[53], with the C, O [3s2p1d]/H [2s1p] contraction. The active space of the CASSCF wave function consists of 14 electrons in 12 orbitals, including four pairs of π_{CC} and π^*_{CC} orbitals from the anthracene moiety, and the π_{OO}, π^*_{OO}, σ_{OO}, and σ^*_{OO} orbitals localized in the endoperoxide bridge, see figure 2.19. Calculated were 5, 4, 5, 5 roots of A_1, B_1, B_2, and A_2 symmetry, respectively. To avoid intruder states a level shift of 0.4 a.u. was used in the MS-CASPT2 calculations[54].
The APO S_1 and the diradical S_0 states were optimized under C_{2v} and C_s symmetry constraints, respectively, with the same active space (see fig. 4.1.b and 4.1.c). Real vibrational frequencies confirm that the resulting structures are minima.
To estimate the influence of $CHCl_3$-solute interactions the ground state geometry was reoptimized using the Polarized Continuum Model[55], and a dielectric constant of 5.0. Vertical excitation energies in solution were estimated on this geometry.
Transition dipole moments (TDM) have been computed with the perturbative modified CASSCF wave function. Oscillator strengths are obtained from these TDMs and MS-CASPT2 energies.
All MS-CASPT2/CASSCF calculations were carried out using the MOLCAS 6.0 quantum chemistry package[56].

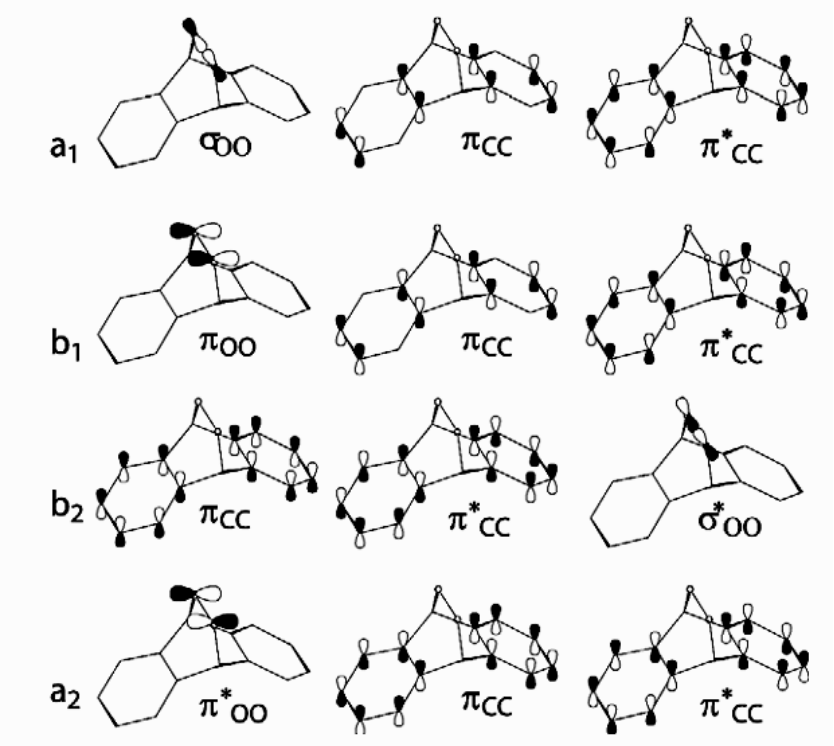

Figure 2.19: CASSCF molecular orbitals for the ground state included in the (14, 12) active space used in the calculation of the vertical spectra and geometry optimization.

3 Spectral Properties of Anthracene-Endoperoxide and its Reaction Products

Reaction Products

Figure 3.1 gives an overview on the chemical structures of the reaction products that are generated from anthracene-9,10-endoperoxide (APO) under various conditions. The thermal reaction (indicated by Δ in fig. 3.1) results only anthraquinone (AQ). Photoexcitation leads to two competing reaction channels depending on wavelength. The primary photoreaction products are anthracene (AC), together with the detached singlet molecular oxygen, and a diepoxide (DE; syn-anthracene 4a,10:9,9a-dioxide according to Rigaudy *et al.* [28]). Photoexcitation of DE leads to formation of a bicyclic acetal (BA). In higher concentrated samples (> 5 mM instead of ≤ 1 mM), two more products could be identified upon photoexcitation: 9,10-dihydroxy-9,10-dihydroanthracene (DHA), and 9-hydroxy-10-anthrone (HA).

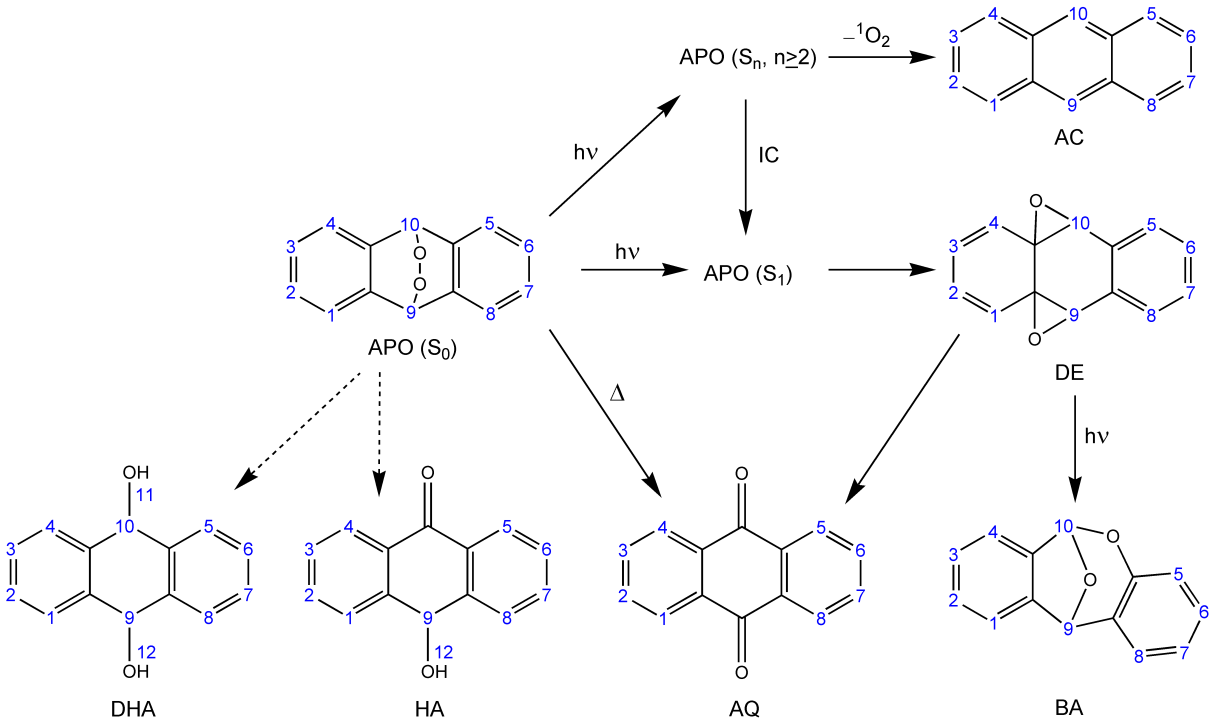

Figure 3.1: Reaction scheme of APO. - *H* positions are numbered for assignment of ^1H NMR signals.

3.1 ^1H NMR Spectra

Comparison with Literature Data

The ^1H NMR spectra of APO, AC, and AQ were recorded on samples containing the respective pure compounds in perdeuterated acetonitrile. The chemical shifts of DE and BA were deduced from partially photoconverted samples and compared to the values given by Rigaudy *et al.* [28]. In higher concentrated samples, two more compounds could be identified by comparison with data of Rigaudy [27] and Criswell [57] as 9,10-dihydroxy-9,10-dihydroanthracene (DHA) and 9-hydroxy-10-anthrone (HA), respectively.

^1H NMR Spectrum of APO

Since APO has two mirror planes, some hydrogen (H) atoms are chemically equivalent, and only three groups of H's are distinguishable in the nuclear magnetic resonance (NMR) experiment. Two equivalent H's are located close to the oxygen bridge (H_A, compare figure 3.2), and two sets of 4 identical H's each are situated at the aromatic rings (H_B, H_C). Thus, three signals are expected in the ^1H NMR spectrum in an intensity ratio of about 2:4:4. Indeed, the following three chemical shift values are observed in the ^1H NMR spectrum of APO: $\delta = 6.2$ ppm, rel. integral 1 (2 H_A),

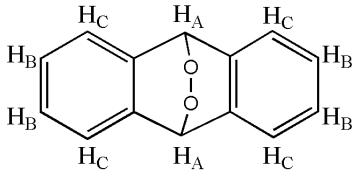

Figure 3.2: Chemical structure of anthracene-9,10-endoperoxide (APO). - H atoms are labeled in groups of same ^1H NMR shifts.

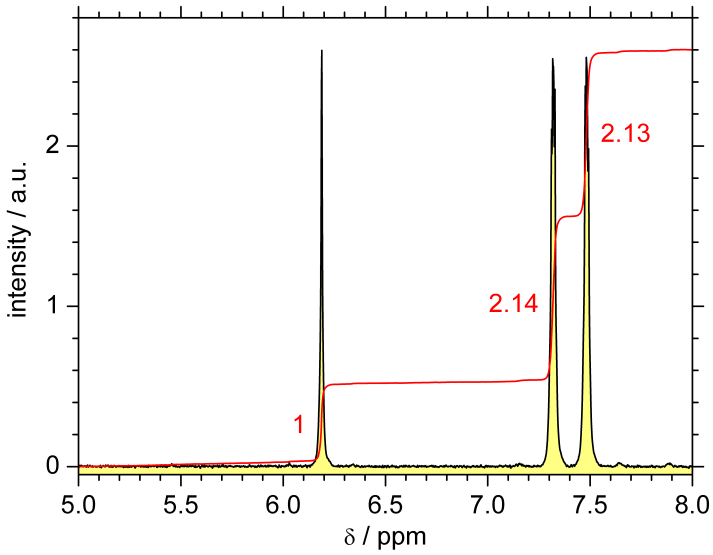

Figure 3.3: ^1H NMR spectrum of APO in deuterated acetonitrile (black). - The red line indicates the integrated signal (scaled).

$\delta = 7.3$ ppm, rel. integral 2.14 (4 H_B), and $\delta = 7.5$ ppm, rel. integral 2.13 (4 H_C), as presented in figures 3.2 and 3.3.

^1H NMR Spectra of Products

Some representative ^1H NMR spectra that were measured for photo-converted samples are shown in figure 3.4. The conditions under which the presented product mixtures were obtained are analyzed in section 5.2. The assignments of the chemical shift values are summarized below. Typical ^1H NMR chemical shift values for aromatic protons lie in the range of 6.5-8.5 ppm; values for protons with adjacent oxygen are expected around 2.5-4.5 ppm, and for protons located at alkene double bonds usually around 4.5-6.5 ppm. The product structures are given in figure 3.1.

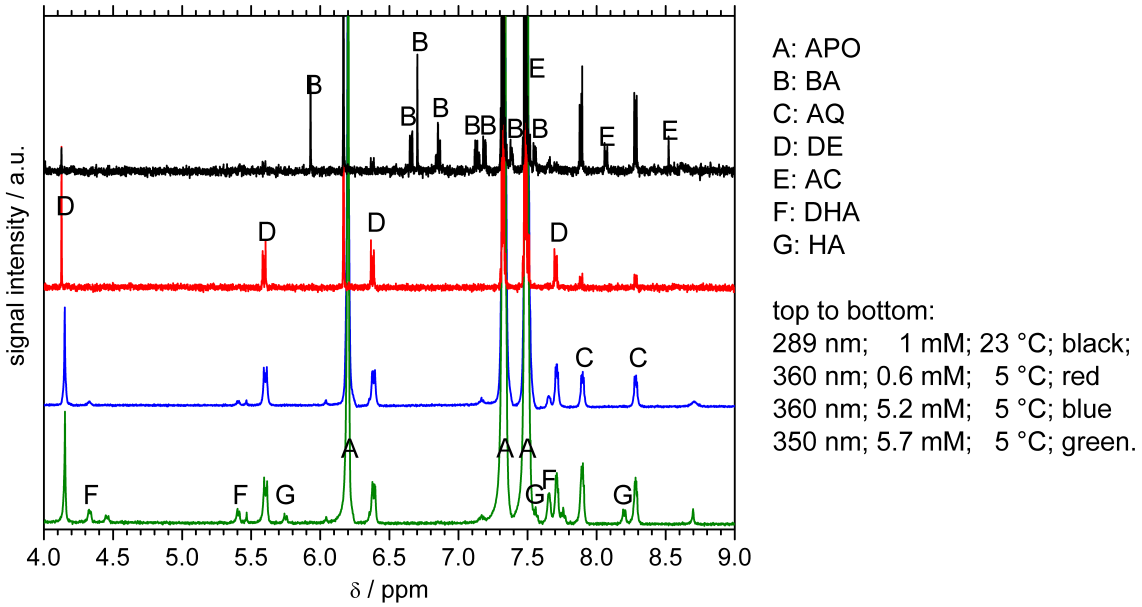

Figure 3.4: ^1H NMR spectra of APO and its products in perdeuterated acetonitrile. - Label assignments as well as excitation wavelengths, initial APO concentrations, and temperatures of the four samples are given in the figure.

Anthracene-9,10-endoperoxide (APO)

$H9, H10 : \delta = 6.15$ ppm $(2H)$
$H2, H3, H6, H7 : \delta = 7.30$ ppm $(4H)$
$H1, H4, H5, H8 : \delta = 7.50$ ppm $(4H)$

Anthracene (AC)

$H9, H10 : \delta = [7.50^*]$ ppm $(2H)$ (*: partially superimposed by APO signal at $\delta = 7.50$ ppm)
$H2, H3, H6, H7 : \delta = 8.00$ ppm $(4H)$
$H1, H4, H5, H8 : \delta = 8.50$ ppm $(4H)$

Anthraquinone (AQ)

$H2, H3, H6, H7 : \delta = 7.85$ ppm $(4H)$
$H1, H4, H5, H8 : \delta = 8.30$ ppm $(4H)$

Diepoxide (DE)

$H9, H10 : \delta = 4.10$ ppm $(2H)$
$H1, H4 : \delta = 5.60$ ppm $(2H)$
$H2, H3 : \delta = 6.35$ ppm $(2H)$
$H6, H7 : \delta = [7.45^{*}]$ ppm $(2H)$ (*: superimposed by APO signal at $\delta = 7.5$ ppm)
$H5, H8 : \delta = 7.65$ ppm $(2H)$

Bicyclic Acetal (BA)

$H9 : \delta = 5.95$ ppm $(1H)$
$H10 : \delta = 6.70$ ppm $(1H)$
$H5, (H6, H7), H8 : \delta = 6.65$ ppm, 6.85 ppm, 7.15 ppm $(4H)$
$H1, (H2, H3), H4 : \delta = 7.20$ ppm, 7.40 ppm, 7.55 ppm $(4H)$

Dihydroxydihydroanthracene (DHA)

$H11, H12 : \delta = 3.90$ ppm $(2H)$
$H9, H10 : \delta = 5.40$ ppm $(2H)$
$H2, H3, H6, H7 : \delta = 7.35$ ppm $(4H)$
$H1, H4, H5, H8 : \delta = 7.65$ ppm $(4H)$

Hydroxyanthrone (HA)

$H12 : \delta = 4.10$ ppm $(1H)$
$H9 : \delta = 5.75$ ppm $(1H)$
$H2, H7 : \delta = 7.55$ ppm $(2H)$
$H3, H6 : \delta = 7.75$ ppm $(2H)$
$H1, H8 : \delta = [7.85^{*}]$ ppm $(2H)$ (*: partially superimposed by AQ signal at $\delta = 7.85$ ppm)
$H4, H5 : \delta = 8.20$ ppm $(2H)$

3.2 Infrared Spectra

Choice of IR Probe Wavelength

Infrared (IR) spectra of APO were taken in butyronitrile (C_4H_7N) and in deuterated chloroform ($CDCl_3$) as solvents. The polarization-resolved UV pump - IR probe experiment described in section 4.2 was conducted in $CDCl_3$. A reasonable choice for the IR probe wavelength would be the O-O streching vibration, which is directly related to the double bond formation upon molecular oxygen generation, or would vanish upon O-O bond cleavage. However, the low frequency ≤ 900 cm^{-1} of this vibration makes a use in a pump-probe experiment unconvenient. Furthermore, a vibration must be chosen that is not hidden under a strong solvent signal. Therefore, the IR spectra of the pure solvents are compared with the respective APO solutions in figures 3.5 and 3.6, and the difference spectra obtained after correcting for the solvent contributions are shown in figure 3.7. Based on these data, the experimentally most evident APO peak at 1170 cm^{-1} is chosen. Butyronitrile has

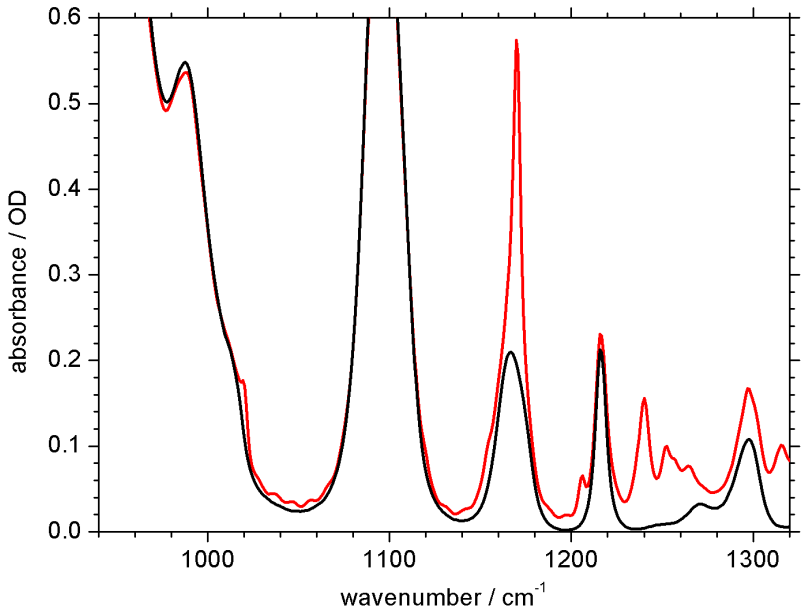

Figure 3.5: APO IR spectrum in perdeuterated chloroform ($CDCl_3$). - Red line: APO solution; black line: $CDCl_3$.

an absorption minimum at this wavelength, as visible in figure 3.6. Unlike butyronitrile, $CDCl_3$ shows a signal around 1167 cm^{-1}, but a sharper APO peak at 1170 cm^{-1} is nevertheless clearly distinguishable (fig. 3.5). The comparison of the difference spectra in figure 3.7 confirms the reliability of the peak.

According to calculations using the Gaussian program [58], the vibration measured at 1170 cm^{-1} corresponds to a $\delta(CH)$ bending vibration calculated at 1188 cm^{-1}, with a TDM orientation along the peroxide bridge.

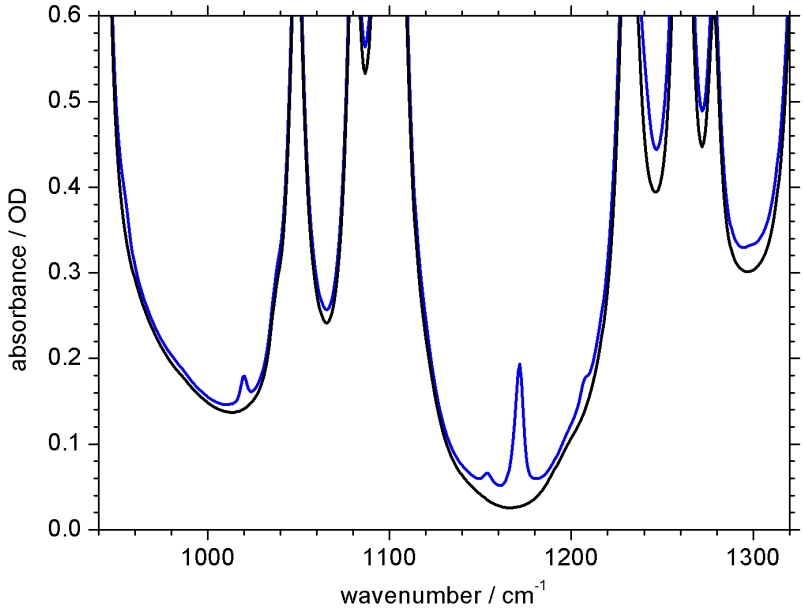

Figure 3.6: APO IR spectrum in butyronitrile. - Blue line: APO solution; black line: butyronitrile.

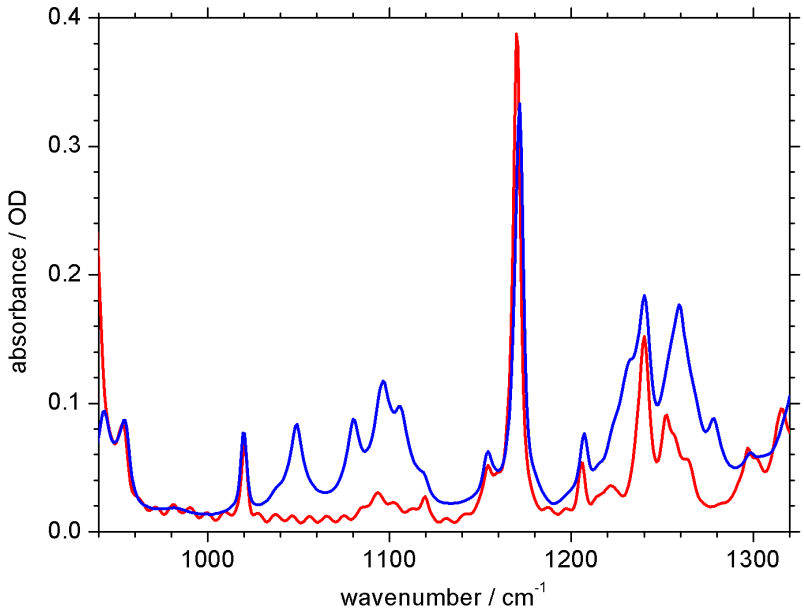

Figure 3.7: APO IR difference spectra after solvent correction. - Red line: APO in deuterated chloroform ($CDCl_3$); blue line: APO in butyronitrile (scaled).

3.3 UV/visible Absorption Spectra

Absorption Spectrum and Extinction Coefficients of APO

The absorption spectrum of APO in acetonitrile is shown in figure 3.8, on a linear scale (red) and on a logarithmic scale (blue). Two shoulders can be clearly distinguished, with positions around

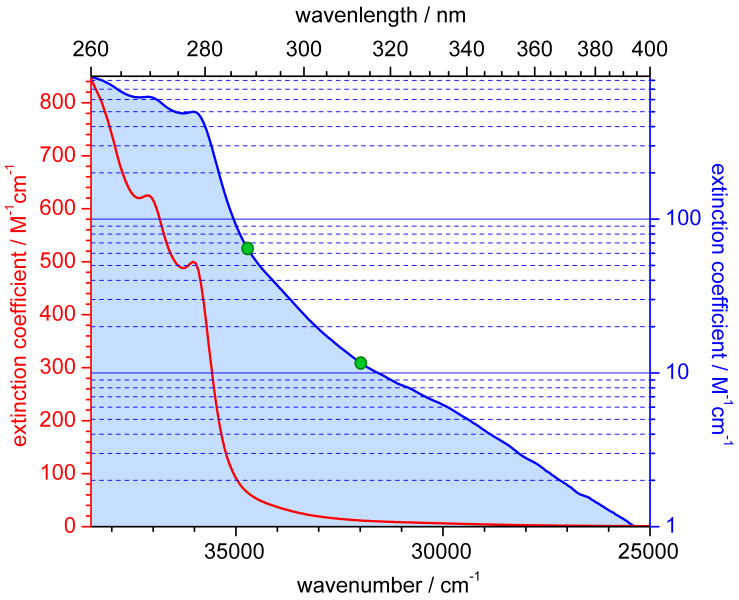

Figure 3.8: APO UV/vis absorption spectrum in deuterated chloroform ($CDCl_3$). - Red line: linear scale; blue line: logarithmic scale; green dots added to guide the eye.

280 nm (35900 cm^{-1}) and 270 nm (37000 cm^{-1}). To shorter wavelengths, the absorption increases steeply up to a maximum around 216 nm (46 300 cm^{-1}, not shown in fig. 3.8). The extinction coefficients at 280 and 270 nm only amount to 500 and 625 $M^{-1}cm^{-1}$, respectively, while the maximum at 216 nm is 44 800 $M^{-1}cm^{-1}$. Since this work deals mostly with wavelengths above 260 nm (850 $M^{-1}cm^{-1}$), extinction coefficients of APO are considered very low. For comparison: the thermal product anthraquinone has an extinction coefficient of 4600 $M^{-1}cm^{-1}$ at 323 nm. Therefore, even tiny amounts of products in the sample could lead to remarkable contributions, and it is important to be careful considering such effects.

The assignment of the electronic excited singlet states of APO has been subject of a controversial dipute in literature[24, 30, 31, 34]: It remains ambiguous whether the lowest absorption band is located at 280 nm, or whether another lower-energy band exists. A closer look at the logarithmic plot reveals two inflection points (green dots) around 34 700 cm^{-1} and 32 000 cm^{-1}. This behavior suggests that there might be an additional very weak absorption band hidden in the tail of the stronger absorption bands. An approach for further analysis is shown in figure 3.9: The absorption is fitted by a sum of Gauss or Lorentz lines. For Gauss lines (fig. 3.9.a), a band around 290 nm is needed to account for the long absorption tail, while for Lorentz lines (fig. 3.9.b) this is not necessary. Hence, this simulation is unfortunately inconclusive with regard to the existence of a lowest absorption band > 280 nm.

To unambiguously identify the lowest electronic excited states, it is therefore necessary to consult quantum chemical calculations, which are presented and discussed in section 4.

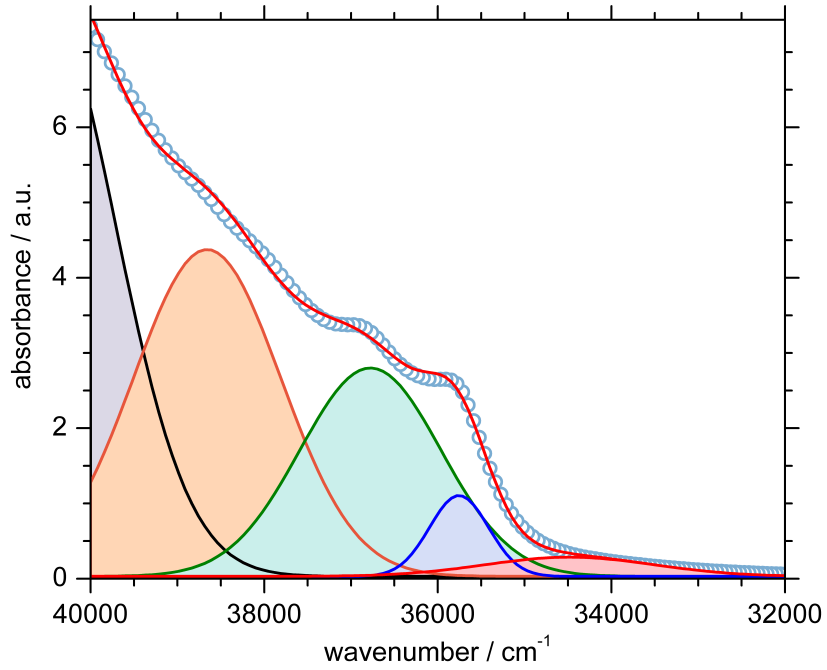

(a)

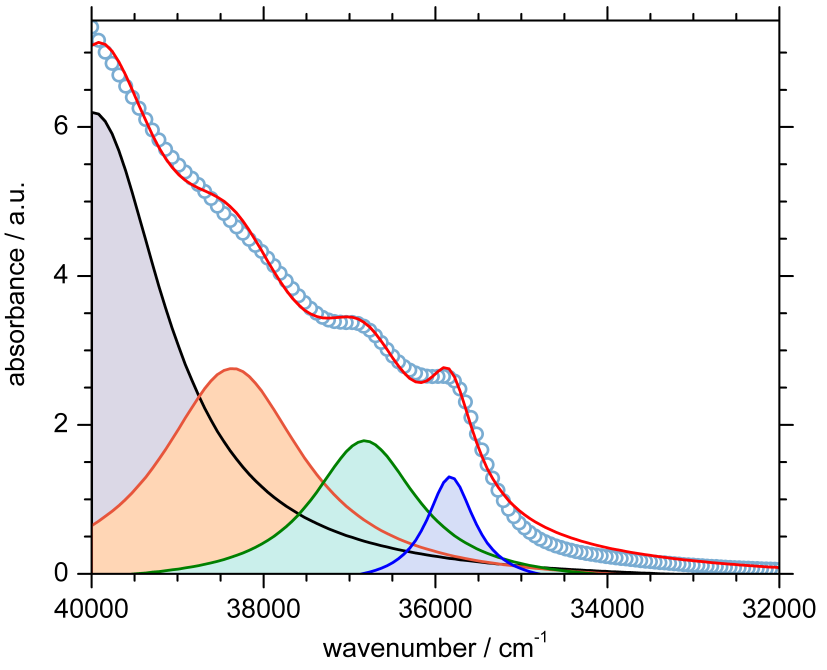

(b)

Figure 3.9: Simulation (red line) of APO absorption spectrum (blue circles) as a sum of (a) Gauss fits and (b) Lorentz fits.

Absorption Spectra and Extinction Coefficients of Products

The UV/vis absorption spectra of the main reaction products of APO are shown below, each in a separate figure. Some of them include two zoom levels to lay emphasis on different features of the spectra. The specific conditions under which the respective products are formed is subject of section 5.2.

Anthracene. For AC (figure 3.10), a sharp strong peak is observed at 252 nm (155000 $M^{-1}cm^{-1}$), and the characteristic vibrational progression with maxima at 376 nm (6 290 $M^{-1}cm^{-1}$), 358 nm (6860 $M^{-1}cm^{-1}$), 341 nm (4670 $M^{-1}cm^{-1}$), and 323 nm (2430 $M^{-1}cm^{-1}$). These spectral absorption features make AC distinguishable in reaction mixtures and play an important role in the analysis of the time-resolved transient absorption spectra in chapter 6.

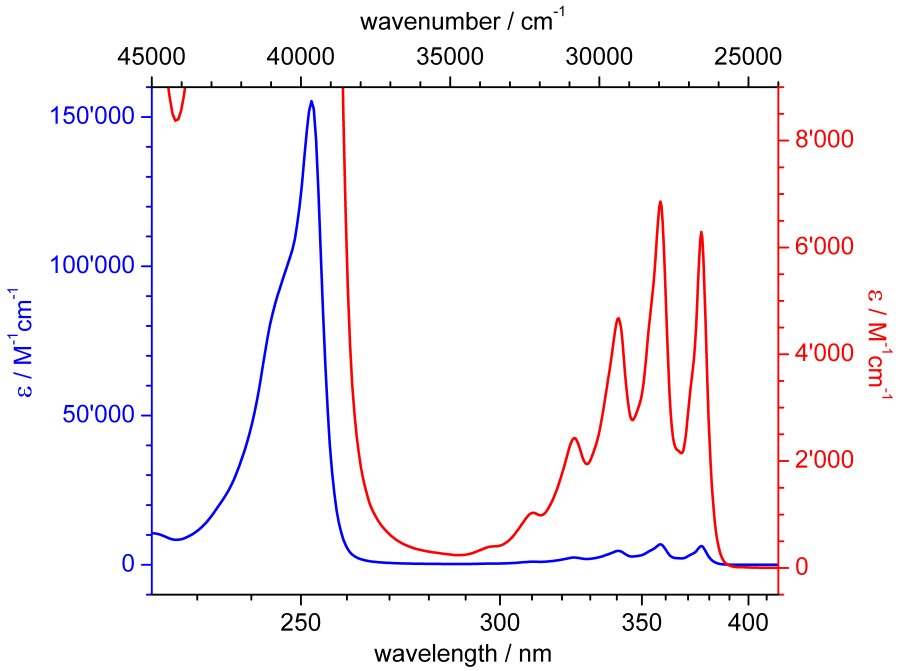

Figure 3.10: UV/vis extinction coefficient spectrum of AC in acetonitrile.

Anthraquinone. AQ (figure 3.11) has an absorption maximum at 251 nm (46 700 $M^{-1}cm^{-1}$), roughly the same position as AC, but with a different shape, and AQ has two shoulders at 262 nm (19 000 $M^{-1}cm^{-1}$) and 272 nm (15 400 $M^{-1}cm^{-1}$). An additional broad band is observed centered at 323 nm (4 610 $M^{-1}cm^{-1}$).

Diepoxide. The absorption spectrum of the diepoxide (figure 3.12) was deduced from partially photoconverted APO samples by subtracting the absorption contributions of the known compounds APO, AC, and AQ from the measured spectra. ^1H NMR spectra of the same samples gave absolute values for the DE concentration in the respective samples. Combining information from UV/vis difference spectra and from the ^1H NMR spectra allowed for the assignment of extinction coefficient values. The maximum absorption in the region above 250 nm is found at 284 nm (3150 $M^{-1}cm^{-1}$), a slightly structured broad band. Because of increasing absorption by APO and other photoproducts in the wavelength region below 290 nm, the error margins of the DE spectrum increase in that

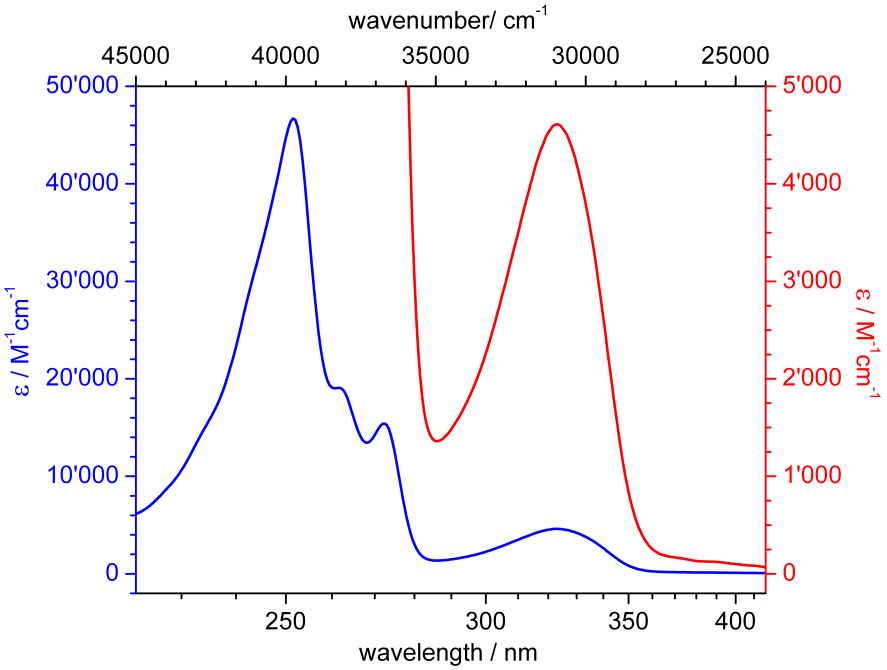

Figure 3.11: UV/vis extinction coefficient spectrum of AQ in acetonitrile.

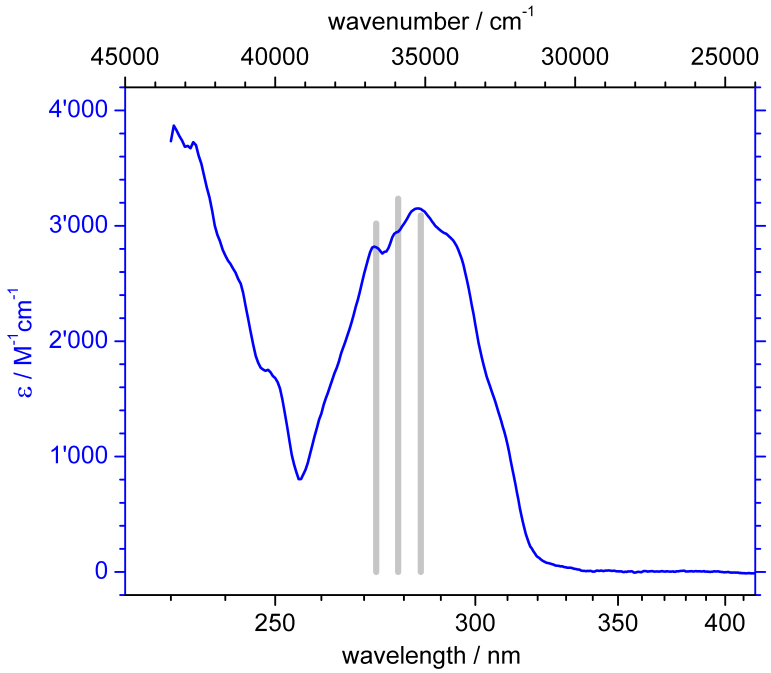

Figure 3.12: UV/vis extinction coefficient spectrum of DE in acetonitrile. - Grey bars indicate the positions and extinction coefficients published by Rigaudy *et al.*, measured in diethyl ether [28].

region. Figure 3.12 also shows literature data for the diepoxide extinction coefficients published by Rigaudy *et al.* [28]: Besides the shift of the maxima by about 5 nm, the overall agreement is reasonable, the extinction coefficient values are almost identical. Since Rigaudy *et al.* did not show the actual spectrum, a comparison of the shape of the absorption band is not possible.

Bicyclic Acetal. Similarly, the absorption spectrum of the bicyclic acetal was derived from photoreaction mixtures, but in this case the DE spectrum had to be subtracted as well. Since the DE spectrum is becoming less reliable below 290 nm, the BA spectrum even more so. Nevertheless, a

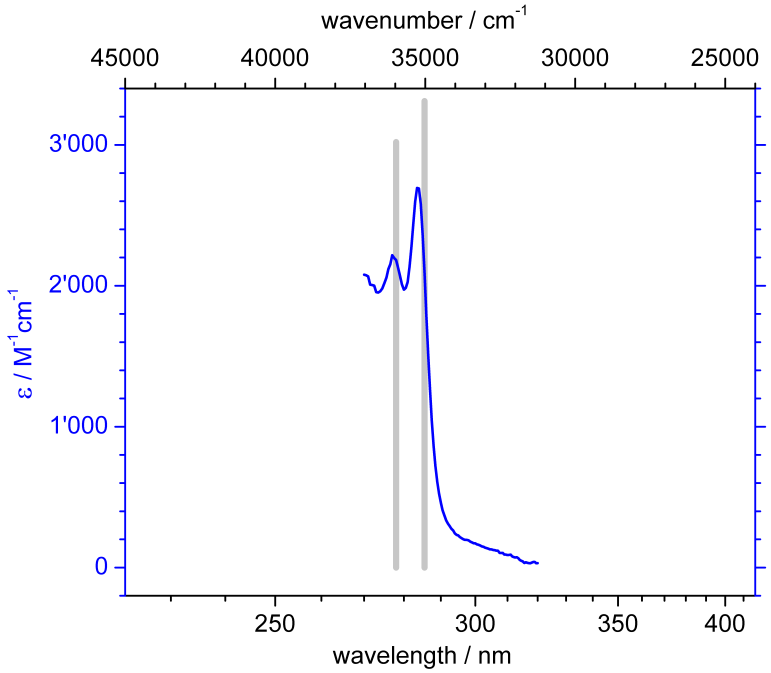

Figure 3.13: UV/vis extinction coefficient spectrum of BA in acetonitrile. - Grey bars indicate the positions and extinction coefficients published by Rigaudy *et al.*, measured in diethyl ether [28].

few sharp absorption peaks remain that clearly do not belong to any of the other compounds. A maximum is observed at 283.5 nm (2690 $M^{-1}cm^{-1}$) and another smaller but equally sharp peak at 277 nm (2220 $M^{-1}cm^{-1}$). The agreement with the peak positions reported by Rigaudy *et al.* [28] (285.5 nm and 278 nm) is good, and the extinction coefficients found by Rigaudy slightly higher (3310 $M^{-1}cm^{-1}$ and 3020 $M^{-1}cm^{-1}$).

Example for Reaction Mixture Absorption Spectrum

Figure 3.14 illustrates how the absorption of a sample, photoconverted by illumination at 277 nm, is composed of APO and the photoproducts AC, AQ, and DE.

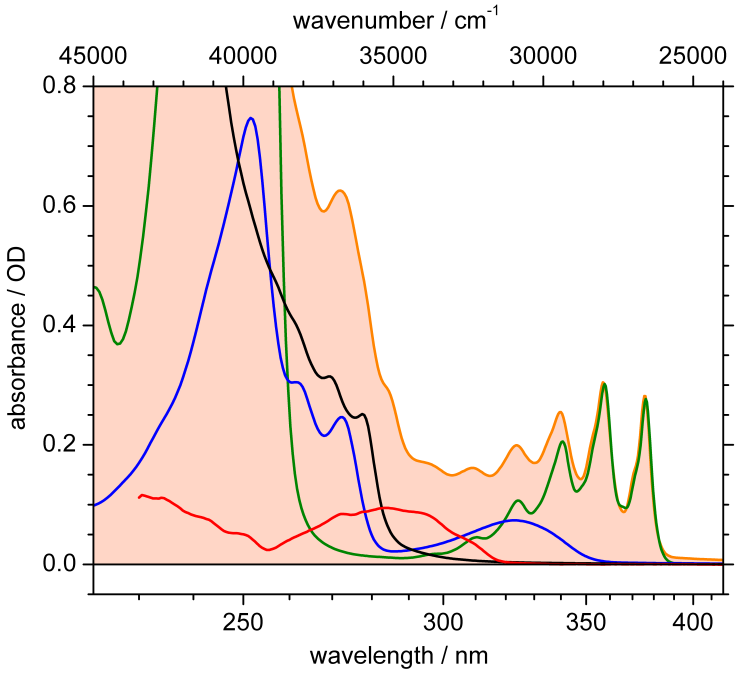

Figure 3.14: UV/vis absorption spectrum of a photoproduct mixture sample, resulting from APO in acetonitrile after illumination at 277 nm (orange). - For comparison, the scaled absorption contributions of APO (black), AC (green), AQ (blue), and DE (red) are shown, which are needed to recompose the measured spectrum.

3.4 Emission Spectroscopy

There are two different ways of monitoring the emission of a molecule: either to excite at a fixed wavelength and to measure the emission ("emission spectrum"), or to monitor the emission at a fixed wavelength and to scan the excitation wavelength ("emission excitation spectrum"). While the first approach is more intuitive, the excitation scan can result in valuable information about the origin of the emission. Usually, the emission excitation spectrum should reflect exactly the absorption spectrum. This is a direct consequence of the excited molecules' unrivaled ultrafast internal conversion (IC) into the lowest excited singlet state, from where all emission occurs (Kasha's rule, see also introduction, page 4). The stronger the absorption at a certain wavelength, the more emission is created upon excitation. Molecules deviating from this "normal behavior" must have other relaxation pathways available from higher excited states that are fast enough to compete with the ultrafast IC and emission pathway.
Complications arise when strongly emitting photoproducts are present in the sample, regardless of whether created deliberately, or generated unintentionally during the measurement itself. Contributions of emission from educt and the products can be separated by subtraction of known emission components.

3.4.1 Emission and Emission Excitation Spectra of APO samples

Emission Spectrum of APO samples. APO was not expected to show any emission according to literature [29]. However, extremly weak emission was indeed observed for the APO samples upon 295 nm (33 900 cm^{-1}) excitation. By contrast, the emission from the photoproduct AC is very strong and becomes visible in the emission spectra already shortly after excitation at 295 nm, indicated in red in figure 3.15. The APO spectrum shown as thick black line in figure 3.15 shows two maxima at 340 nm (29 400 cm^{-1}) and 355 nm (28 200 cm^{-1}), and drops to zero around 500 nm (20 000 cm^{-1}) with a long tail.

Emission Contribution from Anthracene. To verify that the increasing emission contribution is due to AC, the spectrum obtained from a fresh APO sample (red in fig. 3.16) is subtracted from the spectrum of the same sample after repeated emission scans (blue). The difference spectrum (green) shows the additional emission that appeared during the illumination. Comparison with the emission spectrum of pure AC (yellow) clearly identifies the AC emission by its characteristic emission peaks observed around 377, 398, and 422 nm (26 500, 25 100, and 23 700 cm^{-1}). At these positions, even the first spectrum (red) shows slight shoulders.

Emission Contribution from Bicyclic Acetal. After prolonged irradiation at 290 nm, an additional emission contribution that peaks at 297 nm is observed upon 270 nm excitation, depicted as shaded area in figure 3.17. Four samples with different excitation wavelengths ranging from 275 – 305 nm were partially photoconverted, their composition analyzed, and an emission spectrum with 270 nm excitation was taken of each sample. Comparison of the 300 nm emission yields with the sample compositions indicates that the emission yield correlates with the presence of the bicyclic acetal (BA). This product is formed by photoexcitation of the primary reaction product diepoxide (DE, see section 5.2.2), what explains the appearance of this emission only after prolonged illumination at 290 nm, close to the DE absorption maximum (284 nm).

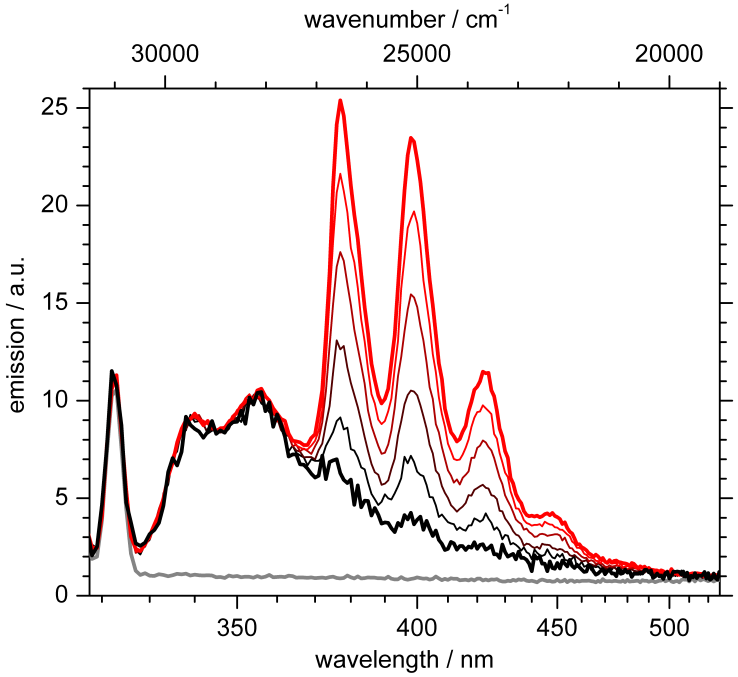

Figure 3.15: Emission spectra of APO in acetonitrile upon excitation at 295 nm. - Thick black line: first scan, 0.05 s accumulation time per data point; thick red line: last scan;. Grey line: solvent acetonitrile for comparison.

Emission Excitation Spectrum of APO samples. The emission of APO samples is reliably detectable, without disturbance by anthracene emission, at wavelengths below 360 nm, and BA emission does not significantly contribute $\geq$ 350 nm. Hence, 350 nm was chosen as the detection wavelength for the emission excitation spectra on APO samples. In figure 3.18, the emission excitation spectrum (blue) is compared with the emission spectrum (red) and the UV/vis absorption spectrum (black) of APO in acetonitrile. The double peak structure observed at the red edge of the emission excitation spectrum around 320 and 330 nm (31 200 and 30 300 cm^{-1}) inversely resembles the emission spectrum; this structure is therefore concluded to represent the emitting states.
As visible in figure 3.18, the emission excitation spectrum is not following the curvature of the absorption spectrum of anthracene-9,10-endoperoxide, but shows distinctly different trends. It appears therefore unlikely that anthracene-9,10-endoperoxide is the origin of the observed emission; the most probable emission source is traced in section 3.4.3.

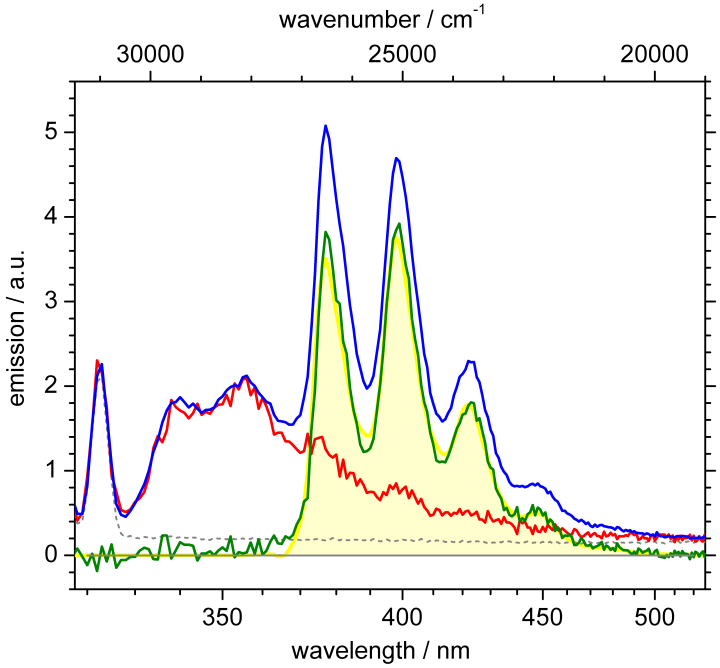

Figure 3.16: Emission spectra upon excitation at 295 nm. - Red: APO, first scan; blue: APO, average of scans 41-50; green: difference between last and first scans; yellow: scaled AC (after solvent correction); grey dotted line: acetonitrile.

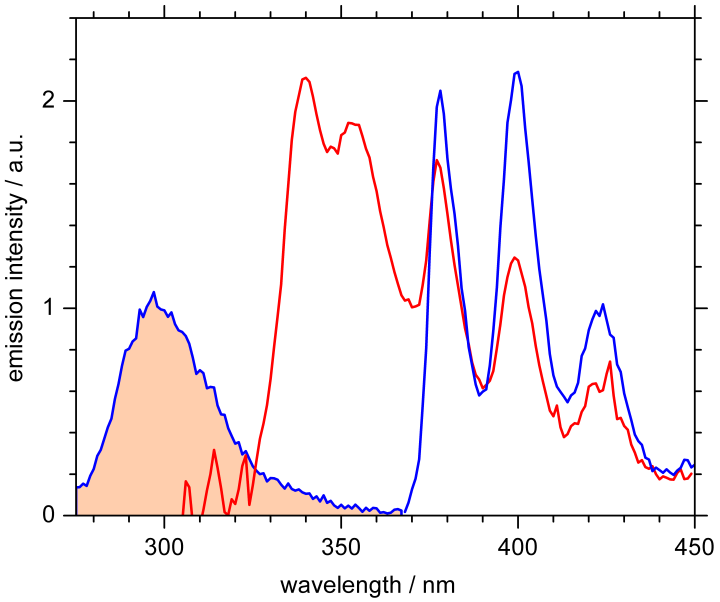

Figure 3.17: Emission spectra of two different, partly photoconverted APO samples. - Red: Shortly exposed to 290 nm, measured with excitation at 290 nm; blue: prolonged exposure at 290 nm, measured with excitation at 270 nm; solvent: acetonitrile.

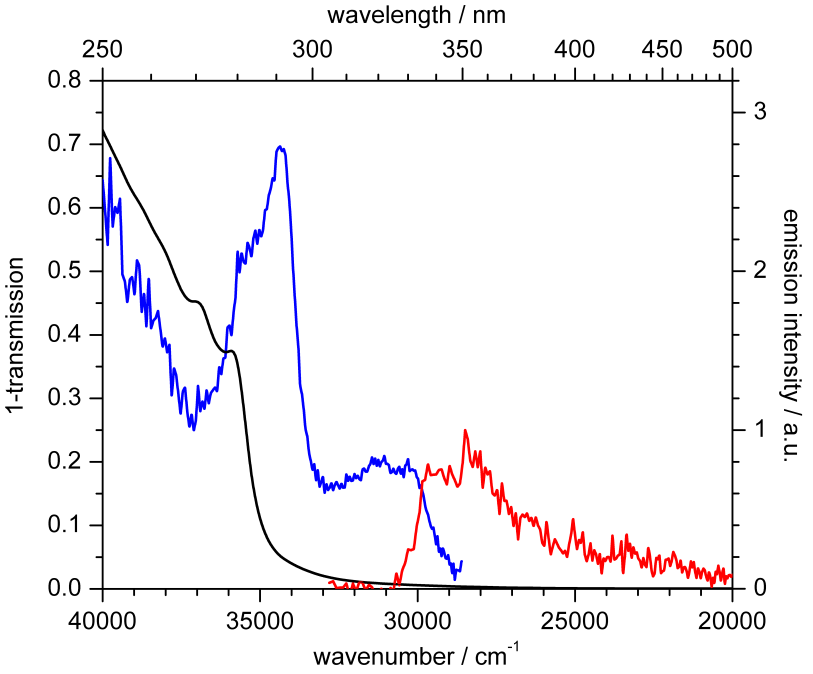

Figure 3.18: Emission excitation spectrum of a fresh APO sample, emission detected at 350 nm (blue line), compared with the emission spectrum from APO samples (red line, exc. 295 nm) and with the UV/vis absorption spectrum of APO (black line); solvent: acetonitrile.

3.4.2 Estimation of Emission QY

Emission QY Estimation: General Procedure. From the emission and absorption data, it is possible to estimate the emission quantum yield (Q), based on comparison with the known emission QY of anthracene, which has a literature value[59] of $Q_{AC} = 0.27$ in ethanol. The emission quantum yield is defined as the number of emitted photons devided by the number of absorbed photons. In practice, the numerator is given by the integrated emission intensity, i.e. the integrated area under the emission intensity spectrum, and the denominator is given by the optical density of the emissive species at the excitation wavelength. The emission quantum yield of the unknown compound X can be calculated[43] from these data by comparison with the reference quantum yield Q_{AC}:

$$Q_X = Q_{AC} \cdot \frac{I_X}{I_{AC}} \cdot \frac{OD_{AC}}{OD_X} \tag{3.1}$$

The QY for the observed emission is calculated for the assumption that 9,10-APO was the origin, as well as for the suggestion that the emission originates from a different compound present in the sample, most probably 1,4-APO.

Estimation for 9,10-APO. In fig. 3.19.a, the emission spectrum is shown for a fresh APO sample and for the same sample after prolonged illumination. The area under the observed emission curve (grey in fig. 3.19) is a measure for its integrated emission intensity I_X; the value for AC I_{AC} is obtained from the total area after subtraction of the APO area (red in fig. 3.19.a). Fig. 3.19.b shows the corresponding absorption spectra of the same fresh and illuminated APO samples. The inset

enlarges the part of the spectrum that is critical for the estimation of the OD of AC. The estimated emission QY has a large error margin, mainly due to very low OD of APO and especially AC in this measurement (compare fig. 3.19.b). If 9,10-APO is considered as emission source, the values for OD and integrated emission intensity for both 9,10-APO and AC determined from the data of figure 3.19 are plugged into equation 3.1, and the calculation returns a value of 0.46 %.

Estimation for Other Emission Source (1,4-APO). In case that a different compound X is responsible for the emission, the OD of the emissive species (most probably the 1,4-APO isomer) is only a fraction of the total APO OD, thus the emission QY must be higher to yield the same amount of emission. Quantitatively, the $OD_X = \epsilon_X \, c_X \, d$ of the emissive species is proportional to the concentration c_X under the assumption that the extinction coefficients $\epsilon(X) \approx \epsilon(9,10-APO)$ are similar. The concentration c_X has an upper limit of 0.5 % of the 9,10-APO concenration, $c(X) \leq 0.005 \cdot c(9,10-APO)$, because otherwise it should have been detectable in ^1H NMR, and the optical density due to X is estimated as $OD_X = x \cdot OD_{APO}$; $x \leq 0.005$. The emission QY for the emitting compound is then given by $Q_X = Q_{APO}/x \geq 0.0046/0.005$, which amounts to 91 %. This is already close to the maximum value of 100 % QY, attained at a concentration of 0.46 % relative to 9,10-APO. Table 3.1 lists the emission QY estimations for some combinations of concentration and extinction coefficient values. It demonstates that lower concentrations are not possible if the same extinction coefficient as for 9,10-APO is assumed.
However, the extinction coefficient of 1,4-APO might be higher than that of 9,10-APO: For the diphenyl-dimethyl and tetramethyl derivatives of 1,4-APO (fig. 3.20), the extinction coefficients at 295 nm are approximately $300 \leq \epsilon \leq 1000$, which is about 10 – 33 times higher than for 9,10-APO. Using these values for ϵ_X, the emission QY is estimated to be 10 – 33 times lower, i.e. $2.7 \leq Q_X \leq 9.1$, and of course all intermediate values up to 91 % are also possible.
Because the emission QY depends on the unknown extinction coefficient of 1,4-APO, only a very vague estimation can be made, which covers all the range from 3 – 90 % emission QY. For comparison: The fluorescence quantum yield of naphthalene is reported[59] as 23 %, and according to the above estimation, the emission QY of 1,4-APO could have a comparable value.

Table 3.1: Emission QY in %, as a function of concentration (columns, in % of 9,10-APO concentration) and extinction coefficient ϵ (rows) of the emissive species. The values of the first column (100 % concentration) belong to 9,10-APO, the next two columns to 1,4-APO (0.5 or 0.1 % of 9,10-APO); the last three columns assume that 0.5 % of 1,4-APO are present, of which 10, 5, or 1 % convert into the emissive species.

	100 %	0.5 %	0.1 %	0.05 %	0.025 %	0.005 %
$\epsilon =$ 30 l mol^{-1} cm^{-1}	0.46	91	–[a]	–	–	–
$\epsilon =$ 300 l mol^{-1} cm^{-1}	n/a	9.1	45	91	–	–
$\epsilon =$ 1000 l mol^{-1} cm^{-1}	n/a	2.8	14	28	55	–
$\epsilon =$ 3000 l mol^{-1} cm^{-1}	n/a	0.91	4.5	9.1	18	91

[a] QY would exceed 100 %

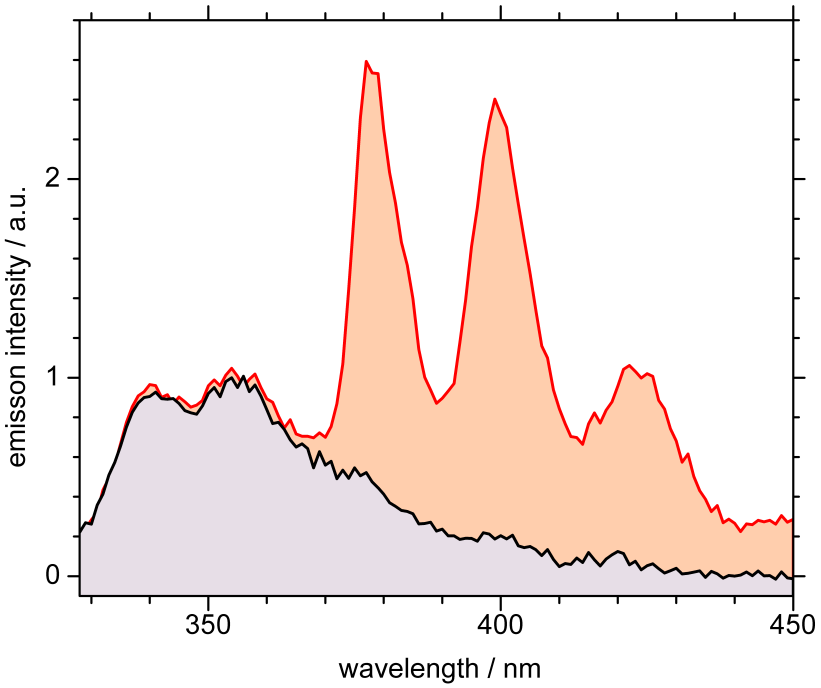

(a)

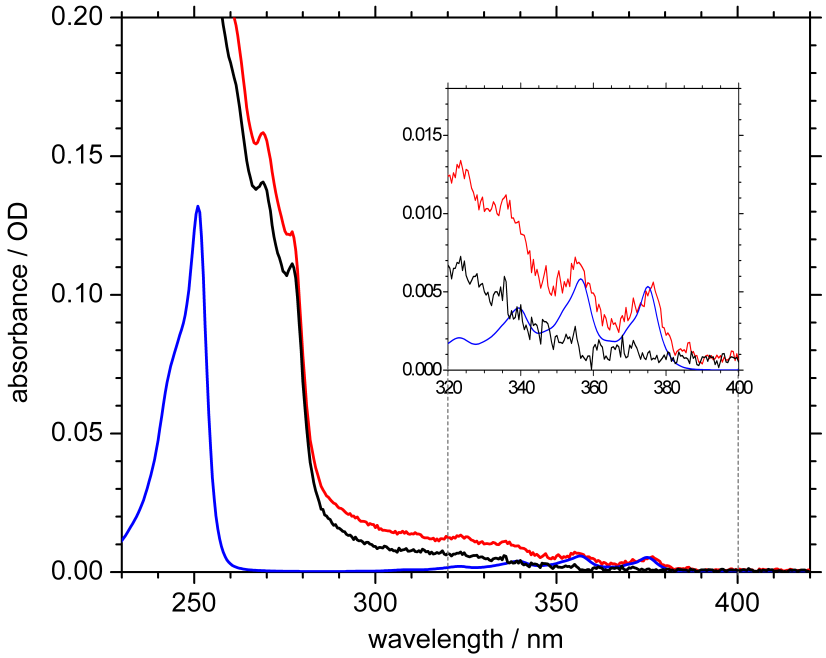

(b)

Figure 3.19: (a) Emission spectra: APO sample, fresh (black), and after prolonged illumination, with AC generated (red). (b) Absorption spectra: APO sample, fresh (black), and after prolonged illumination, with AC generated (red). Spectrum of pure AC (blue) for comparison.

3.4.3 Origin of Emission from APO samples

APO: Probably Excluded. Evidence against 9,10-APO as emission origin is provided by the emission excitation spectrum: If 9,10-APO were the emissive species, the emission excitation spectrum should closely resemble the absorption spectrum, which is not the case (compare figure 3.18.

Contaminations: Probably Excluded. Contaminations in compounds and solvent used in the synthesis of APO[1] are unlikely because of purified substances and reproducible emission for different APO batches. Identical emission from APO samples was also observed using different solvents, cuvettes, and all other equipment involved; even a different fluorescence spectrometer showed the same emission spectrum.

Reaction Products: Probably Excluded. Emission from a stable reaction product would have to increase during prolonged measurements, as the AC emission does. By contrast, the APO emission between 330 and 360 nm, with maxima around 340 and 355 nm, is the same in all scans, and is already visible in a very quick scan performed on a fresh APO sample. Although this argumentation would not hold for an intermediate formed upon APO excitation that subsequently rearranges into a non-emissive species, the intermediate would probably have a closely related structure and thus an absorption spectrum very similar to that of APO. Hence, the arguments against APO as emission source apply as well against reaction intermediates of APO.

Isomer: Plausible. Based on the literature on aromatic endoperoxides, another explanation is conceivable: In the synthesis of anthracene-based endoperoxides, the formation of both 9,10- and 1,4-isomers was reported, depending on molecular structure. Although for anthracene, generation of 100 % 9,10-isomer was reported[15], formation of a small amout of anthracene-1,4-endoperoxide (1,4-APO) could plausibly account for the observed emission. This compound, if formed during the synthesis, would be reproducibly present in every APO batch in the same low percentage (< 1 %). Because of the structural similarity, 1,4-APO would remain unseparated from 9,10-APO in routinely performed chromatographic purification, and stay undetected even in ^1H NMR if less than half a percent of the isomer are present.
Spectroscopic data of a few derivates of 1,4-APO are available in literature[15, 37, 60]; examples are shown in figure 3.20: The absorption spectra of these compounds show a much stronger similarity with the observed emission excitation spectrum. Moreover, the aromatic moiety of 1,4-APO makes it a naphthalene derivative, and naphthalene has a strong fluorescence with a reported quantum yield of 23 % in cyclohexane[59]. The absorption and emission of a naphthalene derivative is dicussed for comparison in the next paragraph.

Reaction Product of Isomer: Probably Excluded. The only alternative emission source that cannot easily be excluded would be an intermediate formed upon 1,4-APO excitation, which rearranges into a non-emissive species. However, higher extinction coefficients need to be assumed to account for the lower concentration of intermediates, as visible in table 3.1: If one assumes 1 % conversion of 1,4-APO (which is at most 0.5 % of 9,10-APO) into an emitting intermediate species (i.e. 0.005 % relative to 9,10-APO, last column), extinction coefficients at least 100 times higher than that of 9,10-APO are required. Since they would also be higher than the extinction coefficients of the two 1,4-APO derivatives of figure 3.20, to assume such extinction coefficients appears implausible.
To assume an extinction coefficient that is only 10 times higher than that of 9,10-APO (second row), on the other hand, requires that at least 10 % of 1,4-APO (i.e. 0.05 % relative to 9,10-APO) are converted into the emissive species. If that were the case, however, the emission would have to

[1] APO was synthesized by Dr. W. Freyer at the Max-Born-Institute, Berlin.

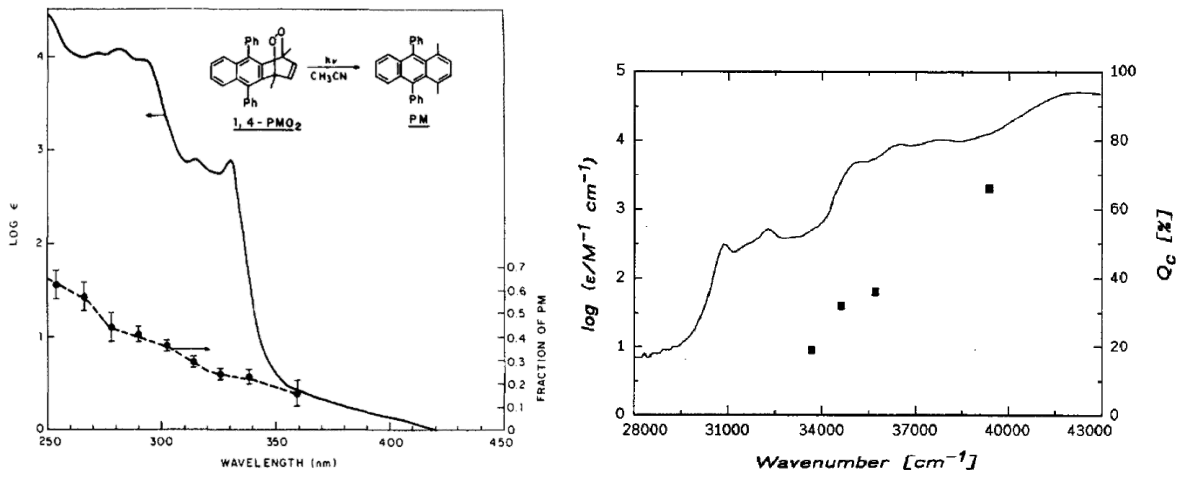

(a) (b)

Figure 3.20: (a) Absorption spectrum of 1,4-dimethyl-9,10-diphenyl-1,4-APO, from Eisenthal *et al.* [37]. (b) Absorption spectrum of 1,2,3,4-tetramethyl-anthracene-1,4-endoperoxide, from Afshari *et al.* [60].

decrease rapidly, because 10 % of the 1,4-APO would be consumed per scan and not be available to produce more of the emissive intermediate species in the following scans.

Since the observed emission does neither increase nor decrease noticably in repeated scans, an intermediate upon excitation of 1,4-APO appears implausible as origin of the emission.
It is therefore concluded that the observed emission originates from anthracene-1,4-endoperoxide.

Comparison with Model Compound

Since 1,4-APO derivatives are not available, a closely related compound that is commercially available, naphthalene-2,3-diol, is analyzed for comparison. The structure of naphthalene-2,3-diol is shown in figure 3.21, compared with 9,10-APO and 1,4-APO.

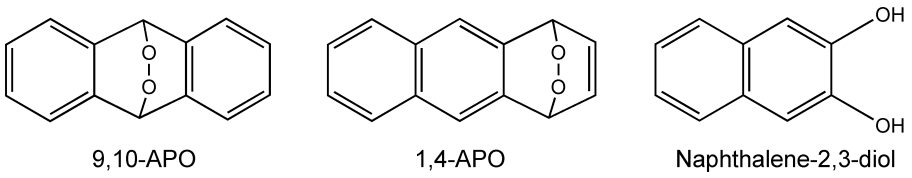

Figure 3.21: Chemical structures of anthracene-9,10-endoperoxide (9,10-APO), anthracene-1,4-endoperoxide (1,4-APO), and naphthalene-2,3-diol.

Figure 3.22.a-b shows the absorption and emission spectra of naphthalene-2,3-diol on linear and logarithmic scales. The naphthalene-diol absorption reaches a first peak at 325 nm, followed by smaller local maxima at 318 and 311 nm, before rising to a more intense, slightly structured broad band peaking around 281 nm, with shoulders at 291 and 272 nm. For comparison, the emission excitation spectrum of the APO sample is depicted in figure 3.22.c-d. Qualitatively, the curve shapes are similar, while quantitatively, the peak and shoulder positions are blue-shifted in the

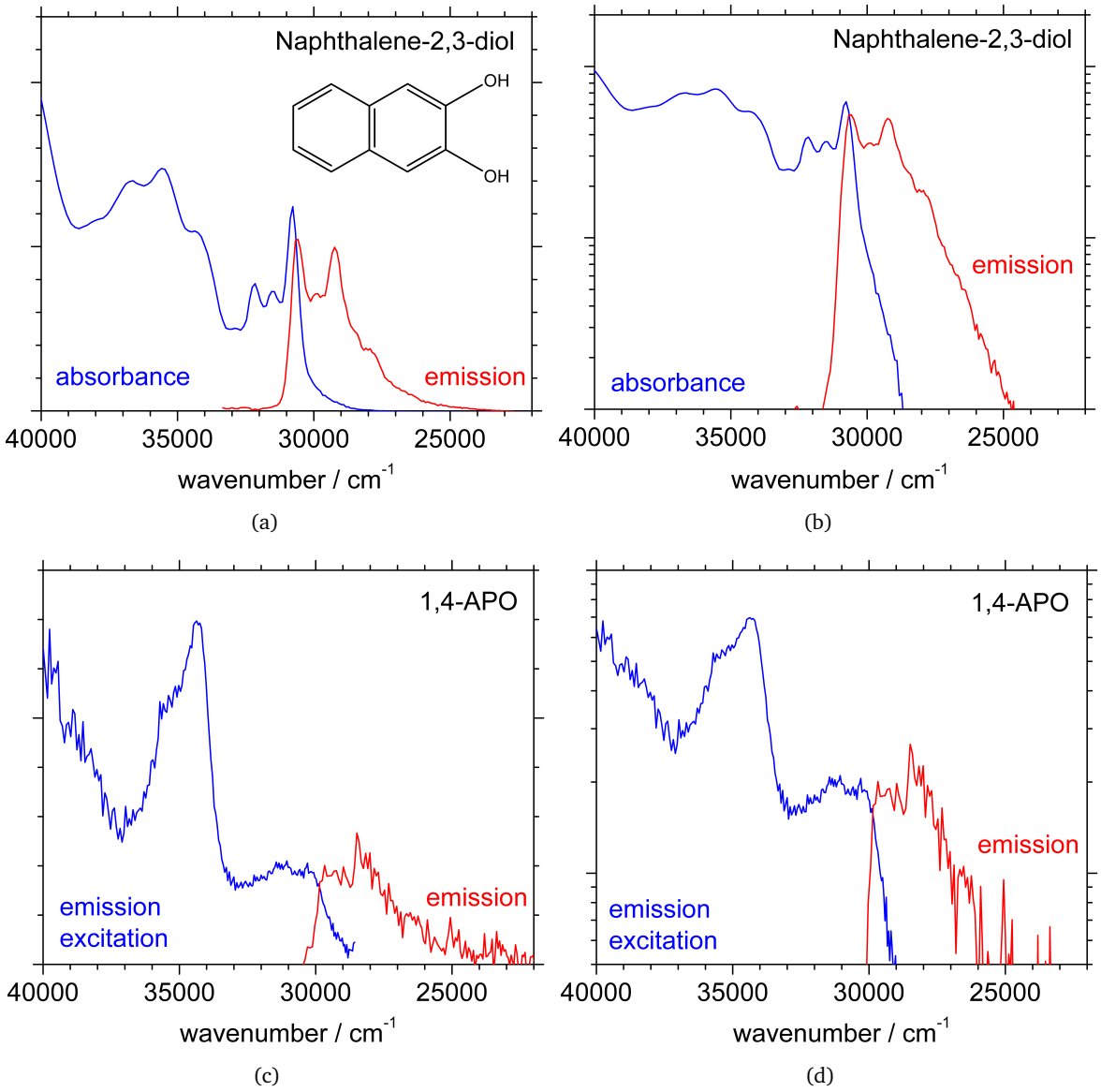

Figure 3.22: (a,b) Absorption (blue) and emission spectra (red) of naphthalene-2,3-diol, on linear (a) and logarithmic scales (b).
(c,d) Emission excitation (blue) and emission spectra (red) measured on APO (c - linear, d - logarithmic scale). - The species responsible is probably either the isomer 1,4-APO (fig. 3.21), or a photoproduct of 1,4-APO.

naphthalene-diol absorption spectrum. Keeping in mind that this is only a model compound, the qualitative similarity suggests that the species responsible for the observed emission could have a similar structure, supporting the assumption of 1,4-APO as the origin.
Similarly, the shape of the emission spectrum of the APO sample resembles that of naphthalene-diol, with both a double peak structure and a tail to the red. Emission maxima are located around 340 and 355 nm in the APO spectrum, and approximately at 327 and 342 nm for naphthalene-diol.

3.4.4 Emission Lifetime

Emission lifetime measurements were performed in cooperation by Emad Mukhtar[2] at the University of Uppsala, Sweden. A fresh APO sample, as well as two partially photoconverted samples were measured for different emission wavelengths, which correspond to the maxima of the emission spectra of a fresh APO sample – 340 nm, AC emission – 400 nm, and BA emission – 300 nm. Emission of a fresh APO sample upon 290 nm excitation was detected at 340 nm (black), and

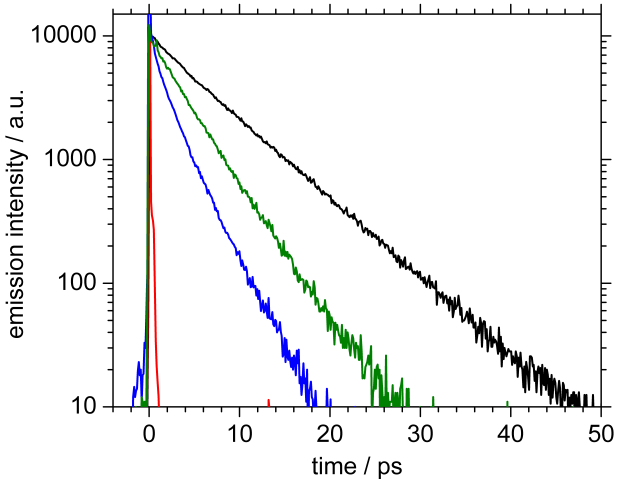

Figure 3.23: Emission lifetime measurements. - See text for details.

a lifetime of (6.9 ± 0.4) ns was observed. For a different APO sample, which was partially photoconverted at 290 nm, emission was measured at 300 nm (290 nm excitation; blue). For this sample, a lifetime of (2.0 ± 0.4) ns was obtained, which is assigned to emission from the bicyclic acetal (for the corresponding emission spectrum, see page 3.4.1). For a third APO sample, also partially photoconverted at 290 nm, emission detection at 400 nm (270 nm excitation, green), revealed a lifetime of (3.7 ± 0.3) ns, which is assigned to AC emission (spectrum see page 3.4.1). The system response is shown for comparison (red).

[2]current address: Univ. Uppsala, Inst. Chemical Physics, S-75120 Uppsala

4 Identifying the Low-lying Electronic Excited States

4.1 Quantum Chemical Calculations

The energetic location of the lowest excited singlet state of anthracene-9,10-endoperoxide (APO) has been controversely disputed in literature[24, 30, 31, 34], as the existence of a low-energy band > 280 nm cannot be deduced unambiguously from the absorption spectrum (sec. 3.3, page 45). To unequivocally identify the lowest electronic excited states, quantum chemical calculations are consulted, which were performed by Inés Corral[1] and Leticia González[2] from the institute for theoretical chemistry of the *Freie Universität Berlin*[3]. Although these are high-level *ab initio* calculations, it appears reasonable to test their correctness by comparison with further experimental data. For this purpose, the electronic transition dipole moment (TDM) orientations within the molecular structure determined by calculations are compared with the TDM orientation that is deduced from polarization resolved pump-probe experiments.
The calculated data include the optimized geometries, which form the basis for the vertical excitation energies. These energies correspond to the energetic locations of the absorption bands. Furthermore, the transition dipole moments (TDM's) are calculated, i.e. the change in charge distribution during the transition, including the direction of the TDM within the molecular structure.

Optimized Geometries. The equilibrium geometries of APO were optimized by Corral and González [35] for the electronic ground state (S_0, fig. 4.1.a), for the first electronic excited singlet state (S_1, $\pi*_{OO} \rightarrow \sigma*_{OO}$), fig. 4.1.c), and for the diradical triplet ground state (T_0, $\pi_{OO} \rightarrow \pi*_{OO}$, fig. 4.1.b). The ground state (S_0) geometry was calculated on both MP2/6-311G(d,p) and CASSCF levels of theory [61] assuming C_{2v} symmetry. Comparison with the data from X-ray structure determination [62] shows that the MP2 geometry is closer to the experimental data and is therefore chosen for the calculations that followed. The S_1 and T_0 geometries were both obtained at the CASSCF(14,12)/ANO-S level of theory. In figure 4.1, the optimized geometries are shown together with structural parameters; the data in parenthesis are X-ray data by Brown and Ehrenberg [62] for comparison.

[1] current address: Univ. Autónoma de Madrid, Dep. de Química, E-28049 Madrid, Spain
[2] current address: Univ. Jena, Inst. Phys. Chem., D-07743 Jena, Germany
[3] Cooperation project within the Collaborative Research Center (Sonderforschungsbereich) SFB450 of the German Research Foundation (Deutsche Forschungsgemeinschaft DFG.)

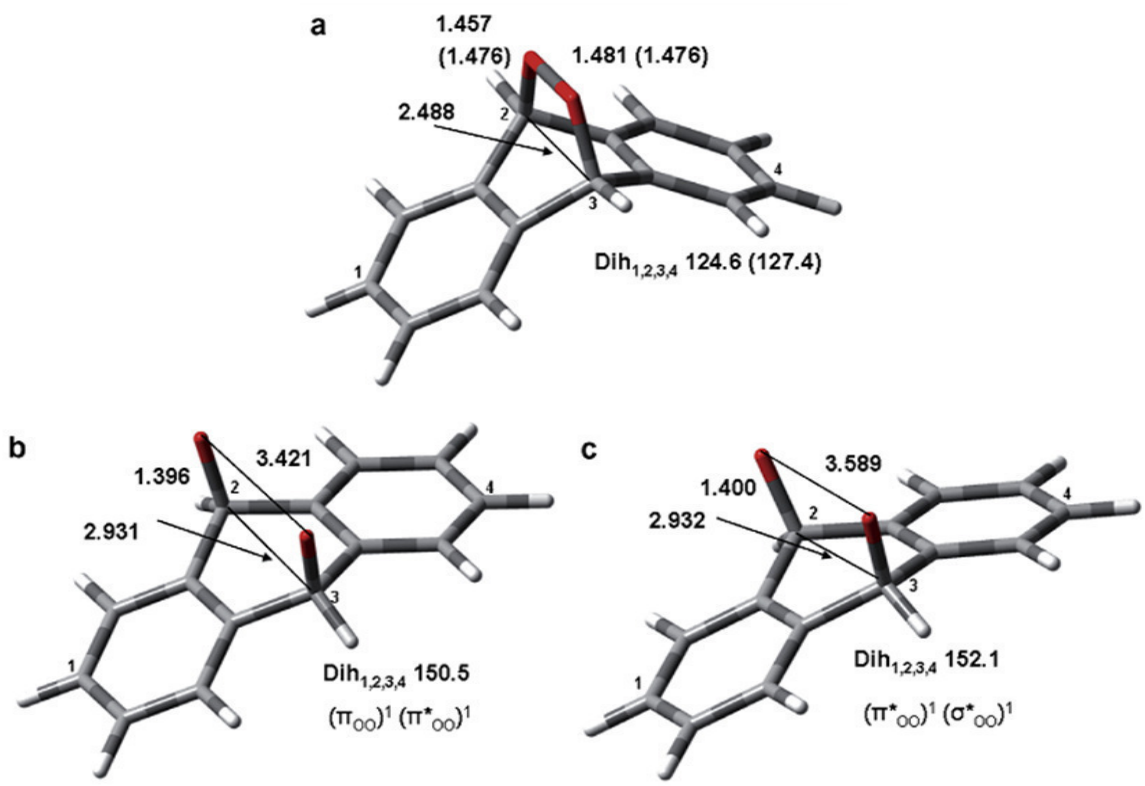

Figure 4.1: APO equilibrium geometries: (a) ground state (S_0); (b) diradical ground state (T_0); (c) first singlet excited state (S_1) [61]. Parameters are given as distances in $\AA$ and dihedral angles in ° (X-ray parameters in parenthesis [62]).

Vertical Excitation Energies. The vertical excitation energies of APO in gas phase were computed by Corral and González [35] on the MS-CASPT2//CASSCF(14,12)/ANO-S level of theory. To estimate the effect of solvent interactions with $CHCl_3$, the ground state geometry was reoptimized assuming a dielectric constant of 5.0. The results are summarized in table 4.1.
A test of different basis sets and active spaces[61] resulted in a slightly deviating order of states. However, as the authors stated: "Gratefully, this state inversion has no influence in the interpretation of the experimental absorption spectrum, since the intercalated excitations are dark states."[61] The experimental values in table 4.1 are derived from the APO absorption spectrum and the simulation by Gauss and Lorentz lines, as shown in figure 4.3. In the same figure, the calculated values in gas phase and in solvent are also shown for comparison. The $S_0 \rightarrow S_3$ transition is calculated to be symmetry forbidden and has therefore no corresponding band in the experimental spectrum. The calculated values for the transition energies in the gas phase all show a systematic shift to lower energies, while the values in solution show good agreement compared with the experimental data. According to these results, the experimental bands at 35 900 cm^{-1} (280 nm) and 37 000 cm^{-1} (270 nm) are assigned to the $S_0 \rightarrow S_2$ and $S_0 \rightarrow S_4$ transitions, respectively. Moreover, the *ab initio* calculations suggest the existence of a low-energy band around 34 700 cm^{-1} (288 nm), assigned to the $S_0 \rightarrow S_1$ transition.
The orbital character of these transitions are calculated as $\pi_{CC} \rightarrow \pi*_{CC}$ (S_2) and $\pi*_{OO} \rightarrow \pi*_{CC}$ (S_4), while the $S_0 \rightarrow S_1$ transition is ascribed to $\pi*_{OO} \rightarrow \sigma*_{OO}$ character. This antibonding character with respect to the O-O bond causes the increased bond length given in figure 4.1.c and facilitates

Table 4.1: The experimental excitation energies (in cm^{-1}) of the low-lying electronic states of APO, compared to the values calculated for gas phase (MS-CASPT2) and including solvent interactions with $CHCl_3$ (CASPT2), and their theoretical electronic transition dipole moment vectors (a.u.). Values for the calculated oscillator strengths are given in brackets.

State	Experiment	Gas phase	Solvent	TDM (x/y/z)
S_1 ($\pi*_{OO}, \sigma*_{OO}$)	34 400 $\pm$ 200	30 562 (0.0003)	34 682	0.06 / 0 / 0
S_2 ($\pi_{CC}, \pi*_{CC}$)	35 900 $\pm$ 200	34 468 (0.0021)	35 593	-0.14 / 0 / 0
S_3 ($\pi*_{OO}, \pi*_{CC}$)	–	34 930 (0)	–	– / – / –
S_4 ($\pi*_{OO}, \pi*_{CC}$)	37 000 $\pm$ 200	35 206 (0.0220)	–	0 / -0.45 / 0

the O-O cleavage reaction, in agreement with previous predictions[11]. The similar geometry of the supposed T_0 state (fig. 4.1.b) may indicate a potential role of T_0 in the thermal reaction, which also yields an O-O cleavage product.
The oscillator strength of the S_1 transition is calculated to be a factor of 7 weaker than the S_2 band, which itself is more than 10 times weaker than the S_4 band. Since even the extinction coefficient at the proposed S_4 position (270 nm) is very weak (630 $M^{-1}cm^{-1}$), it is not surprising that the S_1 band is not easily obtained from the absorption spectrum.

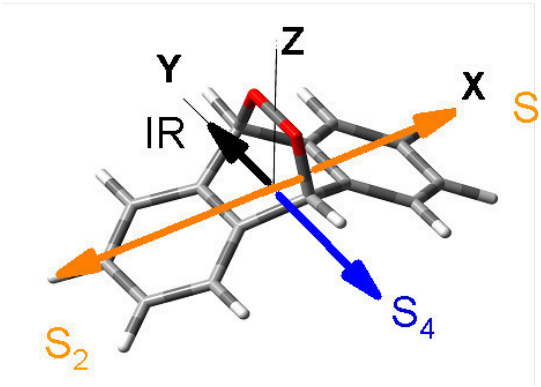

Figure 4.2: APO within cartesian coordinates; TDM orientations indicated by arrows.

Electronic Transition Dipole Moments (TDMs). As indicated in table 4.1, the electronic transition dipole moments (TDMs) of the first two electronic states (S_1 and S_2) are aligned along the x-axis (compare figure 4.2), while the TDM of the S_4 state is oriented along the y-axis. Furthermore, the next higher excited states also have TDM orientations perpendicular to the y-axis, so that the S_4 state is the only one oriented along the y-axis in the whole energy region. Therefore, it can be used to test the correctness of the assignment of the electronic states. In the polarization resolved pump-probe experiment described in section 2.6, the TDM orientation of the transition excited at 272 nm is determined. If the calculated assignment is correct, the $S_0 \rightarrow S_4$ transition is pumped, which should be orientated along the y-axis. If one would assume the 280 nm band were S_1 and 270 nm S_2 instead, the $S_0 \rightarrow S_2$ transition would be pumped, which should be orientated along the x-axis.

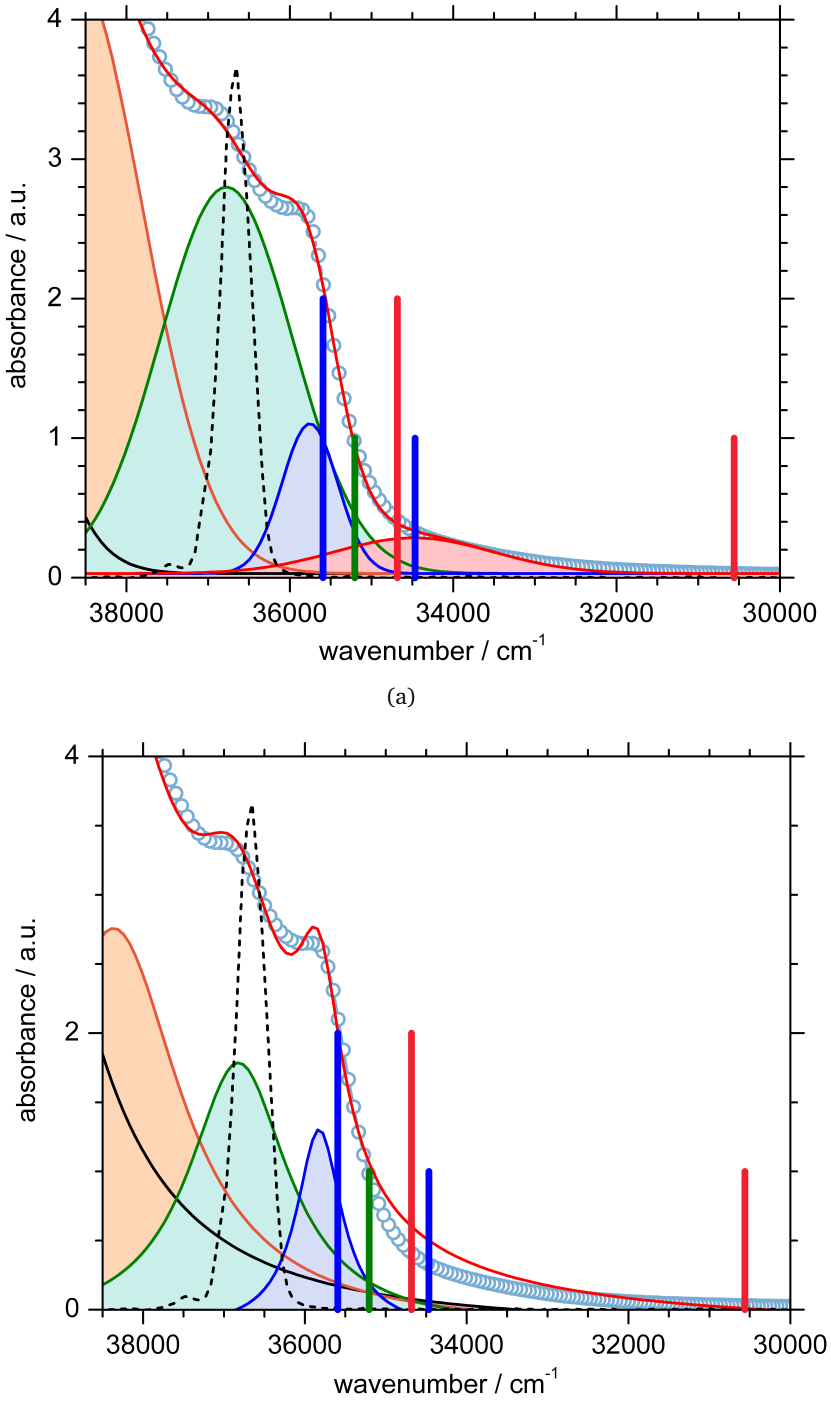

Figure 4.3: Simulation (red line) of APO absorption spectrum (blue circles) as a sum of (a) Gauss fits and (b) Lorentz lines. The vertical excitation energies calculated in gas phase (short bars) and in $CHCl_3$ (long bars) are indicated using the colors red – S_1, blue – S_2, and green – S_4. The spectrum of the pump pulse used in the polarization resolved experiments is shown as black broken line.

4.2 Polarization Resolved UV Pump / IR Probe Experiment

The polarization resolved pump/probe experiment utilizes the linear polarization of the pump and probe pulses to gather information about the relative angle between the pumped and probed transition dipole moment (TDM) orientations. Since the orientation of the probed vibrational TDM within the molecule is known, the orientation of the pumped effective electronic TDM can be derived. Comparison with the calculated effective el. TDM orientation approves the assignment of the lowest electronic states. The setup of the polarization resolved UV pump / IR probe experiment is shown and explained in the experimental section (2.6).

Experiment and Analysis. In a pump-probe experiment, the measured data are the absorption difference of the probe pulse, with and without the pump pulse applied, as a function of both the pump-probe delay time and the probed wavelength. Therefore, spectra for selected delay times, as in figure 4.6, and the temporal evolution for selected wavelengths, as in figure 4.7 are obtained. In the polarization resolved pump-probe experiment, measurements are performed with the linear pump pulse polarization fixed within the laboratory frame, and the linear probe pulse polarization is adjusted either parallel or perpendicular with respect to the pump pulse polarization (fig. 4.4), which results in separate data sets for parallel and perpendicular polarizations, respectively. Due to

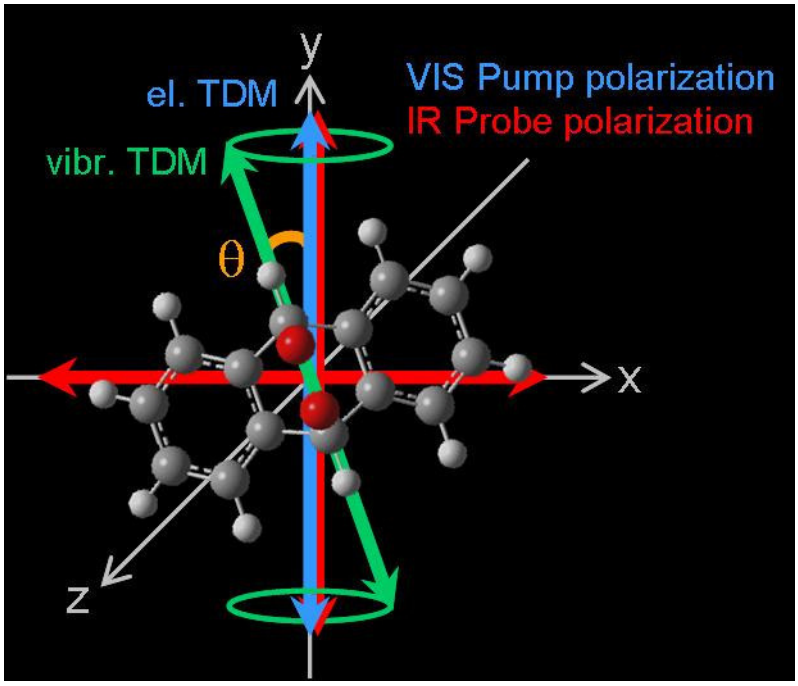

Figure 4.4: Schematic representation of the method to determine the angle θ between pumped and probed transition dipole moment orientations within the molecule [49] . The Cartesian coordinates are laboratory coordinates, where z is the direction of the laser beam which is linearly polarized in either x or y direction (see text for details).

photoselection [63], the pump pulse predominantly excites molecules which are aligned with their effective electronic TDM along the pump pulse polarization (y-axis in fig. 4.4). Changes in the infrared vibrations due to the electronic excitation are detected by the infrared probe pulse. The

measured signal intensity depends on the relative orientation of the probe pulse (either x- or y-axis in fig. 4.4) with respect to the vibrational TDM. In the schematic representation in figure 4.4, the vibrational TDM (green) is closer to the y- than to the x-axis. Therefore, the signal is expected to be stronger in the case of parallel pump and probe polarizations.
Quantitatively, this is expressed in the dichroic ratio D [49], with $A_{\parallel}$ and $A_{\perp}$ as the absorption changes detected with parallel or perpendicular pump and probe pulse polarizations, respectively (eq. 4.1). From the measured dichroic ratio, the angle θ between the pumped and probed TDM orientations can be derived according to equations 4.1 and 4.2. Figure 4.5 illustrates the dichroic ratio as a function of the angle between pumped and probed TDM orientations.

$$D = A_{\parallel}/A_{\perp} \tag{4.1}$$

$$\theta = \arccos\sqrt{\frac{2D-1}{D+2}} \tag{4.2}$$

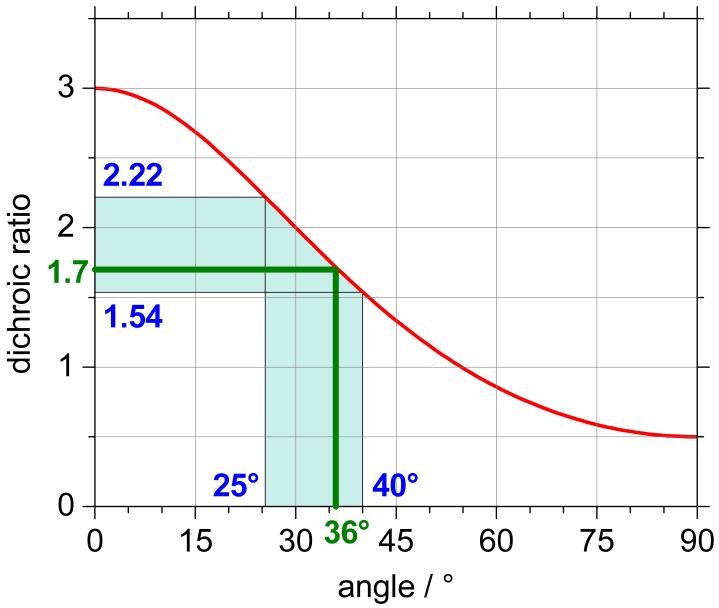

Figure 4.5: Dichroic ratio (red) as a function of the relative angle between the pumped and probed TDM orientations. The predicted values, based on the calculated assignment, are indicated in blue, and the experimentally determined values are shown in green.

Theoretical Angle Prediction. The probed vibrational transition at 1170 cm^{-1} (see section 3.2 for IR spectrum) has a TDM that is oriented along the molecular y-axis (compare fig. 4.2). Although this information is obtained from calculations, they include only vibrational levels within the electronic ground state, and no electronic excited states are involved. Since calculations in the electronic ground state are reliable, the probed TDM orientation is considered as known in the determination of the relative angle between pumped and probed TDM orientations.
At the pump wavelength of 36 700 cm^{-1} (272 nm), the $S_0 \rightarrow S_4$ transition is predominantly excited, if the assignment is correct. Nevertheless, adjacent transitions contribute to the absorption at this wavelength, especially to higher excited states which are associated with larger extinction coefficients. Therefore, the prediction of the effective TDM orientation requires to include the

relative contributions of all transitions absorbing at the pump wavelength region, together with their respective TDM orientations. To identify the contributions of the various electronic transitions in the excitation wavelength region (defined by the spectral profile of the pump pulse), the visible absorption spectrum of APO is simulated as a sum of either Gauss or Lorentz profiles, as shown in figure 4.3 (a) and (b), respectively. In the Gauss simulation (a), the $S_0 \rightarrow S_4$ transition is dominating, which has a TDM orientation parallel to the molecular y-axis (see fig. 4.2). Consequently, the effective TDM orientation is close to the y-axis, and therefore similar to the probed vibrational TDM. As a result, the predicted angle between pumped and probed TDM orientations is quite small, namely 25 °. If Lorentz profiles are used (b), however, the transitions to higher excited states also contribute considerably, which all have TDM orientations perpendicular to the y-axis. Thus, the effective TDM orientation deviates more from the y-axis, and the estimated angle is larger in this case, namely 40 °. Since the Gauss and Lorentz simulations can be regarded as the border cases, the angle is expected to lie within 25 – 40 °.

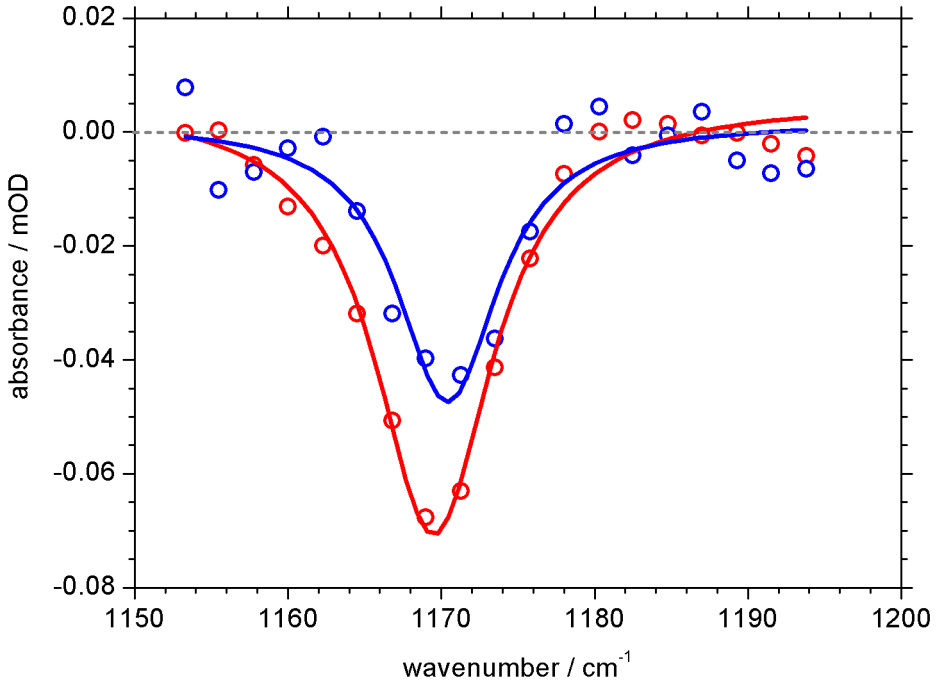

Figure 4.6: Pump-probe signal of APO in $CDCl_3$, with parallel (red) and perpendicular (blue) polarizations. Dots: experimental data; lines: Lorentz fit. Pump wavelength 272 nm.

Experimental Angle Determination. Figures 4.6 and 4.7 present spectra and transients around the bleach band at 1170 cm^{-1}. Because of the negligible signal change between 4 and 100 ps (fig. 4.7), data in fig. 4.6 are averaged over this time span. The bleach signals obtained for parallel and perpendicular pump and probe polarizations are shown in fig. 4.6 in red and blue, respectively, and both are fitted by a Lorentz line. The parallel signal (red) is about 1.7 times stronger than the perpendicular signal (blue). According to equations 4.1 and 4.2, a relative angle between pumped and probed TDM orientation of about 36 ° (+12 °/-28 °) is deduced from this experimental finding. The result lies well within the theoretically predicted frame of 25 – 40 °, as illustrated in figure 4.5. Hence, the agreement confirms the assignment of the absorption band at 36 700 cm^{-1} (272 nm) to the $S_0 \rightarrow S_4$ transition, and moreover, also supports the existence of two

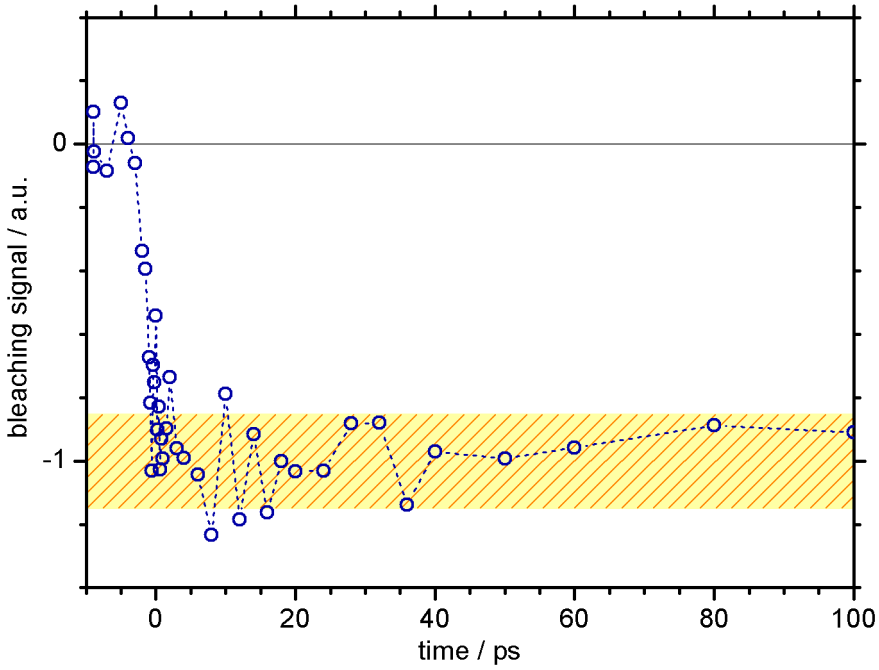

Figure 4.7: Transient bleaching signal. Blue dots: experimental data; yellow bar: estimated error margin of bleaching signal. Pump: 272 nm; probe: 1170 cm^{-1}.

lower absorption bands S_2 and S_1, located around 280 nm and in the region around 290 nm. Figure 4.7 shows the temporal evolution of the bleaching signal. Within experimental error margins (indicated as yellow bar), no recovery of the bleaching signal is observed within the first 100 ps. This finding is in good agreement with results from chapter 5, where a photoreaction quantum yield of about 100 % is concluded. Converting all excited APO into products in turn implies that no formerly excited APO returns back to the ground state, hence no recovery from bleaching is expected.

4.3 The Low-lying Electronic Excited States: Summary and Conclusions

The question whether or not an electronic excited state exists below the lowest discernible absorption shoulder at 280 nm was addressed in this chapter. *Ab initio* calculations by Corral and González[35] identify the lowest excited singlet states in good agreement with the absorption data; the disputed S_1 state is located around 290 nm. The assignment is further substantiated by comparison with a polarization resolved pump-probe experiment. Agreement of the expected and determined angle between the pumped and probed transition dipole moment orientations supports the assignment and therefore the existence of a low-energy S_1 state around 290 nm. This conclusion contradicts previous suggestions by Klein *et al.*[30, 34] that the band at 280 nm would be the lowest electronic excited state. Although the present assignment supports the opinion of Schmidt *et al.*[24, 31] that a lower-energy S_1 state exists, the energetic position of the S_1 state is now located considerably higher, at 290 nm instead of 435 nm.
Moreover, the calculations indicate a σ^*_{OO} character for the S_1 state, antibonding with respect to the peroxide bond that needs to be broken in an O-O cleavage reaction. This result supports the S_1 state as the origin of the O-O cleavage reaction, in agreement with earlier predictions[11]. The calculated low-lying T_0 state with a geometry similar to that of S_1 might be related with the thermal reaction, which also yields an O-O cleavage product.
The main findings are summarized in figure 4.8.

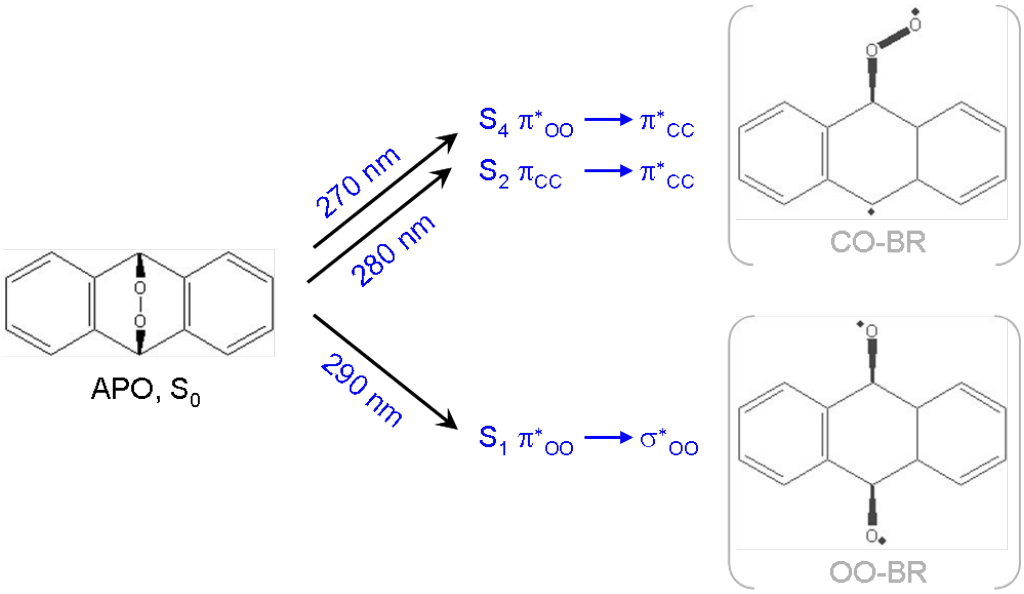

Figure 4.8: Overview on the main findings concerning the excited singlet states of APO (blue).

5 Quantitative Investigation of Reaction Pathways

5.1 Thermal Reaction

Identification of the Thermal Product

When APO is dissolved in acetonitrile and kept in the dark for a few hours at room temperature, the absorption spectrum of the solution changes dramatically. Figure 5.1 shows the initial spectrum of a fresh APO sample (black), in comparison with a spectrum of the same sample after 7 hours in the dark (blue). The difference of these two spectra is depicted in green, together with the scaled spectrum of anthraquinone (AQ) in acetonitrile (orange). Thus, in the thermolysis of APO at room temperature, AQ is virtually the only product.

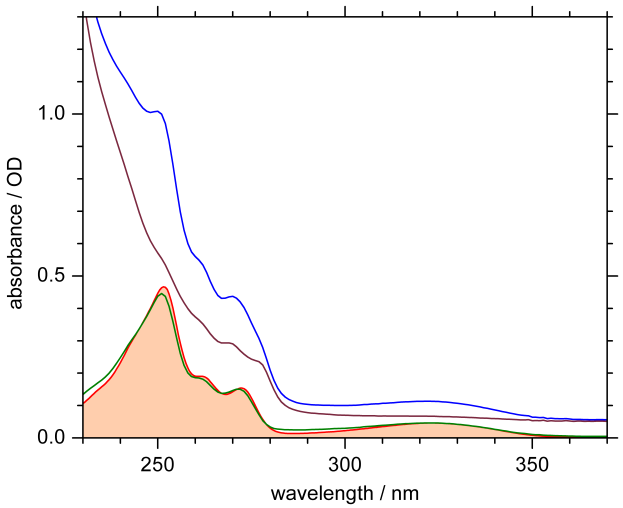

Figure 5.1: UV/vis absorption spectrum of APO in acetonitrile (black), the same sample after 7 h in the dark at room temperature (blue), the difference spectrum (green), and the spectrum of AQ in acetonitrile, scaled (orange).

Comparison with Literature. At higher temperatures of 80 – 110 °C, thermolysis of APO in boiling benzene, toluene, or o-dichlorobenzene only yielded up to 10 % AQ, while the majority had been converted into dimers[20]. Another thermolysis study only distinguished between cycloreversion products versus O-O cleavage products, without further differentiation among the latter. At 139 °C, 99 % of the thermal products were O-O cleavage products[29], similar to the observed ≈ 100 % AQ formation for thermolysis at room temperature. An extensive investigation of thermolysis of endoperoxides of aromatic compounds was reported by Turro *et al.*[18].

Solvent Influence on the Thermal Reaction

The thermolysis of APO at room temperature was followed for 1 – 2 weeks, with samples in acetonitrile with different grades of purity. For APO in perdeuterated acetonitrile (99.96 atom % D) and in non-deuterated acetonitrile of spectrophotometric-grade, AQ was found to be the only thermal end product, but it was formed about 8 times faster in the perdeuterated solvent: About 70 % of the APO was converted to AQ after 6 days, and extrapolation of the single-exponential fit predicts 100 % final conversion, indicating that this conversion process is unimolecular. In HPLC-grade acetonitrile, on the other hand, no noticeable thermal conversion was detected even after 2 weeks, and therefore, the differences in thermal conversion rates most likely are determined by various residue compounds present in commercial-grade solvents rather than by an isotope effect.

Temperature Dependence: Estimation of the Activation Barrier

The thermal reaction was investigated in 0.2 mM APO samples in spectrophotometric grade acetonitrile at five different temperatures between 283 and 343 K. The thermal conversion was followed by the absorption changes on an initally fresh APO sample that were caused upon keeping it at a given temperature for 21 minutes. Side products from bimolecular and follow-up reactions were minimized by restricting the conversion time to 21 minutes, and by working with a fairly low 0.2 mM concentration.

The characteristic AQ spectrum clearly dominates the difference spectra (fig. 5.2.a); only for the lowest temperature (283 K), the AQ yield was too low to be determined. Under the assumption that the thermal conversion to AQ is a (pseudo-) first order chemical reaction, one can calculate a thermal conversion rate from the percentage of APO converted after 21 minutes.

Assuming a first-order reaction, the rate law is given by the temporal change in APO concentration, with the rate constant k:

$$-\frac{d(c_{APO})}{dt} = k \cdot c_{APO}$$

The integrated form of the first-order rate law then is:

$$\ln\left(c_{APO}(t)\right) = -kt + \ln\left(c_{APO}(t=0)\right)$$

The plot of $\ln(c)$ versus $-t$ results in a slope equal to the rate constant k. In this way, rate constants can be found for each temperature, which are then used to determine the activation energy.

The temperature dependence of the rate of a chemical reaction can be described by the Arrhenius equation:

$$k = \mathscr{A} \cdot \exp\left(-\frac{E_A}{RT}\right)$$

The logarithmic form reads:

$$\ln(k) = -\frac{E_A}{R} \cdot T^{-1} + \ln(\mathscr{A})$$

This formula is used in the Arrhenius plot (fig. 5.2.b), where $\ln(k/s^{-1})$ is plotted versus the inverse temperature T^{-1}: $\ln(k) = m \cdot T^{-1} + b$. The resulting slope m is proportional to the activation energy $E_A = -R \cdot m$. Further, the y-intercept b gives the pre-exponential factor $\mathscr{A} = e^b$, in this case $\mathscr{A} = 1.8 \cdot 10^3$.

The activation energy determined for the thermal conversion of APO is $E_A = 51$ kJ/mol ($\approx$ 4300 cm^{-1}).

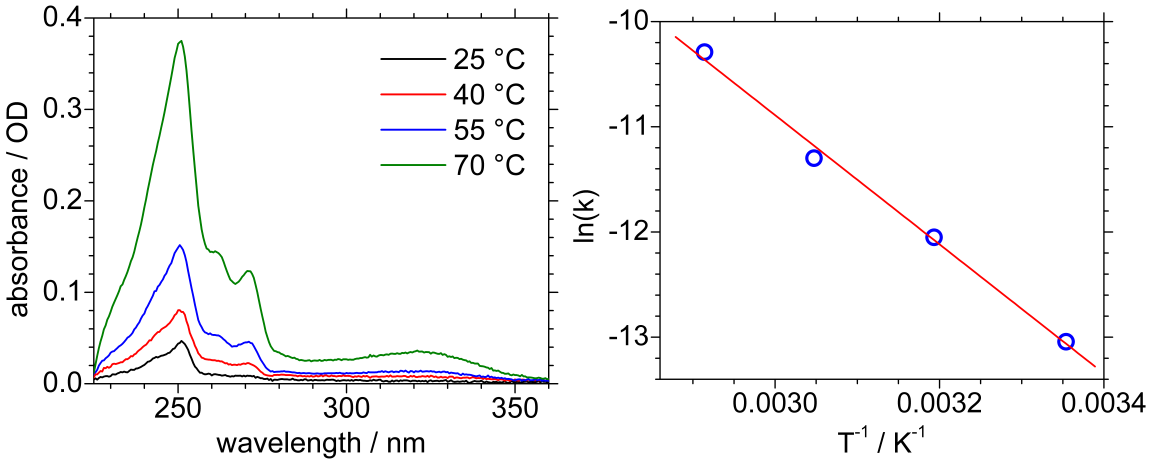

(a) (b)

Figure 5.2: (a) UV/vis absorption spectra of APO in acetonitrile after thermal reaction in the dark for 21 minutes; the APO contribution to absorption is subtracted. (b) Arrhenius plot for the thermal reaction of APO.

5.2 Photoinduced Reactions

5.2.1 Identification of Photochemical Products

Unlike thermolysis, photoinduced reactions lead to a variety of different products, depending on reaction conditions. Two of the main stable products, AQ and AC, are commercially available. Their UV/vis absorption and ^1H NMR spectra are therefore easily obtained and used for comparative measurements in the identification of other products. Spectral characterization of AC and AQ in acetonitrile was already subject of chapter 3.

Excitation Wavelenghts > 310 nm: Diepoxide Formation

Upon excitation with wavelengths above 310 nm, the only electronic excited singlet state of APO that can be involved is the S_1 state (see chapter 4), and the only reaction pathway that occurs is the homolytic cleavage of the endoperoxide bridge. Apart from AQ, the only other product that is found upon 330 – 360 nm excitation is the diepoxide (DE), as deduced from the ^1H NMR spectrum in figure 5.3.

Identification by ^1H NMR. The ^1H NMR spectrum of a sample of APO after illumination at 360 nm for two hours, at 4 °C, is presented in figure 5.3 (red). The positions marked in grey are the signals of APO, and the AQ positions are indicated in green. Four more strong signals are observed, marked in yellow, which are identified as DE signals by comparison with the data published by Rigaudy *et al.*[28], illustrated by the blue lines on top. A fifth DE signal reported by Rigaudy is located at a position where it is overlapped by the much stronger APO signal. An overview is given in table 5.1

The ^1H NMR data lead to the conclusion that AQ and DE are generated from APO upon 360 nm excitation. For further support, the UV/vis absorption data are also analyzed and compared with literature data.

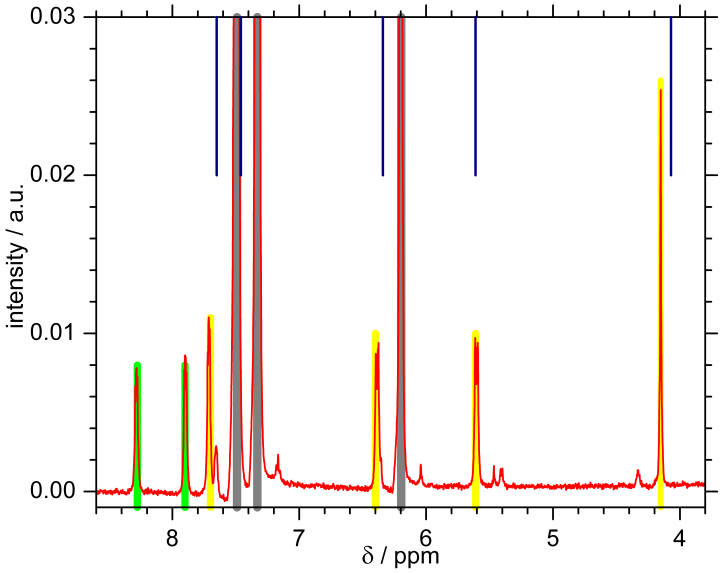

Figure 5.3: Red: ^1H NMR spectrum of APO sample after illumination at 360 nm (2 h, 4 °C). Bars indicate signals of: APO (grey); AQ (green); DE (yellow); DE acc. to Rigaudy *et al.*1 (blue).

Table 5.1: ^1H NMR positions of diepoxide.

	δ / ppm				
this work	4.10	5.60	6.35	–[a]	7.65
Rigaudy *et al.*[28]	4.07	5.61	6.34	7.46	7.65

[a] hidden under a strong APO signal centred at 7.50 ppm

UV/vis Absorption. The absorption spectra of samples of APO after 2 h illumination at 330 nm and 350 nm, respectively, are compared with the spectrum of the sample after 7 h thermolysis at room temperature, which consists of APO and AQ as established in section 5.1. Similarities and differences between the thermal product (black) and the photoproducts (red, blue) are already visible in figure 5.4.a, and become more evident upon subtraction of the APO absorption (grey), as presented in figure 5.4.b. The arrows in figures 5.4.a and .b indicate the wavelength region where the most pronounced deviations are observed: A band is visible in the photoproduct spectra around 280 – 315 nm that is absent in the spectrum of the thermal product. This new band represents the absorption of the diepoxide (DE) photoproduct, separately shown in figure 5.4.c after subtraction of the thermal product absorption spectrum. The grey bars refer to the absorption maxima for DE as published by Rigaudy *et al.*[28]; the values are compared in table 5.2.

The analysis of both ^1H NMR and UV/vis absorption spectra of APO samples that were photoconverted with excitation at 330 – 360 nm shows with high confidence that the additional photoproduct, next to AQ, is the diepoxide.

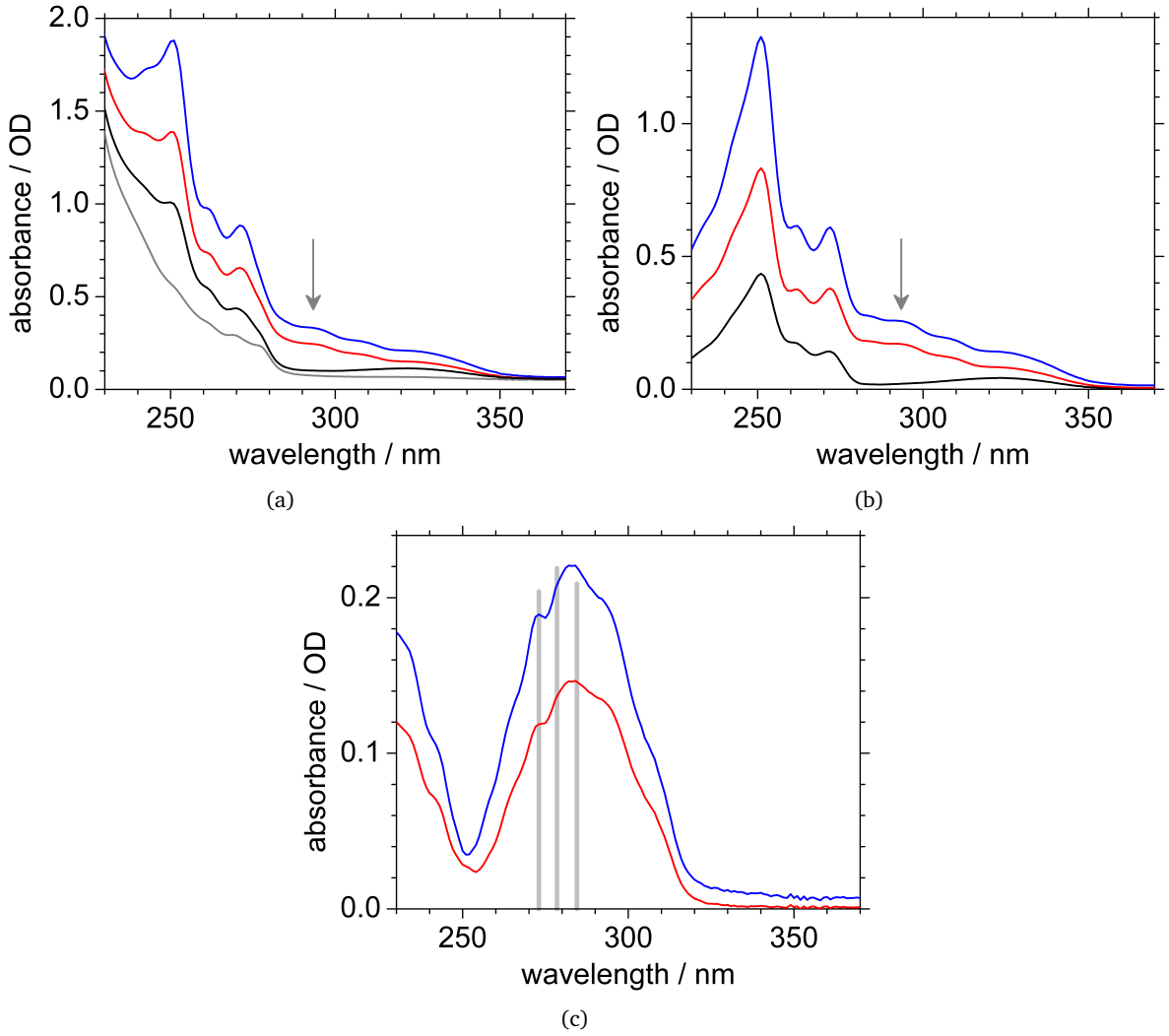

Figure 5.4: UV/vis absorption spectra of APO in acetonitrile after illumination at 330 nm (blue) and 350 nm (red), compared with the spectrum after 7 h in the dark (black). - (a) Grey: Spectrum of the fresh APO sample; (b) spectra after subtraction of the absorption of fresh APO (grey in fig. a); (c) spectra from (b) after subtraction of the spectrum of the thermal product (AQ). Grey bars indicate the spectral positions and relative intensities of the DE absorption according to Rigaudy *et al.*[28].

Table 5.2: Spectral positions and extinction coefficients of diepoxide absorption maxima.

	λ / nm ($\lg \epsilon^a$)			
this work	273.0 (3.45)	-	283.0 (3.51)	292-308
Rigaudy *et al.*1	273.0 (3.48)	278.5 (3.51)	284.5 (3.49)	-

[a] $\epsilon/(\mathrm{l\ mol^{-1}\ cm^{-1}})$

Comparison with Literature. Particular importance should be attributed to this result with regard to the synthesis of the DE, which was reported[28] to be successful only with excitation wavelengths longer than 435 nm. Th reported photo-reaction was performed at 5 – 6 °C, by exposing a 20 mM solution of APO in dry benzene for 40 h to the full emission of a 1600 W xenon lamp, passed through a GG 455 cutoff filter, and resulted in the DE product with 78 % conversion yield. The authors further remarked that at wavelengths shorter than 435 nm mainly AQ and its derivatives were generated.
Since the inability to photochemically synthesize the DE compound with $\lambda < 435$ nm appears to be the main existing support for putting the location of the $S_0 \rightarrow S_1$ transition at $\lambda < 435$ nm, this assignment[24] has now become untenable. This is further supported by the calculations discussed in chapter 4, and by the investigation of the wavelength dependent photochemical quantum yields presented in section 5.2.2.

Excitation Wavelengths < 310 nm: Bicyclic Acetal

While illumination with wavelengths > 310 nm exclusively excites the $S_0 \rightarrow S_1$ transition and leads to formation of the AQ and DE photoproducts, other photoreaction pathways are available upon irradiation at shorter wavelengths. Higher electronic states are excited (S_n, $n \geq 2$), connected to the cycloreversion reaction channel, which is responsible for the formation of AC. Because of competing internal conversion (IC) to the S_1 state, the O-O cleavage products AQ and DE are observed as well. Moreover, a bicyclic acetal (BA) could be identified by ^1H NMR analysis.

Identification by ^1H NMR. The ^1H NMR spectrum of a sample of APO after illumination at 290 nm (110 min, 20 °C) is shown in figure 5.5. In this complex spectrum, five different compounds are identified, indicated by asterisks of different colors: APO (black), AQ (green), AC (violet), DE (blue), and BA (red). The signals close to the positions of the strong APO signals are partly covered, especially around the APO signal at ≈ 7.50 ppm. The ^1H NMR spectrum of BA consists of no less than 8 different signals, as the molecule exhibits a lower degree of symmetry. For an exact assignment of each signal to the corresponding proton in the BA molecule, compare figure 3.1 (page 39) in section 3.1, and page 42. The ^1H NMR positions of BA reported by Rigaudy *et al.*[28] are illustrated as grey bars on top. The values are compared in table 5.3. From the comparison of the ^1H NMR signal positions, the presence of BA in the photoconverted APO sample can be deduced. In addition, the UV/vis absorption spectrum of the same sample is analyzed.

UV/vis Absorption. Figure 5.6.a shows the absorption spectrum of a sample of APO, illuminated at 290 nm (red). This spectrum is decomposed into the components that belong to APO and to the various photoproducts, respectively. Depicted are the scaled spectra of APO (grey), AC (green), AQ (blue), as well as the sum of these contributions (orange). After subtraction of these components, the black spectrum is obtained, and it still contains contributions from DE and BA. In figure 5.6.b, this black spectrum is compared to the scaled DE spectrum (red), and the difference spectrum, assigned to BA absorption, is shown in blue. Further, the absorption maxima reported by Rigaudy *et al.*[28] are indicated by grey bars, and the values are compared in table 5.4.

Table 5.3: ^1H NMR positions of bicyclic acetal.

	δ / ppm								
this work	5.95	6.65	6.70	6.85	-	7.15	7.20	7.40	7.55
Rigaudy *et al.*[21]	5.81	6.65	6.69	6.82	7.07	7.12	7.26	7.27	7.48

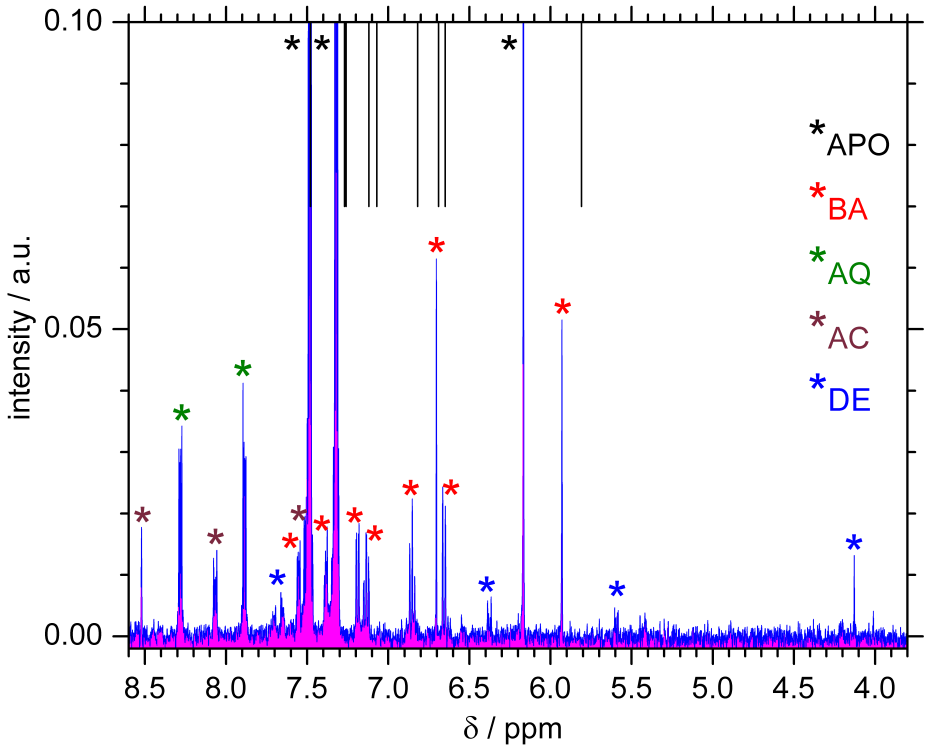

Figure 5.5: ^1H NMR spectrum of APO sample after illumination at 290 nm (110 min, 20 °C; blue). Asterisks indicate signals of APO, AC, AQ, DE, and BA. Grey bars on top: BA acc. to Rigaudy *et al.*[28].

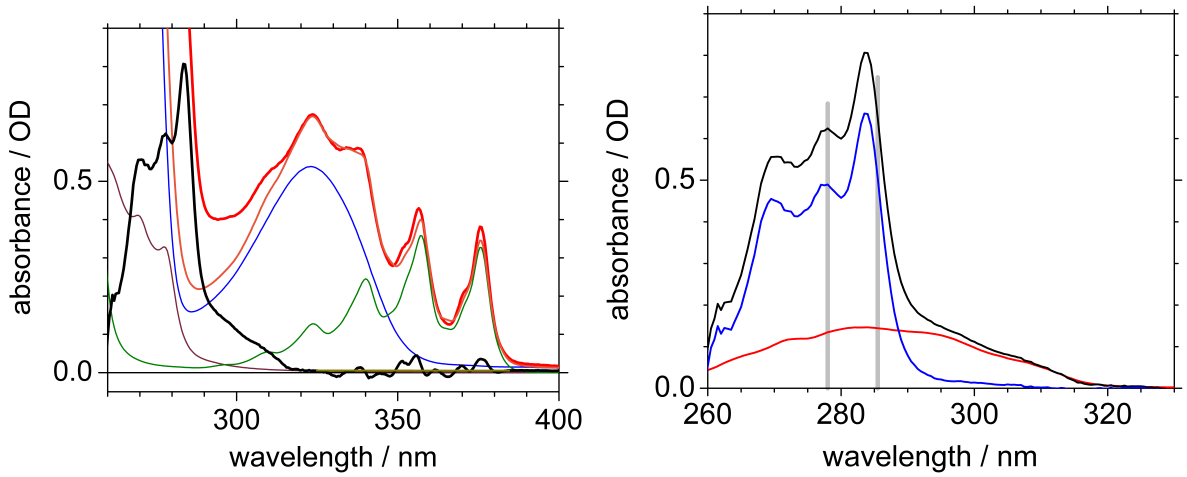

Figure 5.6: UV/vis absorption spectra of APO in acetonitrile after illumination at 290 nm. - (a) Red: sample absorption; compared to the scaled components APO (grey), AC (green), and AQ (blue); orange: sum of these components; black: sample absorption after subtraction of these components. (b) Black: residual spectrum as black in (a); red: scaled DE spectrum; blue: after subtraction of DE absorption.

Table 5.4: Spectral positions and extinction coefficients of bicyclic acetal absorption maxima.

	λ / nm ($\lg \epsilon^a$)	
this work	277.5 (3.34)	283.5 (3.43)
Rigaudy *et al.*[28]	278.0 (3.48)	285.5 (3.52)

[a] $\epsilon/(1\ \mathrm{mol}^{-1}\ \mathrm{cm}^{-1})$

Photoproducts at Higher Concentrations

For samples with higher initial APO concentrations, the photochemistry becomes even more complex. Next to AC, AQ, DE, and BA, two more products could be identified by ^1H NMR spectroscopy. Three of the ^1H NMR signals, seen in both the 350 and 360 nm converted samples, are tentatively assigned to 9,10-dihydroxy-9,10-dihydroanthracene (DHA), a compound not mentioned in previous studies on the photochemistry of APO[16, 24, 28, 20]. Even though the ^1H NMR shifts in perdeuterated DMSO at 110 °C that were reported[57] for DHA do not exactly match the values observed at 5 °C in perdeuterated acetonitrile, the intensity ratio of the three identified peaks in both samples matches the expected intensity ratio, which substantiates the assumption that these three peaks belong to the same compound. Moreover, in investigations of the photochemistry of AC on dry silica and fumed silica surfaces[22] with excitation at 350 nm, in addition to APO, AQ, and four different dimeric products, 15 % of the photoproducts was found to be DHA, and 7-8 % was identified as 9-hydroxy-10-anthrone (HA). The latter compound was also identified here in the 5.7 mM APO sample, photo-converted with 350 nm excitation, and its ^1H NMR positions matched reported[20] values.

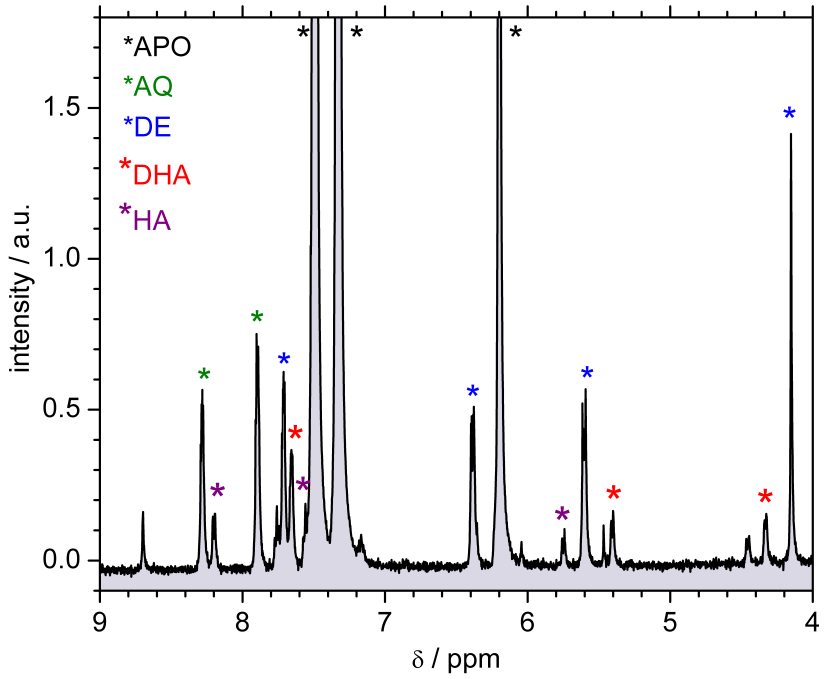

Figure 5.7: ^1H NMR spectrum of APO sample after illumination at 350 nm (5 °C). Asterisks indicate signals of: APO (black); AQ (green); DE (blue); DHA (red); HA (violet).

5.2.2 Wavelength dependent Photoproduct Quantum Yields

Photoproduct Quantum Yield

The photoproduct quantum yield (QY) is defined as the number of product molecules generated divided by the number of photons absorbed by the educt. A total photoproduct QY of 100 % implies that every excitation leads to a product molecule. Furthermore, excited state absorption or 2-photon absorption would reduce the observed maximum total photoproduct QY to less than 100 %, since in these situations at least two photons were absorbed to produce a single photoproduct molecule. Such multiphoton effects were excluded by using a low-intensity excitation source.

Absolute Quantum Yield of AC Formation

The absolute QY of AC formation was determined at 290 nm, using 0.6 – 1.4 mW pulsed excitation on 0.2 and 0.5 mM APO in acetonitrile samples. The results from five measurements were found to vary between 18.7 % and 21.6 %, from which a QY of (20 ± 2) % for AC formation with excitation at 290 nm is deduced. Main sources for errors in this QY determination are the AC extinction coefficient (accuracy ± 5 %), the fluctuations in the laser power during the 10-20 min exposure periods ($\approx$ 5-10 %), and the reliability of the calibration of the laser power meter. In fact, these error sources may warrant a larger error margin than expressed in the variation of the results.

Relative and Absolute Quantum Yield Determination for other Products

The relative QY's for the various photoproducts are extracted from the absorption spectra of partially photo-converted samples (like in figure 5.6) using the extinction coefficients of APO and the photoproducts determined in section 5.2.1. Conversion of these results to absolute QY's was accomplished by scaling all relative QY's to the value determined for the absolute QY of AC formation at 290 nm. A series of photochemical conversion experiments was performed at 10 nm intervals between 240 and 400 nm and at 450 nm to determine the wavelength dependence of the various photoproduct QY's. At each excitation wavelength (240 – 400 nm) a series of two consecutive measurements was run on the same sample. The first and second excitation periods are indicated in figures 5.8 – 5.12 by filled and open symbols, respectively.
Anthraquinone (AQ), which can be produced either thermally or as a secondary photoproduct, shows negligible contributions after 10 or 20 minutes of excitation, i.e. between 0 – 6 % without a clear trend. AQ is therefore not considered in the photoproduct QY determination, except in the total QY. Nevertheless, during prolonged illumination periods of up to 140 minutes, enough AQ is accumulated to show a significant contribution, and it is therefore included in the photoproduct accumulation analysis in section 5.2.3.

Anthracene QY. The AC quantum yields depicted in figure 5.8 show a maximum of 29 % at 270 nm, which corresponds to the absorption maximum of the $S_0 \rightarrow S_4$ transition as determined in chapter 4. At 320 nm, the antracene QY has dropped to 0.35 %, and at longer wavelengths no detectable amount of AC is generated. The fact that the anthracene QY clearly drops at both shorter and longer wavelengths than 270 nm indicates that the cycloreversion reaction is significantly more efficient from the S_4 state than from other nearby electronic states. In addition, it makes it implausible that the 270 nm peak could be a vibronic transition related to the 277.5 nm electronic

transition, in agreement with the theoretical results[35] discussed in chapter 4.

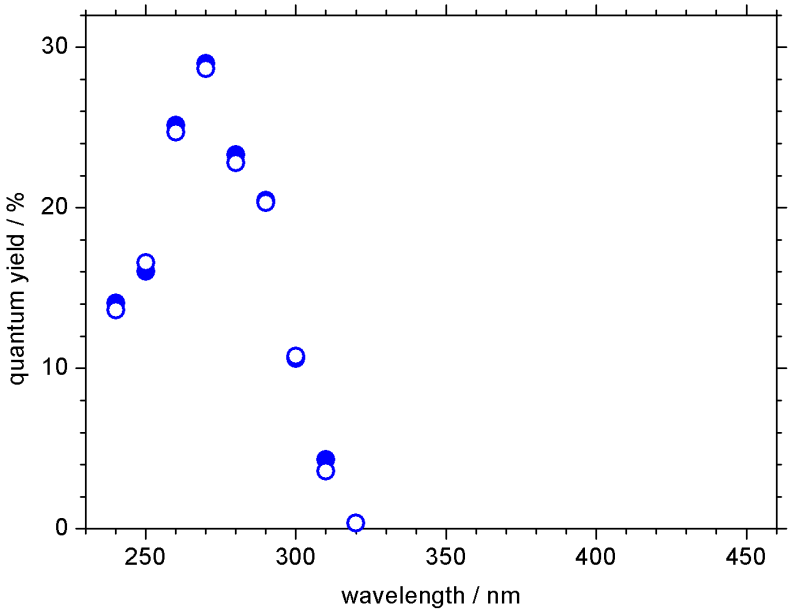

Figure 5.8: AC photochemical quantum yield.

Comparison with Literature. Absolute quantum yield measurements for the AC formation were previously performed by Schmidt *et al.*[24] for APO in CH_2Cl_2. They concluded that the QY for AC formation, associated with the cycloreversion reaction, reaches a maximum of 22 % at 270 nm and drops to 1.5 % at 313 nm[24]. In general, Schmidt *et al.* observed the same trends in CH_2Cl_2 as presented here in acetonitrile, but the published AC formation QY's are slightly lower. In light of the observation[30, 34] for APO in argon matrices at 22 K that with 275 nm excitation, anthracene is the only photolysis product, the photochemistry of APO may well be temperature and environment dependent[34].

Diepoxide QY. Figure 5.9 shows the wavelength dependence of the diepoxide (DE) quantum yield. The most important result is that at all wavelengths between 240 and 400 nm there is a significant QY for DE, varying from 30 % to almost 80 %. Indeed, DE is the dominating primary photoproduct.

Comparison with Literature. This result is in sharp contrast with the conclusion of Rigaudy *et al.*[28] that DE cannot be synthesized at wavelengths shorter than 435 nm. This seems to be the only experimental basis for the claim by Schmidt *et al.*[24, 31] that the $S_0 \rightarrow S_1$ transition is situated above 435 nm. The diepoxide QY data in figure 5.9 clearly demonstrate that this claim has now become untenable. Instead, the $S_0 \rightarrow S_1$ transition has been localized around 290 nm with the help of calculations, as described in chapter 4.
The present results also agree with conventional wisdom[64]:Typically, for states S_n with $n \geq 2$ photochemistry is expected to compete with rapid internal conversion to the S_1 state. Since it has

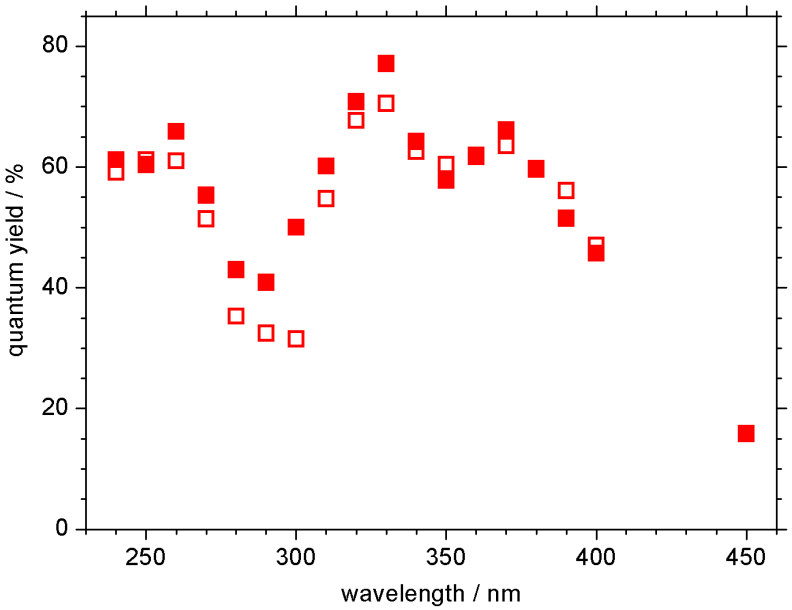

Figure 5.9: DE photochemical quantum yield.

generally been accepted that excitation to the APO S_1 state leads to homolytic cleavage of the peroxide bridge, and both the present study and Schmidt *et al.*[24] show that the other photochemical reaction channel (cycloreversion to anthracene and singlet oxygen) always has a QY below 30 %, it follows that at least 70 % of the excited-state population will probably end up in the S_1 state, prior to consecutive further decay and photochemical conversion.
At 450 nm, with 20 nm excitation bandwidth, a diepoxide QY of $\approx$ 16 % was still obtained, confirming Rigaudy *et al.*'s[28] result that the DE can be synthesized at these wavelengths, albeit with an efficiency more than three times lower than at 360 nm. Although one cannot conclude the position of the $S_0 \rightarrow S_1$ transition from the data in figure 5.9, the argument can be made that the clear drop in the DE quantum yield with excitation above 380 nm indicates that this absorption should occur at $\lambda \leq 380$ nm. As mentioned above, it is concluded in chapter 4 that the $S_0 \rightarrow S_1$ transition is located around 290 nm for APO in chloroform.

Diepoxide Consumption. In the region 270 – 310 nm, the diepoxide QY shows a clear dip, compared to both shorter and longer wavelengths. Moreover, particularly the data at 280 – 300 nm gave a significantly higher diepoxide QY after a single irradiation period than after the double exposure time. As the DE absorption spectrum in figure 5.4 shows, the DE has significant absorption in this wavelength region. Below 280 nm, DE absorption has to compete with APO and at later stages with the other photoproducts, whereas at longer wavelenghts, DE initially has little competition of the other compounds. These data therefore clearly suggest that absorption of light by DE reduces the diepoxide QY. This means that the excited DE is further converted into a different compound, which is identified to be the bicyclic acetal in the next paragraphs.
The diepoxide QY also shows a decreasing trend at wavelengths longer than 310 nm. However, in this wavelength region no significant difference is seen between the diepoxide QY after the first and second exposure periods.

Bicyclic Acetal QY. Figure 5.10 shows the wavelength dependence of the bicyclic acetal QY. The bicyclic acetal is obtained only upon excitation at wavelengths of 310 nm or lower, with a maximum of almost 50 % at 300 nm. The QY for this compound is much higher in the region 280 – 310 nm than in the region 240 – 270 nm. Moreover, between 280 and 310 nm the QY's become significantly higher after the second irradiation period. Comparison with the reverse trend for DE, i.e. the reduced QY of DE after the second illumination time (fig. 5.9), demonstrates that the optically excited DE is converted into the bicyclic acetal. The wavelength region where DE is rearranged to BA, 280 – 310 nm, matches the absorption region of DE; below 280 nm, DE absorption competes with APO, AQ and BA absorption.

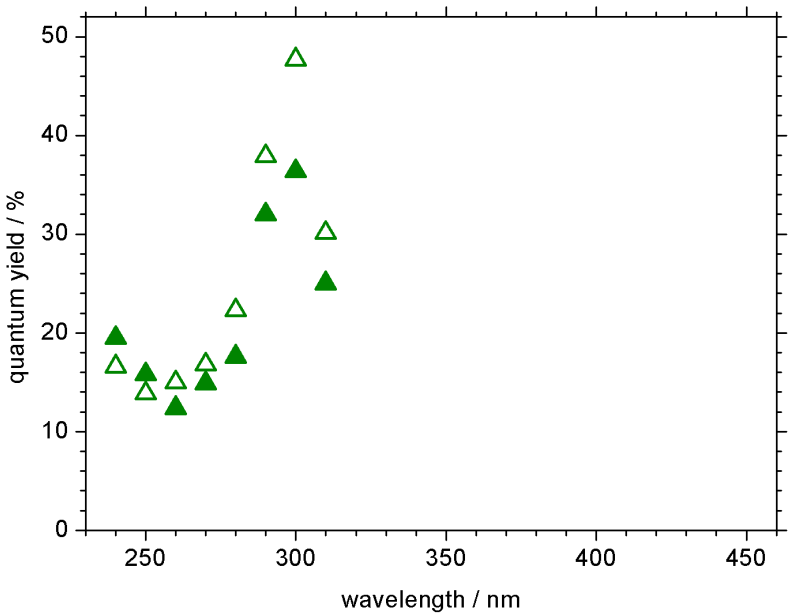

Figure 5.10: BA photochemical quantum yield.

Comparison with Literature. The formation of BA from isolated DE was reported[28] to occur only after addition of acids[1] to the photoproduct. In case of 9,10-diphenylanthracene-9,10-endoperoxide, though, it was deduced[27] that optical excitation of the corresponding diepoxide led to formation of a bicyclic acetal. The present results demonstrate that the latter process is also possible for the DE created from APO. As a conclusion, BA is formed from the precursor DE after activation, either by acid or by photo-excitation.

[1] protic acids, or Lewis acids like $ZnCl_2$

Total photoproduct QY. Figure 5.11 shows the total photoproduct quantum yield as a function of excitation wavelength, including the AC, DE, BA, and AQ yield (if any). At wavelengths $\lambda \leq 310$ nm the total photoproduct QY is roughly constant and close to unity, given a realistic error margin of $\pm$ 15 %. Between 300 and 450 nm, on the other hand, a fairly linear decline of the total photoproduct QY is observed from $\approx$ 100 % at 300 nm to $\approx$ 17 % at 450 nm. One approach to explain this behavior could be the presence of other weak absorption bands related to singlet-triplet absorption, which could increasingly contribute to the long wavelength tail of the APO absorption spectrum. Furthermore, the observed steady decline with lower excitation energy could indicate that the molecules associated with absorption further out in the wings would gradually obtain insufficient energy for overcoming energy barriers that would result in photochemistry. The most probable competing decay channel, responsible for the drop in photoproduct QY, is internal conversion to the APO electronic ground state. Other investigations of photoproduct QY's extending this far into the wings of a molecular absorption spectrum would be required to evaluate whether or not the observed behavior can be called uncommon.

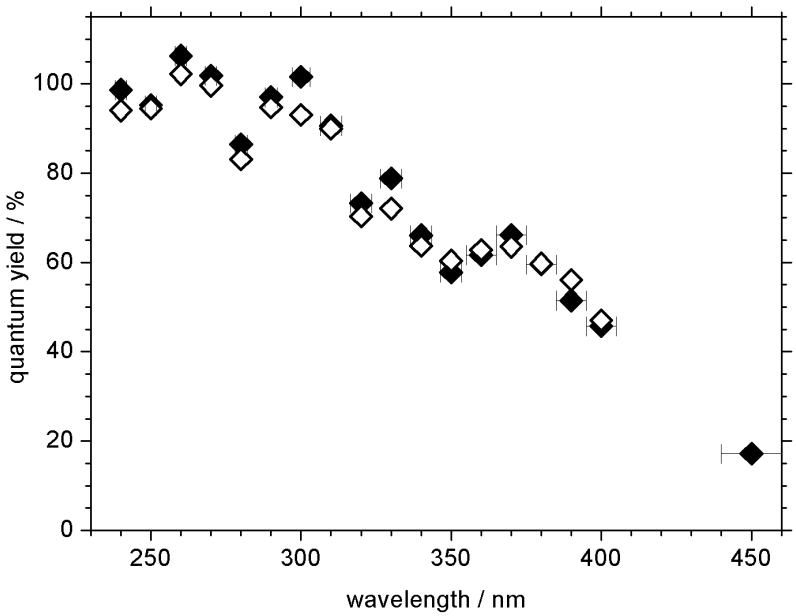

Figure 5.11: Total photoproduct quantum yield, including AC, DE, BA, and AQ contributions.

For easier comparison, figure 5.12 summarizes the results of the wavelength dependent photochemistry QY study.

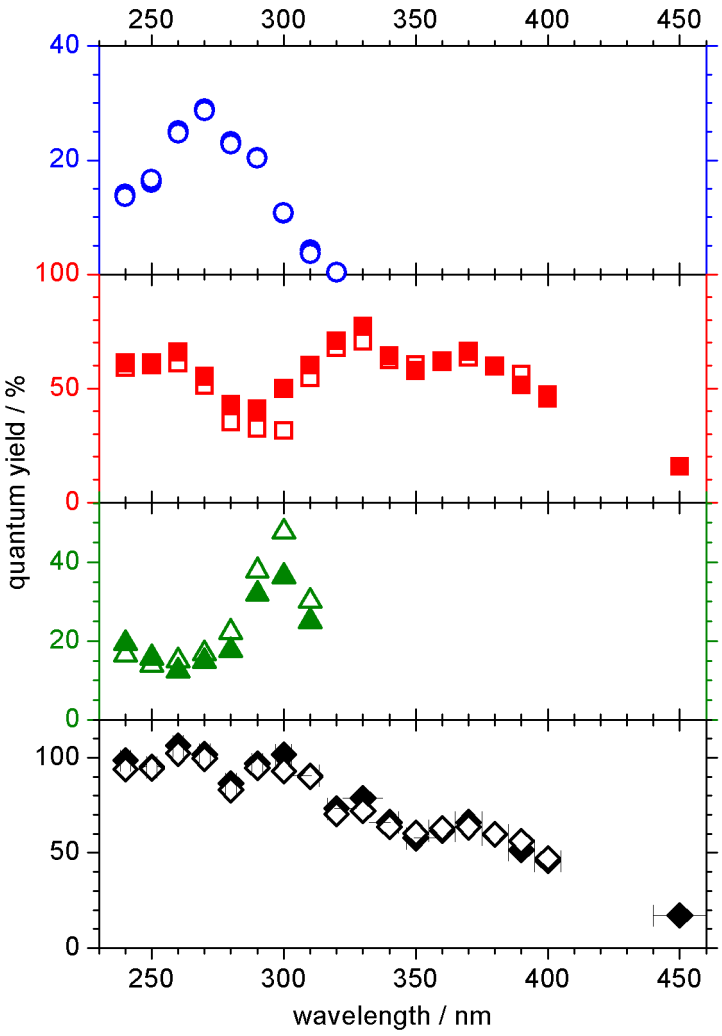

Figure 5.12: Overview of figures 5.8-5.11; from top to bottom: AC, DE, BA, and total photoproduct quantum yields.

5.2.3 Photoproduct Accumulation

The photoproduct acculmulation was followed for up to 140 minutes during illumination at various wavelengths between 289 and 360 nm. After each excitation period, an absorption spectrum was taken of the partially photoconverted sample, resulting in a series of spectra as the one shown in figure 5.13 for 325 nm excitation.

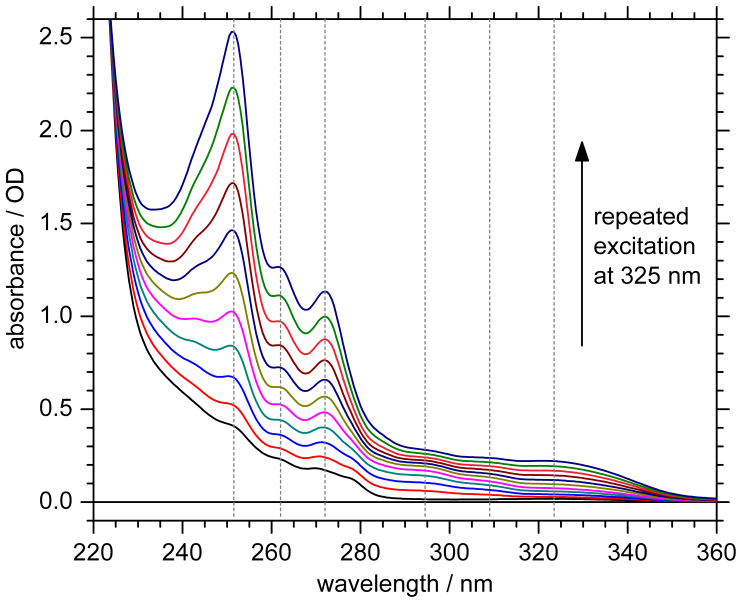

Figure 5.13: Increasing absorption spectra of APO sample, partially photoconverted with repeated excitation at 325 nm.

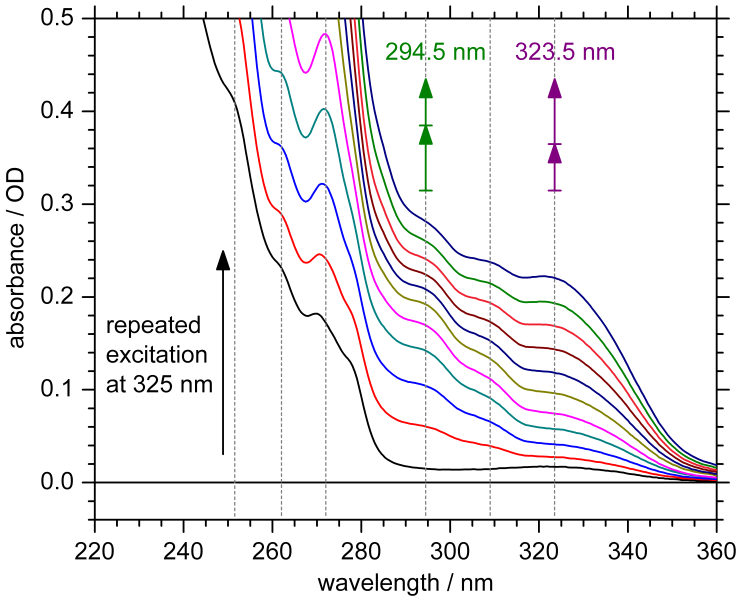

Figure 5.14: Detail of figure 5.13.

For better visibility, figure 5.14 shows an enlarged view of figure 5.13. Using the known extinction coefficients, the build-up of the various photoproducts can be monitored quantitatively. While the speed of photoproduct build-up increases e.g. at 323 nm, it decreases at 295 nm. Figures 5.15 and 5.16 illustrate the different behavior depending on wavelength.

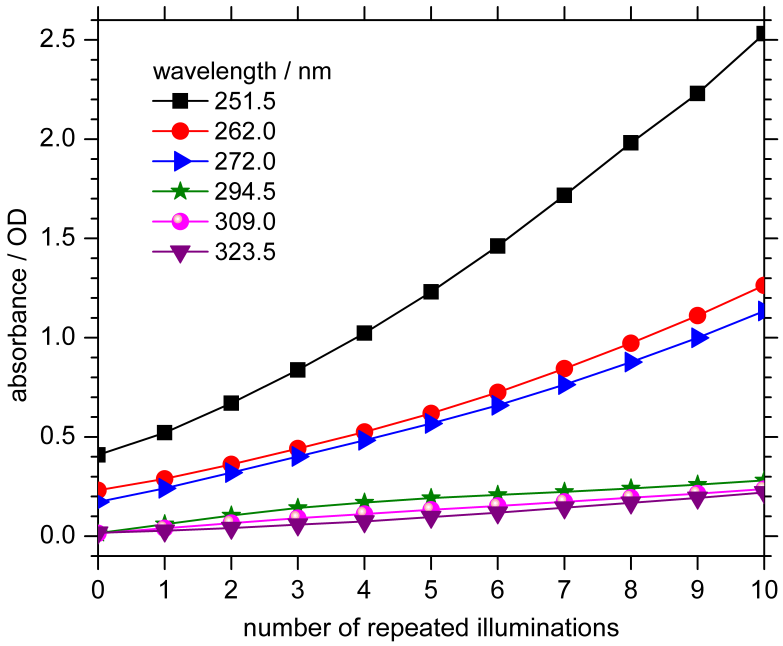

Figure 5.15: Increasing absorption with repeated excitation of an APO sample at 325 nm, plotted for different wavelengths.

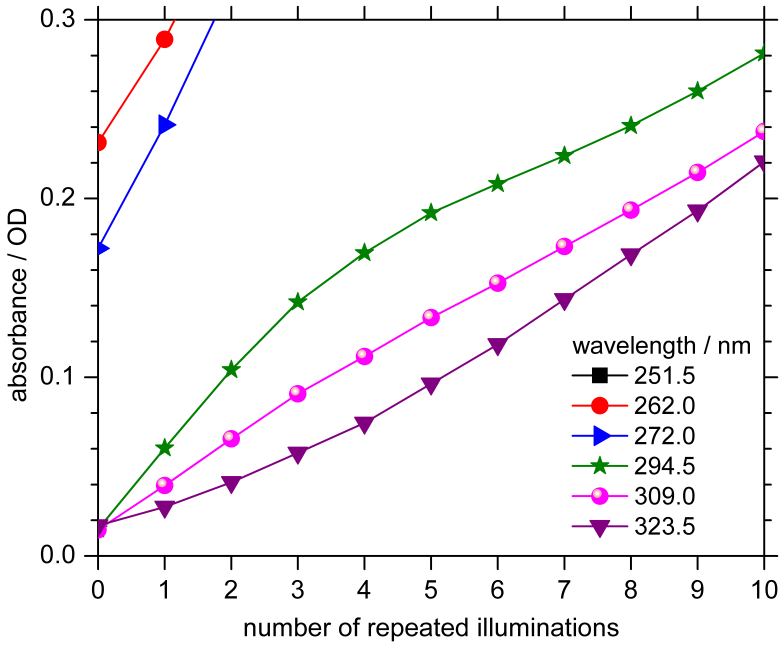

Figure 5.16: Detail of figure 5.15.

For three measurement series with excitation at 289, 327, and 360 nm, absorption spectra were taken every 10 or 20 minutes and decomposed into the various photoproduct contributions. The photoproduct accumulation is illustrated in figure 5.17 for all three series. At the end of each series, the exact compositions of the sample was determined by ^1H NMR.

360 nm Excitation. The kinetics for 360 nm is shown in figure 5.17.c. With excitation at 360 nm, predominantly DE was created, with AQ as a minor byproduct. For presentation purposes in figure 5.17.c the AQ yield has been multiplied by 10. The composition, as determined by ^1H NMR, of this initially 0.6 mM APO sample after 140 min exposure is listed in table 5.5. With 23 % of the APO converted, the DE yield is 88 %, implying that higher chemical reaction yields than the 78 % achieved by Rigaudy *et al.*[28] are in principle possible.

Table 5.5: Composition of partially photoconverted APO samples, determined by ^1H NMR. The first three columns list the excitation wavelength, temperature, and initial APO concentration; the other columns list the molar percentages of APO and the identified products after photoconversion. At most 1.2 % of the ^1H NMR signal integrals belongs to unidentified compounds.

λ / nm	T / °C	$c_0(APO)$ / mM	APO/%	BA/%	AQ/%	DE/%	AC/%	DHA/%	HA/%
289	23	1.0	58.4	22.8	10.7	2.2	4.7	-	-
360	5	0.6	77.0	-	2.7	20.3	-	-	-
360	5	5.2	85.1	-	3.4	10.4	-	0.9	-
350	5	5.7	81.0	-	4.0	8.8	-	2.5	2.7

327 nm Excitation. With excitation at 327 nm (figure 5.17.b), the photoproducts were predominantly DE and AQ. However, after 40 min, when about one-quarter of the APO had been converted, a third component started to make its appearance in the absorption spectra, with a broad absorption band starting below 290 nm and a maximum at 269 nm (spectrum not shown). The late appearance and exponential rise of the absorption of this unidentified component point to a product from a bimolecular reaction, and AQ must be one of the starting compounds, because the exponential rise requires a compound whose concentration still increases significantly after 40 min exposure. Fitting the kinetics with various reaction schemes is unfortunately inconclusive in determining whether the second reaction component is APO or DE.

289 nm Excitation. Excitation at 289 nm results in even more complex photochemistry (final composition see table 5.5). The dominating product is now the bicyclic acetal (BA). For presentation purposes in figure 5.17.a its yield is scaled down by a factor 0.4. Initially the increase of the AQ yield is proportional to the BA yield but clearly starts to deviate after 40 min. The DE concentration is already after 20 min close to its plateau value of ≈ 30 μM, which is about one-half the plateau concentration reached with 327 nm excitation and more than four times less than the DE concentration after 100 min conversion with 360 nm light.

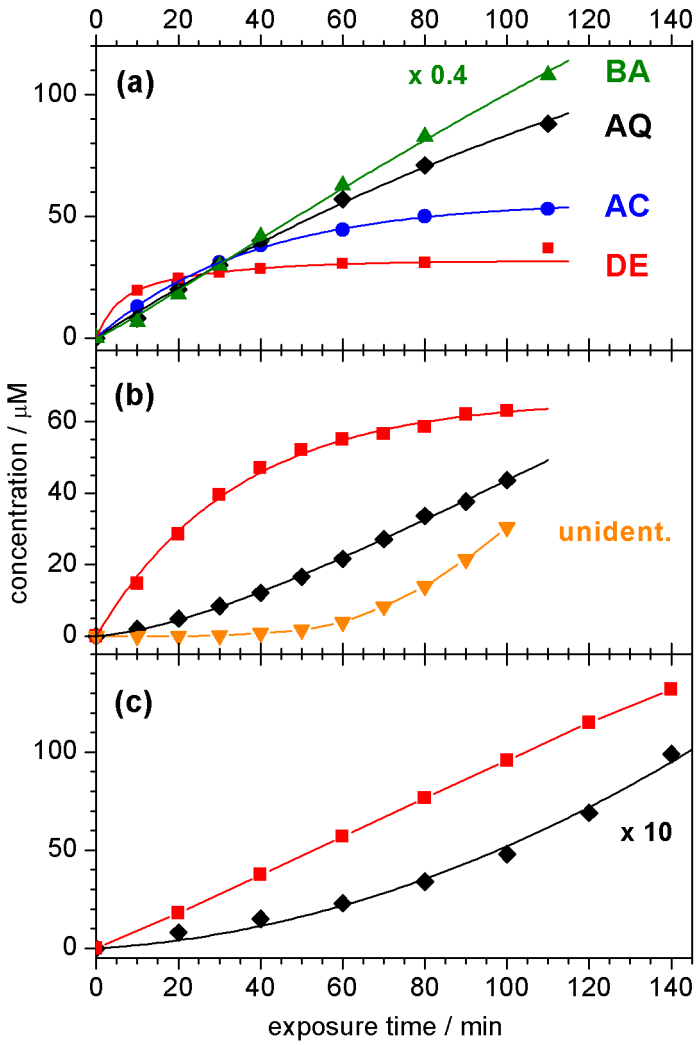

Figure 5.17: Photoproduct generation kinetics.
(a): exc. 289 nm, 23 °C, initial concentration 1 mM;
(b): exc. 327 nm, 23 °C, initial concentration 0.22 mM;
(c): exc. 360 nm, 5 °C, initial concentration 0.6 mM.
AC, AQ, DE, BA, and an unidentified compound are symbolized as indicated.

In the discussion of the absolute QY data of figure 5.12 it was already established that excitation of DE leads to formation of BA. Obviously this process is very efficient and therefore severely reduces the maximum concentration of DE that can be attained, despite the fact that the sample exposed to 289 nm initially had the highest APO concentration. The trend seems clearly that higher DE concentrations can be obtained with longer excitation wavelengths.
This observation provides an explanation for Rigaudy *et al.*'s[28] inability to synthesize DE with excitation at $\lambda \leq 435$ nm. Their result that mainly AQ and its derivatives are obtained at shorter wavelengths[28] corroborates the suggestion that excitation of DE promotes the conversion to BA, and possibly also to AQ.

Bimolecular Reactions. Another interesting issue to notice is that the QY of AC after the total 110 min of 289 nm exposure is only 11.3 % (compare table 5.5), approximately one-half the value determined in the five absolute QY determinations for AC at 290 nm. As the data in figure 5.12 clearly demonstrated that at all wavelengths the AC formation QY does not change with prolonged exposure, the build-up of AC in time in figure 5.17.a can be regarded as a measure for the photochemical consumption of APO by optical excitation of APO. The overall reduction of the AC QY therefore indicates that the APO concentration now has also been reduced by reactions that do not involve optical excitation of APO. Since unimolecular thermal decomposition can be neglegted (sec. 5.1), the conclusion must be that formation of BA, and perhaps also AQ, potentially also proceeds via a bimolecular mechanism with ground-state APO, thereby causing nearly a doubling of the APO consumption rate.

Higher Concentrated Samples. The possibility of bimolecular reaction pathways affecting the (photo)chemistry outcome is also demonstrated by ^1H NMR analysis of two more concentrated APO samples (> 5 mM), partially converted at 5 °C with excitation at 350 and 360 nm, respectively. These experiments were already used to identify the HA and DHA photoproducts in section 5.2.1 (see page 78); their composition is listed in table 5.5. With excitation at 360 nm the DE yield dropped from 88 % in the 0.6 mM sample to 70 % in the 5.2 mM sample and decreased even further to 46 % with excitation at 350 nm in a 5.7 mM sample. At the same time the AQ yield changed from 12 % to 23 % and 21 %, respectively, for these three samples. In addition, several new peaks appeared in the ^1H NMR spectra, assigned to HA and DHA (compare sec. 5.2.1, page 78).
Because DHA contains two more hydrogen atoms than APO or AC, it is clear that formation of this compound is only viable through a bimolecular mechanism. In fact, it is interesting to note that in Dabestani *et al.*'s[22] experiments the yields of DHA and AQ, which has two hydrogen atoms less, are similar. Sigman *et al.*[65] noted for the 350 nm photochemical conversion of AC in water that with 10 % of the AC converted, only APO and AQ had been formed, whereas after 70 % conversion, also minor fractions of DHA and HA were found in equal amounts. It can therefore be concluded that DHA and HA are formed more with increasing APO concentrations.

Photoproducts at Elevated Temperatures. The thermal evolution of the 5.7 mM APO sample, partially converted with 350 nm light (see table 5.5), was also followed for 2 h with ^1H NMR at 55 °C. In these spectra the DE concentration dropped more than 70 % during this time, and a best single-exponential fit indicates a decay time of 0.67 h, which can be compared to a reported[28] decay time of 9.4 h at 28 °C. At higher temperatures several new thermal products were formed, increasing the complexity of the photoreactions even further, and therefore it cannot be concluded which products DE evolves into in this case.

5.3 Quantitative Investigation of Reaction Pathways: Summary and Conclusions

Reaction Products

Six different photoproducts are identified, of which two (9-hydroxy-10-anthrone, HA, and 9,10-dihydroxy-9,10-dihydroanthracene, DHA) are only formed at higher concentrations and/or higher temperatures. The cycloreversion product anthracene (AC) is only formed at excitation wavelengths < 300 nm, contrary to the O-O cleavage products, which are found even in the region > 400 nm. The primary O-O cleavage product is a diepoxide (DE), which is stable for few hours at RT, before being converted into anthraquinone (AQ). AQ is both a secondary O-O cleavage product and the only detected thermal product. For the thermal reaction, an energy barrier of ≈ 51 kJ/mol is deduced. A bicyclic acetal (BA) is generated upon photoexcitation of the precursor DE.

The Photoinduced Cycloreversion Reaction

Anthracene formation is only observed upon excitation below ≈ 300 nm, indicating that cycloreversion does not proceed from the lowest electronic excited state S_1, which is located around 290 nm according to the conclusions of chapter 4. Moreover, the quantum yield for anthracene formation is with ≈ 30 % highest at the proposed S_4 position around 270 nm, thus cycloreversion is most efficient from the second shoulder visible in the absorption spectrum. Note that this result would still suggest a maximal cycloreversion efficiecy from a higher excited state, even if one would assume Klein's assignment[30] of S_2 at 270 nm and S_1 at 280 nm.

The Photoinduced O-O Cleavage Reaction

The diepoxide was found to be the dominating primary reaction product at all excitation wavelengths that induce photoreactions. This finding is in sharp contrast to the previously accepted opinion[28, 24] that the DE could be formed only with illumination ≥ 435 nm. The claim that the S_1 state of APO should be located in this wavelength region has now become untenable, in agreement with the theoretical results from chapter 4. The reason for the previous failure to synthesize DE with shorter wavelengths lies in the prolonged and intense illumination, which allowed all of the primary photoproduct diepoxide to be converted into the secondary product anthraquinone.

The photoproduct quantum yield for all O-O cleavage products together is highest at ≈ 300 nm, close to the supposed $S_0 \rightarrow S_1$ transition (≈ 290 nm), thus at a considerably lower energy than the cycloreversion maximum (270 nm).

Implications on Dual Photochemistry

These results, together with the assignment established in chapter 4, clearly support the occurence of dual photochemistry in APO. While the cycloreversion reaction proceeds only from higher excited states, the O-O cleavage reaction is available both from S_1 and after internal conversion from higher excited states. An overview is given in figure 5.18.

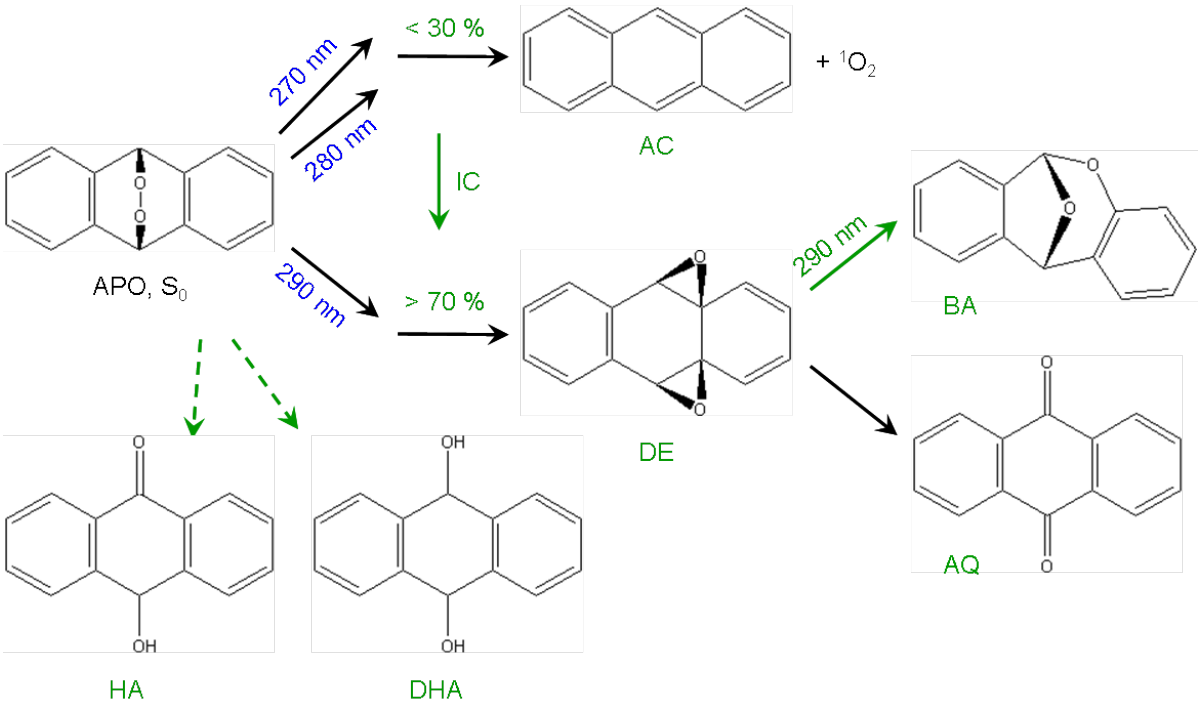

Figure 5.18: Overview on the photoproducts and the main findings concerning the competing reaction pathways of APO (green).

6 Primary Steps of Photoinduced Reactions studied in Real Time

Photoinduced Reactions of APO

A reaction scheme for anthracene-9,10-endoperoxide (APO) is given in figure 6.1, which illustrates the two competing photoreaction channels upon excitation of S_1 and higher excited singlet states ($S_n, n \geq 2$). The primary reaction products are anthracene (AC) and a diepoxide (DE), for which an intermediate biradical (BR) precursor was proposed. The bicyclic acetal (BA) is only formed as secondary reaction product upon photoexcitation of DE, while anthraquinone (AQ) can be either a rearrangement product of DE, or a thermal product of APO. Upon 282 nm excitation, the quantum yields are expected to be approximately 25 % AC, 45 % DE, 20 % BA, and 0 – 6 % AQ, according to the results presented in chapter 5.2.2. These values were derived after 10 min of illumination, which provides sufficient time for secondary reactions like the BA formation after excitation of the primary photoproduct DE.

By contrast, in time resolved experiments that study reactions on a (sub-)picosecond time scale, only processes that occur within the first 100 ps after a short excitation pulse are monitored. Therefore, secondary processes are most likely not observed.

When several scans on the same sample are measured consecutively, however, primary products present in the sample might be excited and observation of secondary products is possible. To avoid secondary effects, the previously excited sample is rapidly exchanged by circulating the sample volume, and only the very first scans of a measurement series are considered in the analysis of the primary photoreaction steps. The consecutive scans can still be evaluated and provide valuable information on secondary processes.

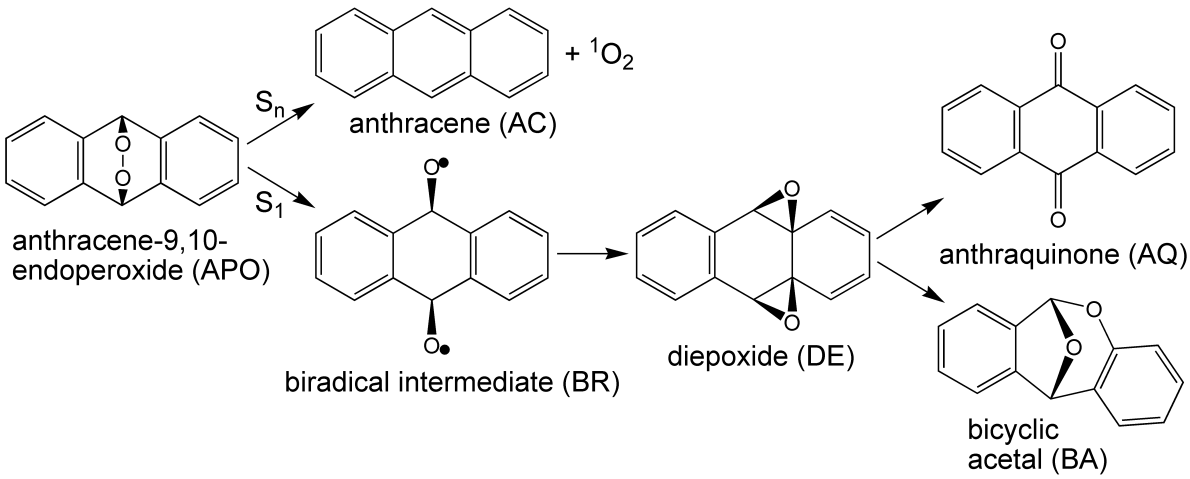

Figure 6.1: Reaction scheme of APO.

Excitation Wavelengths for APO

Time resolved pump-probe experiments were performed for anthracene-9,10-endoperoxide (APO) at 266 nm and 282 nm excitation. In figure 6.2, the extinction coefficient spectra of APO, AQ, AC, and DE are shown; note that the black APO spectrum is enlarged by a factor of 20 for better visibility. The excitation wavelengths, 266 nm for APO, AQ and AC, 282 nm for APO, and 376 nm

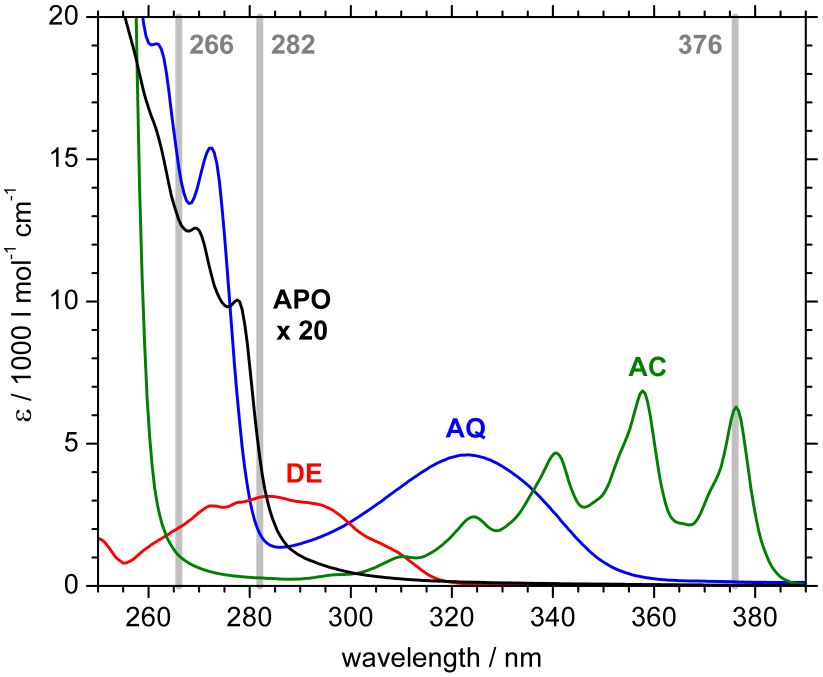

Figure 6.2: Extinction coefficient spectra: Black: APO, enlarged by factor 20; blue: AQ; green: AC; red: DE. Excitation wavelengths 266 nm, 282 nm, and 376 nm are indicated by grey bars.

for AC, are indicated by grey bars. In case of APO excitation at 266 nm, a problematically strong product contribution from excited AQ is observed. AQ is always generated in a thermal reaction, and if it absorbs strongly at the excitation wavelength, as is the case at 266 nm (see fig. 6.2), the transient spectra are dominated by signals from AQ, making it impossible to separate and analyze the underlying APO data. By switching to 282 nm excitation, the AQ contribution could be minimized, since this wavelength is almost at a local minimum in the AQ absorption, and the relative ratio of the extinction coefficients of AQ and APO, $\epsilon_\lambda(AQ)/\epsilon_\lambda(APO)$, reaches a minimum of ≈ 7, down from ≈ 22 at 266 nm. Consequently, the APO data at 282 nm excitation are -as far as perceivable- free from AQ contributions, and only the primary photoproducts AC and DE (and possibly a biradical intermediate BR) have to be taken into account in the analysis.
Furthermore, HPLC grade acetonitrile was used as solvent in the 282 nm experiment, because room temperatre thermolysis of APO, which also produces AQ, was noticed to be slow in this high-quality solvent (section 5.1, page 5.1).

Anthracene and Anthraquinone

AC and AQ were originally measured only for comparison with the APO measurements, to establish whether or not, or to what extend, signals from photoexcited products contribute to the experimental

data on APO. But it turned out that interesting information about the dynamics of photoexcited AC and AQ can be extracted from these data.
Anthraquinone (AQ) was measured with 266 nm excitation, as APO in the first attempt. Transient data of AC were measured after excitation with both 266 nm and 376 nm, as indicated in fig. 6.2. The reason for the different excitation wavelengths is that different excited states are pumped, resulting in complementary information. While at 376 nm, the $S_0 \rightarrow S_1$ transition is pumped vibrationlessly, i.e. without excess energy, 266 nm excitation presumably leads to initial population of the S_2 state (absorption maximum at 251 nm). After fast internal conversion, AC resides in the vibrationally hot S_1 state. The vibrational relaxation (or cooling) process can be followed by analysis of the transient spectra.
Similar experiments were not done on DE or BA, as they are not commercially available; in addition, DE is thermally unstable[28, 66]. Signal contributions from BA are expected to be minimal in short scans with little chance for absorption by DE. Actually, BA can be neglected in the analysis, as can be deduced by analysis of consecutive scans, as shown in section 6.3.3.5.

6.1 Time Resolved Experiments on Anthraquinone

6.1.1 Transient Data of AQ, excitation at 266 nm

Transient Spectra. The transient data of AQ upon excitation at 266 nm were recorded in steps of 20 fs, 200 fs, and 2 ps. For clarity, transient spectra are shown in separate graphs for different delay time ranges.
In figure 6.3, absorption changes up to 340 fs after excitation are shown. Immediately after excitation, a broad signal with two maxima at 390 and 420 nm, and a minimum around 332 nm is observed. Up to 340 fs, the 390 nm band increases strongly, while the 420 nm maximum only increases until 60 fs, before reducing to a shoulder at 340 fs. To both red and blue sides of this double band, signals are decreasing. The 332 nm minimum shifts to 323 nm during the first 340 fs and can be identified as the bleach band; the signal at this wavelength does not become negative until 200 fs due to overlap with decreasing positve bands.
The next delay time range up to 5 ps is depicted in figure 6.4. On this time scale, little dynamics is observed, only a slight signal decrease at the 390 nm band and a minor increase between 550 and 650 nm.
These trends are inverted after 5 ps, as shown in figure 6.5. Up to 100 ps, the 390 nm band increases again, and signals between 400 and 550 nm decrease. In addition, a blue shift is observed for the former 390 nm band, arriving at 374 nm after 100 ps. Similarly, the bleach band shifts from 323 to 319 nm.
Between 100 and 800 ps, the transient signals do not change significantly any more. The spectrum after 800 ps is depicted in figure 6.7.

Comparison with Literature. The transient spectrum of AQ after 800 ps can be compared directly with the spectrum presented by Hamanoue *et al.* [67], which was recorded in EPA[1] at 77 K after a delay time of 2 μs. The authors assigned this spectrum to the $T_1 \rightarrow T_n$ absorption of AQ. The wavelength positions of spectral features match quantitatively the observed spectrum after

[1] EPA: solvent mixture of ether, isopentane, and ethanol in a volume ratio of 5:5:2.

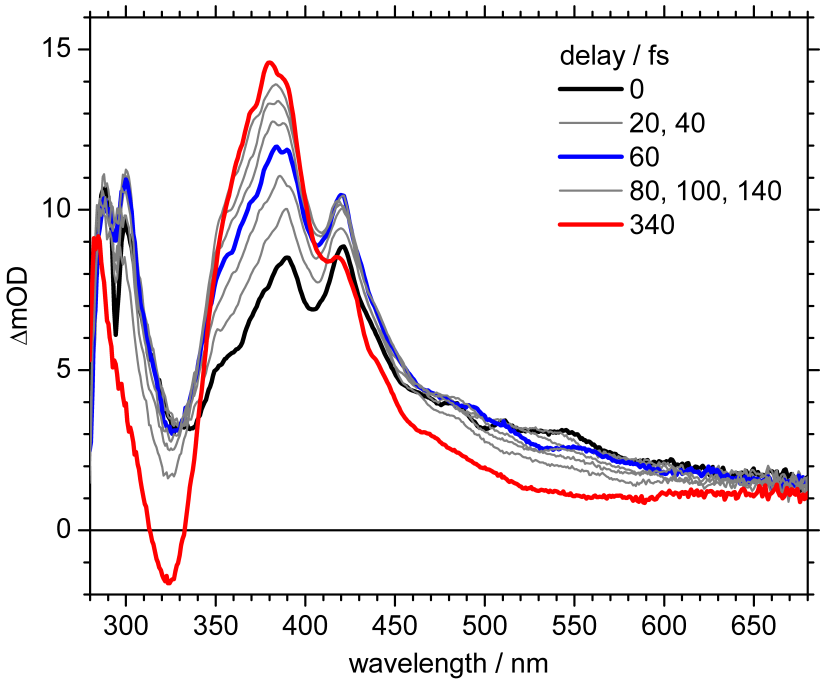

Figure 6.3: Transient absorption of AQ in acetonitrile, excitation at 266 nm, measured in 20 fs steps. Delay times from 0 fs to 340 fs.

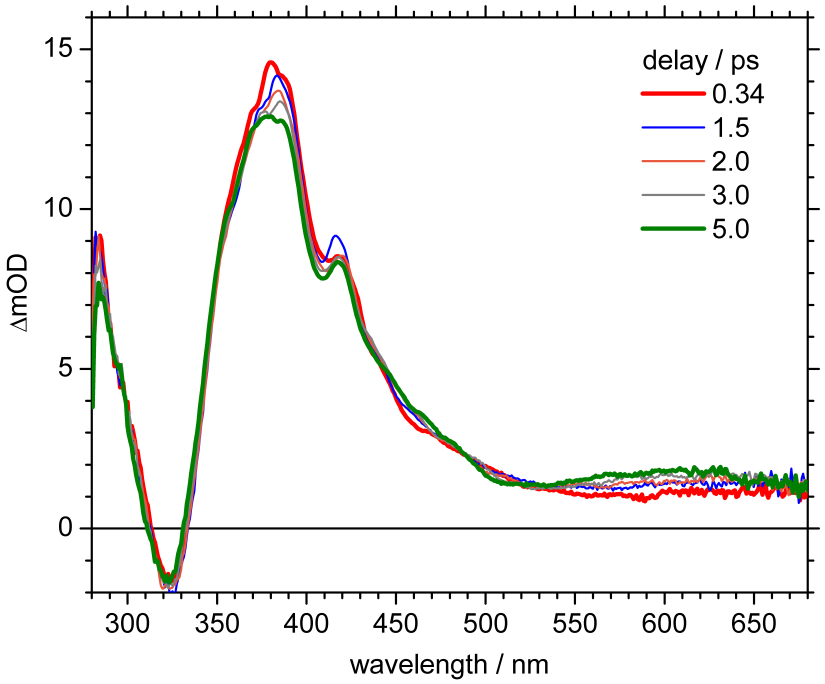

Figure 6.4: Transient absorption of AQ in acetonitrile, excitation at 266 nm, measured in 20 fs steps. Delay times from 340 fs to 5 ps.

800 ps, as visible in fig. 6.6, and their relative intensities still match qualitatively. When scaled to the main band around 374 nm, the signals at wavelengths longer than 550 nm are smaller than

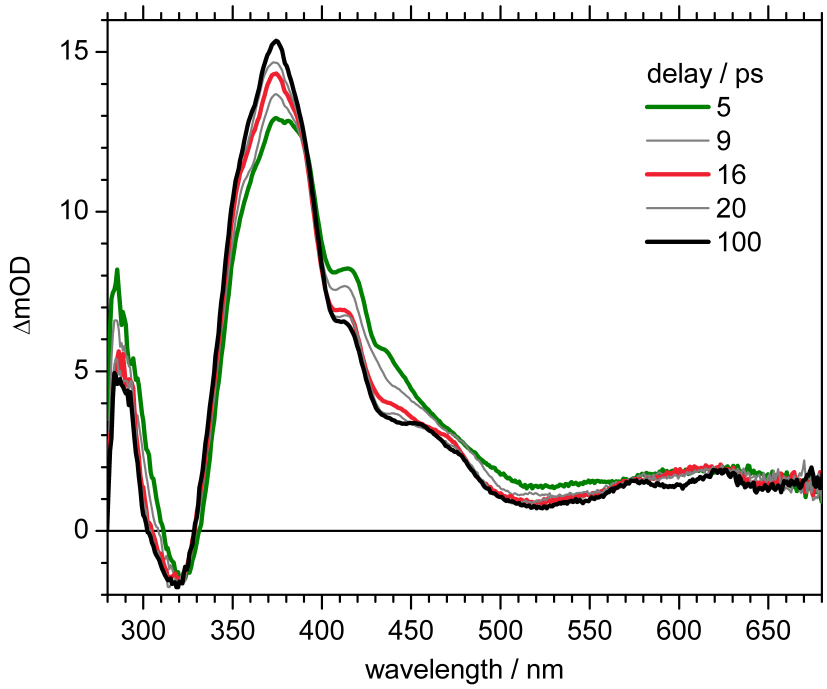

Figure 6.5: Transient absorption of AQ in acetonitrile, excitation at 266 nm, measured in 200 fs steps. Delay times from 5 ps to 100 ps.

in the data by Hamanoue *et al.*[67]. The differences may be explained by (a) use of different solvent, (b) recording at a much lower temperature, and/or (c) a longer delay time of 2 μs instead of 800 ps. Therefore, one can reasonably conclude that the $T_1 \rightarrow T_n$ transition is also responsible for the transient spectrum recorded after 800 ps. Comparison with the spectrum after 340 fs (fig. 6.7) suggests that the transient spectrum is dominated by the triplet absorption already within the first hundreds of femtoseconds. Quantitative analysis suggests that the intersystem crossing proceeds as fast as (160 ± 40) fs - see below, under *Early Dynamics*.

Transients. Figure 6.8 shows representative transient signals of AQ for various wavelength regions. After 20 – 25 ps, all signals remain constant, and for earlier delay times, two time constants seem distinguishable at a first glance, obviously similar for all wavelengths.

Integrated Transients. The decreasing and increasing transients can be merged to give the red and blue transients in figure 6.9, respectively. These two traces seem very much mirror-like and show the same time constant of about 7 ps. This behaviour is rationalized as a vibrational cooling process, in this case within the lowest electronic triplet state. An analogous analysis for anthracene in section 6.2 strongly suggests this interpretation.
In case of mere cooling, the total integrated signal should stay constant, since the whole population remains in the same electronic state, resulting only in a shift of spectral features. The observed slight decrease in the total signal, black in fig. 6.9, is probably a consequence of the limited window of observation.

Early Dynamics. Additional dynamics are found within the first 2 ps. Figure 6.10 shows four transients at selected wavelengths.

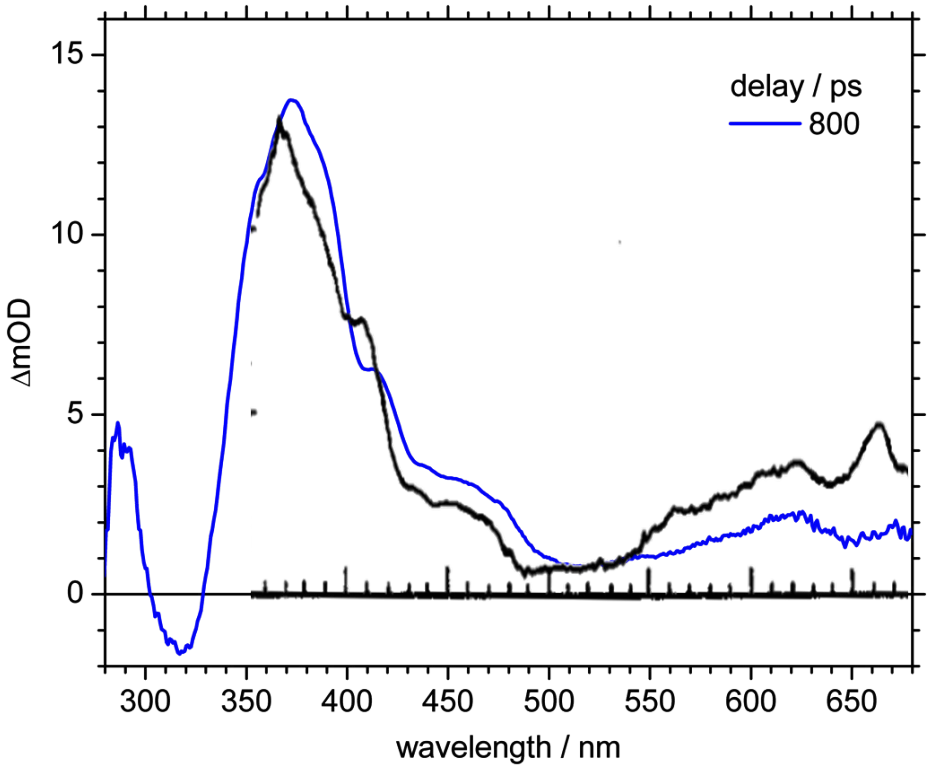

Figure 6.6: Transient absorption of AQ in acetonitrile, excitation at 266 nm, delay time 800 ps (2 ps steps, blue), compared with the transient spectrum after 2 μs (in ETA at 77 K) by Hamanoue *et al.*[67].

Clearly, dynamics are observed within the first 500 fs, after an initial rise with the system response. Around 323 nm, an instantaneous negative bleach signal is expected, and the initially positive contribution must stem from an overlapping early increased absorption signal from excited singlet states. The transients for the presented wavelengths can be compared with the early spectral behavior depicted in figure 6.3.
The decay time of the singlet excited states is estimated by comparison with the system response time given by the solvent signal, as depicted in figure 6.11. The transient at 315 nm shows the instantaneous rise of the excited state absorption with the system response time, and a subsequent decay of the excited state absorption signal with a time constant of (160 ± 60) fs. In the spectral region around 380 nm, an increased absorption signal grows in with the same time constant. This 160 fs time constant is interpreted as the intersystem crossing time, since it is clear from spectral comparison that the triplet-triplet absorption dominates transient spectra already within the first hundreds of femtoseconds (see also fig. 6.7). Hence, the decaying excited singlet state absorption should be due to intersystem crossing to the triplet manifold.

Global Fit. A global fit was performed on the transient AQ data, using the 160 fs time constant determined above as fixed, and two additional shared time constants and a non-decaying offset for all wavelengths. The resulting decay associated spectra (DAS) are shown in figure 6.12. The DAS associated with the time constant of 160 fs shows a maximum around 300 nm, related to excited state absorption (ESA) of AQ, and a rising signal of a new state with a maximum at 375 nm. The two additional time constants from the global fit, (850 ± 200) fs and (19 ± 2) ps, are

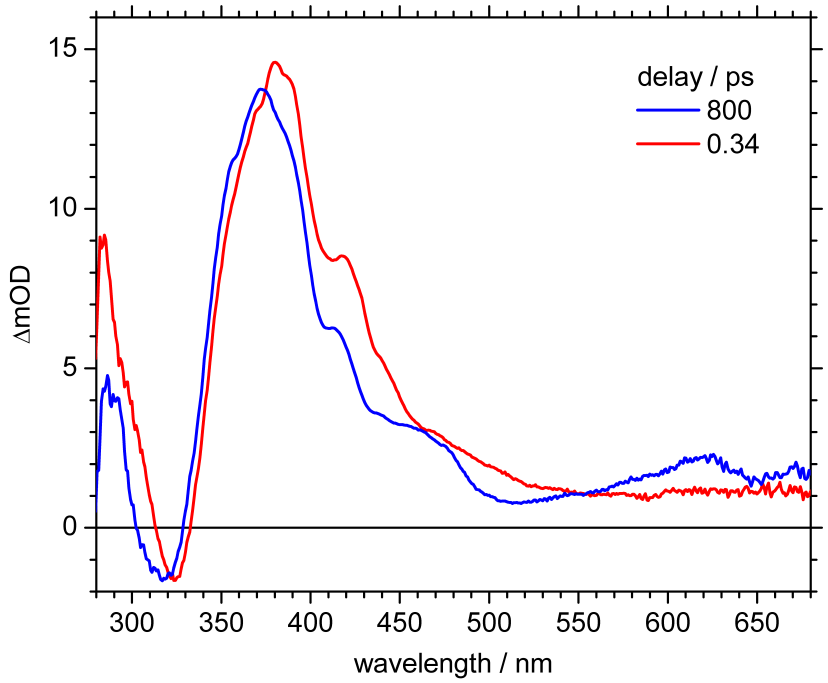

Figure 6.7: Transient absorption of AQ in acetonitrile, excitation at 266 nm. Delay times 800 ps (2 ps steps) and 340 fs (20 fs steps).

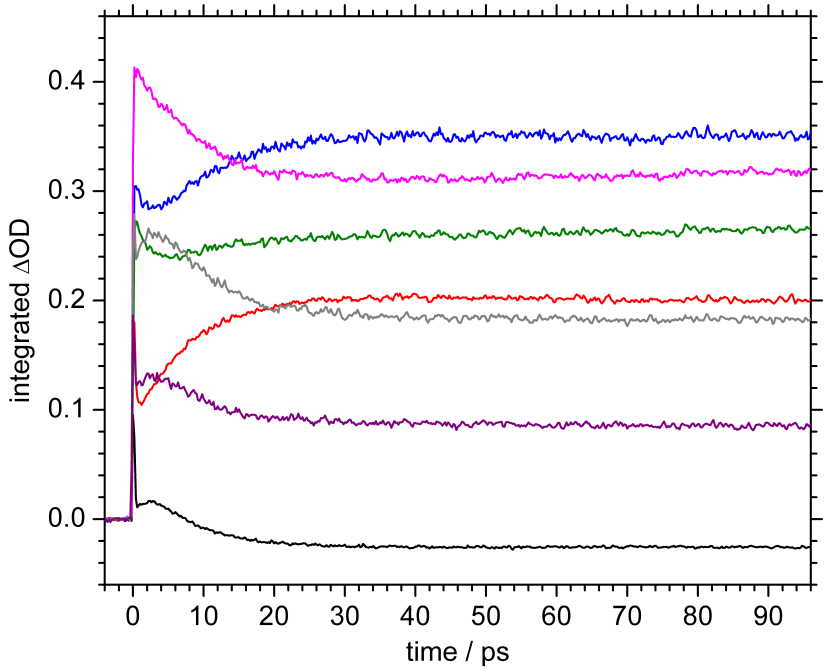

Figure 6.8: Transients of AQ in acetonitrile, excitation at 266 nm, measured in 200 fs steps. Signals are integrated over the following wavelength regions: 300 – 320 nm (black), 320 – 355 nm (red), 355 – 375 nm (blue), 375 – 390 nm (green), 390 – 425 nm (magenta), 425 – 470 nm (grey), and 470 – 520 nm (violet).

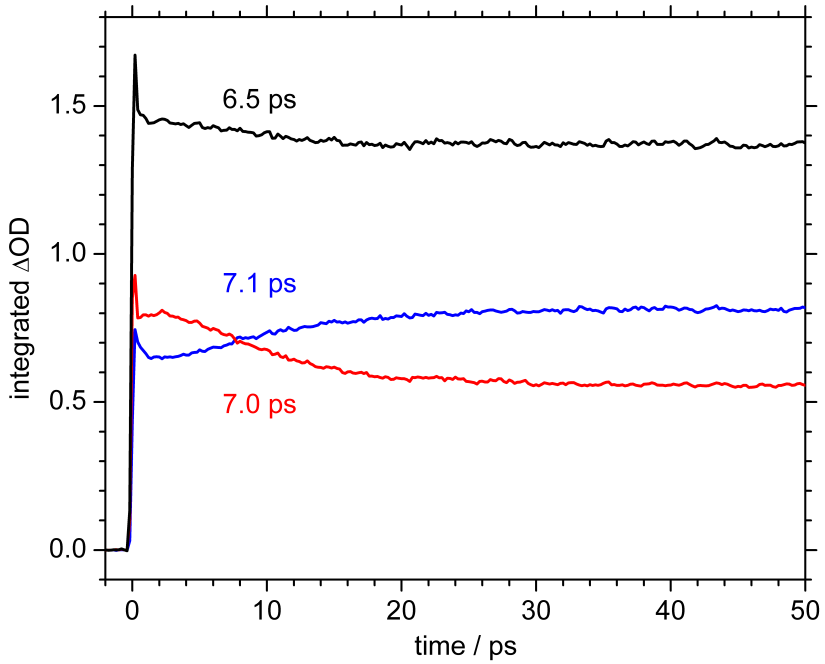

Figure 6.9: Transients of AQ in acetonitrile, excitation at 266 nm, measured in 200 fs steps. Signals are integrated over the wavelength regions where signals are increasing (blue, 7.1 ps) and decreasing (red, 7.0 ps). Additionally, the sum of both rising and decaying signals is shown in black (6.5 ps).

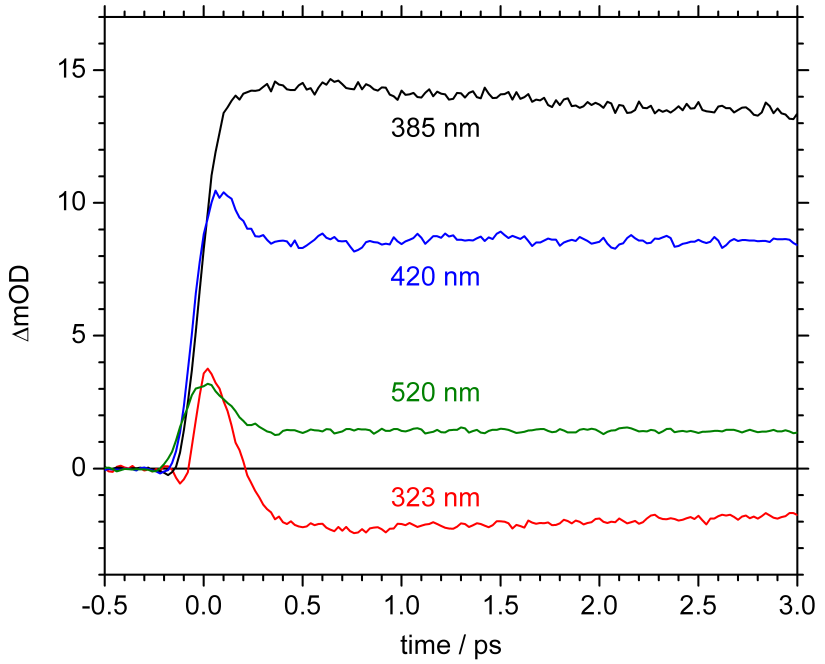

Figure 6.10: Transients of AQ in acetonitrile, excitation at 266 nm, measured in 20 fs steps.

supposed to represent a minor decaying reaction pathway and the cooling of the generated new state, respectively. This new state is concluded to be of triplet character, as the spectral features

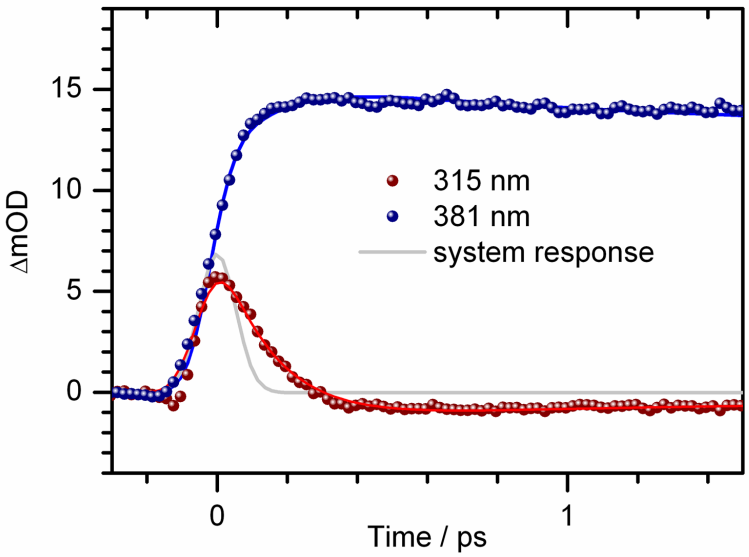

Figure 6.11: Transient of AQ in acetonitrile at 315 nm (red) and 381 nm (blue) (excitation at 266 nm, measured in 20 fs steps). Acetonitrile signal (grey) for comparison.

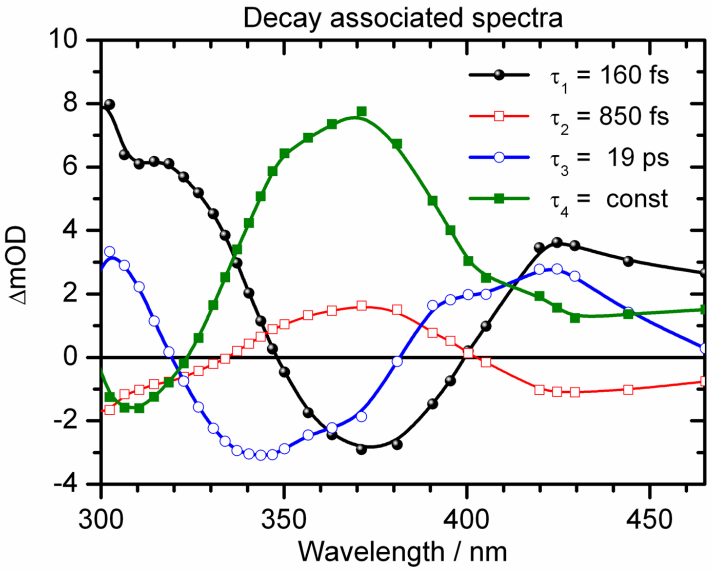

Figure 6.12: Decay associated spectra (DAS) of AQ in acetonitrile (exc. at 266 nm); black: DAS related to (160 ± 60) fs; red: DAS related to (850 ± 200) fs; blue: DAS related to (19 ± 2) ps; green: non-decaying contribution.

appearing within the first hundreds of fs are the same as those assigned to triplet-triplet absorption of AQ (see above). It is not clear, however, what is the origin of the discrepancy between the 7 ps cooling time, determined above from the transients, and the 19 ps cooling time, deduced from the global fit. Probably the numbers from the global fit need to be considered with care.

6.2 Time Resolved Experiments on Anthracene

6.2.1 Transient Data of AC, excitation at 376 nm

Transient Spectra. A comparison of AC transient absorption spectra, 400 fs and 69 ps after excitation at 376 nm, shows only marginal spectral changes, as presented in figure 6.13. The main absorption maximum is slightly more intense after 69 ps and is located at 368 nm. Almost identical bands are found around 550 nm and 600 nm.

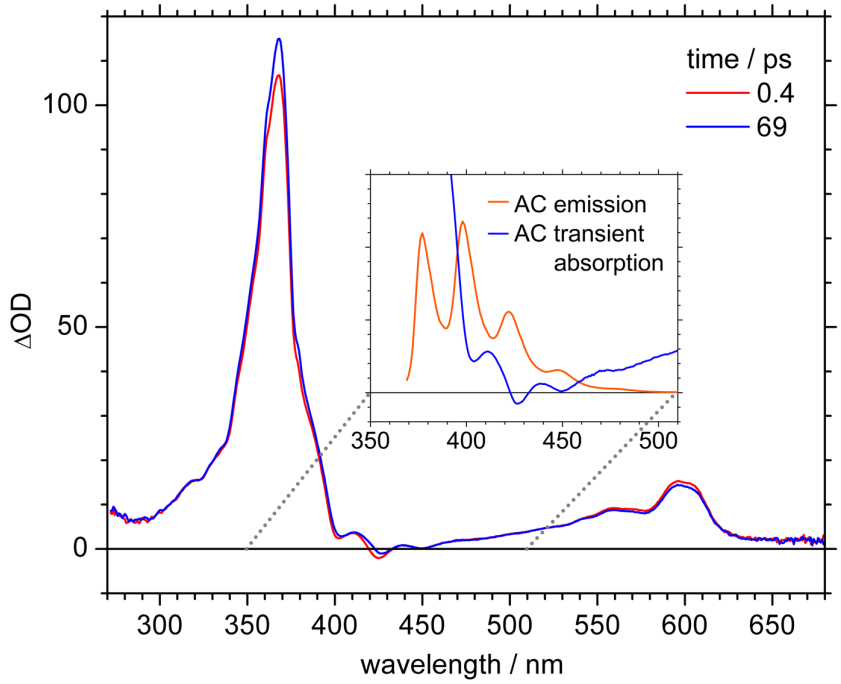

Figure 6.13: Transient absorption of AC in acetonitrile, excitation at 376 nm, and emission spectrum for comparison (Inset).

The negative signal contributions that are observed at 404 nm, 427 nm, and 450 nm are rationalized as stimulated emission (SE, compare fig. 2.12) by comparison with the AC emission spectrum, see inset in figure 6.13. Around 427 nm, the SE contribution leads to an overall negative peak.
The persistence of stimulated emission of AC even after a delay time of 100 ps is as expected, given its 3.7 ns fluorescence lifetime in acetonitrile, presented in section 3.4.4, and is also in agreement with the fluorescence lifetime reported by Jasny and Sepiol[68].

Comparison with Literature. The transient absorption spectrum of anthracene in PMM[2] and 3PM[3] was already presented by Bebelaar in 1974[69] using 2.8 ns pulses at 347 nm. Bebelaar proposed assignments both for the $S_1 \rightarrow S_n$ and for the $T_1 \rightarrow T_n$ transitions.
A comparison is shown in fig. 6.14. The transient spectrum after 69 ps (right panel) exhibits

[2]PMM: polymetyl methacrylate
[3]3MP: 3-methyl pentane

spectral features that are qualitatively identical with those assigned to the $S_1 \rightarrow S_n$ transition by Beblelaar (left panel, solid line). Quantitative variations in relative intensities might be due to differences in solvent, excitation pulse wavelength and duration, and delay time. Based on the presented data, the positive transient absorption signals of AC after excitation at 376 nm are assigned to the $S_1 \rightarrow S_n$ transition.

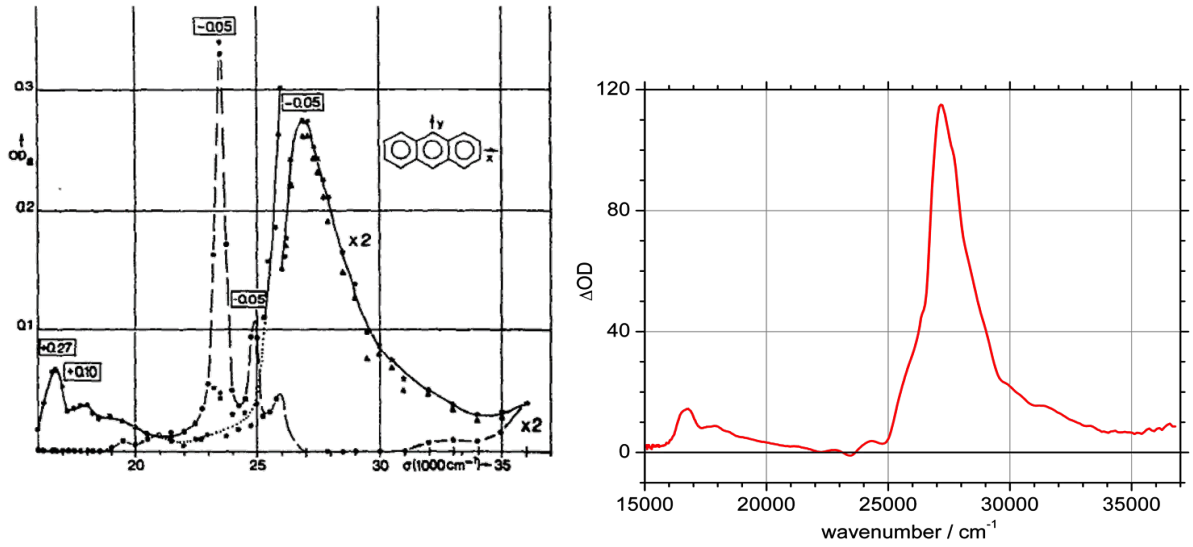

Figure 6.14: Left panel: Transient absorption of AC in PMM[2] ($16\,000 - 26\,000$ cm^{-1}) and 3MP[3] ($26\,000 - 36\,000$ cm^{-1})[69]; right panel: Transient absorption of AC in acetonitrile, 69 ps after excitation at 376 nm.

In summary, upon AC excitation at 376 nm, the early transient spectrum after 400 fs does not change significantly any more and already constitutes the relaxed $S_1 \rightarrow S_n$ absorption spectrum, verifying the assumption that mainly the lowest vibrational state within the electronic S_1 state is pumped at 376 nm.

6.2.2 Transient Data of AC, excitation at 266 nm

Transient Spectra. In contrast to 376 nm, excitation at 266 nm leads to transient spectra that show dynamic changes, as depicted in figure 6.15. Upon excitation at 266 nm, high vibrationally excited levels within the S_1 state of AC are populated, either directly, or through internal conversion after pumping S_2, which has its first absorption peak at 251 nm. The maximal vibrational excess energy that AC can gain this way is calculated[4] to be as much as 11 000 cm^{-1}. The vibrational excess energy in S_1 is expected to result in vibrational relaxation processes (vibrational cooling), showing in the transient spectra as band sharpening and spectral blue-shift[48].
While the main peak at 367 nm (fig. 6.15) increases during the first 100 ps, the shoulder at 379 nm disappears, and signals in the spectral region to longer wavelengths up to 500 nm decrease. Both the bands at 367 nm and at 600 nm show a similar spectral blue shift.
These dynamics can be compared directly to the data shown in figure 6.13, obtained when exciting

[4] Excitation energy: 266 nm $\widehat{=}$ 37 600 cm^{-1}; energy of lowest vibrational level in S_1 (rel. to ground state): 376 nm $\widehat{=}$ 26 600 cm^{-1}; energetic difference: 37 600 cm^{-1} − 26 600 cm^{-1} = 11 000 cm^{-1}.

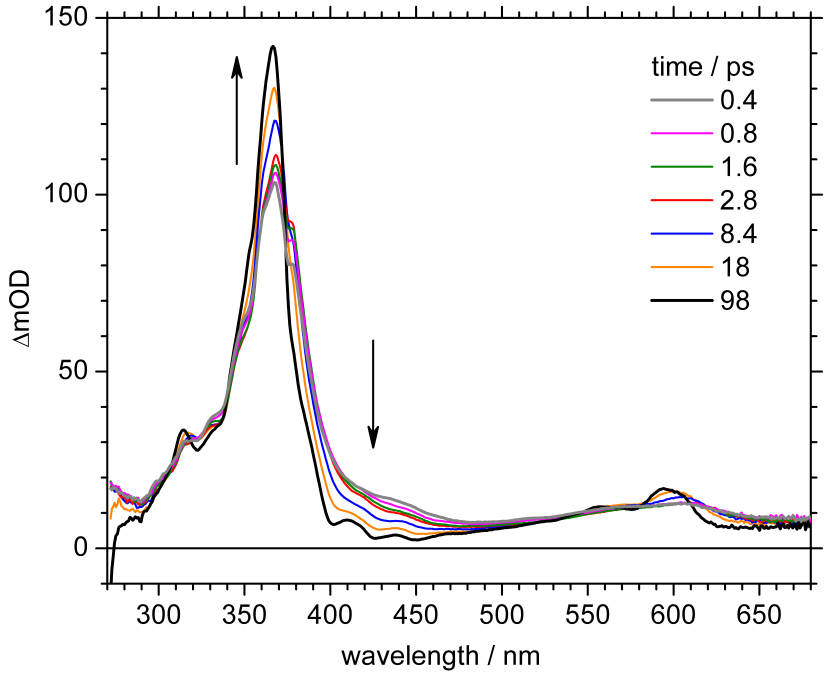

Figure 6.15: Transient absorption of AC in acetonitrile after excitation at 266 nm, delay times between 400 fs (grey) and 98 ps (black).

the AC $S_0 \rightarrow S_1$ 0-0 transition at 376 nm, which exhibit virtually no dynamics even during the first 100 ps. Moreover, the initial spectra with 376 nm excitation are similar to the spectra after 100 ps with 266 nm excitation, as shown in figure 6.16. The dynamics seen with 266 nm excitation is therefore ascribed to vibrational cooling of $\approx 11\,000$ cm^{-1} vibrational excess energy that AC acquires through rapid internal conversion from the higher electronic state, associated with the 251 nm absorption maximum, to the S_1 state.
The tiny peak seen at 314 nm with 266 nm excitation shows no decay within 100 ps and is absent in case of 376 nm excitation. This 314 nm peak is not associated with AC $S_1 \rightarrow S_n$ or AC $T_1 \rightarrow T_n$ absorption[69], and therefore may be related to a photochemical reaction product involving AC or another contamination that absorbs at 266 nm but not at 376 nm. Apart from that, the transient spectra are almost identical, indicating that vibrational relaxation is complete after 70 ps.

Transients. The temporal evolution of the transient absorption signal is depicted in figure 6.17 for some single wavelengths. As can be seen, and is already obvious from the transient absorption spectra in figure 6.15, the transients show different trends, some increase and others decrease in time, depending on the spectral position.

Integrated Transients. The dynamic behavior can be separated into two regions by the isobestic point at 378 nm. Integrated signals for the regions 272 – 378 nm and 378 – 689 nm are shown in figure 6.18, together with the sum of these two integrated signals.
For vibrational cooling processes[48], the total population stays constant, while population from vibrationally excited ("hot") states is transferred to lower vibrational states, finally giving the

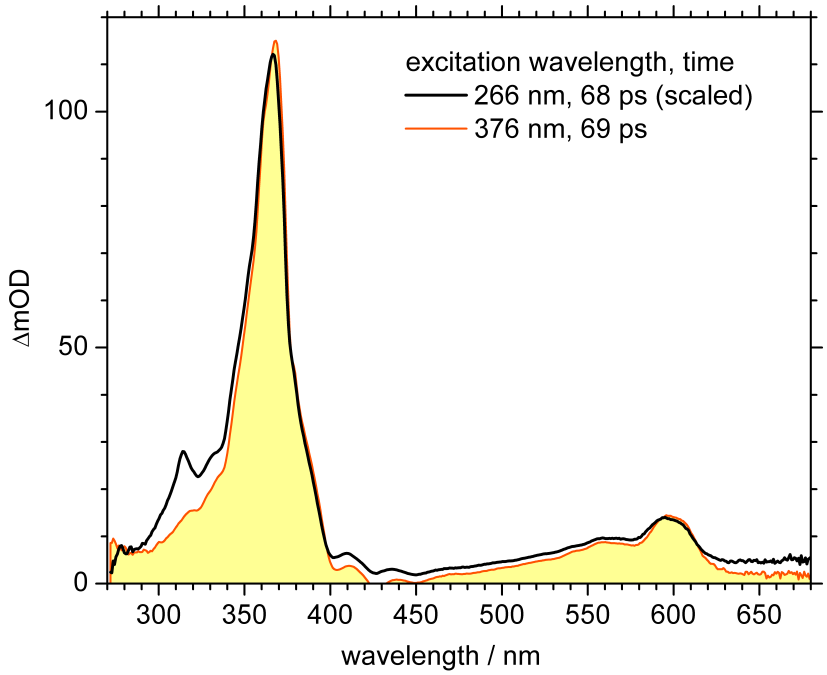

Figure 6.16: Transient absorption of AC in acetonitrile after excitation at 266 nm (black) and 376 nm (orange), in both cases after delay times of 68 – 69 ps.

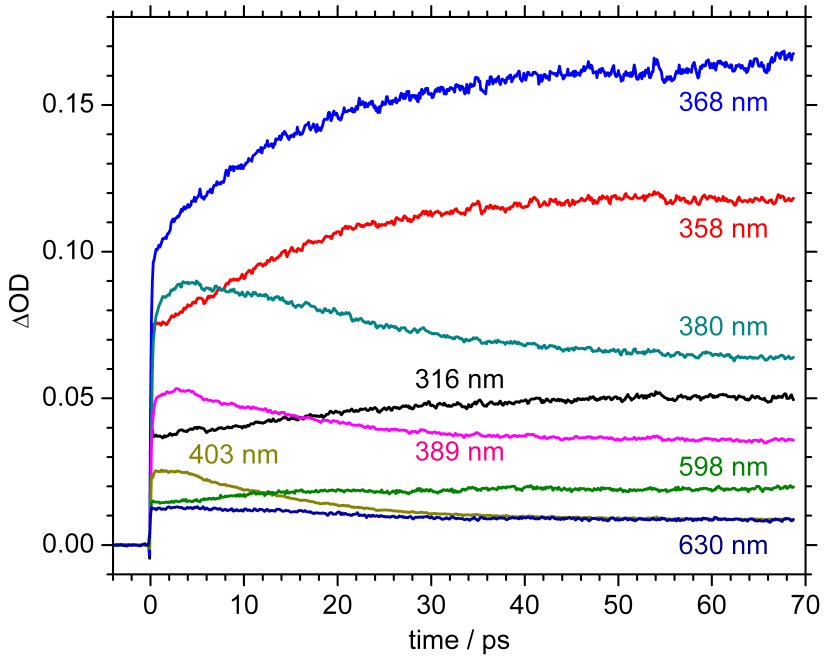

Figure 6.17: Transients for single wavelengths (as indicated) of AC in acetonitrile after excitation at 266 nm.

Boltzmann distribution for the ambient temperature. Therefore, the integrated signal over the whole concerned wavelength range stays constant, and a blue-shift of the excited state absorption is observed (see 2.14, p. 35).

The transients from figure 6.18 can be fitted monoexponentially. For the 272 – 378 nm integrated signal, the dynamics contain a (14 ± 3) ps rising contribution, while the 378 – 698 nm integrated signal contains a (19 ± 3) ps decay component. The sum of both these integrals is nearly at its peak value immediately after excitation, showing only a tiny additional rise with a (4 ± 2) ps time constant, which is too long to be associated with the $S_n \rightarrow S_1$ internal conversion process. Instead this 4 ps component may be indicative of a minor dependence of the electronic dipole moment on excited vibrational states.

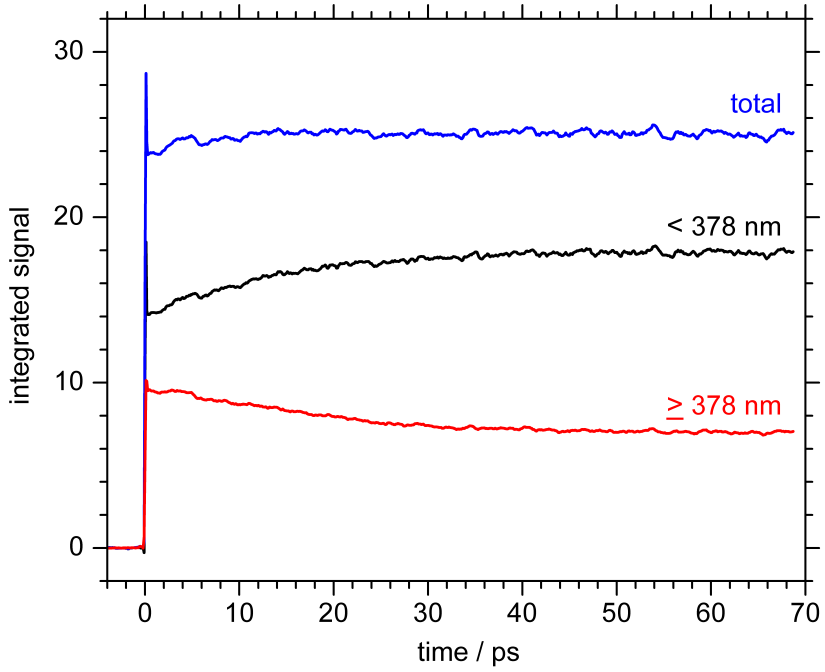

Figure 6.18: Transients for AC in acetonitrile after excitation at 266 nm, integrated for wavelengths above (red, (19 ± 3) ps) and below 378 nm (black, (14 ± 3) ps), together with the sum (blue, (4 ± 2) ps).

6.3 Time Resolved Experiments on APO

6.3.1 Transient Data of APO, excitation at 266 nm

Transient Absorption Spectra. Figure 6.19 shows the transient spectrum of APO upon 266 nm excitation after ≈ 100 ps (blue), which is compared with the corresponding transient spectrum upon 282 nm excitation (dark grey, scaled) and with the transient spectrum of AQ (266 nm excitation, 100 ps, light grey). It seems that the APO-266nm spectrum combines the general appearance of the AQ spectrum with the distinctive peaks of the APO-282nm spectrum, indicating that next to the processes observed at 282 nm, AQ excitation plays a major role. The APO-266nm spectrum can almost completely be reproduced as a sum of the AQ and the APO-282nm spectra (red line in fig. 6.19).

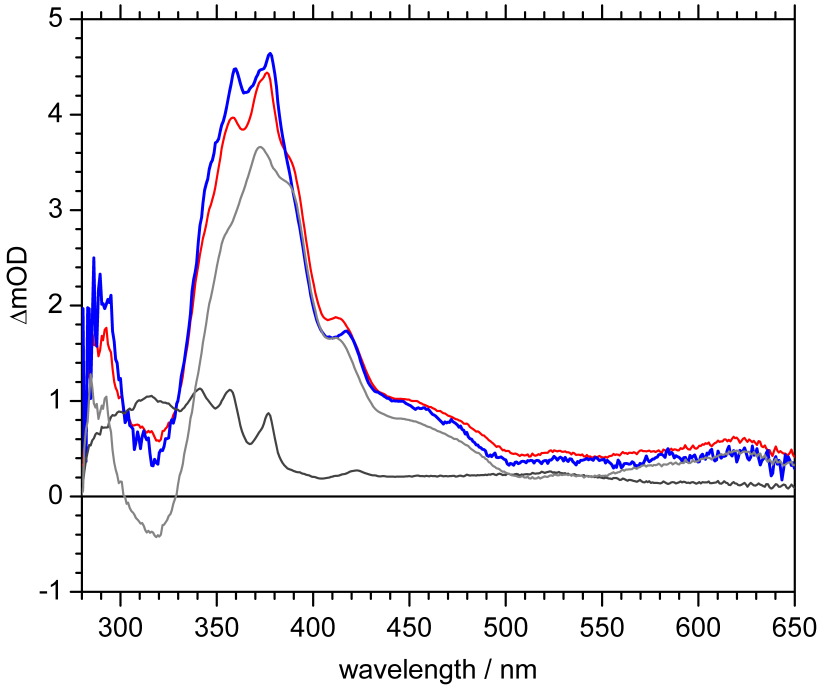

Figure 6.19: Transient absorption spectra of APO and AQ in acetonitrile after 100 ps delay time (excitation wavelengths in brackets). Blue: APO (266 nm); light grey: AQ (266 nm); dark grey: APO (282 nm); red: Sum of the two grey spectra, i.e. the spectrum of APO at 266 nm can be approximated as a sum of the spectra of APO at 282 nm and of AQ at 266 nm.

6.3.2 Transient Data of APO, excitation at 282 nm

Transient Absorption Spectra, 20 fs Steps. Some represenative transient spectra of the short time measurements are depicted in figure 6.20. A band up to ≈ 380 nm is observed, next to a broad signal that spans the whole spectral range up to 650 nm. As these spectra are very noisy and show no assignable spectral features, they are not useful for analysis.

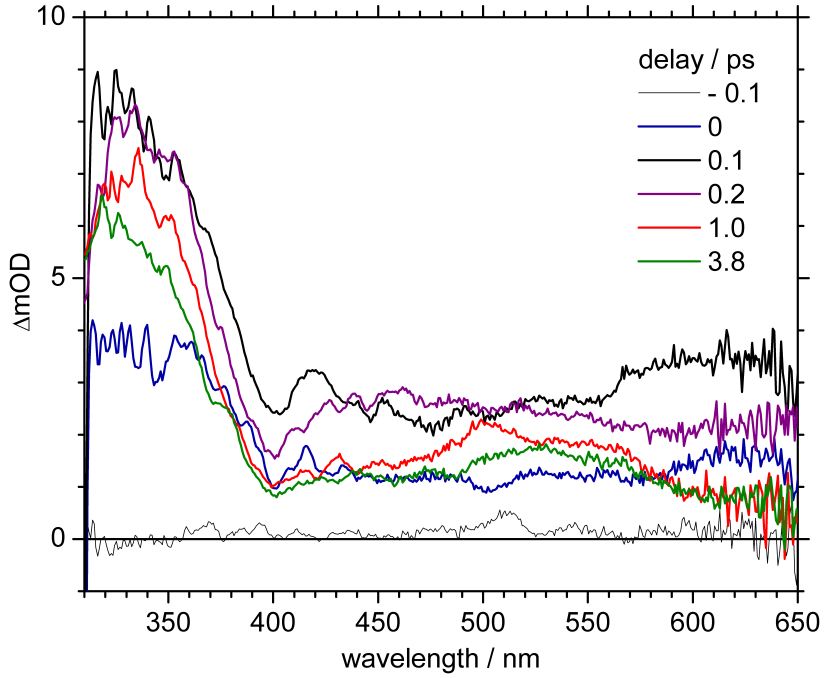

Figure 6.20: Transient absorption spectra of APO in acetonitrile, excitation wavelength 282 nm, after short delay times.

Transient Absorption Spectra, 200 fs Steps. The transient APO spectra following 282 nm excitation in 200 fs steps are depicted in figure 6.21. At early times (< 2 ps), the transient spectra show a broad band around 330 nm, together with a fairly featureless signal extending over the remainder of the detection range, both dropping ≈ 30 % during the first 2 ps. Additional sharper peaks emerge at later times at wavelengths well-known from the AC ground state absorption spectrum, i.e. 341, 358 and 376 nm, as compared in figure 6.26. The peak at 422 nm can be assigned to triplet-triplet absorption from the AC triplet ground state[70]. A comparison is shown in figure 6.22. The spectral blue-shift necessary to shift the peaks from their position in benzene to the position measured upon APO excitation in acetonitrile is indicated by blue arrows; note that the shift reported by Bensasson from benzene to cyclohexane is almost as large.

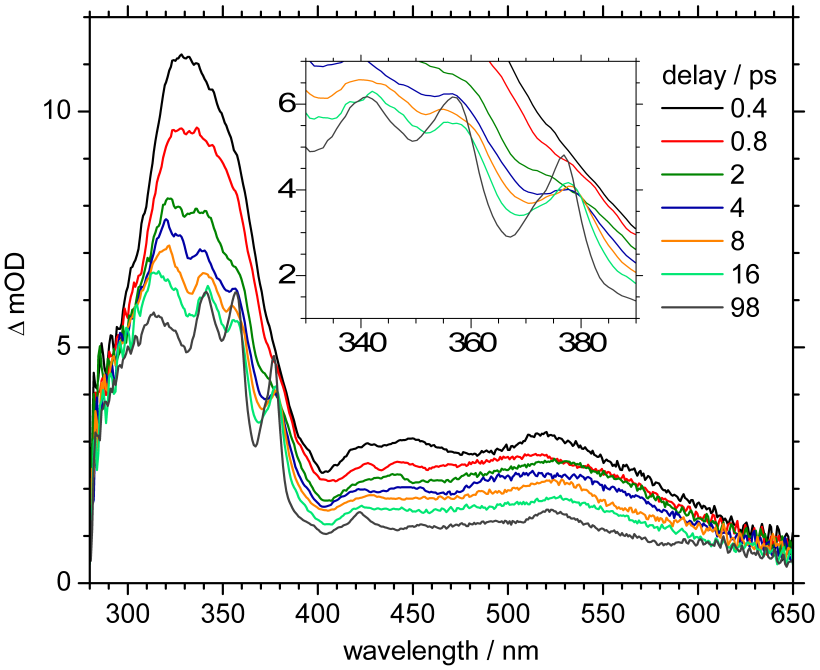

Figure 6.21: Transient absorption spectra of APO in acetonitrile, excitation wavelength 282 nm.

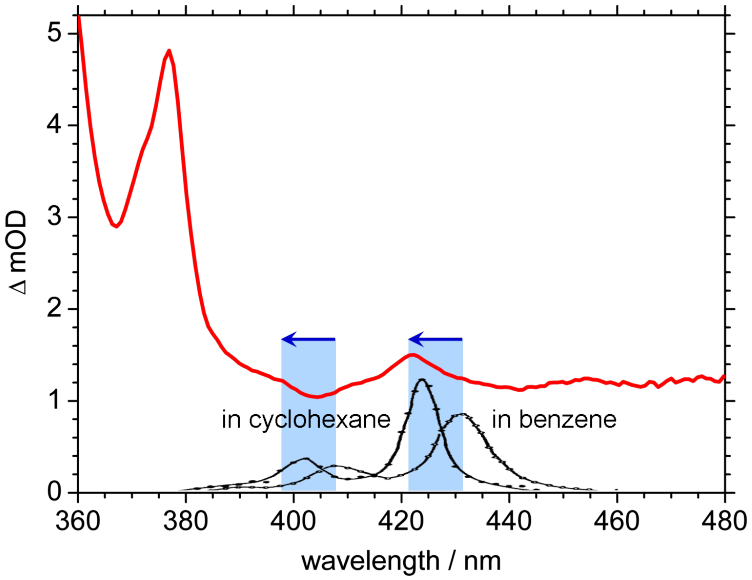

Figure 6.22: Transient absorption spectra of APO in acetonitrile, 98 ps after excitation at 282 nm (red), compared with the triplet-triplet transition of AC reported by Bensasson[70] in benzene and cyclohexane.

Transient Absorption Spectra, Successive Scans. The transient absorption spectra after ≈ 100 ps for ten successive scans are shown in figure 6.23, with the scan number increasing from black to red. An overall approximately linear signal rise is observed, but no new features are discernible. The sharp peaks at 377 nm and 422 nm (both assigned to AC) seem unchanged. The successive scans will be analyzed in section 6.3.3.5.

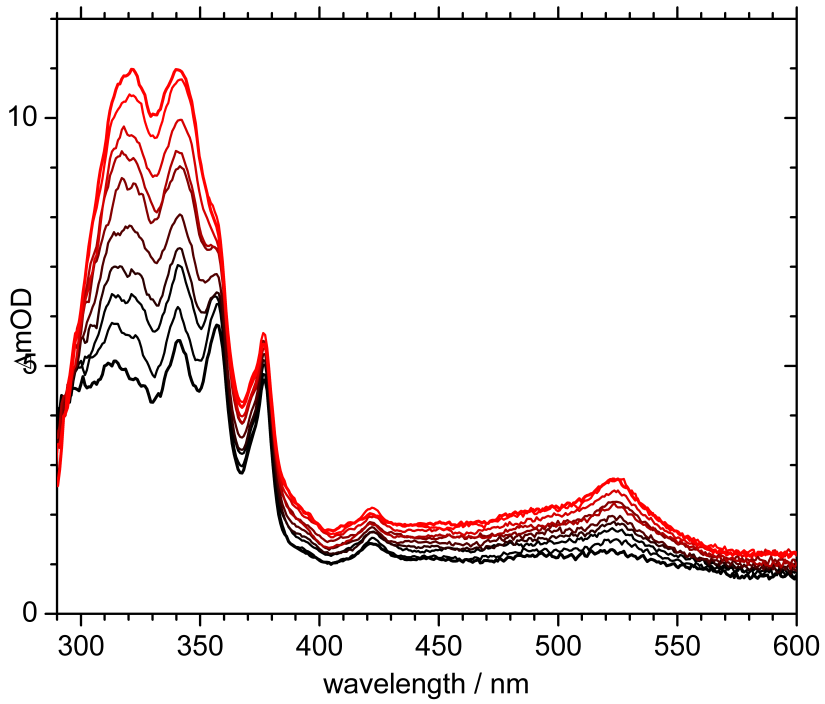

Figure 6.23: Transient absorption spectra of APO in acetonitrile, excitation wavelength 282 nm, after 98 ps; from black to red increasing scan number with the same sample.

Transients. The transient signal evolution for some wavelengths is shown in figure 6.24. Since signal contributions from more than one photoproduct need to be included, the transient signal evolution is difficult to interpret, unless the spectra are disassembled into their components, as is done in the analysis approaches 1 and 2.

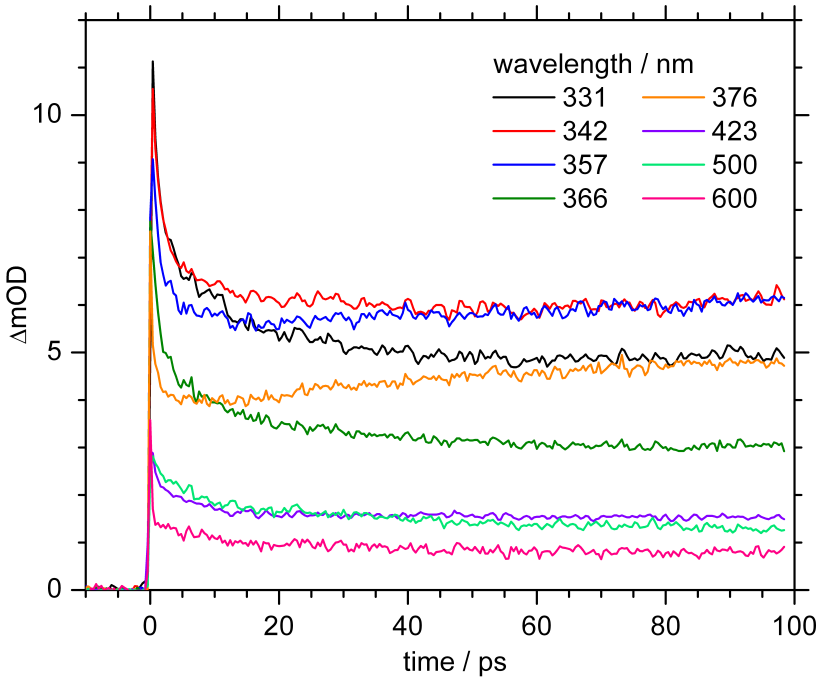

Figure 6.24: Transients of APO in acetonitrile, excitation wavelength 282 nm.

6.3.3 Analysis of Transient APO Data (282 nm exc.)

6.3.3.1 Comparison with Transient Absorption Spectra of AC and AQ

Both AC and AQ could in principal be formed during the measurements on APO, and it is useful to establish whether or not the excitation of generated AC or AQ contributes to the recorded data upon APO excitation.

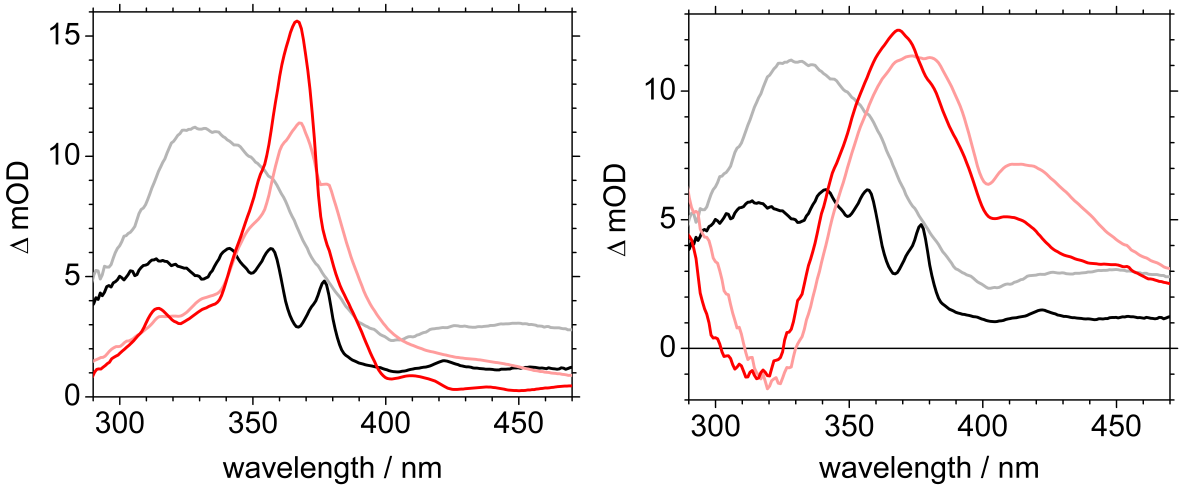

Figure 6.25: Comparison of transient spectra after 0.4 ps (light color) and 98 ps for APO (grey/black) and AC (a) or AQ (b) (light red/red). All measurements in acetonitrile, excitation wavelengths 282 nm (APO) and 266 nm (AQ, AC), respectively.

Comparing the transient data on AC and AQ to the data on APO, as in figure 6.25, it is clear that the most pronounced excited state absorption (ESA) signals of AC and AQ, which are all located in the region of 365 – 380 nm, are not observed in the transient spectra of APO, neither within the first 100 ps of the first scan on a fresh APO sample, nor in later scans on the same APO sample.
Further, spectral features of ground state AC are found in transient APO spectra, and they do not change in consecutive scans. In addition, a peak could be assigned to triplet-triplet absorption of AC, and the amount of triplet is estimated to be around 1 – 2 % of the generated AC.
Of AQ, no spectral features, bleach or other, are found in transient APO spectra at any time.
Spectral signatures other than ground state and triplet AC are supposed to be related to diepoxide (DE), or its presumed precursor, a biradical (BR). The ground state absorption spectrum of the DE is fairly known (fig. 3.12), and no ground state absorption of DE is observed in transient APO spectra. These are valuable pieces of information, and can be interpreted as follows.

1. **Anthracene (AC)**

   - As no ESA of AC is observed in transient APO spectra, it is concluded that no electronic excited AC is found in the sample at any time, i.e. AC is neither generated in an electronic excited state, nor is in later scans previously generated AC excited by the pump pulse.
   - AC is generated in its electronic ground state, as can be seen from the appearence of the characteristic AC absorption bands upon excitation of APO. Only freshly generated AC is observed, proven by the unchanged size of AC peaks in later scans, and the absence of bleach or ESA from excited AC.

   - To a minor extend of $\approx 1 - 2$ %, AC is generated directly in an electronic triplet state, as visible from the peak previously assigned to triplet-triplet absorption of AC.

2. **Anthraquinone (AQ)**

   - The amount of AQ in the APO sample remains unnoticable and hence negligible in all APO data measured upon 282 nm excitation, as no ESA of AQ is observed in transient APO spectra,...

   - ... no ground state absorption of AQ is visible in transient APO spectra, as little as any features that could be related to AQ, like bleach or emission signatures, and ...

   - ... the absence of any signs of AQ persists even after successive scans on the same APO sample.

3. **Diepoxide (DE)**

   - As no ground state absorption of DE is seen in transient APO spectra,...

   - ... DE is supposed to be generated in an electronic excited state (although the ESA of DE is so far unknown), since it is known (from the results in section 5.2.2) that DE must be generated upon 282 nm excitation of APO. This is also verified by comparison of stationary absorption spectra on the APO sample after the time-resolved measurement series, which clearly show DE absorption.

4. **Bicyclic acetal (BA)**

   - According to the results of section 5.2.2, BA is generated upon illumination of DE. As DE, generated during the measurement, does absorb at the excitation wavelength of 282 nm (see fig. 6.2), it seems likely that BA is formed, at least after some time, during the APO measurements.

   - However, no new spectral characteristics arise in successive scans on the same APO sample (fig. 6.23) that had not been visible in the first scan on a fresh APO sample. Therefore, even if BA is generated, it remains unnoticable in transient APO spectra.

Analysis Approaches for Time-Resolved APO Analysis

Four more or less different methods are applied to analyze the APO data upon 282 nm excitation.

- *Analysis Approach 1*: Direct Comparison of AC and APO Data.
  Based on the characteristic AC peaks observed at later times, the AC spectrum at room temperature is fitted at each delay step.

- *Analysis Approach 2*: Temperature Model for AC Spectra.
  A refined model, assuming a monoexponential decay of internal temperature for the AC contribution, thereby facilitating the simulation of early AC spectra.

- *Global Analysis*.
  Without separation of AC and other contributions, a global fit gives not as much information, but the results confirm the findings of the second analysis approach in an independent way.

- *Successive Scans Analyis*.
  In this approach, the spectral changes accumulated after longer illumination periods are analyzed, inherently giving information only about the residual contribution, because the AC part remains unchanged.

Analysis Approaches 1 and 2: Separation of AC Contribution

The transient absorption data of APO excited at 282 nm suggest that AC is formed during the photoreaction in its electronic ground state, recognizable from the characteristic peaks at 341, 358, and 376 nm. A comparison of the late transient absorption spectrum after 100 ps with the stationary absorption spectrum of AC at room temperature (RT) is shown in figure 6.26. Obviously, the AC that was generated from APO in the photoreaciton is cooled down to RT, and the RT spectrum can be subtracted from the transient spectrum to give a residual spectrum (which will be ascribed to DE later on).
Now the question arises how the AC spectra can be *accurately* subtracted from the APO data, especially at earlier times, when the photoproduct AC is still vibrationally hot.

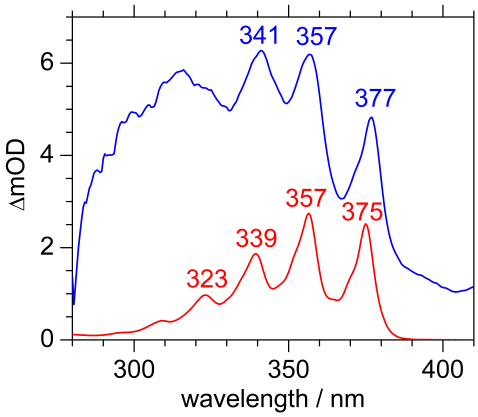

Figure 6.26: Transient absorption spectrum of APO in acetonitrile, delay time ≈ 100 ps, excitation wavelength 282 nm (blue). Stationary absorption spectrum of AC in acetonitrile at RT for comparison in red. Spectral positions of band maxima are given in nm.

6.3.3.2 Analysis Approach 1: Direct Comparison of AC and APO Data

Simulation of AC Spectra. As the characteristic spectral feature of vibrational cooling processes is band narrowing and blue shift, a first approach would be to simulate the AC RT spectrum as superposition of some Gaussian peak functions, and to implement some variables. The function needs to account for variation in band width and spectral position, as well as for the rising AC concentration during AC formation. This function is then fitted to match the AC peaks in the APO data. The most obvious problem of this approach is the tiny size the AC peaks at early times, and furthermore the overlap with much larger transient signals.

Separation of APO Data into AC and Residual Contributions. The result of this analysis attempt is shown in figure 6.28. The simulated AC spectra (fig. 6.28.b) -tiny in the beginning- increase with time up to the final 100 ps spectrum, which is by definition identical with the spectrum at RT. starting Figure 6.28.c shows the residual part, i.e. the result of the subtraction of

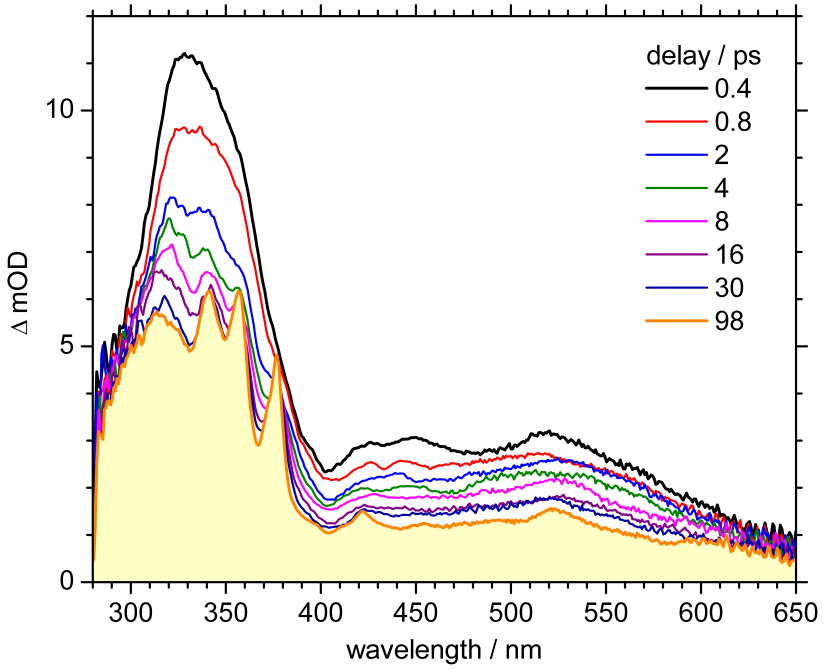

Figure 6.27: Transient absorption spectra of APO in acetonitrile, excitation wavelength 282 nm, delay time as indicated.

the simulated AC spectra (fig. 6.28.b) from the original transient spectra of the APO experiment (fig. 6.28.a). As expected, the residual spectra are quite smooth in the regions of the former AC peaks, which was requested as fit criterion.

Integrated Transients. Since the stationary spectrum of AC at RT lies within $\approx 300 - 400$ nm, the simulated transient AC spectra are located in the same spectral region. Therefore, the separation of the APO data into an AC contribution and a residual contribution is only valid within this spectral range; the wavelength region above 400 nm is not separated. Consequently, integrated transients

are shown in figure 6.28.d for the following signals: (1) AC contribution, 300 – 400 nm; (2) Residual contribution, 300 – 400 nm; (3) 400 – 600 nm (without separation).

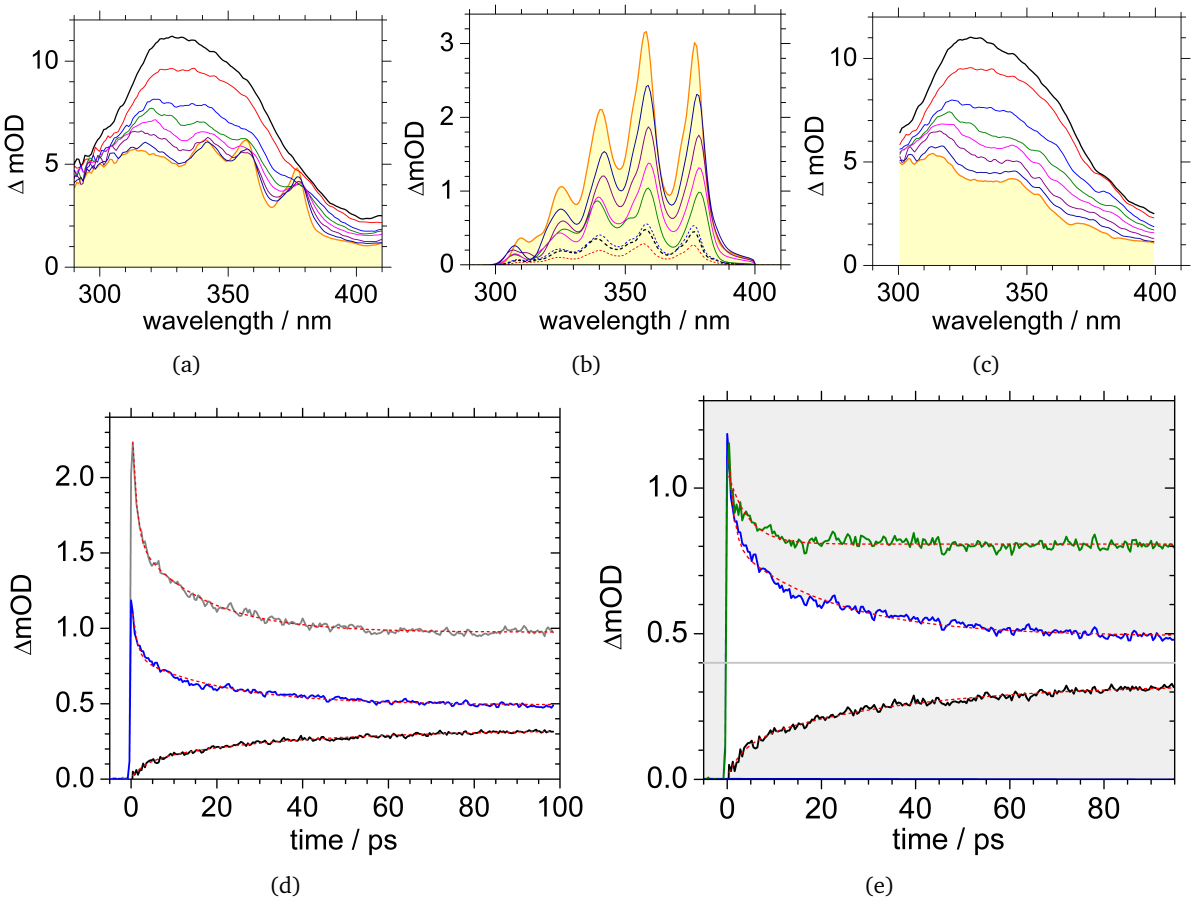

Figure 6.28: (a-c) Transient absorption spectra of APO in acetonitrile between 300 – 400 nm, excitation wavelength 282 nm, delay times as in figure 6.27. (a) Total signal, (b) AC contribution, (c) residual contribution (total minus AC).
(d-e) Integrated transients of APO in acetonitrile, excitation wavelength 282 nm (fits indicated as dotted red lines). Black: AC contribution, 300 – 400 nm (1), bi-exponential fit, $t_1 \approx 3.6$ ps, $t_2 \approx 36$ ps; blue: 400 – 600 nm (2), bi-exponential fit, $t_1 \approx 3.4$ ps, $t_2 \approx 36$ ps; (d) grey: residual contribution, 300 – 400 nm, bi-exponential fit, $t_1 \approx 1.0$ ps, $t_2 \approx 16$ ps; (e) green: sum of (1) and (2), single exponential fit, $t \approx 4.3$ ps.

Exponential Fits. The transients in figure 6.28.d can be fitted exponentially. If fitted mono-exponentially, the resulting time constant for the residual contribution in the region of 300 – 400 nm is ≈ 21 ps. For the AC contribution in 300 – 400 nm and for the (unseparated) data in 400 – 600 nm, the time constants are very similar, both ≈ 35 ps.
The bi-exponetial fits give values of $t_1 \approx 3.6$ ps, $t_2 \approx 36$ ps for AC (300 – 400 nm), $t_1 \approx 3.4$ ps, $t_2 \approx 36$ ps for the 400 – 600 nm region (unseparated), and $t_1 \approx 1.0$ ps, $t_2 \approx 16$ ps for the residual contribution (300 – 400 nm).

Interpretation of Signals in the region of 400 – 600 nm. The astonishingly close time constants for AC (300 – 400 nm) and the signal in the 400 – 600 nm region motivate to think about a relation between the respective signals. As they are mirror-like (figure 6.28.e), it seems not too far-fetched to sum both transients, the result of which is also shown in figure 6.28.e. The mirror-like behavior and the almost flat sum of the two transients strongly reminds of the data of figure 6.18, where the transients characterize the cooling process within the excited state of AC upon 266 nm excitation. Presuming the same reasoning for the transients of figure 6.28.e would lead to the assumption that the signals in the 400 – 600 nm region correspond to vibrationally excited states of AC, which are shifted into the 300 – 400 nm region during the vibrational relaxation of AC. This would imply a huge blue-shift during the cooling process, induced by initial population of extremely high-lying vibrational states. Whether or not this explanation holds cannot be proven, but arguments both pro and contra will be presented in the following paragraphs.

Arguments Supporting High Vibrational AC States in the 400 – 600 nm Region

The vibrational structure of the AC absorption spectrum in the gas phase at 428 K is depicted in figure 6.29.a (blue line). The maximum with the longest wavelength, i.e. the lowest energy, corresponds to the transition from the lowest vibrational level ($v = 0$) in the electronic ground state into the lowest vibrational level ($v' = 0$) in the first electronic excited state. Under the assumption that only the vibrational ground state $v = 0$ is populated, the tranisitons $0 \rightarrow 0$, $0 \rightarrow 1$, $0 \rightarrow 2$, $\ldots$ $0 \rightarrow n$ are possible, as illustrated in figure 6.29.b. According to the Franck-Condon-Principle[5], significant transition probability exists only for a limited number n of final vibrational states v', because the overlap integral vanishes for high levels.

When the first vibrationally excited state $v = 1$ of the initial electronic state is also populated, additional transitions $1 \rightarrow 1$, $1 \rightarrow 2$, $\ldots$ $1 \rightarrow n$ contribute to the spectrum. If the vibrational states had identical spacings in both electronic states, no difference would be observed in the absorption spectrum. However, due to different anharmonicities[6] in different electronic states, the vibrational spacings differ, and the transitions $0 \rightarrow 0$ and $1 \rightarrow 1$ (or $0 \rightarrow 1$ and $1 \rightarrow 2$, $\ldots$) have not exactly the same energy, as indicated in figure 6.29.b. Consequently, as the $0 \rightarrow 0$ band, for instance, is a superposition of bands with slightly different energies, the band is spectrally broadend. And further, because the additional transitions tend to have lower energies, the band is red-shifted with higher temperatures. This behavior is illustrated by the red line in figure 6.29.a, which corresponds to the AC absorption spectrum in the gas phase at 750 K.

Moreover, another effect upon population of higher vibrational states v need to be taken into accout. For $v = n$, apart from $n \rightarrow n+1$, $n \rightarrow n+2$, $\ldots$, transitions to *lower* vibrational states are possible: $n \rightarrow n-1$, $n \rightarrow n-2$, $\ldots$, e.g. $1 \rightarrow 0$ for $v = 1$, $2 \rightarrow 1$ and $2 \rightarrow 0$ for $v = 2$, etc. These vibrational transitions are indicated in yellow and red in figure 6.29.b, and they do not shift the existing vibronic bands, but they consitute *new* absorption bands that could only be observed if higher vibrational states are *significantly* populated.

[5] Franck-Condon Transition: The motions of the nuclei are assumed to be slow compared with the motions of the electrons, so that electronic transitions are "vertical" within the potential of the nuclei. Hence, the transition intensity depends on the probablitiy to find the electron *in the same nuclear configuration* in the final state as it was in the initial state, represented by the overlap integral.

[6] Anharmonicity means that vibrations are not sufficiently described by the harmonic oscillator model, and a consequence is the decreasing energy spacing between vibrational levels. Furthermore, the spacings tend to be smaller in higher electronic states. Both effects are illustrated in figure 6.29.

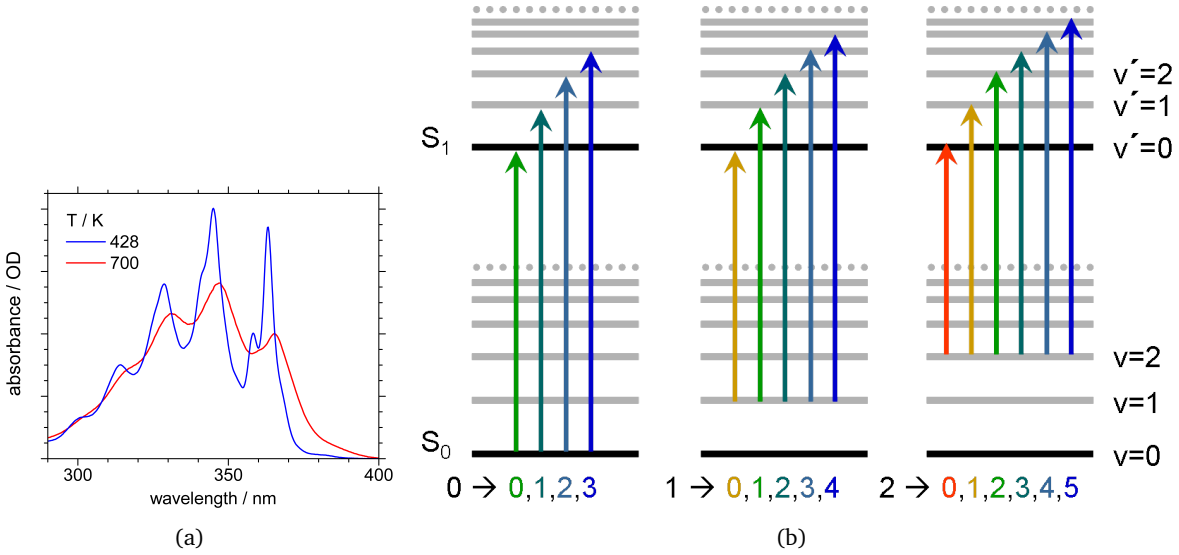

(a) (b)

Figure 6.29: (a) Stationary absorpion spectra of AC in gas phase, at 428 K (155 °C, blue) and 700 K (427 °C, red). (b) Left: Schematic illustration of the origin of the vibrational structure of absorption spectra. Middle and right: Schematic illustration of the origin of the broadening, the red-shift, and the emergence of new lower-energy transitions (yellow and red arrows) upon population of higher vibrational levels in the electronic ground state.

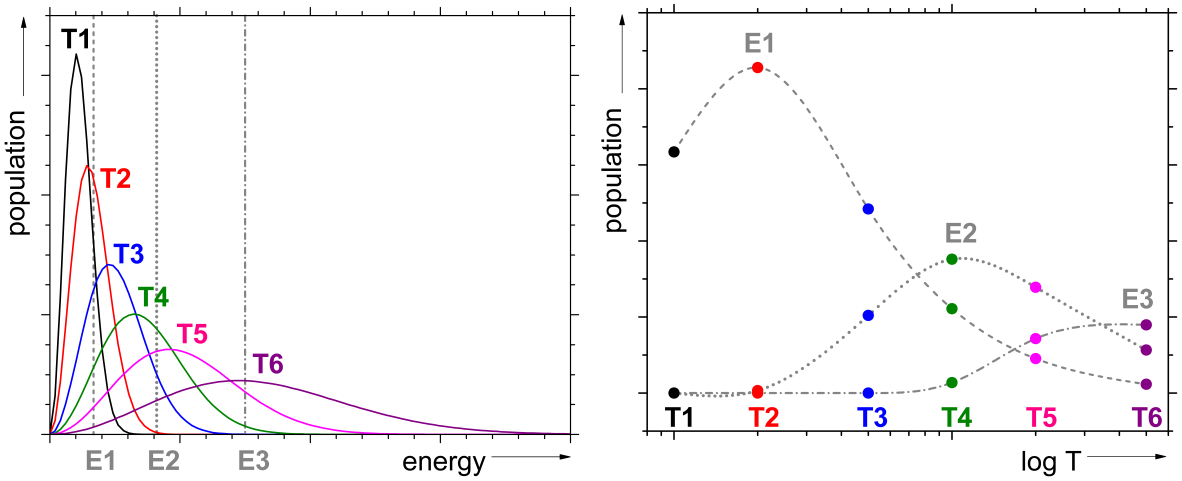

(a) (b)

Figure 6.30: (a) Boltzmann distribution: Population of energy levels, exemplary for temperatures T1...T6 (100, 200, 500, 1000, 2000, and 5000 K). The higher the temperature, the more energy levels are occupied. (b) Population of energy levels E1, E2, E3 indicated in (a) as function of (logarithmic) temperature. High temperatures are required to give considerable contributions of higher energy levels.

The bands observed in the 400 – 600 nm region in the transient APO data could be due to such new low-energy transitions from high-lying vibrational states, which might be populated during the photochemical formation of AC.

Arguments Against High Vibrational AC States in the 400 – 600 nm Region
The population distribution within the vibrational states of one electronic state *in thermal equilibrium* is given by the Boltzmann distribution, illustrated in figure 6.30.a:

$$N_a = N_0 \cdot g_a \cdot e^{-\Delta E/k_B T}$$

(with N_a - population of (here: vibrational) state a; N_0 - population of the (vibrational) ground state; g_a - degree of degeneracy; k_B - Boltzmann constant[7]; $\Delta E = E_a - E_0$ - Energy of state a (E_a) relative to (vibrational) ground state with Energy E_0.)
High vibrational states are populated only at high temperatures, and even then it is only a minor part of the total population, as visible in figure 6.30.b, where the exemplified temperatures are 100, 200, 500, 1000, 2000, and 5000 K. Strictly speaking, this only holds for a thermal equilibrium situation. However, if the photochemical process forms AC to a large part in high-lying vibrational states, this non-equilibrium distribution would very rapidly decay into an equilibrium distribution, leaving no *significant* population of high vibrational states.

In conclusion, it might be possible that new transitions from high-lying vibrational states of AC could be observed in spectral regions above 400 nm, but the responsible population should rapidly relax into an equilibrium distribution corresponding to a high (internal) temperature, so that even initially observable transitions should decay fast – presumably much faster than the 35 ps decay time observed for the signals in the 400 – 600 nm region.

6.3.3.3 Analysis Approach 2: Temperature Model for AC Spectra

Thermal Equilibrium Distribution. Based on the arguments above, it can be assumed that thermal equilibrium distributions are reached very rapidly after AC formation, leading to a situation equivalent to a certain -internal- temperature. During the vibrational relaxation, or cooling process, the thermal equilibrium distributions corresponding to decreasing temperatures are involved, until the final RT distribution is reached after complete relaxation.

New Temperature-Based Model for AC Spectra[8]
Assuming thermal equilibrium distributions at all times during vibrational relaxation of AC, it appears reasonable to model the transient AC spectra based on the AC spectrum at RT after adaptation to initially high and subsequently decreasing temperatures. The parameters needed are the shift $\delta\nu$ of the spectral position ν, and the broadening Δ of the spectral width.
To calibrate the relationship between the temperature T and the spectral broadening parameter Δ, AC spectra measured at various temperatures are used. As the temperature range for spectra in acetonitrile is limited by the evaporation temperature of the solvent (82 °C), gas phase spectra

[7] $k_B = 1.38066 \cdot 10^{-23} JK^{-1}$

[8] Calculations involved in this modelling were done by Dr. S. Kovalenko and Dr. A. Dobryakov from the research group of Prof. N. P. Ernsting at the Chemistry Institute of the Humboldt Universität zu Berlin, in a cooperation within the Collaborative Research Center (Sonderforschungsbereich) SFB450 of the German Research Foundation (Deutsche Forschungsgemeinschaft DFG).

are used at higher temperatures, shown in figure 6.31.a. For direct comparison with spectra in acetonitrile, they need to be corrected for the broadening due to solvent interaction, which is done by broadening using the empirical value of 120 cm^{-1}. Next, the spectra at higher T can be modelled by convolution of the RT spectrum $AC(RT)$ with a broadening function F:

$$AC(T,\nu) \otimes F(\Delta,\delta\nu) = AC(T,\nu+\delta\nu)$$

with T - temperature; ν - spectral position; $\otimes$ - convolution; Δ - spectral broadening; $\delta\nu$ - spectral shift. The broadening function is defined as

$$F(\Delta,\delta\nu) = \frac{1}{2}\left(\frac{\Delta}{\pi}\frac{1}{(\nu+\delta\nu)^2} + \frac{1}{\pi\Delta}\frac{1}{\cosh((\nu+\delta\nu)/\Delta)}\right) \tag{6.1}$$

The time dependence of the broadening Δ and shift $\delta\nu$ describes the vibrational cooling process. From AC spectra in the temperature range 283 – 700 K, a linear correlation can be deduced between the spectral broadening and the temperature, as presented in figure 6.31.b, and the time-dependent molecular temperature can be obtained.

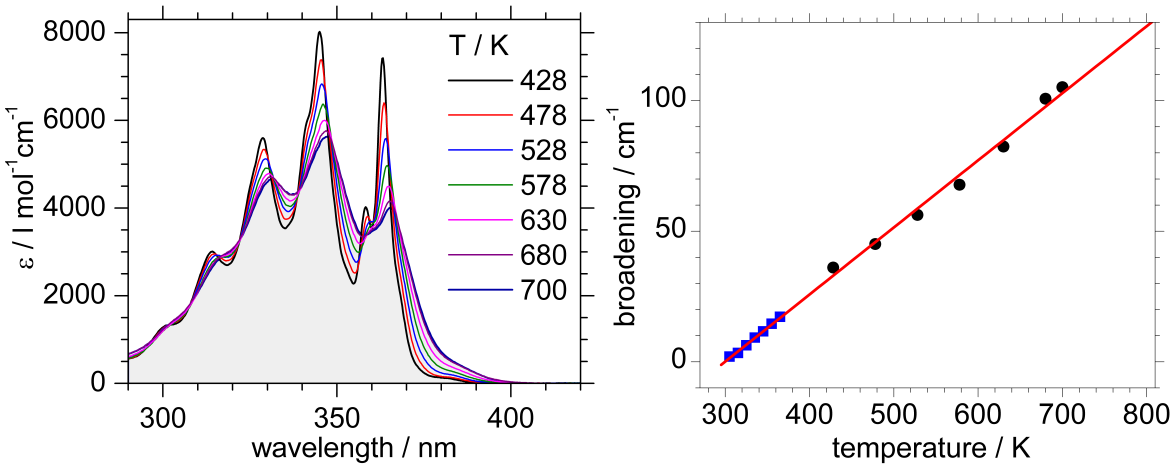

(a) (b)

Figure 6.31: (a) Gas phase absorption spectra (extinction coefficient) of AC, temperatures between 428 K (155 °C, black line) and 700 K (427 °C, grey area).
(b) Broadening Δ as a function of temperature. - Black circles: gas-phase AC data, corrected for solvent broadening; blue squares: AC in acetonitrile, 10 – 80 °C; red line: linear fit ($\Delta(T) = a + b \cdot T$, $b = 0.26$ cm^{-1}/K.

Modelling of APO Spectra. The overall transient signal is decomposed into an AC contribution and a residual signal

$$APO(\nu,t) = n(t) \cdot AC(\nu,t) + \text{residual}(\nu,t) \tag{6.2}$$

The residual(ν,t) is described by a multipeak lognormal function without additional specification. $n(t)$ is a concentration factor that describes the overall formation of AC as a function of time. In a first step, $n(t)$ is set to be constant and equal to the final amount of AC after 98 ps, assuming an instantaneous rise of AC: $n(t) = n(98\text{ ps})$.

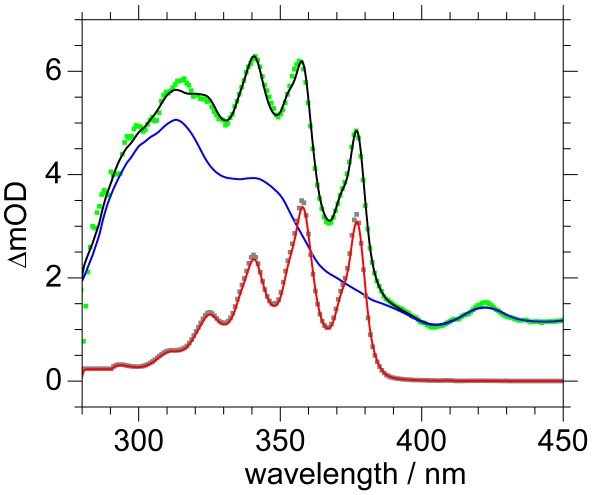

Figure 6.32: Transient absorption spectrum of APO (excitation 282 nm) after 98 ps (green, fit black) and its decomposition into the AC spectrum at RT (grey, fit red) and a residual contribution (blue).

The hot anthracene contribution $AC(\nu,t)$ at arbitrary delay times t is modelled by convolution of the spectrum at room temperature $AC(\nu,RT)$ with the broadening function of equation 6.1:

$$AC(\nu,t) = AC(\nu,RT) \otimes F(\Delta,\delta\nu) \tag{6.3}$$

The decomposition of the transient spectrum at $t = 98$ ps is shown in figure 6.32. The measured spectrum (green/black) is separated into a component $AC(t = 98\text{ ps})$ due to AC in the electronic ground state (grey/red) and a residual (blue). The AC absorption spectrum measured at RT in acetonitrile $AC(RT)$ is compared with the extracted $AC(t = 98\text{ ps})$ contribution to verify that the last AC spectrum is cold, i.e. $AC(t = 98\text{ ps}) = AC(RT)$.

Non-Instantaneous AC Rise. So far the concentration of the photogenerated (hot) AC was assumed to be constant, $n(t) = n(98\text{ps})$. In general a rise is expected; this possibility will be explored in a second, refined model. The AC concentration $n(t) \leq n(98\text{ps})$ is assumed to rise

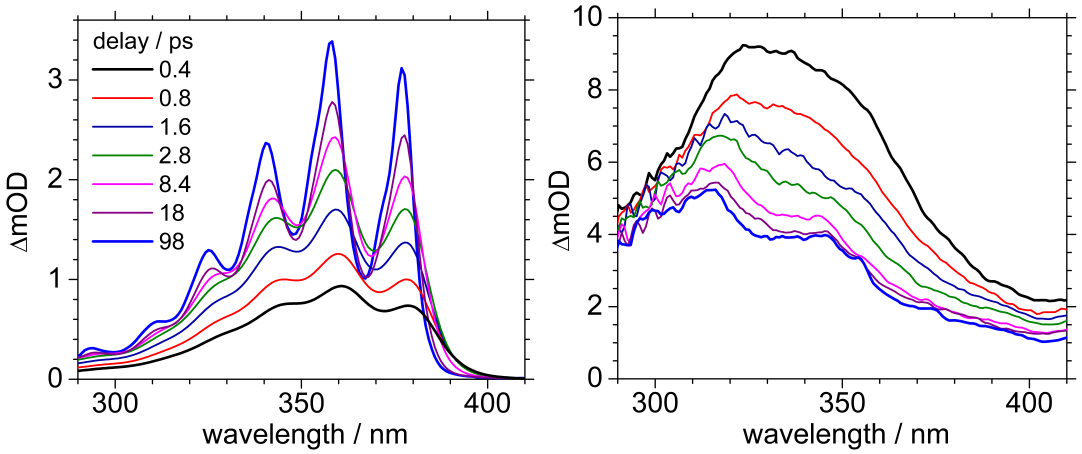

(a) (b)

Figure 6.33: (a) AC contribution to the transient APO spectra according to the refined model with rising AC concentration, delay times as indicated. (b) The residual contribution after subtraction of the AC contribution shown in (a) from the total measured signal.

monotonically. The parameters $\Delta(t)$ from the previous fit are used as a starting point. The quality of the new fit is required to be at least as good as the previous fit, i.e. $\chi^2[n(t) \leq n(98\text{ps})] \leq \chi^2[n(t) = n(98\text{ps})]$. In this way the time-dependent $n(t)$ and $\Delta(t)$ parameters are extracted simultaneously. The decomposition of the transient APO spectra into a temperature dependent AC contribution and the corresponding residual is shown in figure 6.33. In figure 6.34, the decomposed spectra are given for some delay times, and the molecular (or internal) temperature values are indicated relative to RT, which is approached after 98 ps.

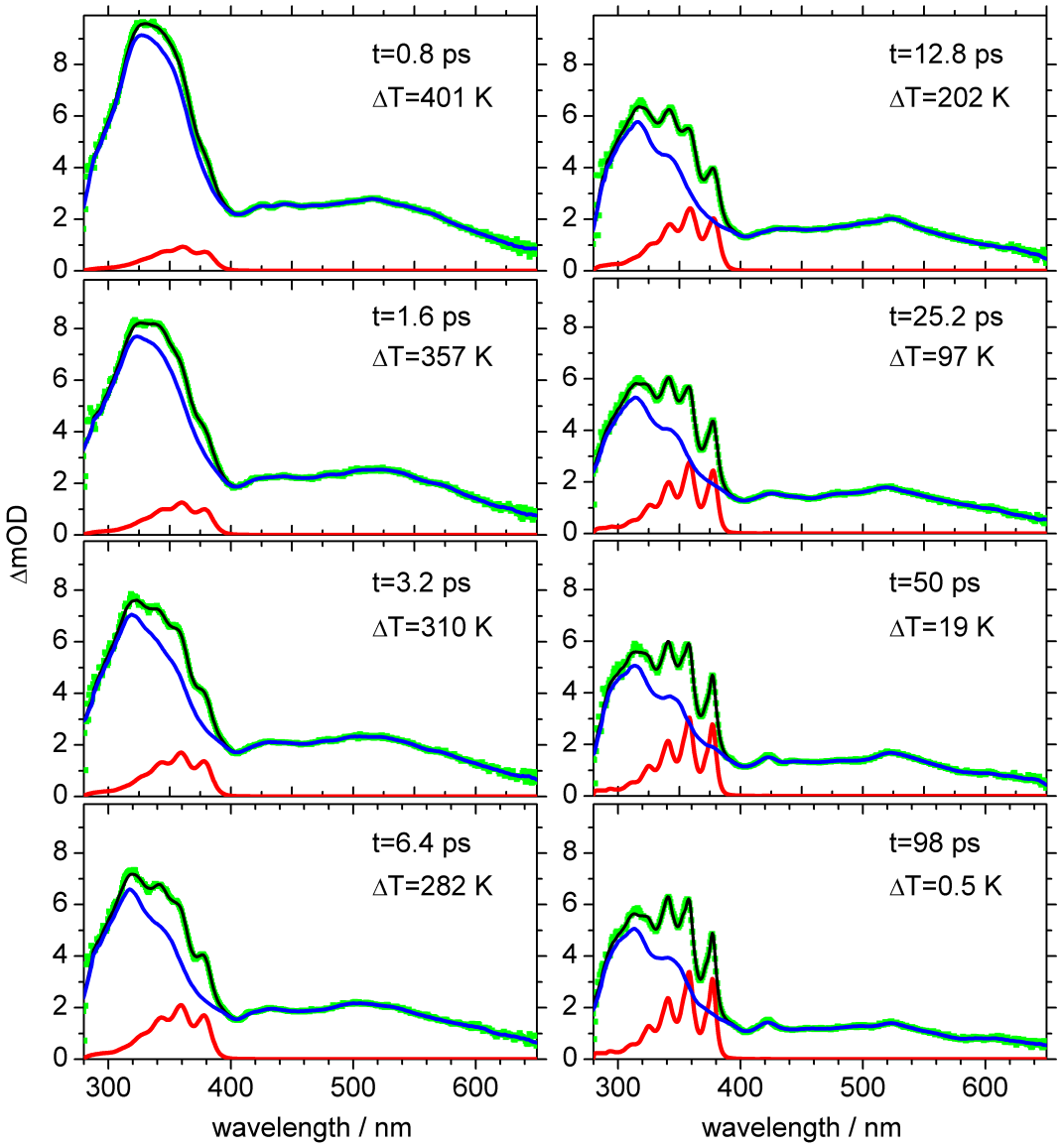

Figure 6.34: Transient absorption spectra of APO (excitation 282 nm) after eight delay times (green, fit black) and its decomposition into the AC spectrum at RT (red) and a residual contribution (blue).

Transient Temperature. The decay of the internal temperature is plotted in figure 6.35. While (a) shows the the result for the assumption of constant AC concentration, a rising AC concentration is considered in case (b). The monoexponential fits give similar time constants of (a) 17.4 ps and (b) 18.7 ps for the vibrational cooling process.
The monoexponential temperature decay can be explained as an indication of weak solute-solvent coupling[48], according to the following equation (with C - molecular heat capacity; $T_0 = 295K$ (RT); β - strength of solute-solvent coupling: $C\,d\,T/d\,t = -\beta(T - T_0)$

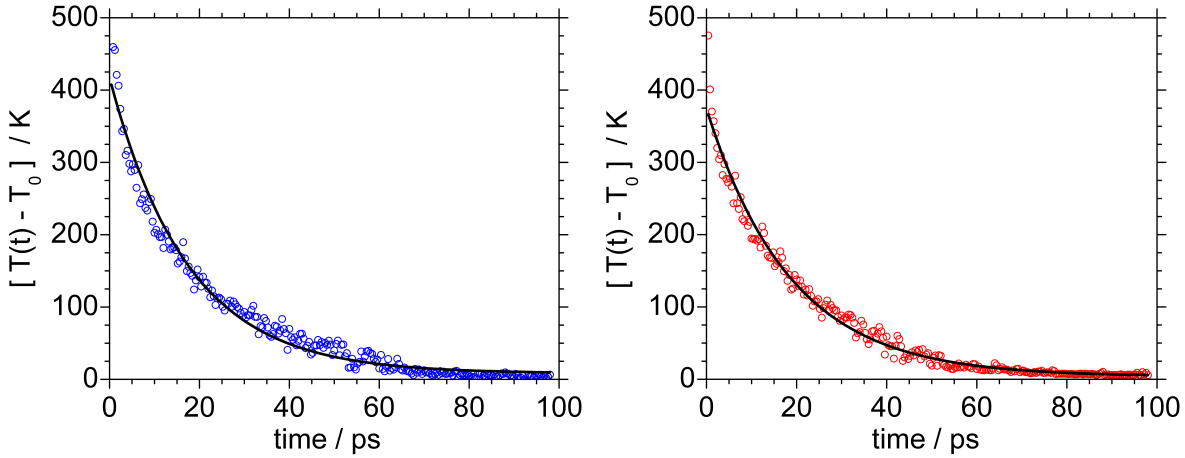

Figure 6.35: Time-dependent temperature decay, (a) for $n(t) = n(98ps)$, i.e. constant AC concentration; (b) for rising AC concentration ($n(t) \leq n(98ps)$). Black line: monoexponential fits, (a) 17.4 ps, (b) 18.7 ps.

Anthracene Rise. The rise of the AC concentration is shown in red in figure 6.36, together with a monoexponential fit of 2.8 ps (black).

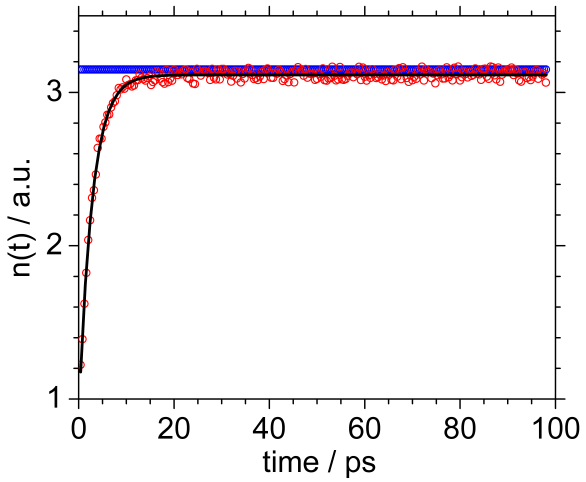

Figure 6.36: Time-dependent concentration; blue: constant concentration $n(t) = n(98ps)$; red: increasing concentration $n(t) \leq n(98ps)$; black: monoexponential fit: 2.8 ps.

Residual – Transient Absorption Signal

Another result of this analysis, next to the AC behavior, is the transient absorption development of the residual contribution. As seen in figure 6.33, the residual signal, after subtraction of the AC contribution from the total signal, shows smooth spectra with an emerging doublepeak structure at later times, and an overall signal decrease. The integrated transient is depicted in figure 6.37; it can be fitted biexponentially with 1.5 ps and 21 ps. A deeper investigation of the residual signal will follow in the *Successive Scans Analysis* (sec. 6.3.3.5).

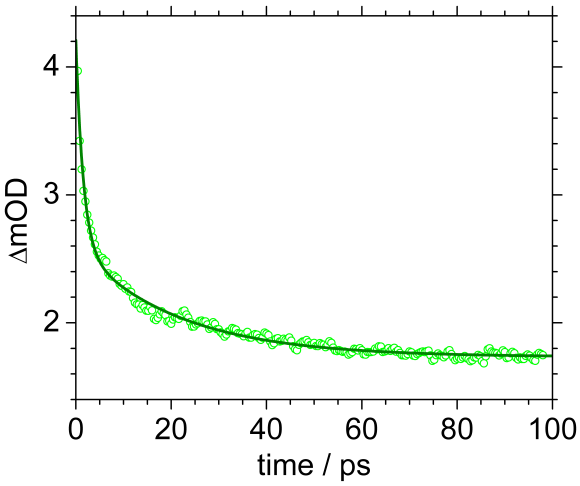

Figure 6.37: Transient absorption signal of the residual contribution, integrated over the whole wavelength region; biexponenial fit (green line): 1.5 ps and 21 ps.

Comparison of Analysis Approaches 1 and 2

A comparison of the results of the two analysis approaches is shown in figure 6.39 for AC, and in figure 6.38 for the residual contribution. While the residual spectra appear at least qualitatively similar, strong deviations are found for the AC spectra. For short times, the contributions are considerably smaller if the AC RT spectrum is fitted directly to the transient APO spectra (fig. 6.39.a), and by comparison with the spectra in figure 6.39.b, it seems clear that only the small peaks are fitted, while the bulks of the early signals are ignored by the fist approach. Furthermore, spectra in figure 6.39.a show implausible features at early times. The spectrum for 0.4 ps is larger than the spectra for 0.8 ps and 1.6 ps, and the spectral positions for times $\lesssim$ 3 ps are shifted opposit to the trend for later times.

Hence, the results of the second approach - assuming a decaying internal temperature for the vibrationally hot AC produced by APO - appear more appropriate. Additional support is obtained from the global analysis in the next subsection.

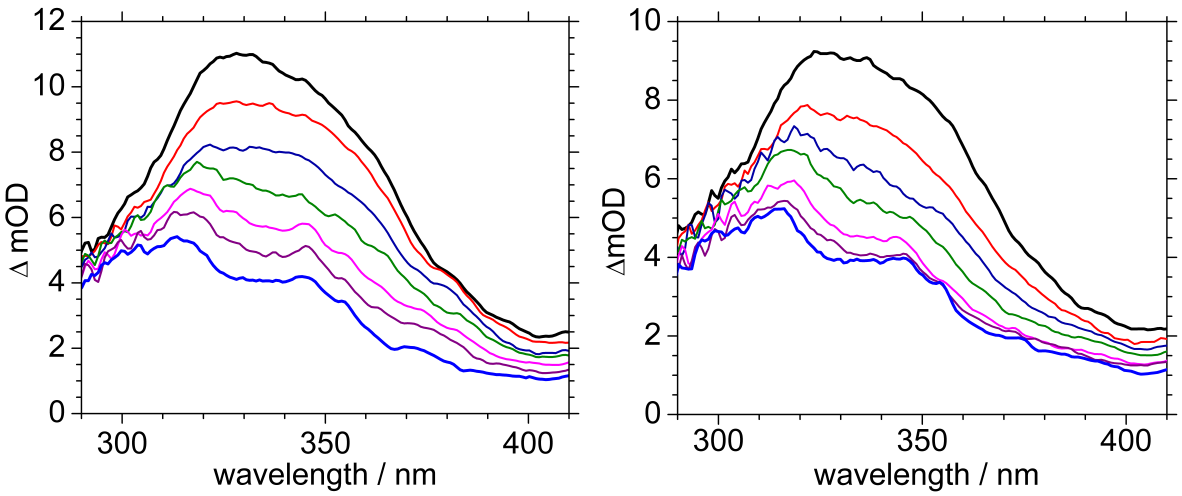

(a) (b)

Figure 6.38: Residual contribution to the transient APO spectra, (a) according to *Analysis Approach 1* – Direct Comparison of AC and APO Data; (b) according to *Analysis Approach 2* – Temperature Model for AC Spectra; delay times are the same as in fig. 6.39.

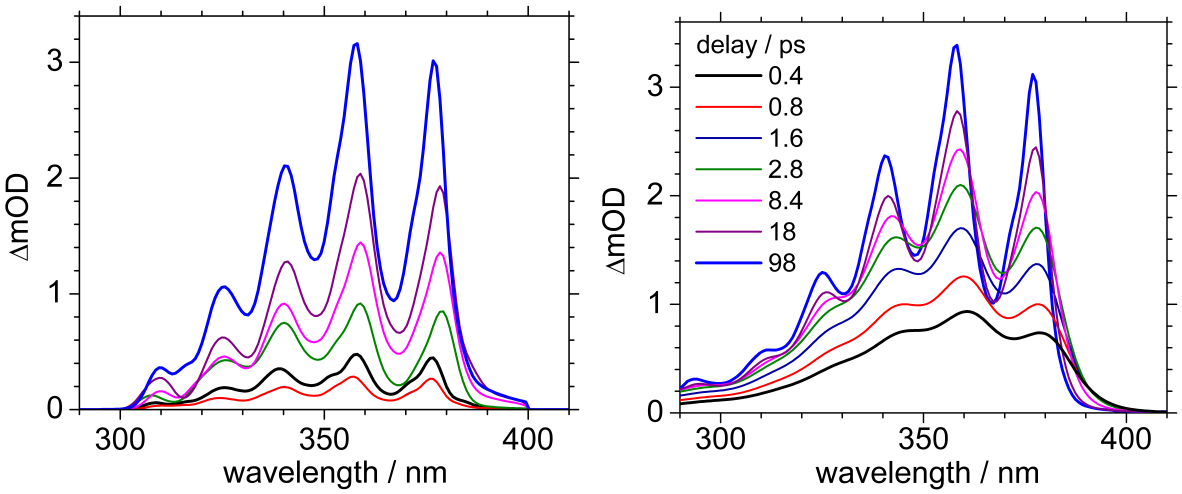

(a) (b)

Figure 6.39: AC contribution to the transient APO spectra, (a) according to *Analysis Approach 1* – Direct Comparison of AC and APO Data; (b) according to *Analysis Approach 2* – Temperature Model for AC Spectra.

6.3.3.4 Global Analysis

Another analysis approach is used for comparsion, without spectral separation of different product contributions. The transient APO data, measured upon excitation at 282 nm, are fitted globally with two time constants shared for all wavelengths, and with an additional non-decaying contribution. Extracted time constants are 1.4 ps and 18 ps. The decay-associated spectra (DAS), given by the spectral amplitudes associated with the time constants, are presented in figure 6.40.

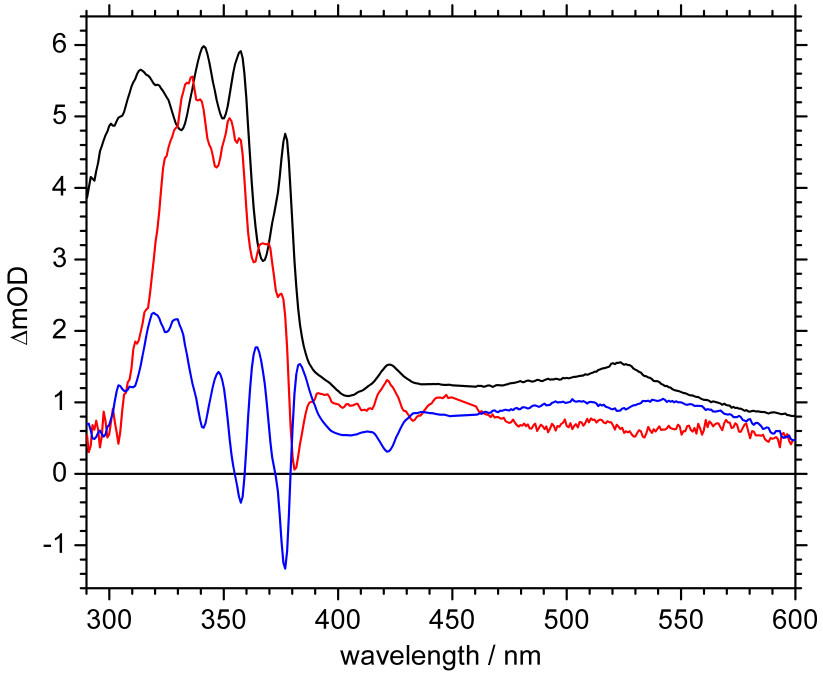

Figure 6.40: Decay associated spectra obtained by global analysis of the APO data (in acetonitrile, exc. at 282 nm, fit started at 0.4 ps). Red: spectrum associated with (1.4 ± 0.4) ps decay constant; blue: spectrum associated with (18 ± 3) ps decay constant; black: non-decaying contribution.

Decay Associated Spectra

The 1.4 ps DAS component (red in fig. 6.40) shows a strong positive signal between 320 nm and 380 nm, with sharp dips at 347, 364 and 382 nm. The 18 ps DAS component (blue in fig. 6.40) is dominated by a sharp peak structure in the region of the known anthracene signature, and the non-decaying contribution (black in fig. 6.40) is identical to the transient spectrum recorded after 100 ps, with the three AC peaks at 341, 357, and 377 nm. The minima in the 18 ps DAS correspond to these AC peak positions, while the maxima are at the dip positions of the 1.4 ps DAS. An interpretation could be that the 1.4 ps DAS is composed of a smooth decaying DE or biradical signal (positive in DAS) and a sharply structured rising AC signal (visible as dips). The 18 ps DAS clearly shows the sharp signature of the AC peaks that are shifting in time from their initial to their final positions, due to the cooling process and hence decreasing influence of vibrational anharmonicity; superimposed is a slightly structured broad DE signal.
Therefore, the 1.4 ps is concluded to be approximately the time constant for AC generation and DE formation, while the 18 ps is assigned to be the vibrational cooling time of vibrationally hot ground state AC.

6.3.3.5 Successive Scans Analysis

Residual Transient Absorption Signal

The focus will now be shifted from the generated AC to the residual contribution. The residual transient absorption spectra, derived upon subtraction of the AC contribution from the APO data, was already depicted in figure 6.38. These spectra show a broad band around 330 nm, which decreases after 0.4 ps. After ≈ 4 ps, a double peak structure emerges, with maxima at 345 and 321 nm. The latter peak shifts from 321 nm to 315 nm in 100 ps. More insight into the origin of these signals is obtained from a comparsion of successive scans, run on the same APO sample.

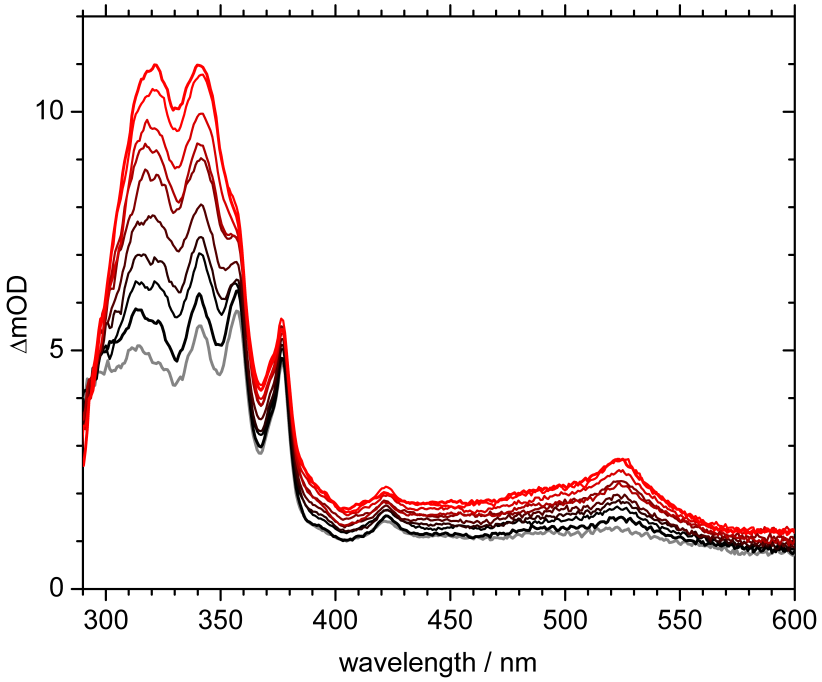

Figure 6.41: Transient absorption spectra measured at 100 ps delay time for 10 consecutive scans on the same APO sample excited at 282 nm.

Transient Absorption Spectra from Successive Scans

In figure 6.41, transient spectra after 100 ps are presented for 10 consecutive scans. Starting from the spectrum at 100 ps for the first scan (grey), signal increases are seen over the entire detected spectral range for consecutive scans. However, the intensities of the clearly identifiable AC ground state absorption band at 376 nm, and the AC triplet absorption band at 422 nm, do not appear to change significantly for the scans, in line with a modest degree of photo-conversion. The characteristic AC peaks appear only for newly created AC, because signals of previously generated species do not cause absorption *changes*. Only if AC were excited by the pump pulse, its ESA would increase with number of scans, but AC does hardly absorb at the excitation wavelength of 282 nm (fig. 6.2).

On the other hand, in later scans a double peak structure between 300 and 350 nm, as well as a peak at 525 nm, become more intense and distinct. The double peak structure bears a resemblance

to the two bands emerging in the residual transient spectra, and will be examined using difference spectra.

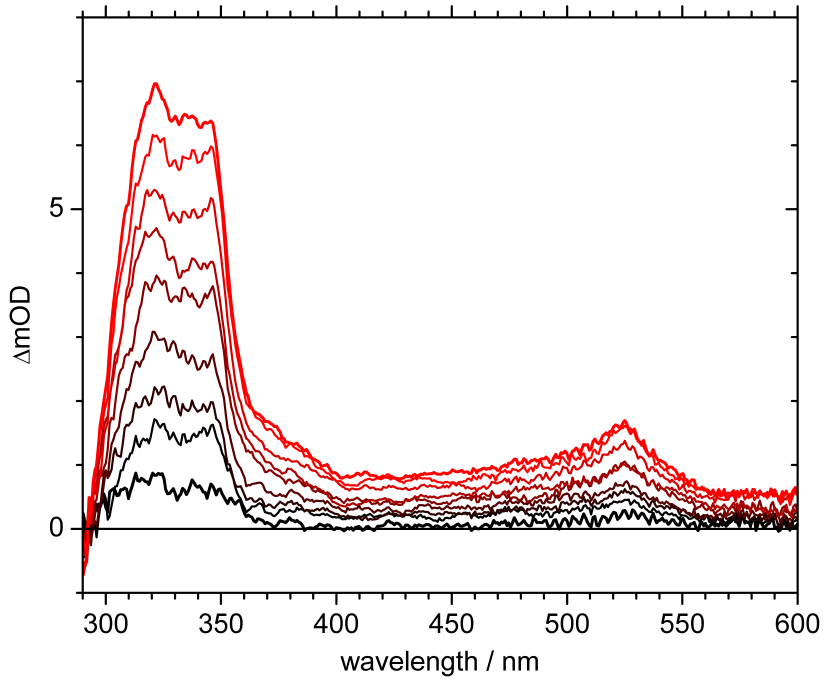

Figure 6.42: Spectra of scans 2 to 10 from figure 6.41, after subtraction of the first scan.

Difference Spectra

Subtraction of the first scan from each of the other scans gives the difference spectra that are presented in fig. 6.42. After the first scan, the transient absorption maxima at 322, 345, and 525 nm all increase approximately linear with the scan number. The resemblance of the double peak structure in the 300 – 350 nm region with the residual transient spectrum is emphasized in figure 6.43. The comparison suggests that the species responsible for the accumulating signals is already formed within the first 100 ps of the first scan on a fresh APO sample, which excludes secondary reaction products like the bicyclic acetal as origin of these signals. Moreover, it is unimaginable that the biradical (BR) resulting from the O-O homolytic cleavage could be stable even for seconds, and therefore it can also not be responsible for accumulation in repeated scans. The primary reaction product responsible for these signals must therefore be the diepoxide (DE). Because the observed bands do not correspond to ground state absorption bands of DE (or any identified reaction product), it is concluded that the created primary photoproduct DE resides in an electronic excited state within 100 ps. The signals can accumulate in repeated scans, since the DE absorbs at the excitation wavelength of 282 nm, so that all previously generated DE can contribute ESA signals in later scans.

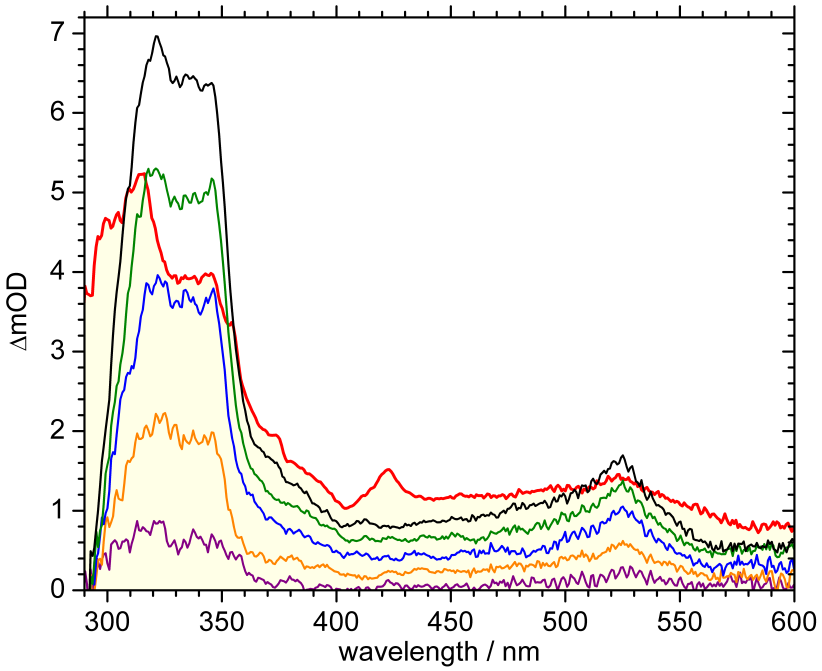

Figure 6.43: Difference spectra of scans 2, 4, 6, 8, and 10 from figure 6.42, compared with the residual contribution after subtraction of the AC contribution from fig. 6.33.

Scan-to-Scan Changes. The total time span for recording 10 scans on the same APO sample covered about two hours, and by comparing the sample's linear absorption spectrum before and after the 10 scans one can conclude that ≈ 12% of the initial amount of APO has been consumed during these 10 scans. Therefore, from scan to scan only a slight decrease (< 2%) is expected of all signals caused by excitation of APO. Based on the ≈ 25% quantum yield for the cycloreversion channel, determined from steady-state investigations (sec. 5.2.2), the sample's DE concentration would be 2.5 mM at most after 10 scans. The slow increase in the DE ESA signals with on average ≈ 10% per scan (see fig. 6.41) confirms the disappearance of DE in between consecutive scans because of its limited thermal stability of a few hours at room temperature (chapter 5, page 89). Figure 6.44 shows the scan-to-scan increase in absorption after 100 ps, calculated by subtraction of scans 2, 5, and 8 from the scans 3, 6, an 9, respectively. Within error margins, all three difference spectra show the same shape and size, illustrating the linear increase already seen in figure 6.42.

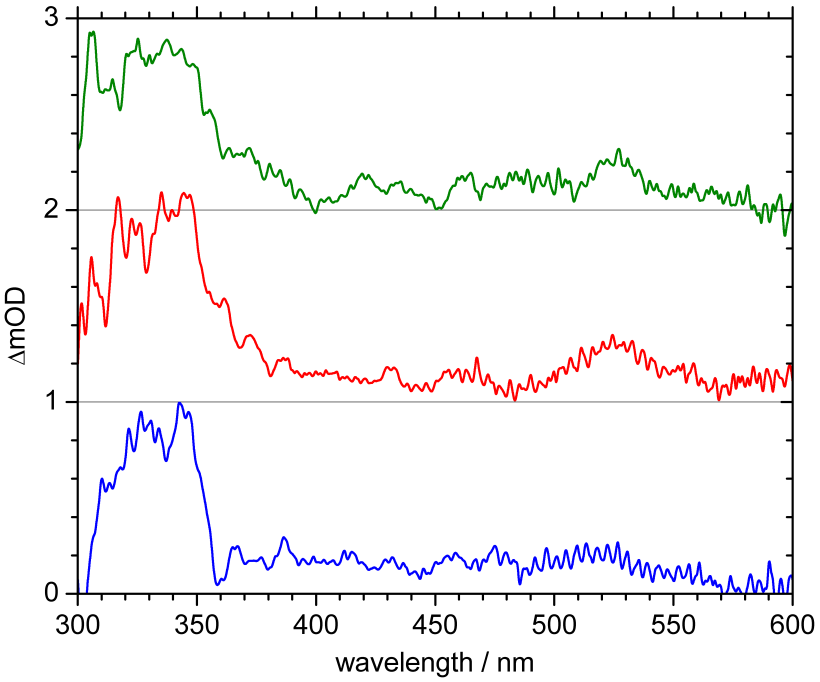

Figure 6.44: Spectra of scans 3, 6, and 9 from figure 6.41, after subtraction of the previous scans 2, 5, and 8, respectively.

Temporal Evolution of Residual Signal. The temporal behavior of the residual signal, now assigned to ESA of DE, was already shown in figure 6.37, resulting two time constants of 1.5 ps and 21 ps. Furthermore, the global analysis, presented in figure 6.40, gives two very similar time constants of 1.4 ps and 18 ps, which needs to be considered with care, as it includes both AC and residual dynamics.
The $\approx$ 1.5 ps time constant could represent the lifetime of the biradical created by O-O homolytic cleavage and therefore the formation time of the DE. The 21 ps time constant is comparable with the cooling rates extracted for hot ground state AC generated by cycloreversion of APO, and could be related to vibrational cooling of the DE upon formation.

6.4 Primary Steps in Photoinduced Reactions: Summary and Conclusions

Anthraquinone and Anthracene

Anthraquinone (AQ) in acetonitrile was investigated by excitation at 266 nm, and it is concluded that the lowest triplet state of AQ is generated with a time constant of $\approx$ 160 fs, followed by relaxation dynamics on a time scale of picoseconds.
Anthracene (AC) in acetonitrile was investigated by excitation both at 266 nm and at 376 nm. At 376 nm, AC is prepared in the lowest vibrational level of the S_1 state. At 266 nm, it is excited either directly to high-lying vibrational levels of S_1, or first to the S_2 state, from where it is rapidly converted to the vibrationally hot S_1 state. From there, vibrational cooling processes occur on a time scale of approximately 14 – 19 ps.

Anthracene-9,10-Endoperoxide

Anthracene-9,10-endoperoxide (APO) was investigated by excitation both at 266 nm and at 282 nm. At 266 nm, AQ is generated, which is also excited by the pump pulse and gives comparably large excited state absorption (ESA) signals, rendering it difficult to gather information on APO. At 282 nm, anthracene (AC) and diepoxide (DE) are generated as the primary photoproducts (schematic illustration in fig. 6.45), both on time scales below 3 ps. AC is formed in vibrationally hot electronic ground state (S_0) and undergoes vibrational cooling with 18 ps. As a minor product, 1 – 2 % of triplet AC are generated. DE is formed in an electronic excited state (indicated by an asterisk in fig. 6.45) with excess vibrational energy, and undergoes vibrational cooling, similar to AC, with 21 ps. The existence of a biradical (BR) intermediate could not be established, although the ultrafast formation time of DE could well be related to the lifetime of a biradical precursor. Neither of the secondary reaction products bicyclic acetal and anthraquinone was observed in this measurement series.
The deduced AC formation time of < 3 ps is significantly shorter than most of the cycloreversion time constants that were published for aromatic endoperoxides[37, 71, 72, 36, 39, 38], which were in the range of 50 – 95 ps. The only exception is the endoperoxide of dimethylhomoeocoerdianthrone (HOCD-PO), for which a cycloreversion time of 1.6 – 1.7 ps were found[38, 32]. The latter time constant is very close to the one deduced here for APO.

Implications of the Ultrafast Product Formation

The question why dual photochemistry is possible in case of APO can now be answered based on the results of the time resolved investigation on cycloreversion. This reaction, which is only accessible from higher excited states S_n, $n \geq 2$, occurs with an ultrafast primary step and is therefore able to efficiently compete with fast internal conversion to S_1. Moreover, AC is directly formed in the electronic ground state within < 3 ps, implying that the a proposed[38, 32] biradical intermediate (CO-BR in fig. 6.45), if it occurs, has a very short lifetime; alternatively, the cycloreversion reaction could in fact proceed via a concerted mechanism. The data do not allow to distinguish between these two possibilities.
The primary step of the O-O cleavage reaction is found to proceed on a similarly short time scale < 2 p. In this case, however, it appears plausible to assume the intermediate existence of a biradical (OO-BR in fig. 6.45), because the initial transient absorption signals differ from the diepoxide

ESA observed at later times. An ultrafast primary O-O cleavage step is also in agreement with the results from chapter 4: The S_1 state is supposed to have σ^*_{OO} character and a strongly enlarged O-O distance that should facilitate the O-O bond cleavage.

The main results of this chapter are summarized in figure 6.45.

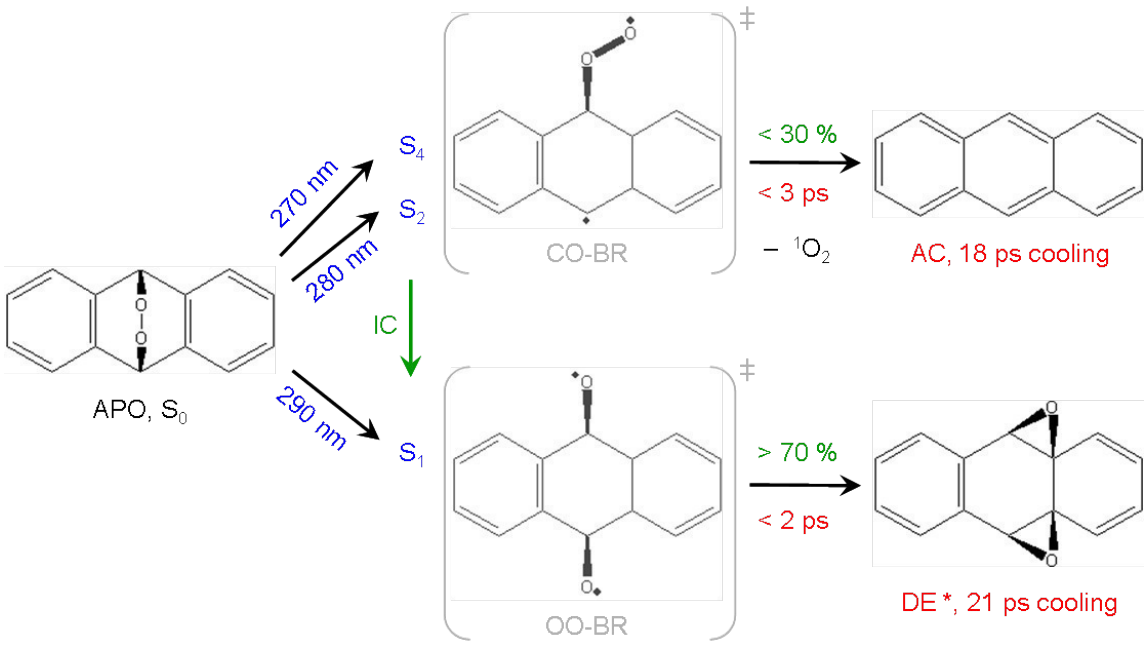

Figure 6.45: Overview on the main findings concerning the primary photoreaction steps of APO upon 282 nm excitation (red).

7 Final Summary and Conclusions

Electronic Excited Singlet States of Anthracene-9,10-Endoperoxide: New Assignment

Electronic transition energies to excited singlet states of a molecule can usually be obtained from the energetic positions of absorption bands in the UV/vis absorption spectrum. In the case of anthracene-9,10-endoperoxide, however, it is not clearly visible whether or not another electronic excited singlet state exists below the lowest discernible shoulder at 280 nm. The issue has now been settled by femtosecond polarization resolved UV pump – IR probe experiments, in combination with high-level *ab initio* calculations by Corral and González[35]. According to the calculated assignment, the $S_0 \rightarrow S_1$ transition is located around 290 nm, and the S_2 and S_4 states are associated with the bands at 280 and 270 nm, respectively; the $S_0 \rightarrow S_3$ transition is calculated to be symmetry forbidden. The calculated values for S_2 and S_4 are in good agreement with the band positions deduced from the absorption spectrum. Furthermore, the assignment is tested by comparison of calculated and experimentally determined TDM orientations: The result of the femtosecond polarization resolved UV pump – IR probe experiment is in good agreement with the theoretical expectations based on the above assignment and therefore supports the existence of the S_1 state around 290 nm.

Wavelength Dependent Photoproduct Quantum Yields: Dual Photochemistry

With the assignment clarified, the next issue was the determination of the reaction pathways that are associated with excitation of S_1 and higher electronic excited singlet states. To answer this question, the wavelength dependence of the photoproduct quantum yields was studied. Anthracene, the product of the cycloreversion reaction, was obtained only with excitation wavelengths shorter than 300 nm. The observation that the maximum yield of 29 % is reached upon excitation at 270 nm implies that the cycloreversion reaction is most efficient upon S_4 excitation. The residual > 70 % of the molecules excited at 270 nm are found as diepoxide, bicyclic acetal, or anthraquinone, which are all products of the initial O-O cleavage pathway. It is therefore concluded that > 70 % of the molecules in S_4 or S_2 undergo internal conversion to S_1, from where they enter the competing reaction pathway of homolytic O-O cleavage. The observation of two different photoreaction pathways, from which one is available at considerably longer wavelenths, while the other only starts contributing at shorter wavelengths, is a clear indication of dual photochemistry, where one photoreaction occurs from the S_1, and the other from higher excited singlet states.

The total photoproduct quantum yield is close to 100 % for wavelengths < 310 nm, indicating negligible non-reactive deactivation of the excited molecules, and suggesting that the chemical conversions are essentially irreversible. The O-O cleavage products are also found for wavelengths longer than 310 nm, in agreement with the long weak absorption tail. The ratio of the primary photoproduct diepoxide and the secondary product bicyclic acetal depends on the wavelength and the duration of illumination: Around 280 – 300 nm, the bicyclic acetal yield increases with prolonged illumination, while that of the diepoxide decreases. It is therefore concluded that the

bicyclic acetal is formed in a secondary photoreaction upon exciation of the diepoxide.
Furthermore, emission from an aromatic endoperoxide was observed for the first time[29]. The weak emission that is observed upon excitation of APO samples at $\approx$ 290 nm is concluded to originate from the anthracene-1,4-endoperoxide isomer, which is deduced to be a < 0.5 % side product in the synthesis of 9,10-APO.

Real-Time Study: Ultrafast Primary Photoreaction Steps

The question how the reaction from higher excited states can compete efficiently (up to 29 %) with rapid internal conversion to $S_1$is address in a time resolved investigation of the primary reaction steps. The femtosecond UV pump – supercontinuum probe transient absorption experiment reveals that both primary reaction steps, the homolytic O-O cleavage from S_1 as well as the C-O cleavage from higher excited states, occur on ultrafast time scales < 3 ps. This result reasonably explains the competition between cycloreversion and internal conversion upon S_2 or S_4 excitation.
Vibrational cooling processes in AC and DE show similar time scales of 14 – 21 ps. AC is formed in the vibrationally hot electronic ground state and undergoes vibrational cooling with 18 ps, similar to the cooling process observed for AC in the vibrationally hot S_1 state (14 – 19 ps). The DE, on the other hand, is formed in an electronic excited state; the cooling time of 21 ps is again similar.
The results are summarized in figure 7.1.

Outlook

To return to the starting point, the singlet oxygen generation by cycloreversion from aromatic endoperoxides is the reaction of interest in future application as photosensitizers. The present results on the dual photochemistry of APO show that the cycloreversion reaction has to compete with other photoreactions that proceed from S_1. A maximum yield of only 29 % cycloreversion indicates that the ratio of cycloreversion to the internal conversion to S_1 leaves room for improvement. Optimal control schemes using shaped femtosecond laser pulses[73, 74] are developped to steer chemical reactions along the desired pathway. These concepts could be applied to enhance the singlet oxygen generation from APO by adjusting tailored laser pulses to optimally lead the excited APO molecule into the cycloreversion channel, thereby circumventing potential relaxation paths tho the S_1 state. Recent progress[45] in the field of reaction optimization using tailored laser pulses make this approach appear feasilble and worth exploring.

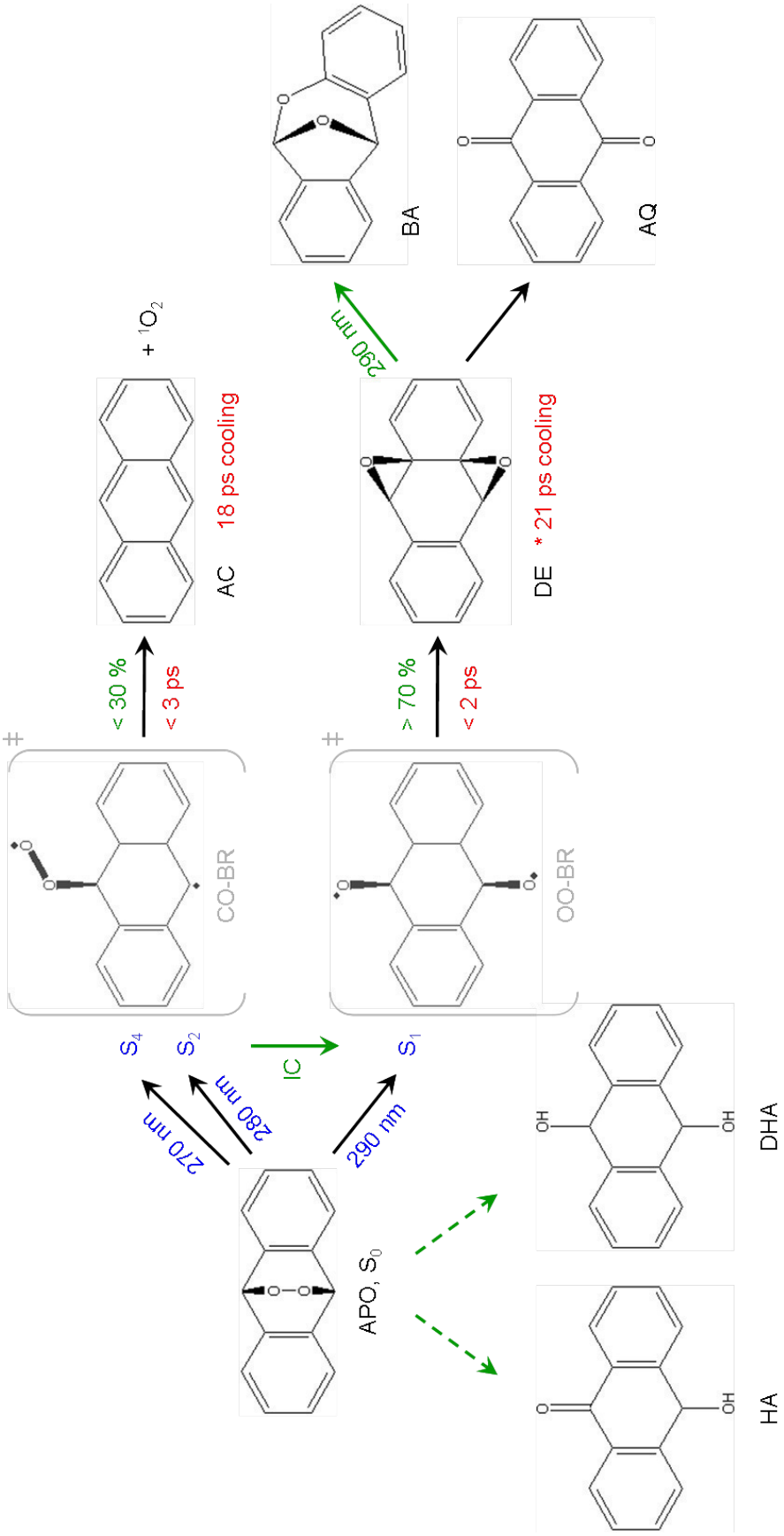

Figure 7.1: Overview on the main findings concerning the photoinduced reactions of APO.

Bibliography

[1] E. Niederlaender. Causes of death in the eu, 2006.

[2] R. Bonnett. Photosensitizers of the porphyrin and phthalocyanine series for photodynamic therapy. *Chem. Soc. Rev.*, 24:19–33, 1995.

[3] D. E. J. G. J. Dolmans, D. Fukumura, and R. K. Jain. Photodynamic therapy for cancer. *Nature Reviews*, 3:380–387, 2003.

[4] David R. Kearns. Physical and chemical properties of singlet molecular oxygen. *Chem. Rev.*, 71:395–427, 1971.

[5] A. F. Hollemann, E. Wiberg, and N. Wiberg. *Lehrbuch der Anorganischen Chemie*. de Gruyter, 33. edition, 1985.

[6] M. Kasha and A. U. Khan. The physics, chemistry, and biology of singlet molecular oxygen. *Ann. N.Y. Acad. Sci.*, 171:5–23, 1970.

[7] M. Prein and W. Adam. The schenck ene reaction: Diastereoselective oxyfunctionalization with singlet oxygen in synthetic applications. *Angew. Chem. Int. Ed. Engl.*, 35:477–494, 1996.

[8] P. Esser, B. Pohlmann, and H.-D. Scharf. The photochemical synthesis of fine chemicals with sunlight. *Angew. Chem. Int. Ed. Engl.*, 33:2009–2023, 1994.

[9] M. R. Hamblin and T. Hasan. Photodynamic therapy: a new antimicrobial approach to infectious disease? *Photochem. Photobiol. Sci.*, 3:436–450, 2004.

[10] M. C. DeRosa and R. J. Crutchley. Photosensitized singlet oxygen and its applications. *Coord. Chem. Rev.*, 233-234:351–371, 2002.

[11] David R. Kearns. Selection rules for singlet-oxygen reactions. concerted addition reactions. *J. Am. Chem. Soc.*, 91:6554–6563, 1969.

[12] W. Freyer and S. Flatau. The first annulated porphyrazine containing four endoperoxide bridges. *Tetrahedron Letters*, 37:5083–5086, 1996.

[13] M. Kasha. Characterization of electronic transitions in complex molecules. *Discuss. Faraday Soc.*, 9:14–19, 1950.

[14] P. Klán and J. Wirz. *Photochemistry of organic compounds: from concepts to practice*. Postgraduate chemistry series. Wiley-Blackwell, 2009.

[15] J. Rigaudy. Photooxidation des dérivés aromatiques. *Pure Appl. Chem.*, 16:169–186, 1968.

[16] J.-M. Aubry, C. Pierlot, J. Rigaudy, and R. Schmidt. Reversible binding of oxygen to aromatic compounds. *Acc. Chem. Res.*, 36:668–675, 2003.

[17] J. W. Breitenbach and A. Kastell. Die geschwindigkeit des thermischen zerfalls von anthracenperoxyd. *Monatsh. Chem.*, 85:676–683, 1954.

[18] N. J. Turro, M.-F. Chow, and J. Rigaudy. Mechanism of thermolysis of endoperoxides of aromatic compounds. activation parameters, magnetic field, and magnetic isotope effects. *J. Am. Chem. Soc.*, 103:7218–7224, 1981.

[19] J. W. Breitenbach and A. Kastell. Polymerisationsanregung durch freie diradikale. *Monatsh. Chem.*, 84:645–647, 1953.

[20] J. Rigaudy, J. Baranne-Lafont, A. Defoin, and N. K. Cuong. Transformations thermiques des photooxydes meso des acenes - ii cas du photooxyde d'anthracene. *Tetrahedron*, 34:73–82, 1978.

[21] A. Defoin, J. Baranne-Lafont, J. Rigaudy, and J. Guilhem. Transformations thermiques des photooxydes meso des acenes - iii dimeres de l'o-quinodimethane issu du photooxyde d'anthracene. *Tetrahedron*, 34:83–93, 1978.

[22] R. Dabestani, K. J. Ellis, and M. E. Sigman. Photodecomposition of anthracene on dry surfaces: products and mechanism. *J. Photochem. Photobiol. A*, 86:231–239, 1995.

[23] W. Drews, R. Schmidt, and H.-D. Brauer. The photolysis of the endoperoxide of 9,10-diphenylanthracene. *Chem. Phys. Lett.*, 70:84–88, 1980.

[24] R. Schmidt, K. Schaffner, W. Trost, and H.-D. Brauer. Wavelength-dependent and dual photochemistry of the endoperoxides of anthracene and 9,10-dimethylanthracene. *J. Phys. Chem.*, 88:956–958, 1984.

[25] H. H. Wasserman and J. R. Scheffer. Singlet oxygen reactions from photoperoxides. *J. Am. Chem. Soc.*, 89:3073–3075, 1967.

[26] H. H. Wasserman, J. R. Scheffer, and J. L. Cooper. Singlet oxygen reactions with 9,10-diphenylanthracene peroxide. *J. Am. Chem. Soc.*, 94:4991–4996, 1972.

[27] J. Rigaudy, C. Breliere, and P. Scribe. Photochemistry of 9,10-diphenylanthacene endoperoxide. *Tetrahedron Letters*, 7:687–690, 1978.

[28] J. Rigaudy, A. Defoin, and J. Baranne-Lafont. syn-anthracene 4a,10:9,9a-dioxide. *Angew. Chem. Int. Ed. Engl.*, 18:413–415, 1979.

[29] R. Schmidt and H.-D. Brauer. Comparison of the photochemical and thermal rearrangement reaction of endoperoxides. *J. Photochem.*, 34:1–12, 1986.

[30] A. Klein, M. Kalb, and M. S. Gudipati. New assignment of the electronically excited states of anthracene-9,10-endoperoxide and its derivatives: a critical experimental and theoretical study. *J. Phys. Chem. A*, 103:3843–3853, 1999.

[31] H.-D. Brauer and R. Schmidt. Comment on "new assignment of the electronically excited states of anthracene-9,10-endoperoxide and its derivatives: a critical experimental and theoretical study". *J. Phys. Chem. A*, 104:164–165, 2000.

[32] N. P. Ernsting, R. Schmidt, and H.-D. Brauer. Subpicosecond transient absorption studies of the photocycloreversion of an aromatic endoperoxide. *J. Phys. Chem.*, 94:525–5255, 1990.

[33] P. Kukura, D. W. McCamant, and R. A. Mathies. Femtosecond time-resolved stimulated raman spectroscopy of the s2 (1bu+) excited state of beta-carotene. *J. Phys. Chem. A*, 108:5921–5925, 2004.

[34] M. S. Gudipati and A. Klein. Reply to the comment on "new assignment of the electronically excited states of anthracene-9,10-endoperoxide and its derivatives: a critical experimental and theoretical study". *J. Phys. Chem. A*, 104:166–167, 2000.

[35] I. Corral, L. Gonzalez, A. Lauer, W. Freyer, H. Fidder, and K. Heyne. Identifying the low-lying electronic states of anthracene-9,10-endoperoxide. *Chem. Phys. Lett.*, 452:67–71, 2008.

[36] Th. Blumenstock, K. Jesse, F. J. Comes, R. Schmidt, and H.-D. Brauer. Picosecond studies on the photodissociation dynamics of aromatic endoperoxides. *Chem. Phys.*, 130:289–298, 1989.

[37] K.B. Eisenthal, N. J. Turro, C. G. Dupuy, D. A. Hrovat, J. Langan, T. A. Jenny, and E. V. Sitzmann. State-selective photochemistry of singlet oxygen precursors: Kinetic and wavelength dependence of the photodissociation of anthracene endoperoxide. *J. Phys. Chem.*, 90:5168–5173, 1986.

[38] K. Jesse and F. J. Comes. Rate parameters for the two-step photofragmentation of aromatic endoperoxides in solution. *J. Phys. Chem.*, 95:1311–1315, 1991.

[39] K. Jesse, R. Markert, F. J. Comes, R. Schmidt, and H.-D. Brauer. Picosecond photochemistry: The mechanism of photocycloreversion of aromatic endoperoxides. *Chem. Phys. Lett.*, 166:95–100, 1990.

[40] K. J. Jesse. Structural impacts on the photodissociation dynamics of aromatic endoperoxides in solution. *Chem. Phys. Lett.*, pages 193–198, 1997.

[41] M. Hesse, H. Meier, and B. Zeeh. *Spektroskopische Methoden in der organischen Chemie*. Thieme Verlag, 2002.

[42] J. M. Hollas. *Moderne Methoden in der Spektroskopie*. Vieweg, 1995.

[43] J. R. Lakowicz. *Principles of fluorescence spectroscopy*. Springer, 2006.

[44] M. Y. Ivanov and J. P. Marangos. Time-resolved imaging of atomic-scale electron and nuclear dynamics. *J. Modern Optics*, 54:899–903, 2007.

[45] C. Brif, R. Chakrabarti, and H. Rabitz. Control of quantum phenomena: past, present and future. *New Journal of Physics*, 12:075008, 2010.

[46] S. A. Kovalenko, A. L. Dobryakov, J. Ruthmann, and N. P. Ernsting. Femtosecond spectroscopy of condensed phases with chirped supercontinuum probing. *Phys. Rev. A*, 59:2369–2384, 1999.

[47] R. A. Kaindl, M. Wurm, K. Reimann, P. Hamm, A. M. Weiner, and M. Woerner. Generatin, shaping, and characterization of intense femtosecond pulses tunable from 3 to 20 mum. *J. Opt. Soc. Am. B*, 17:2086–2094, 2000.

[48] S. A. Kovalenko, R. Schanz, H. Hennig, and N. P. Ernsting. Cooling dynamics of an optically excited molecular probe in solution from femtosecond broadband transient absorption spectroscopy. *J. Chem. Phys.*, 115:3256–3273, 2001.

[49] M. Linke, A. Lauer, T. VonHaimberger, A. Zacarias, and K. Heyne. Three-dimensional orientation of the q(y) electronic transition dipole moment within the chlorophyll a molecule determined by femtosecond polarization resolved vis pump-ir probe spectroscopy. *J. Am. Chem. Soc.*, 130:14904–14905, 2008.

[50] W. Freyer, S. Mueller, and K Teuchner. Photophysical properties of benzoannelated metal-free phthalocyanines. *J. Photochem. and Photobiol. A: Chemistry*, 163:231–240, 2004.

[51] B. O. Roos. *Ab initio methods in quantum chemistry - II*. Wiley, 1987.

[52] J. Finley, P.-A. Malmqvist, B. O. Roos, and L. Serrano-Andrés. The multi-state caspt2 method. *Chem. Phys. Lett.*, 288:299–306, 1998.

[53] K. Pierloot, B. Dumez, P.-O. Widmark, and B. O. Roos. Density matrix averaged atomic natural orbital (ano) basis sets for correlated molecular wave functions iv. medium size basis sets for the atoms h-kr. *Theor. Chim. Acta*, 90:87–114, 1995.

[54] B. O. Roos and K. Anderson. Multiconfigurational perturbation theory with level shift - the cr2 potential revisited. *Chem. Phys. Lett.*, 245:215–223, 1995.

[55] M. Cossi, N. Rega, G. Scalmani, and V. Barone. Polarizable dielectric model of solvation with inclusion of charge penetration effects. *J. Chem. Phys.*, 114:5691–5701, 2001.

[56] G. Karlstrom, R. Lindh, P.-A. Malmqvist, B.O. Roos, U. Ryde, V. Veryazov, P.-O. Widmark, M. Cossi, B. Schimmelpfennig, P. Neogrady, and L. Seijo. Molcas: a program package for computational chemistry. *Comput. Mater. Sci.*, 28:222–239, 2003.

[57] T. R. Criswell and B. H. Klanderman. Studies related to the conversion of 9,10-anthraquinones to anthracenes. *J. Org. Chem.*, 39:770–774, 1974.

[58] M. J. Frisch, G. W. Trucks, H. B. Schlegel, G. E. Scuseria, M. A. Robb, J. R. Cheeseman, J. A. Montgomery, Jr., T. Vreven, K. N. Kudin, J. C. Burant, J. M. Millam, S. S. Iyengar, J. Tomasi, V. Barone, B. Mennucci, M. Cossi, G. Scalmani, N. Rega, G. A. Petersson, H. Nakatsuji, M. Hada, M. Ehara, K. Toyota, R. Fukuda, J. Hasegawa, M. Ishida, T. Nakajima, Y. Honda, O. Kitao, H. Nakai, M. Klene, X. Li, J. E. Knox, H. P. Hratchian, J. B. Cross, V. Bakken, C. Adamo, J. Jaramillo, R. Gomperts, R. E. Stratmann, O. Yazyev, A. J. Austin, R. Cammi, C. Pomelli, J. W. Ochterski, P. Y. Ayala, K. Morokuma, G. A. Voth, P. Salvador, J. J. Dannenberg, V. G. Zakrzewski, S. Dapprich, A. D. Daniels, M. C. Strain, O. Farkas, D. K. Malick, A. D. Rabuck, K. Raghavachari, J. B. Foresman, J. V. Ortiz, Q. Cui, A. G. Baboul, S. Clifford, J. Cioslowski, B. B. Stefanov, G. Liu, A. Liashenko, P. Piskorz, I. Komaromi, R. L. Martin, D. J. Fox, T. Keith, M. A. Al-Laham, C. Y. Peng, A. Nanayakkara, M. Challacombe, P. M. W. Gill, B. Johnson, W. Chen, M. W. Wong, C. Gonzalez, and J. A. Pople. Gaussian 03, Revision D.01. Gaussian, Inc., Wallingford, CT, 2004.

[59] D. F. Eaton. Reference materials for fluorescence measurement. *Pure Appl. Chem.*, 60:1107–1114, 1988. International Union of Pure and Applied Chemistry, Organic chemistry division, commission on photochemistry.

[60] E. Afshari, H.-D. Brauer, R. Schmidt, M. Lachgar, and J. Rigaudy. Wavelength-dependent photocycloreversion of the endoperoxides of 1,2,3,4-tetramethylanthracene and 1,2,3,4-tetramethyl-9,10-diphenylanthracene. *J. Photochem. Photobiol. A: Chem.*, 63:319–325, 1992.

[61] I. Corral and L. Gonzalez. Theoretical investigation of anthracene-9,10-endoperoxide vertical singlet and triplet excitation spectra. *J. Comput. Chem.*, 29:1982–1991, 2008.

[62] C. J. Brown and M. Ehrenberg. 9,10-dihydro-9,10-epidioxyanthracene, c14h10o2. *Acta Cryst.*, C40:1059–1060, 1984.

[63] A. C. Albrecht. Polarizations and assignments of transitions: The method of photoselection. *J. Mol. Spectr.*, 6:84–108, 1961.

[64] J. Michel and V. Bonacic-Koutecky. *Electronic aspects of organic photochemistry*. Wiley-Interscience, 1990.

[65] M. E. Sigman, S. P. Zingg, R. M. Pagni, and J. H. Burns. Photochemistry of anthracene in water. *Tetrahedron Lett.*, 32:5737–5740, 1991.

[66] H. Fidder, A. Lauer, W. Freyer, B. Koeppe, and K. Heyne. Photochemistry of anthracene-9,10-endoperoxide. *J. Phys. Chem. A*, 113:6289–6296, 2009.

[67] K. Hamanoue, T. Nakayama, Y. Kajiwara, T. Yamaguchi, and H. Teranishi. The lowest triplet states of anthraquinone and chloroanthraquinones: The 1-chloro, 2-chloro, 1,5-dichloro, and 1,8-dichloro compounds. *J. Chem. Phys.*, 86:6554–6659, 1987.

[68] J. Jasny and J. Sepiol. Nanosecond transient absorption spectrophometer with dye laser probe. *J. Phys. E: Sci. Instrum.*, 14:493–497, 1981.

[69] D. Bebelaar. Time resolved molecular spectroscopy using high power solid state lasers in pulse transmission mode. a re-examination of the sn<-s1 spectra of naphthalene and anthracene. *Chem. Phys.*, 3:205–216, 1974.

[70] R. Bensasson and E. J. Land. Triplet-triplet extinction coefficients via energy transfer. *Trans. Farad. Soc.*, 67:1904–1915, 1971.

[71] E. V. Sitzmann, J. G. Langan, D. A. Hrovat, and K. B. Eisenthal. Picosecond kinetics of state-selective singlet oxygen producing photochemistry of aromatic endoperoxides. *Chem. Phys. Lett.*, 162:157–162, 1989.

[72] Th. Blumenstock, F. J. Comes, R. Schmidt, and H.-D. Brauer. Picosecond laser photolysis study of the photocycloreversion of heterocoerdianthrone endoperoxide. *Chem. Phys. Lett.*, 127:452–455, 1986.

[73] A. Assion, T. Baumert, M. Bergt, T. Brixner, B. Kiefer, V. Seyfried, M. Strehle, and G. Gerber. Control of chemical reactions by feedback-optimized phase-shaped femtosecond laser pulses. *Science*, 282:919–922, 1998.

[74] H. Rabitz, R. de Vivie-Riedle, M. Motzkus, and K. Kompa. Whither the future of controlling quantum phenomena? *Science*, 288:824–828, 2000.

Danksagung

Finanzielle Unterstützung

Zuerst einmal geht ein besonderer Dank für die Finanzierung meiner Doktorandenstelle an den Sonderforschungsbereich SFB 450 der Deutschen Forschungsgemeinschaft.

Betreuung

Prof. Karsten Heyne gebührt großer Dank für die Betreuung meiner Doktorarbeit, die Bereitstellung von Thema, Diskussionen, Unterstützung, Paper-Veröffentlichung, Teilnahme an z.T. internationalen Tagungen, und und und. Und die Begutachtung dieser Arbeit natürlich auch.
Dr. Henk Fidder begleitete den Großteil meiner Arbeit als PostDoc, er half mir besonders durch kritische Dikussionen bei der Analyse und Interpretation von Messdaten. Außerdem hatte er auch ein Auge auf meine Experimente und "erzog" mich zum sorgfältigen Arbeiten, insbesondere was Fluoreszenz betrifft.
Prof. Ludger Wöste sei an dieser Stelle für die Übernahme der Zweitkorrektur gedankt. Des weiteren war es "sein" SFB 450, der mich erst nach Berlin gebracht hat – und meine Finanzierung sicherte, siehe oben.
Prof. Hans-Heinrich Limbach möchte ich ebenfalls danken, da er mir duch die *Dahlem Research School – Molecular Science* zusätzliche Möglichkeiten bot, nicht zuletzt den *International Student Workshop on Communicating the Chemical Sciences* in Amman, Jordanien (2009).

Wissenschaftliche Unterstützung

Dr. Wolfgang Freyer danke ich für die Synthese der APO-Proben.
Leticia González und Inés Corral sei gedankt für die produktive Zusammenarbeit für das gemeinsame Paper (Referenz [35]); mit ihren quantenchemischen Berechnungen zu "meinem" Molekül haben sie einen nicht unwichtigen Baustein zur Interpretation meiner Ergebnisse geliefert (siehe Kapitel 4). Außerdem danke ich Inés Corral für die ersten spanischen Worte, was die Idee tatsächlich Spanisch zu lernen initiierte.
An **Emad Mukhtar** ergeht Dank für die Fluoreszens-Lebensdauer-Messungen, die an der Universität von Uppsala (Schweden) an unseren APO-Proben durchgeführt wurden.
Benjamin Koeppe und Dr. Schäfer vom Institut für Chemie haben dankenswerterweise NMR Spektren meiner Proben aufgenommen.
Prof. Alexievund ihrer Arbeitsgruppe sei für die Bereitstellung von Messmöglichkeiten am Fluoreszenzspektrometer gedankt.
Ebenso ergeht Dank an **Prof. Bittl** und dessen Arbeitsgruppe, die uns freundlicherweise über Jahre hinweg am UV/vis Spektrometer messen ließen.

Wissenschaftliche Unterstützung von der Humboldt Universität

Prof. N.P. Ernsting gebührt Dank für die Möglichkeit, in seinem Labor zeitaufgelöste Messungen durchzuführen.
Dr. Sergey A. Kovalenko bin ich zu Dank verpflichtet, da er mich bei den zeitaufgelösten Messungen unterstützte und auch wichtige Anstöße für die Auswertung beigetragen hat.

Danken möchte ich auch **Dr. Alexander Dobryakov**, der mich mit Rechnungen für das zeitabhängige Temperatur-Modell unterstützt hat.

Administrative und Sonstige Unterstützung

Sabine Simon sei für ihre stets gut gelaunte Arbeit als langjährige Sekretärin der AG Heyne gedankt, sowie für viele unabdingbare Kleinigkeiten wie Büromaterial und Faxgerät.
Frau Pasanec, der guten Seele des Promotionsbüros, möchte ich für ihre Arbeit danken, für freundliche Auskünfte und aufmunternde Worte.
Es gibt noch einige weitere Menschen, die bisweilen das Leben und Arbeiten an der FU erleichtern, darunter **Roswitha Brunn** und **Ingrid Wallat**, die bei so manchem Chemikalien-bezogenen Problem halfen. Außerdem seien die Mitarbeiter der Verwaltung erwähnt, wie z.B. der Haus- und Drittmittel (SFB450) Sekretariate.
Bei **Prof. Schwentner** und seiner Arbeitsgruppe möchte ich mich für unkomplizierte Laborgeräte-Ausleihen und gemütliche Weihnachtsfeiern bedanken.
Für einige Kaffee-und-Kuchen-Feiern im Kaffeeraum sei **Prof. Vieth** und dessen Arbeitsgruppe gedankt.

Arbeitsgruppen-Mitglieder

Was wäre die Doktoranden-Zeit ohne die Kollegen aus der eigenen Arbeitsgruppe?
In mehr oder weniger chronologischer Reihenfolge waren das **Henk Fidder, Gerome Weiland, Martin Linke, Tom Rubin, Till Stensitzki, Dagmar Jones, Moritz Theisen, Yang Yang, Jörg Schnitzbauer, Theo von Haimberger, Sven Augustin, Mathias Hartmann, Alexander Helmke**... und ein paar "Neue", die erst auftauchten nachdem ich mich zum Schreiben hinter meinem Laptop verkrochen hatte. Auch ein paar Mitglieder befreundeter Arbeitsgruppen möchte ich nicht vergessen, nämlich **Falk Königsmann** (AG Schwentner), **Talea Köchling** (AG Vieth) und **Ringo Wenzel** (AG Bittl). Des weiteren möchte ich mich an dieser Stelle bei der gesamten Arbeitsgruppe von Prof. Ernsting (HU) für die stets freundliche Aufnahme und den Kaffee bedanken. Grüße gehen an **Heidi Steingräber, Sabrina Penn, Mohsen Sajadi Hezaveh, Dr. Sergey A. Kovalenko, Dr. Alexander Dobryakov, Jens Breffke, Mario González Jiménez und Iris Suter**.
Ich hoffe, dass ich niemanden vergessen habe, und falls sich doch jemand findet, so soll er meine Nachlässigkeit bitte entschuldigen.

Und am allerwichtigsten...

... ist es natürlich denjenigen zu danken, die mich am längsten begleitet und mich immer unterstützt haben:

Danke an meine Eltern, und Danke an Alexander!

SCIENTIFIC PUBLICATIONS

J. Am. Chem. Soc., 130: 14904-14905 (**2008**).
M. Linke, A. Lauer, T. von Haimberger, A. Zacarias, and K. Heyne:
Three-dimensional orientation of the Q(y) electronic transition dipole moments within the chlorophyll a molecule determined by femtosecond polarization resolved VIS pump– IR probe spectroscopy.

Chem. Phys. Lett., 452: 67-71 (**2008**).
I. Corral, L. González, A. Lauer, W. Freyer, H. Fidder, and K. Heyne:
Identifying the low-lying electronic states of anthracene-9,10-endoperoxide.

J. Phys. Chem. A, 113: 6289-6296 (**2009**).
H. Fidder, A. Lauer, W. Freyer, B. Koeppe, and K. Heyne:
Photochemistry of anthracene-9,10-endoperoxide.

Phys. Chem. Chem. Phys., submitted (**2010**).
A. Lauer, A. L. Dobryakov, A. Kovalenko, H. Fidder, and K. Heyne:
Dual photochemistry of anthracene-9,10-endoperoxide studied by femtosecond spectroscopy.

In preparation (**2010**).
H. Fidder, E. Mukhtar, A. Lauer, and K. Heyne:
Emission experiments indicate the existence of anthracene-1,4-endoperoxide.

CONFERENCE CONTRIBUTIONS

DPG Spring Meeting (German Physical Society), Düsseldorf, Germany (2007).
Lauer, Corral, González, Fidder, Heyne:
Singlet oxygen generation from aromatic endoperoxides.

XXIII International Conference on Photochemistry, Köln, Germany (**2007**).
Corral, Gonzalez, Lauer, Freyer, Fidder, Heyne:
The dual photochemistry of anthracene-9,10-endoperoxide.

DPG Spring Meeting (German Physical Society), Darmstadt, Germany (2008).
Lauer, Fidder, Heyne:
Investigation of the photochemical and thermal reactions of anthracene-9,10-endoperoxide.

XXIV International Conference on Photochemistry, Toledo, Spain (**2009**).
Lauer, Fidder, Heyne, Kovalenko:
Cycloreversion dynamics of anthracene-9,10-endoperoxide.

ACU IV Symposium: Analysis and Control of Ultrafast photoinduced reactions (German Research Foundation DFG, Collaborative research center SFB 450), Berlin, Germany (2009)
Lauer, Kovalenko, Fidder, Heyne:
Photoinduced reactions and ultrafast dynamics of anthracene-9,10-endoperoxide.